UNIVERSIDADE ESTADUAL DE CAMPINAS
Faculdade de Engenharia Elétrica e de Computação

Raul Torres Bernardo

Data-Driven Control and Protection Methods to Improve Power System Angular Stability Performance

Métodos de Controle e Proteção Orientado a Dados para a Melhoria da Estabilidade Angular de Sistemas de Energia.

Campinas

2023

Raul Torres Bernardo

Data-Driven Control and Protection Methods to Improve Power System Angular Stability Performance

Métodos de Controle e Proteção Orientado a Dados para a Melhoria da Estabilidade Angular de Sistemas de Energia.

Thesis presented to the School of Electrical and Computer Engineering of the University of Campinas in partial fulfillment of the requirements for the degree of Doctor in Electrical Engineering in the area of Electrical Energy.

Tese apresentada à Faculdade de Engenharia Elétrica e de Computação da Universidade Estadual de Campinas como parte dos requisitos exigidos para a obtenção do título de Doutor em Engenharia Elétrica, na Área de Energia Elétrica.

Supervisor/Orientador: Prof. Dr. Daniel Dotta

Co-supervisor/Coorientador: Prof. Dr. Antonio Felipe da Cunha de Aquino

Este trabalho corresponde à versão final da tese defendida pelo aluno Raul Torres Bernardo, e orientada pelo Prof. Dr. Daniel Dotta.

Campinas

2023

Ficha catalográfica
Universidade Estadual de Campinas
Biblioteca da Área de Engenharia e Arquitetura
Rose Meire da Silva - CRB 8/5974

Bernardo, Raul Torres, 1990-
B456d Data-driven control and protection methods to improve power system angular stability performance / Raul Torres Bernardo. – Campinas, SP : [s.n.], 2023.

Orientador: Daniel Dotta.
Coorientador: Antonio Felipe da Cunha de Aquino.
Tese (doutorado) – Universidade Estadual de Campinas, Faculdade de Engenharia Elétrica e de Computação.

1. Sistemas elétricos de potência (Estabilização). 2. Controle automático. 3. Energia elétrica - Transmissão - Corrente contínua. I. Dotta, Daniel, 1978-. II. Aquino, Antonio Felipe da Cunha de. III. Universidade Estadual de Campinas. Faculdade de Engenharia Elétrica e de Computação. IV. Título.

Informações Complementares

Título em outro idioma: Métodos de controle e proteção orientado a dados para a melhoria da estabilidade angular de sistemas de energia
Palavras-chave em inglês:
Electric power systems stability
Automatic control
Electrical Energy - Transmission - Direct Current
Área de concentração: Energia Elétrica
Titulação: Doutor em Engenharia Elétrica
Banca examinadora:
Daniel Dotta [Orientador]
Renato Machado Monaro
Guido Rossetto Moraes
Cecília de Freitas Morais
Diego Issicaba
Data de defesa: 16-02-2023
Programa de Pós-Graduação: Engenharia Elétrica

Identificação e informações acadêmicas do(a) aluno(a)
- ORCID do autor: https://orcid.org/0000-0003-3952-797X
- Currículo Lattes do autor: http://lattes.cnpq.br/7204415885849096

COMISSÃO JULGADORA - TESE DE DOUTORADO

Candidato(a): Raul Torres Bernardo RA: 180575
Data de defesa: 16 de FEVEREIRO de 2023
Título da Tese: "Data-Driven Control and Protection Methods to Improve Power System Angular Stability Performance"

Prof. Dr. Daniel Dotta (Presidente)
Profa. Dra. Cecília de Freitas Morais
Prof. Dr. Diego Issicaba
Dr. Guido Rossetto Moraes
Prof. Dr Renato Machado Monaro

A Ata de Defesa, com as respectivas assinaturas dos membros da Comissão Julgadora, encontra-se no SIGA (Sistema de Fluxo de Dissertação/Tese) e na Secretaria de Pós-Graduação da Faculdade de Engenharia Elétrica e de Computação.

Dedico esta tese à minha querida esposa Larissa.

Agradecimentos

Foi uma longa jornada e eu estou muito feliz e agradecido por esta conquista. Todo o trabalho envolvido na construção desta tese não seria possível sem a ajuda de muitas pessoas muito especiais para mim. Infelizmente é impossível agradecer a todos, mas espero que todos se sintam contemplados neste agradecimento.

Eu tive o privilégio de estudar numa universidade pública brasileira e pude aproveitar muitos dos seus benefícios. Eu gostaria de agradecer à Universidade Federal de Ouro Preto e seus docentes, pela oportunidade de aprender engenharia, mas também pela fascinante experiência de ser um estudante em Ouro Preto. Por isso, estendo esse agradecimento à República Alambique, seus moradores e ex-alunos, e a todas as repúblicas amigas. Todo o aprendizado e experiência da minha graduação, incluindo minha participação no programa Ciência Sem Fronteiras, foram fundamentais para minha formação e para que eu chegasse até aqui.

Gostaria de agradecer à Faculdade de Engenharia Elétrica da Universidade Estadual de Campinas e seus docentes, por todo o aprendizado adquirido. Entrar num programa de pós-graduação em uma das maiores universidades da américa latina era algo que estava além das minhas expectativas e foi uma experiência muito engrandecedora. Por isso, faço um agradecimento especial ao professor Daniel Dotta que me acolheu como aluno de mestrado e me orientou por todo esse percurso de pós-graduação. O seu apoio, para além da orientação, foi fundamental para que eu chegasse até aqui. Obrigado professor!

Agradeço também ao professor Antonio Felipe da Cunha de Aquino, da Universidade Federal de Santa Catarina, meu coorientador no doutorado, que contribuiu enormemente para desenvolvimento desta tese.

Durante o doutorado, tive a oportunidade de participar do projeto SEP-PMU, numa parceria UFSC/UNICAMP/ONS, e parte dos resultados dessa tese são frutos dos estudos realizados no âmbito do projeto. Gostaria de agradecer a todo o grupo de pesquisa, em especial ao professor Ildermar Decker, pela oportunidade de poder estudar um tema tão interessante e importante.

Aos membros da banca, professora Cecília de Freitas Moraes, professor Diego Issicaba, Guido Rossetto Moraes e professor Renato Machado Monaro, muito obrigado por aceitarem o convite, por dedicarem o seu tempo na leitura deste documento, pelas palavras no dia da defesa e pelas sugestões que contribuíram para melhoria deste documento.

Gostaria de agradecer a todos os amigos que eu fiz durante a minha passagem pela Unicamp, em especial ao Lucas, Marciano, Elmer, Amanda, Tábitha e ao professor

Ricardo. Muito obrigado pela companhia e pelas longas conversas no café do LE-16.

Agradeço também aos amigos de Poços de Caldas, Rafa, Johnny, Gabi, Dani e Diegão, por todo o carinho, preocupação, torcida e apoio durante esses anos.

Esta conquista não seria possível sem o apoio da minha família. Meus pais, Maria Aparecida e Carlos Fernando, e meu irmão, Fernando, além de serem grandes exemplos e inspiração para mim, sempre me deram todo o apoio e carinho. Muito obrigado por tudo. Amo vocês!

Agradeço também aos meus sogros, Fernando e Maria, e a toda a família da minha esposa Larissa, pelo carinho, acolhimento e torcida durante esta caminhada.

Por fim, agradeço a minha querida esposa Larissa. Minha maior companhia e meu maior suporte durante todos esses anos. Ninguém sabia o quão desafiador esses últimos anos seriam. A sua força e determinação foram inspiração pra mim e pra todos ao seu redor. Muito obrigado pelo apoio, carinho, paciência e por acreditar em mim!

O presente trabalho foi realizado com apoio da Coordenação de Aperfeiçoamento de Pessoal de Nível Superior - Brasil (CAPES) - Código de Financiamento 001. Também contou com o apoio da Fundação de Aparo à Pesquisa do Estado de São Paulo (FAPESP), códigos 2016/08645-9, 2018/07375-3 e 2019/10033-0. E o projeto intitulado "Desenvolvimento de Projeto Piloto de Sistema Especial de Proteção (SEP) Utilizando-se a Tecnologia de Sincrofasores – SEP-PMU" contou com o financiamento do INESC P&D Brasil, código OC_0001856.

Acknowledgements

This study was financed in part by the Coordenação de Aperfeiçoamento de Pessoal de Nível Superior – Brasil (CAPES) – Finance Code 001; by the São Paulo Research Foundation (FAPESP), under grant numbers 2016/08645-9, 2018/07375-3 and 2019/10033-0; and by the INESC P&D Brasil during the research project "*Desenvolvimento de Projeto Piloto de Sistema Especial de Proteção (SEP) Utilizando-se a Tecnologia de Sincrofasores* – SEP-PMU", code OC_0001856.

Abstract

The growing complexity of interconnected power systems, with significant penetration of intermittent renewable sources, makes the tasks of devising power system models and defining the operating point challenging. Therefore, power systems control and protection techniques must be constantly improved to maintain the desired performance and security of operation. Exploring the availability of data from Wide-Area Monitoring Systems (WAMS), the present thesis investigates the use of measurement-based strategies for the problem of angular stability of power systems. The research was divided into two branches and the results are presented separately.

The first part of this work is dedicated to the adaptation of a data-driven control design procedure for the small-signal angular stability problem, focusing on the improvement of the inter-area oscillation damping performance. Most of the data-driven methods available need a large database and a training process or rely on a constant updating of the control law that depends on initial condition setting. In the present work, a data-driven control design method, called Virtual Reference Feedback Tuning (VRFT), is applied to design oscillation damping controllers for power systems using remote input signals from Phasor Measurement Units (PMUs). The VRFT method is a simple one-shot design procedure that uses a set of measure input and output data to design a controller in a model reference paradigm. The only requirement is a reference model for the closed-loop dynamics and two strategies are proposed for building such models, focusing on the inter-area oscillation mode of interest. The use of remote signals in a Wide-Area Damping Control (WADC) approach leads to very efficient inter-area damping controllers. Also, the fast-solving characteristic of the method is explored in an online implementation, where a previously designed controller is retuned to re-establish the damping performance after a change in operating condition. The proposed method is tested with two IEEE benchmark power systems, with one of them having a high penetration of Inverter-Based Source (IBS) generation. In both cases, the critical inter-area oscillation mode is successfully damped. Also, a Multiple-Input Multiple-Output (MIMO) formulation is presented as a secondary result. This formulation is applied to simultaneously retune multiple Power System Stabilizers (PSSs) in a coordinated control strategy, with interesting preliminary results.

The second part of the research is dedicated to the development of a generator-rejection control scheme for the transient stability assurance of power systems with parallel AC and DC transmission lines. The research was inspired by a practical challenge of the Brazilian power system, where an Special Protection Scheme (SPS) is responsible for assuring the transient stability of the system by rejecting generation at the north region in case of blocking of pole/bipole of a critical High Voltage Direct Current (HVDC) system. The proposed strategy makes use of a reduced model, considered to be simple enough so it can

be constantly updated using key measurements from the system. By doing so, the SPS can be constantly adjusted to the operating condition of the system. Assuming that such model exists, an analytical formulation is proposed to compute the generation rejection. Based on a constant current premise, an equation for the approximation of the power-angle dynamics of two-area systems with parallel AC and DC transmission is proposed. This equation is then used to compute the minimum generation rejection by means of the Equal-Area Criterion (EAC). Preliminary results are presented for a Single-Machine Infinite-Bus (SMIB) system. Then, in order to model a proper ratio between total generated power and DC transmission, as well as to model the reactive support needed to assure the correct functioning of the HVDC system, the methodology is extended to account for capacitive filters and loads. Lastly, the results for an equivalent two-machine system are presented.

Keywords: data-driven control, high voltage direct current, small-signal stability, transient stability, special protection schemes, virtual reference feedback tuning, wide-area damping control.

Resumo

A crescente complexidade dos sistemas de potência interconectados, somada a significativa penetração de fontes renováveis intermitentes, torna desafiadora a tarefa de modelagem de sistemas de potência, bem como a definição precisa das condições de operação. Explorando a disponibilidade de dados advindos dos *Wide-Area Monitoring Systems* (WAMS), a presente tese investiga a utilização de estratégias baseadas em medições no problema de estabilidade angular. A pesquisa foi realizada em duas frentes distintas e os resultados são apresentados separadamente.

A primeira parte do trabalho é dedicada a adaptação de um método de controle orientado a dados para o problema de estabilidade a pequenas perturbações, focando na melhoria de desempenho no amortecimento de oscilações interárea. A maioria dos métodos orientados a dados precisam de uma grande base de dados e de um processo de treinamento ou então são baseados na constante atualização leis de controle, que dependem de parâmetros iniciais. No presente trabalho, um método de controle orientado a dados chamado de *Virtual Reference Feedback Tuning* (VRFT) é aplicado para projetar controladores para o amortecimento de oscilações em sistemas de potência utilizando sinais de entrada remotos advindos de Unidades de Medição Fasorial (PMUs do inglês *Phasor Measurement Units*). O VRFT é um método simples que usa um conjunto de dados de entrada e saída para projetar um controlador segundo o paradigma do controle por modelo de referência (model reference control). A única exigência do método é o modelo de referência para a dinâmica em malha fechada e duas estratégias são propostas neste trabalho para a construção de tais modelos, focando nos modos de oscilação de interesse. A utilização de sinais remotos em uma abordagem *Wide-Area Damping Control* (WADC) resulta em controladores muito eficientes em amortecer as oscilações interárea. Além disso, a característica de rápida solução do método é explorada em uma aplicação de sintonia de controle online, onde o controlador projetado previamente é novamente sintonizado para reestabelecer o desempenho do sistema após uma mudança do ponto de operação. O método proposto é testado com dois sistemas de referência do IEEE, em que um desses sistemas é modificado para ter uma alta penetração de geração baseada em inversores (IBS do inglês *Inverter-Based Source*). Em ambos os casos, o modo de oscilação interárea crítico é amortecido com sucesso. Ainda, uma formulação para o caso com múltiplas entradas e saídas (MIMO do inglês *Multiple-Input Multiple-Output*) é apresentada como um resultado secundário. Essa formulação é aplicada para sintonizar múltiplos Estabilizadores de Sistema de Potência (PSSs do inglês *Power Systems Stabilizers*) do sistema de forma simultânea em uma estratégia de controle coordenado.

A segunda parte da pesquisa é dedicada ao desenvolvimento de um esquema de controle para

a rejeição de geração para assegurar a estabilidade transitória de sistemas com transmissão em CA e CC em paralelo. A pesquisa é motivada por um problema prático do sistema Brasileiro em que existe um Sistema Especial de Proteção (SEP) responsável por realizar a desconexão de geradores na região norte em caso de bloqueio de polo/bipolo de um sistema de transmissão *High Voltage Direct Current* (HVDC) crítico. A estratégia proposta faz uso de um modelo reduzido, considerado simples o suficiente para ser constantemente atualizado utilizando dados de medição do sistema. Dessa forma, o SEP pode ser constantemente ajustado para a condição de operação atual do sistema. Assumindo que tal modelo existe, uma formulação analítica é proposta para calcular o corte de geração. Baseado numa premissa de operação em corrente constante, é proposta uma equação para aproximar a dinâmica potência-ângulo de sistemas duas áreas com transmissão CA e CC em paralelo. Esta equação é então utilizada para o cálculo da mínima rejeição de geração por meio do critério das áreas iguais (EAC do inglês *Equal-Area Criterion*). Resultados preliminares são apresentados para um sistema máquina contra barramento infinito. Em seguida, de forma a considerar uma proporção mais realista entre potência total gerada e potência transmitida em CC, bem como modelar o suporte de reativo necessário para garantir o funcionamento adequado dos elos CC, a metodologia é estendida para contabilizar os filtros capacitivos e cargas. Por fim, os resultados são apresentados para um sistema equivalente de duas máquinas.

Palavras-chaves: controle orientado a dados, estabilidade à pequenas perturbações, estabilidade transitória, HVDC, VRFT, WADC.

List of Figures

List of Tables

List of Abbreviations and Acronyms

AC Alternate Current

AFPSS Adaptive Fuzzy Logic PSS

ANN Artificial Neural Networks

AVR Automatic Voltage Regulator

DC Direct Current

DFIG Doubly Fed Induction Generators

DMI Data-driven Matrix Inequality

EAC Equal-Area Criterion

EPS Electric Power System

FACTs Flexible AC Transmission Systems

GrHDP Goal representation Heuristic Dynamic Programming

GRS Generation Rejection Scheme

GUs Generator Units

HVDC High Voltage Direct Current

IBS Inverter-Based Sources

LCC Line-Commutated Converter

LMI Linear Matrix Inequality

LQR Linear Quadratic Regulator

LTI Linear Time-Invariant

MFAC Model-Free Adaptive Control

MIMO Multiple-Input Multiple-Output

NETS New-England Test System

NMP Non-Minimum Phase

ONS National Operator of the System

PMU Phasor Measurement Unit

POD Power Oscillation Damper

PPD Pseudo-Partial Derivative

PSS Power System Stabilizer

rPSS remote input Power System Stabilizer

SIN Brazilian National Interconnected System

SIPS System Integrity Protection Scheme

SISO Single-Input Single-Output

SMIB Single-Machine Infinite-Bus

SPS Special Protection System

SVCs Static VAr Compensators

VRFT Virtual Reference Feedback Tuning

WADC Wide-Area Damping Controllers

WAMS Wide-Area Monitoring Systems

List of Symbols

j	Imaginary unit, defined as $j^2 = -1$
$_{,t}$	Subscript notation used to indicate a time-varying parameter
$\mathbb{R}^p$	The set of real numbers with dimension p
$a^\top,\ A^\top$	Transposed vector a or matrix A
$\angle$	Phase angle of a complex number
$\lvert c \rvert$	Magnitude (absolute value) of a complex number c
ω_n	Natural frequency of an oscillation mode
ζ	Damping ratio of an oscillation mode
ζ_{min}	Minimum damping ratio of the reference model
s	Complex variable used for the Laplace transform
q	Forward shift operator
z	Complex variable used for the z-transform
$\mathcal{L}$	Laplace transform operator ($\mathcal{L}^{-1}$ inverse Laplace transform operator)
$\mathcal{Z}$	z-transform operator ($\mathcal{Z}^{-1}$ inverse z-transform operator)
$\lVert x[n] \rVert_2$	2-norm of the signal $x[n]$
$\lVert \mathbf{x} \rVert_2$	2-norm of the vector (data array) $\mathbf{x}$
$\mathbf{u}$	Data row vector with N samples of the signal $u[n]$, i.e., $\mathbf{u} = \{u[1], \ldots, u[N]\}$
$\mathbf{\Theta}$	$p \times N$ data matrix that contains N samples of the p-dimensional signal $\Theta[n]$, i.e., $\mathbf{\Theta} = \{\Theta[1], \ldots, \Theta[N]\}$
$u(t),\ y(t)$	Continuous-time signals
$u(nt),\ y(nT)$	Sampled signals
$u[n],\ y[n]$	Discrete-time signals
$\bar{r}[n]$	Discrete-time *virtual* reference input signal
$g(t)$	Impulse response of a continuous-time LTI system

$G(s)$	Transfer function of a continuous-time LTI system
$g[n]$	Impulse response of a discrete-time LTI system
$G[\mathsf{q}]$	Transfer operator of a discrete-time LTI system
$G[z]$	Transfer function of a discrete-time LTI system
$y_d[n]$	Desired closed-loop output signal
$y_p[n]$	Predicted closed-loop output signal
$y_{est}[n]$	Output signal of the estimated model
$y_{CL}[n]$	Simulated output signal of the closed-loop system with the controller $C[z, \rho]$
$M_d(s)$	Continuous-time reference model
$M_d[z]$	Discrete-time reference model
$C[z, \rho]$	Discrete-time controller transfer function parameterized in terms of ρ
$C_i[z]$	Discrete-time ideal controller transfer function
ρ	Real vector used to parameterize the controller; dimension p
$\bar{C}(s)$	Array of p rational continuous-time transfer functions which forms a linear parameterized controller with ρ
$\bar{C}[z]$	Array of p rational discrete-time transfer functions which forms a linear parameterized controller with ρ. Discretized version of $\bar{C}(s)$
$\hat{\gamma}$	Remotely measured signal filtered by a washout filter
$y[n] = \hat{f}_{a-b}$	filtered frequency difference between bus a and b
δ_r	Relative rotor angle
δ_{ep}^{sta}	Relative angle at the stable equilibrium point
δ_{ep}^{uns}	Relative angle at the unstable equilibrium point
$\lvert S_{\mathrm{rec},t}\rvert\angle\varphi_{\mathrm{rec},t}$	Magnitude and phase angle of the apparent power drained by all converters at the rectifier side
$\lvert S_{\mathrm{inv},t}\rvert\angle\varphi_{\mathrm{inv},t}$	Magnitude and phase angle of the apparent power drained by all converters at the inverter side

Contents

1 Introduction

1.1 Motivation

The Electric Power System (EPS) generation paradigm is currently experiencing remarkable changes. Around the world, the conventional fossil fuel based power plants have been replaced by renewable generation, e.g. large scale photovoltaic and wind power plants, motivated by the development of more sustainable and competitive energy sources (MILANO, 2018). Additionally, in order to integrate the energy from this large scale renewable sources into the main centers of a power grid, the existing capacity of the transmission system needs to be enhanced and modified so that the High Voltage Direct Current (HVDC) links can be more efficient at transmitting bulk power over larger distances (HUMPERT, 2012).

The physical characteristics of the renewable sources and HVDC transmission and the fact that they are connected to the Alternate Current (AC) system via power electronics, makes their interaction with the grid substantially different from the traditional AC network and generation devices. The major challenge of substituting directly connected synchronous machines and their well-known dynamics and controllers for power electronics-interfaced generation and transmission is that their regulation and interaction with the rest of the system is yet to be fully understood. Besides that, the growing penetration of Inverter-Based Sources (IBS) increases the difficulty of determining the operating conditions of the system, due to the intermittent characteristics of these generations. Also, the high order of the power electronic device models available may turn the model-based analysis and control design impracticable, or even unfeasible, for practical large-scale power systems.

Nowadays, thanks to the advance of the Wide-Area Monitoring Systems (WAMS), the power system operators have access to a large amount of data containing valuable information about the power system dynamics. The easy access to the data is changing how the operators evaluate the power system dynamics, with the model-based analysis increasingly being complemented by data-based approaches. In this new environment, there is a clear need for new tools capable of extracting information directly from data in order to improve the power system analysis, control and protection. In this context, this work proposes to explore new data-based methodologies capable of improving the power system dynamic performance, focusing on the angular stability.

1.2 Power Systems Angular Stability

The power system stability, in general terms, is defined as the capability of the system to stay at an equilibrium point under normal operating conditions and to return to an acceptable operating condition when subjected to disturbances (KUNDUR, 1994).

During its operation, an electric power system is subjected to a great variety of disturbances, such as load fluctuations, short-circuits, line tripping, etc. Those disturbances have different consequences over the system dynamics and may lead to instability in different ways. The power system stability was originally classified over three main categories: the angular stability, voltage stability and frequency stability. Recently, due to the increased penetration of IBS, two more categories were added: the resonance stability and converter-driven stability (HATZIARGYRIOU, 2021). This classification, presented in Figure 1.1, facilitates the analysis of the different phenomena related to the system dynamics and allows a better understanding of the different sources of instability which a power system is subjected.

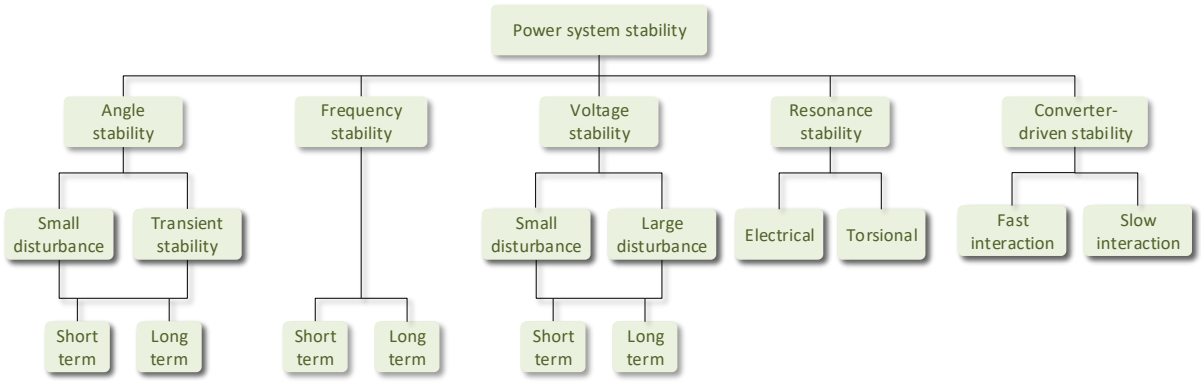

Figure 1.1 – Power system stability classification (HATZIARGYRIOU, 2021)

The present work is dedicated to study and design of control techniques regarding the angular stability of power systems. The study is divided over two parts, exploring the two subcategories of the angular stability, the small-signal stability and the transient stability.

The power system angular stability (or rotor angle stability) is the ability to maintain all the synchronous machines of the system in synchronism, after a large or small disturbance. This synchronism is kept by the equilibrium between the electromagnetic torque and the mechanical torque at each synchronous machine (GÓMEZ-EXPÓSITO, 2018).

Small-signal stability: Is the capability of maintaining the synchronism after small disturbances. The disturbances are considered to be sufficiently small so that the linearization of system equations is permissible for purposes of analysis (KUNDUR, 1994). The analysis is done using the linearized model of the power system at a specific equilibrium

point or at a set of equilibrium points. In the context of small-signal stability, the instability is characterized by the non oscillatory increasing of the rotor angle, due to the lack of synchronizing torque, or by the oscillations with increasing amplitude of the rotor angle, due to the lack of damping torque (KUNDUR, 2004).

Large-disturbance rotor angle stability or transient stability: Is the ability of the power system to maintain its synchronism when subjected to large disturbances. Those disturbances may cause large excursions of generator rotor angle. In these scenarios, the nonlinearities of the power system dynamics cannot be neglected. The instability is characterized by aperiodic angular separation, due to insufficient synchronizing torque, usually in the first swing of the oscillation (KUNDUR, 2004).

1.3 Objective

The main goal of this work is to adapt existing techniques and propose new ones for the data-driven control and protection of power systems, to improve their dynamic performance, focusing on the angular stability (small-signal and transient stability).

During the research period that resulted in this thesis, two main problems were studied. Both of them related with the usage of measured data to improve specific performance criteria of power systems and regarding angular stability enhancement. However, different type of phenomena were studied, each one associated with a subcategory of angular stability. The first branch of the research was dedicated to the study of a data-driven control design method and its adaptation for the design of power system damping controllers using remotely measured signals as control inputs. Thus, it is related with the direct use of measured data to enhance the small-signal stability of power systems. The second branch of the research focused on the transient stability analysis of two-area power systems interconnected by parallel AC and Direct Current (DC) lines, i.e., with embedded HVDC systems. In that scenario, an strategy to approximate the power-angle dynamic response of such systems was studied and the embryo of an special protection scheme to assure the transient stability of the system is proposed. Even though no measurement data is directly used, the study is focused on reduced models, simple enough to be easily updated in the future using measurements from the system. So, the research was divided in two parts and the specific objectives of each branch of the research are presented as follows.

Part I - Data-driven control method for power system small-signal angular stability enhancement

For the first part of this work, the objective is to propose a data-driven methodology for the design of power system damping controllers using remotely measured signals. This main goal can be separated in intermediary objectives:

- To successfully adapt a traditional offline data-driven control method, that was never applied for power system oscillation damping problem before, for the design of Single-Input Single-Output (SISO) power system damping controllers.
- To propose a data-driven solution to build the reference model needed for the data-driven control design method chosen.
- To successfully design remote-input power system damping controllers using measured data from nonlinear time domain simulations, without needing the linearized model of the system.
- Improve the damping performance of benchmark power system models using the proposed technique.

The following tasks are defined as secondary objectives:

- To perform the online re-tuning of a power system damping controller using the proposed technique.
- To adapt the methodology for the Multiple-Input Multiple-Output (MIMO) case.

Part II - Transient stability assurance with a generator-rejection control for parallel AC and DC transmission systems

For the second part of this work, the goal is to develop a generation-rejection protection scheme for power systems with parallel AC and DC transmission lines to assure the transient stability of the system in case of forced outage of the HVDC transmission. To achieve this main goal, the following intermediary objectives are proposed:

- To propose a mathematical expression to model the electric power output of two-machines systems with parallel AC and DC transmission lines as a function of the relative rotor angle between the generators (power-angle equation).
- To successfully perform the transient stability analysis of a two-machine test system using the proposed power-angle equation.
- To propose an algorithm based on the proposed equation and the Equal-Area Criterion (EAC) to compute the minimum generation rejection needed to assure the transient stability of the system in case of forced outage of the HVDC transmission.

1.4 Structure of the work

The rest of this document is divided in three parts, one for each branch of the research and one for the conclusions and final comments. Each part is divided in chapters and the structure of each part is presented as follows.

Part I - Data-driven control method for power system small-signal angular stability enhancement (Chapters 2 to 5)

The Part I of the work focus on the small-signal angular stability enhancement using a data-driven control method. Chapter 2 begins with an introduction about the small-signal stability problem followed by a review of the literature at Section 2.1, focusing on data-driven applications. The problem statement and contributions of this part of the work are also presented at this chapter at Sections 2.2 and 2.3. The theoretical background needed for the proposed application is summarized in Section 2.4, including the mathematical formulation of the data-driven control method and the control structure explored in this work. The Chapter 3 contains the methodology for the data-driven design of power systems damping controllers. The chapter begins with the proposed modification of the data-driven method to cope with the desired power systems application and a series of discussions about the proposed method is presented in sections 3.1 to 3.4. The data-driven method explored in this work relies on a reference model to perform the control design and two methodologies to build such reference model are presented in Section 3.5. A discussion regarding the proposed application of the method is presented in Section 3.6. The results obtained with the proposed methodology are presented in Chapter 4. Two benchmark test systems are used, Section 4.1 presents the results with the Brazilian 7-Bus Equivalent System and Section 4.2 is dedicated to the 39-Bus New-England Test System. Lastly, some comments about the results are presented in Section 4.3. Chapter 5 is the last chapter of this part of the work and it is dedicated to a further discussion regarding the proposed method, where a strategy to expand the method for the MIMO case is proposed and preliminary results are presented.

Part II - Transient stability assurance with a generator-rejection control for parallel AC and DC transmission systems (Chapters 6 to 9)

The Part II of the work is dedicated to the transient stability assurance of power systems with parallel AC and DC transmission, where a generator-rejection control algorithm is proposed. The research problem is introduced in Chapter 6, with a review of the literature in Section 6.1, the problem statement in Section 6.2, the contributions of the work in Section 6.3, and the fundamentals about HVDC systems and transient stability analysis in Section 6.4. The next chapter is dedicated to the methodology applied, so Chapter 7 begins with the proposition of an equation to model the electric power output of two-machine systems with parallel AC and DC transmission in Section 7.1. Then, a series

of assumptions are proposed in Section 7.2 so this equation can be reduced to a power-angle equation. The transient stability criterion for the proposed problem is introduced in Section 7.3 together with a preliminary algorithm for generator-rejection control. In Section 7.4 the stability criterion is modified to consider a time interval between the fault occurrence and the control action and an updated algorithm for generator-rejection control is presented. Chapter 8 is dedicated to the proof of concept and preliminary results. First, the proposed equation for the approximation of the power-angle curve and the preliminary algorithm for generator-rejection control are tested with a Single-Machine Infinite-Bus (SMIB) system and the results are presented in Section 8.1. Then, the updated algorithm for generator-rejection control is tested with a two-machine test system and the results are presented in Section 8.2. A discussion regarding the voltage support influence over the results and the expected dynamics in a practical application of the method are also presented in this section. The results of this chapter are commented in Section 8.3. In Chapter 9 the methodology is extended to include shunt filters and loads, so the dynamic response of the system is closer to the expected one, based on the discussion presented in the previous chapter. The updated formulation to cope with those modifications is presented in Section 9.1. The methodology is tested with an updated version of the two-machine system, presented in Section 9.2 together with the results obtained. Section 9.3 summarizes the chapter and present some comments about the results.

Part III - Conclusions and final comments (Chapter 10)

The conclusions and final comments regarding both branches of the research presented in this work are concentrated in Chapter 10. First, a summary of the thesis is presented in Section 10.1. Then, Section 10.2 is dedicated to the conclusions about Part I and II of this document. Published works related to the research of this thesis are cited in Section 10.3. Lastly, final comments regarding future works are presented in Section 10.4.

Part I

Data-driven control method for power system small-signal angular stability enhancement

2 Introduction

Small Signal Stability

As it was introduced in Section 1.2, the *small-signal stability* of a power system is related with the capability of the power system to maintain angular stability after a small disturbance. And, in this context, the instability is usually characterized by oscillations with increasing amplitude. Those oscillations are of an electromechanical nature and are classified depending on which component of the power system they affect (PAL; CHAUDHURI, 2005).

- *Intraplant mode oscillations*: Corresponds to oscillations between machines of the same power generation site. The frequency of those modes varies between 2.0 and 3.0 Hz depending on the parameters of each machine and the reactance connecting them. These oscillations happens within the generation plant and do not affect the rest of the power system.
- *Local plant mode oscillations*: Are oscillations between a generator and the rest of the system, with frequencies between 1.0 and 2.0 Hz. This type of oscillation impacts the local generator and the line connecting it to the system.
- *Inter-area mode oscillations*: These are oscillations of 1.0 Hz or less, between two coherent generator groups. They are complex phenomena, that involves many parts of the power system.
- *Control mode oscillations*: Oscillations with frequency greater that 3.0 Hz, associated with poorly tuned controllers such as exciters, HVDC converters and Flexible AC Transmission Systems (FACTs) devices (DILL, 2013).
- *Torsional mode oscillations*: Are caused by the interaction of a turbine generator shaft system with the grid. The frequency ranges between 10 and 46 Hz.

From a global power system stability point of view, poorly damped inter-area oscillation modes represents the greatest threat since they affect different areas of the system and can lead to system separations or even wide-scale blackouts (PAL; CHAUDHURI, 2005). The damping ratio of those oscillation depends of different attributes of the system, such as the transmission line parameters, the nature of the loads, the power flow (specially at the lines connecting the two areas of the system). Thus, in the context of small-signal stability, one of the main goals is to assure that those oscillation modes are properly damped and different strategies have been proposed over the years to reach

this goal. The most common and cost-effective control strategy applied to damp local and inter-area modes is the Power System Stabilizer (PSS). Traditionally designed as a lead-lag compensator, the PSS is installed at the voltage loop control of a generator to provide extra damping to rotor oscillations by adding an auxiliary stabilizing signal to its excitation input (KUNDUR, 1994). However, the effectiveness of the PSS over inter-area oscillations is limited due to its local implementation. That is, the inter-area modes may not be sufficiently controllable and observable in the local signals available at the generator at which the PSS is installed (ABOUL-ELA, 1996). Besides the PSSs, other devices can be applied to improve the damping performance of power systems. The FACTs devices, that are commonly used to extend the usability of existing transmission systems, can also be used to damp inter-area oscillations (CHAUDHURI; PAL, 2004; SIMÕES, 2009). Supplementary controllers for HVDC systems can be designed to damp inter-area oscillations (AZAD, 2013). Also, PODs (Power Oscillation Dampers) of wind turbines can be applied to damp inter-area modes (LIU, 2015).

With the development of WAMS, various strategies have been proposed using remote measurements to overcome the limitations of local controllers in damping inter-area oscillations. The WAMS are monitoring systems that can keep track of various parameters of the power system, such as voltage, current, phase angle, and frequency (XIE, 2006; PHADKE, 2008). As the WAMS are based on PMUs (Phasor Measurement Units), the measured data is synchronized by Global Positioning System (GPS) clocks, making it possible to combine signals from geographically distant points of the system to design Wide-Area Damping Controllers (WADC). Different techniques have been proposed to improve the damping performance of the PSSs such as the multi-input PSS (KAMWA, 1998; CHOW, 2000), were remote measure signals can be used to enhance the observability of the controllers over the inter-area oscillation mode. This multiple input PSS approach can also be efficient in system with high penetration of wind generation (NANNI, 2019). More complex control structures can be obtained by combining multiple measurements of WAMS. In Kamwa, Grondin and Hebert (2001), remote Phasor Measurement Unit (PMU) signals are used as inputs for PSSs in a decentralized/hierarchical architecture. In Dotta, Silva and Decker (2009), multiple PMU signals are used in a two-level hierarchical control based on PSS-like controllers, combining a decentralized and a centralized MIMO structures. The controllers of photovoltaic plants can also be used in a WADC strategy, as described in Nanni (2021). In Gupta, Pal and Vittal (2021), PSSs, Static VAr Compensators (SVCs) and HVDC based Supplementary Damping Controllers (DC-SDCs) are coordinately tuned in a WADC strategy. Besides the various control structures that can be applied to improve the oscillation damping performance of power systems, the control design method is also a key point of any control strategy and large variety of methods have been explored. A brief review of the most common methods is presented as follows.

2.1 Review of the Literature

Model Based Control Design for Power Systems Oscillation Damping

As mentioned above, the most common type of controller applied to damp electromechanical oscillations is the PSS. The phase compensation method, by means of the frequency-response analysis, is the traditional method used to design this type of controllers (LARSEN; SWANN, 1981). However, other classical control design methods, such as the root-locus design or the pole placement with state-space models, can be applied to design PSS (CHOW, 2004). Using equivalent single machine infinite bus systems to model the power systems, those classical methods were used to design controllers to damp local oscillation modes (CHOW; SANCHEZ-GASCA, 1989). One approach for improving the inter-area damping performance of power systems is the coordinated design of multiple local controllers. A method based on the frequency response analysis is presented in Dysko, Leithead and O'Reilly (2010) to simultaneously tune two independent PSSs.

Considering the high variability of the power systems parameters (load changes, faults, intermittent renewable sources) the precise modeling of power system is a challenging task. Therefore, robust control design methods have been applied to overcome uncertainties in the power system modeling stage. Even though there are many different approaches for the coordinated design of power system damping controllers in the literature, the robust control design methods can be divided into two basic types: evolution-based search and optimization/search analytical methods (BENTO, 2018). One of the most common evolution-based search approaches is the genetic algorithm method (BOMFIM, 2000; CASTOLDI, 2014). Another common approaches are the Ant Colony Optimization (LU, 2013) and Particle Swarm Optimization (SHAHGHOLIAN; MOVAHEDI, 2016). Among the optimization/search analytical methods, a widely explored one is the Linear Matrix Inequality (LMI) approach, where the control design is formulated as a convex optimization problem and solved with an interior point algorithm (BOYD, 1994). The LMIs have been applied to coordinately design PSSs (RAMOS, 2004; RAMOS, 2005; BERNARDO, 2018) and Thyristor-Controlled Series Compensators (KUIAVA, 2006). In Elkington and Ghandhari (2013), LMIs and regional pole placement are used to determine the feedback gains for multiple wind farms simultaneously so that the power system satisfies a minimum damping ratio. One approach to overcome the limitation of the LMIs' convex formulation is to use a Bilinear Matrix Inequality formulation and solve it with a two-step LMI method (DENG; ZHANG, 2014). Another extensively explored optimization/search analytical method is the Linear Quadratic Regulator (LQR). By applying structural constraints to the LQR formulations, it is possible to design output feedback controllers for power systems through the generalized Riccati equation (COSTA, 1995; SIMÕES-COSTA, 1997; BENTO, 2018).

With the development of PMUs and the establishment of WAMS, strategies

based on WADC have become the most common approach to improve the inter-area damping performance of power systems. As it was mentioned previously, different structures are possible and also different control design methods can be applied. Commonly, the WADC design problem is formulated as an optimization/search problem in the literature (KAMWA, 1998; KAMWA, 2001; LI, 2016). In Chow, Sanchez-Gasca, Ren and Wang (2000), the multi-input PSS is designed with an LMI method. In Dotta, Silva and Decker (2009), the generalized Riccati equation is used to solve the LQR problem and design the two-level hierarchical control. In Bernardo and Dotta (2018) a quase-Newton BFGS (Broyden-Fletcher-Goldfarb-Shanno) search method is combined with robust verification step based on LMIs to design a centralized WADC. The same quasi-Newton search method is applied in Nanni, Bernardo and Dotta (2019) and Nanni (2021). In Gupta, Pal and Vittal (2021), a model reduction method is applied and a LMI-based mixed H_2/H_∞ robust control formulation is used to design the WADC.

One common factor of all aforementioned control design methods is the necessity of detailed information about the power systems in order to build the dynamic models. However, the challenge of building accurate power system models grows continuously. The increasing penetration of renewable IBS also increases the complexity of the power system models, due to the high order of the inverter models and the intermittent characteristics of those energy sources. A similar difficulty is posed by HVDC links, with high order converter models and complex dynamic interactions between AC and DC transmission systems. Even though robust control techniques have been proposed to account for uncertainties related with power system modeling, the high complexity of modern interconnected power systems can still be a threat to those model-based approaches. Another approach to overcome those uncertainties is to use data-driven methods. Considering the large amount of synchronized data available in modern power system, due to the increasing implementation of WAMS, and the challenge of building accurate power system models, data-driven methods seem to be the natural choice to improve WADCs and keep them efficient in the face of the new challenges.

Model-free Control Design for Power Systems Oscillation Damping

A large variety of measurement-based approaches have been proposed in the context of power system oscillation damping. One of the first strategies described in the literature is the use of fuzzy logic controllers. In Abido and Abdel-Magid (1998) a Fuzzy Basis Function Network based Power System Stabilizer (FBFN PSS) is proposed, combining the neural networks and fuzzy logic systems methodologies. A predefined set of data is used to train the function network that is used later to constantly update the parameters of a PSS, using power and voltage measurements. A similar approach is used in Abdelazim and Malik (2003) to propose an Adaptive Fuzzy Logic PSS (AFPSS), where the authors claim that, compared to a conventional neural network, the training time is

dramatically decreased, because of the a priori knowledge embedded in the fuzzy system. An online training method is applied to identify the model of a simple SMIB system and, based on the identified model, the AFPSS tracks the plant variations as they occur. In both cases a training stage, either online or offline, is necessary.

The two aforementioned methods are examples of data-driven approaches applied to design local damping controllers. However, it is known that local controllers have limited affect over inter-area oscillations. As for the model-based approaches, WAMS have been explored to propose WADC using data-driven methods. In Chaudhuri, Domahidi, Chaudhuri, Majumder, Korba, Ray and Uhlen (2010), an indirect adaptive power oscillation damping (IAPOD) is proposed, using wide-area measurements. An adaptive controller with a fixed structure is used, whose parameters are updated by a pole-shifting control algorithm. The algorithm is applied to an auto regressive moving average (ARMA) model of the power system, whose parameters are estimated using a Kalman Filtering technique. So, a model-based control design is used, but the model itself is estimated from data. Different devices can also be coordinately tune to improve the inter-area damping performance, as in Eriksson and Söder (2010), where the pole placement method is applied to coordinately design controllers for multiple HVDC links, based on an estimated open-loop system model.

With the evolution of the Artificial Neural Networks (ANN), more efficient data-driven methods were proposed for the WADC design. In Zeng, Yao, Zeng, Li, Fang, Ai, Wen and He (2019), a Goal representation Heuristic Dynamic Programming (GrHDP) is used to develop a data-driven adaptive wide-area damping controller (D-WADC) for back-to-back voltage source converter HVDC (BTB-VSC-HVDC) systems. The GrHDP adopts three ANN structures whose weights are updated to adapt to the change of system operating condition. The ANN training process is done with offline simulation data and historical operation data. In Zhang, Hu, Cao, Yi, Huang, Liu, Chen and Blaabjerg (2020), a deep reinforcement learning (DRL) technique, called deep deterministic policy gradient (DDPG), is applied to adjust the parameters of a Static Synchronous Compensator Additional Damper Controller (STATCOM-ADC) using measured data. The parameters of the STATCOM-ADC are selected to accomplish a pole placement requirement and this tuning procedure depends on the accuracy of an ANN model from which the transfer function of the actual system is estimated. This ANN is trained using a one-yearlong realistic wind speed data set. In Chakrabortty (2021), the authors invite engineers to explore an hierarchical reinforcement learning methods to the wide-area control problem. It is assumed that a sufficient number of current and voltage sensors are placed in order to estimate the states of the system, as a state-feedback control is proposed using a linear quadratic regulator. Also, reduced-order model learning and offline training of the ANNs are required.

In Xu, Qu, Harvey and Namerikawa (2020), two novel tools are applied to the power system control, the analytical framework of passivity-short dynamic systems and an efficient computational algorithm involving Data-driven Matrix Inequality (DMI). Reduced-order load flow equations are identified using WAMS data and the impact of passivity-short subsystems of coherent generators and their interconnections are quantified using DMI. The dynamic matrices of the system may be built from data, but are still needed for DMI procedure. In Mukherjee, Babaei, Chakrabortty and Fardanesh (2020), frequency measurements from PMU are used to identify a reduced-order state-space model of the grid that is used to design a linear quadratic gaussian (LQG) based optimal FACTS controller. The design method is applied to an ultra-large scale power system. However, as a model-based control design was used, the success of the method dependents on the efficiency of the identification methods and accuracy of the estimated models.

A method independent of models and estimations is presented in Lu, Zhao, Men, Tu and Han (2015), where the Model-Free Adaptive Control (MFAC) is applied to design a Wide-Area Power System Stabilizer (WAPSS). A concept called Pseudo-Partial Derivative (PPD) vector is used to dynamically linearise the non-linear system along the dynamic operation points and is updated at every time step with the I/O measurement data. In Zhao, Yuan, Lu, Zhang, Li and Chen (2016), the authors extended the method for the MIMO case, where a coordinated design is achieved considering the multiple controller interactions and system noises. In both cases the initial parameter settings of the MFAC-WAPSS are obtained using a genetic algorithm and simulation data. In Shi, Cao, Li, Ma, Shahidehpour, Wu and Li (2020), a modified version of the MFAC method is used to design a WADC for Doubly Fed Induction Generators (DFIG) wind generators. The authors combined a control direction correction method with a PPD updating law to develop a Data-Driven Adaptive Control WADC (DDAC-WADC). The controller is capable of finding the right control direction during the initial stage of the simulation.

In summary, a large variety of measurement-based techniques have been proposed regarding power systems stability and control. Considering the ones that focus on the electromechanical oscillation damping problem, they can be roughly divided into three main groups. Some of them apply traditional model-based control techniques at reduced order models, which are built using measurement-based approaches (CHAUDHURI, 2010; XU, 2020; MUKHERJEE, 2020). Another large group is formed by methods that uses ANN (usually combined with other techniques) to design various types of damping controllers using data acquired from the system (ABIDO; ABDEL-MAGID, 1998; ZENG, 2019; ZHANG, 2020). A drawback for those ANN approaches is the management of the data needed to build a representative database for the training process, which usually requires manual data labeling. Also, the training process can be time demanding, discouraging their use. Lastly, there is a group of methods that do not need a training procedure and uses online data measurements to constantly update a control law (LU, 2015; ZHAO,

2016; SHI, 2020). Initial parameters for those control laws are necessary and may be challenging to find. Also, the constant update of the control law, despite resulting in a satisfactory damping performance, may be difficult to implement on practical power system applications. In the present work, a control design method that do not fit into any of those groups is studied for a WADC application.

The data-driven approach is a change of paradigm in field of power system oscillation damping control and new methodologies are being proposed and tested daily. The present work intends to contribute to research field of data-driven applications to small-signal stability of power systems, specially in the inter-area oscillation damping problem. Focusing on the cost-effectiveness of traditional PSSs, a one-shot data-driven method is adapted for the design of WAPSS controllers, using remote measurements.

2.2 Problem Statement

The growing penetration of IBS increases the difficulty of determining the system operating conditions because of the intermittent characteristics of these generations. This increasing variability may cause the system to operate in conditions not considered during the modeling and control design stages. Thus, the previously designed model-based controllers may not be sufficient to guarantee the desired performance under this new operating conditions. At the same time, the advance in WAMS increased the availability of real-time data measurements with valuable information about the current dynamic condition of the power systems. That is, variations on the operating condition can be constantly monitored. Therefore, data-driven methods are very convenient for nowadays power systems applications.

The main goal of the study presented in this part of the thesis is to obtain a simple data-driven procedure to design PODs that use remotely measured PMU signals and focus on poorly damped inter-area oscillations. In addition, a cost-effective and simple structure is desired, therefore, the method must be suitable for the design of PSS-like controllers. Considering the high variability of nowadays power systems, the capability of adapting the method to new operating conditions is very important. Therefore, the second goal is to be able to automatically re-tune the previously designed controller with minimum effort, in cases of variations in the operating condition. So, the following questions are addressed in this part of the work.

- Is it possible to design a traditional[1] power system damping controller using measured input/output data from the system, without using a model-based control design

[1] By traditional the author means a controller defined as a rational transfer function, with fixed parameters.

technique, without an extensive/costly training procedure and without setting an initial condition closed-loop controller or control law?

- Is it possible to use a new set of measured input/output data from the system to update (re-tune) the previously designed controller to manage changes in the operating condition?

2.3 Contribution

In the present work, a data-driven control design method, called Virtual Reference Feedback Tuning (VRFT) (CAMPI, 2002a), is adapted to design power system damping controllers. Those controllers are designed to enhance the damping ratio of inter-area oscillations that were deteriorated by variations on the operating conditions of the system. Variations that are either uncertain or very hard to model, what encourages the use of a data-driven procedure. The VRFT method has a simple one-shot design procedure that uses only input/output data from the system, making it convenient for the proposed application. It does not require any training procedure or initial closed-loop controller setting. The only requirement of the method is the desired closed-loop dynamic of the system expressed as a transfer function. In the VRFT approach, the controller design is converted into an identification problem that can be solved with a least-squares method. Its one-shot characteristic avoids any iterative procedure or optimization method. Those qualities encouraged the search for VRFT controllers application on power systems, however, until the research proposed in this thesis, the VRFT method had not yet been applied to the problem of damping oscillations in electrical power systems. Therefore, this work intents to investigate the feasibility of applying VRFT to design power systems WADC.

The main contributions of this work are:

- The adaptation of the VRFT formulation for the power system damping control. This adaptation is done by positioning the controller in the feedback path (traditional PSS location) instead of the forward path position used for the reference-track problem, for which the VRFT was originally proposed for.
- Since the literature lacks reference methodologies for building the reference model for the proposed application, two procedures are proposed in this work, taking into account the oscillation damping requirement.
  - The predominant oscillation mode detected on the measured data is used to build a traditional second order transfer function that matches the overshoot and steady-state characteristics of the measured output data, but with an improved damping ratio.

  - By combining a standard black-box identification method with the traditional pole-placement used in small-signal stability control design, the reference model is built to match the measured input/output dynamics of the measured data, but with an enhanced damping performance. As a consequence, one has a simple procedure for the challenging task of devising the reference model for the proposed application.

- Two features are explored: first a WAPSS is designed, using remotely measured signals to compose the controller input signal and taking into account the communication delay; then, the proposed method is applied to re-tune the previously designed WAPSS, so the damping performance is preserved after variations in the operating conditions.

- The use of two nonlinear power system models that belong to a set of benchmark models for the analysis and control of small-signal oscillatory dynamics in power systems. Also, a large penetration of IBS generation is considered in the larger power system model, decreasing significantly the inter-area damping performance of the system.

2.4 Fundamentals

2.4.1 Linear Systems Representation

Consider a Linear Time-Invariant (LTI) system, it is known that for a given input signal $u(t)$, its output $y(t)$ can be described as follows (LJUNG, 1999)

$$y(t) = \int_{\tau=0}^{\infty} g(\tau)u(t-\tau)d\tau, \tag{2.1}$$

where $g(t)$ is the impulse response of the system. In the context of data-driven systems it is common to deal with discrete-time signals, obtained directly from discrete-time systems or, as in the cases explored in this work, sampled signals from continuous-time systems. So, the sampled output of the LTI system $y(kT)$ can be defined as

$$y(kT) = \int_{\tau=0}^{\infty} g(\tau)u(kT-\tau)d\tau, \tag{2.2}$$

where $k = 1, 2, \ldots$ and T is the sampling interval. Assuming that the input signal $u(t)$ is kept constant between the sampling instants and that T is one time unit (for ease of notation) and using n to enumerate the sampling instants, one can write (2.2) as [2] (LJUNG, 1999)

[2] In this work, the brackets [] are used to represent discrete signals (or sequences of samples) and the parentheses () are used for continuous-time signals. Note that some of the references used in this work do not follow this same notation. This difference in notation between continuous-time and discrete-time signals was chosen to avoid misinterpretations.

$$y[n] = \sum_{k=1}^{\infty} g[k]u[n-k], \qquad n = 0, 1, 2, \ldots \tag{2.3}$$

Using the concept of *forward shift operator* q

$$\mathsf{q}u[n] = u[n+1]$$

and *backward shift operator* q^{-1}

$$\mathsf{q}^{-1}u[n] = u[n-1],$$

the Equation (2.3) can be written as

$$y[n] = \sum_{k=1}^{\infty} g[k](\mathsf{q}^{-k}u[n]) = \left[\sum_{k=1}^{\infty} g[k]\mathsf{q}^{-k}\right] u[n] = G[\mathsf{q}]u[n], \tag{2.4}$$

where $G[\mathsf{q}]$ is called the *transfer operator* of the linear system. Even though the *transfer operator* is normally used to represent the systems in the VRFT literature, the *transfer function* approach, with a complex variable, is adopted in the present work.

Consider a discrete-time LTI system, with impulse response $g[n]$, and let z represent a complex number. The output response $y[n]$ of this system to a complex exponential input in the form z^n is (OPPENHEIM, 1997)

$$y[n] = G[z]z^n, \tag{2.5}$$

where

$$G[z] = \sum_{n=-\infty}^{+\infty} g[n]z^{-n}. \tag{2.6}$$

This summation is referred to as the *bilateral z-transform* of $g[n]$ and the $\mathcal{Z}$ operator is used to represent this transformation, as in $G[z] = \mathcal{Z}\{g[n]\}$. Due to the convolution property of the z-transform, the following equation is true

$$Y[z] = G[z]U[z], \tag{2.7}$$

where $U[z]$, $Y[z]$ and $G[z]$ are the z-transforms of the system input, output and impulse response, respectively. So, once $G[z]$ of an LTI system is known, it is possible to compute the output of that system for any given input[3]. The function $G[z]$ is refereed as the *transfer function* of the LTI system and it is frequently used to represent the dynamic model of a discrete-time LTI system. The output $y[n]$, in the time-domain, can be represented using the *inverse z-transform*

$$y[n] = \mathcal{Z}^{-1}\{Y[z]\}. \tag{2.8}$$

Equivalently, for the continuous-time LTI systems, the *bilateral Laplace transform* can be used to build the transfer function of a system and compute its output for a given input.

[3] Assuming that the initial conditions are null.

The $\mathcal{L}$ operator is used to represent the Laplace transform as in $U(s) = \mathcal{L}\{u(t)\}$ and the transformation is defined as

$$U(s) = \int_{-\infty}^{+\infty} u(t)e^{-st}dt, \tag{2.9}$$

where s is a complex variable. So a continuous-time LTI system can also be represented as

$$Y(s) = G(s)U(s), \tag{2.10}$$

where $U(s)$, $Y(s)$ are the Laplace transforms of the system input and output and $G(s)$ is the Laplace transform of impulse response of the system, also known as its continuous-time transfer function. The time-domain output of the system can be defined using the inverse Laplace transform

$$y(t) = \mathcal{L}^{-1}\{Y(s)\}. \tag{2.11}$$

In the end, the choice for the transfer function notation instead of the more traditional transfer operator do not have any impact on the practical application of the data-driven control method explored in this work. However, as the power-system controllers studied in this work are represented by transfer functions, the use of the transfer function notation helps keeping the document more coherent, despite being a more complex notation.

2.4.2 Model Reference Control

Consider a SISO LTI discrete-time system represented by a transfer function $G[z]$, as illustrated in Figure 2.1[4]. Its output $y[n]$ for a given input signal $u[n]$ can be computed by means of the z-transform as described in the previous section. Now, consider

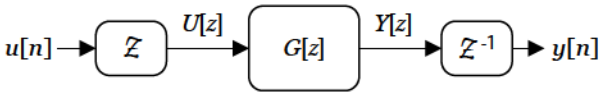

Figure 2.1 – Open-loop system.

that $C[z, \rho]$ represents a controller that will be designed for the reference tracking problem, with the closed-loop connection illustrated in Figure 2.2, where ρ represents a tunable parameter. The closed-loop transfer-function of the system is

$$M[z, \rho] = \frac{C[z, \rho]G[z]}{1 + C[z, \rho]G[z]}. \tag{2.12}$$

The reference tracking problem is a classical control problem where the fundamental objective is to make the output of the closed-loop system as close as possible to a given

[4] In Figure 2.1, the z-transform and inverse z-transform blocks are explicit. For simplicity, the z-transform related blocks are omitted from the following block diagrams.

reference signal. One way to represent the performance criterion for this problem is to use the two-norm of the tracking error, as follows (BAZANELLA, 2011)

$$J(\rho) = \|r[n] - y_r[n, \rho]\|_2 \,, \tag{2.13}$$

where $r[n]$ is the reference signal and $y_r[n, \rho]$ is the output of the closed-loop system for the reference signal. That is, $y_r[n, \rho] = \mathcal{Z}^{-1}\{M[z, \rho]R[z]\}$, where $R[z]$ is the z-transform of the reference signal.

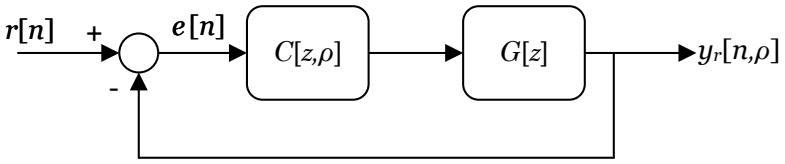

Figure 2.2 – Reference tracking closed-loop system.

In a practical application, it is not reasonable to assume that zero tracking error is possible and different approaches are used to relax this objective. For example, the tracking objective can be defined by means of performance measures (e.g., settling time, maximum overshoot, rising time). Another possibility is to apply the Model Reference control, that is particularly suited for the data-driven control method explored in this work.

The Model Reference control is a classical control design paradigm, where the performance criteria are described by means of the desired closed-loop dynamics, usually called reference model. Thus, the controller design consists in finding the controller parameters that make the output of the closed-loop system as close as possible to the output of the reference model (BAZANELLA, 2011). That is, instead of using the performance criterion of Equation (2.13), the following function is used (CAMPESTRINI, 2016)

$$J^{MR}(\rho) = \|y_r[n, \rho] - y_d[n]\|_2 = \left\|\mathcal{Z}^{-1}\left\{\left(M[z, \rho] - M_d[z]\right) R[z]\right\}\right\|_2^2 \,, \tag{2.14}$$

where $M_d[z]$ represents the reference model and $y_d[n]$ is its output for the reference input $r[n]$. Then, in the Model Reference control, the designer's task becomes the construction of this reference model (RODRIGUES, 2019).

2.4.3 VRFT Method

This section presents the VRFT algorithm formulation for the SISO ideal case. The formulation is based on the method describe in Bazanella, Campestrini and Eckhard (2011), but using the transfer function notation.

Let $G[z]$ represent the transfer-function of a SISO discrete-time LTI system, for which an output feedback controller is desired, and $y[n]$ represent the output response of this system for a given input signal $u[n]$, as illustrated in Figure 2.1. Now, consider a

reference model $M_d[z]$ that represents the dynamics of the closed-loop system, as presented in the previous section. This reference model can be seen as the desired dynamics for the plant. Thus, all performance requirements for the controller are embedded in $M_d[z]$. The VRFT method makes use of this reference model $M_d[z]$ and the signals $u[n]$ and $y[n]$ to find a controller for the Model Reference control problem.

Suppose that an ideal controller $C_i[z]$ exists. That is, a controller for which the closed-loop system exactly matches the reference model. The following assumptions are made over this ideal controller and the closed-loop system (BAZANELLA, 2011):

1. The system is not affected by noise;
2. The ideal controller $C_i[z]$ belongs to a class of parameterizable controllers, that is, $\exists \rho_i \in \mathbb{R}^p : C[z, \rho_i] = C_i[z]$;
3. The transfer function of the controller is parameterized linearly, that is, $C[z, \rho] = \rho^\top \bar{C}[z]$, where $\bar{C}[z]$ is an array of p rational transfer functions independent of the parameter ρ.

Now, suppose that there is a *virtual* reference signal $\bar{r}[n]$ that when applied to the *virtual* closed-loop system produces the output $y[n]$, as illustrated in Figure 2.3. Note that $y[n]$ is the same response of the open-loop plant $G[z]$ for the input $u[n]$. Once the dynamics of *virtual* closed-loop system, with the ideal controller, is the same as the dynamics of the reference model $M_d[z]$, the output of $M_d[z]$ for the same input signal $\bar{r}[n]$ is $y[n]$, Figure 2.4.

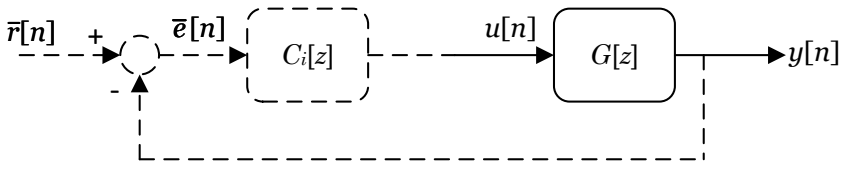

Figure 2.3 – Virtual closed-loop system.

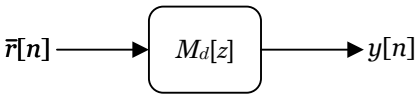

Figure 2.4 – Reference Model.

Then, the *virtual* reference signal can be defined in function of the reference model as follows,

$$\bar{r}[n] = \mathcal{Z}^{-1}\left\{(M_d[z])^{-1} Y[z]\right\}, \tag{2.15}$$

where $Y[z]$ is the z-transform of the output signal $y[n]$. The *virtual* error signal is defined as

$$\bar{e}[n] = \bar{r}[n] - y[n]. \tag{2.16}$$

The term *virtual* here refers to signals that are not applied to the plant but inferred from the data. In the ideal scenario described here, where the ideal parameterizable controller $C_i[z] = C[z, \rho_i] = \rho_i^\top \bar{C}[z]$ exists and the closed-loop dynamics matches $M_d[z]$ exactly, the output of the controller equals the input signal $u[n]$, that is,

$$u[n] - \bar{u}[n, \rho_i] = 0, \tag{2.17}$$

where

$$\bar{u}[n, \rho_i] = \mathcal{Z}^{-1}\left\{C[z, \rho_i]\bar{E}[z]\right\} \tag{2.18}$$

and $\bar{E}[z]$ is the z-transform of the *virtual* error signal.

To solve the Model Reference control problem by minimizing the Model Reference criterion (2.14), it is necessary to know the transfer function $G[z]$, to build the closed-loop model $M[z, \rho]$. However, it is possible to use an alternative criterion to design the controller using only the signals $u[n]$ and $y[n]$ and the reference model $M_d[z]$. This criterion is called Virtual Reference criterion and it is defined as

$$\begin{aligned} J^{VR}(\rho) &= \|u[n] - \bar{u}[n, \rho]\|_2^2 = \left\|\mathcal{Z}^{-1}\left\{U[z] - C[z, \rho]\bar{E}[z]\right\}\right\|_2^2, \\ &= \left\|\mathcal{Z}^{-1}\left\{U[z] - C[z, \rho]\left((M_d[z])^{-1} - 1\right)Y[z]\right\}\right\|_2^2. \end{aligned} \tag{2.19}$$

The VRFT procedure consists on using measured input/output data from the system to minimize (2.19), considering that the controller complies with Assumption 3. The procedure is described as follows.

Consider a set of data arrays $\left(\mathbf{u} \in \mathbb{R}^{1\times N}, \mathbf{y} \in \mathbb{R}^{1\times N}\right)$, where each array is composed of N samples of the input and output signals of the system, respectively, i.e. $\mathbf{u} = \{u[1], \ldots, u[N]\}$ and $\mathbf{y} = \{y[1], \ldots, y[N]\}$. If $M_d[z]$ is known, the *virtual* reference data array $\bar{\mathbf{r}} = \{\bar{r}[1], \ldots, \bar{r}[N]\}$ can be computed with Equation (2.15). Thus, the VRFT method consists in impose a structure to $\bar{C}[z]$ and find the array of parameter ρ that minimizes the error array $\boldsymbol{\epsilon}$, defined as

$$\boldsymbol{\epsilon} = \mathbf{u} - \rho^\top \boldsymbol{\Theta}, \tag{2.20}$$

where $\boldsymbol{\Theta} \in \mathbb{R}^{p\times N}$ and is defined as $\boldsymbol{\Theta} = \{\Theta[1], \ldots, \Theta[N]\}$, where $\Theta[n] = \mathcal{Z}^{-1}\left\{\bar{C}[z]\bar{E}[z]\right\}$ [5]. This is done by minimizing the criterion (2.19). Then, the VRFT criterion is a prediction error identification criterion, formulated as the square of the 2-norm of the prediction error as follows,

$$J_N^{VR}(\rho) = \frac{1}{2}\left\|\mathbf{u} - \rho^\top \boldsymbol{\Theta}\right\|_2^2 = \frac{1}{2}\left\|\boldsymbol{\Theta}^\top \rho - \mathbf{u}^\top\right\|_2^2. \tag{2.21}$$

Note that (2.21) is the criterion (2.19) for a limited data set of N samples and with $C[z, \rho] = \rho^\top \bar{C}[z]$. Then, the control tuning problem consists of a least-square problem and

[5] Note that $\Theta[n]$ is the output of $\bar{C}[z]$ for the input $\bar{e}[n]$. So, the data matrix $\boldsymbol{\Theta}$ is built using N samples of the *virtual* error signal $\bar{\mathbf{e}} = \bar{\mathbf{r}} - \mathbf{y} = \{\bar{r}[1] - y[1], \ldots, \bar{r}[N] - y[N]\}$.

the value of ρ that optimally solves it is

$$\rho^* = \arg\min_{\rho} J_N^{VR}(\rho) = (\boldsymbol{\Theta}\boldsymbol{\Theta}^\top)^{-1}\boldsymbol{\Theta}\mathbf{u}^\top \tag{2.22}$$

Depending on the reference model chosen, the inverse $(M_d[z])^{-1}$ may be unstable or improper, so an alternative cost function is used to avoid calculating this inverse. By applying the transfer function $M_d[z]$ as a filter in the signals $u[n]$ and $\bar{e}[n]$, a new cost function $J_N^{VR2}(\rho)$, with the same optimum solution, is obtained (NAKAMOTO, 2004; CAMPI, 2002b)

$$J_N^{VR2}(\rho) = \frac{1}{2}\left\|\mathbf{y_d} - \rho^\top\boldsymbol{\Phi}\right\|_2^2, \tag{2.23}$$

where $\mathbf{y_d} \in \mathbb{R}^{1\times N}$ and $\boldsymbol{\Phi} \in \mathbb{R}^{p\times N}$ and are defined as $\mathbf{y_d} = \{y_d[1], \ldots, y_d[N]\}$ and $\boldsymbol{\Phi} = \{\Phi[1], \ldots, \Phi[N]\}$, where $\Phi[n] = \mathcal{Z}^{-1}\left\{\bar{C}[z]M_d[z]\bar{E}[z]\right\}$ and $y_d[n] = \mathcal{Z}^{-1}\{M_d[z]U[z]\}$[6]. The value of ρ that optimally solves the problem is

$$\rho^* = \arg\min_{\rho} J_N^{VR2}(\rho) = (\boldsymbol{\Phi}\boldsymbol{\Phi}^\top)^{-1}\boldsymbol{\Phi}\mathbf{y_d}^\top. \tag{2.24}$$

In the end, the VRFT is an identification procedure. The goal is to identify the transfer function $C[z,\rho]$ that produces an output as close as possible to $\bar{u}[n]$ when $\bar{e}[n]$ is applied as an input. If $C[z,\rho]$ is linearly parameterizable, then, for a given set of data arrays $(\mathbf{u}, \mathbf{y}, \bar{\mathbf{r}})$, the identification problem is reduced to a least-squares problem and the array of parameters ρ that optimally solves it can be computed with Equation (2.22) or, alternatively, with Equation (2.24).

2.4.4 Control Structure

The most common control device applied to power system oscillation damping is the PSS, whose basic function is to extend the power systems stability limits by modulating generator excitation to provide damping to the oscillations of synchronous machine rotors relative to one another (LARSEN; SWANN, 1981).

Installed in the voltage control loop, the PSS provides a stabilizing signal added to the Automatic Voltage Regulator (AVR) input, as displayed in Figure 2.5, where V_{ref} is the reference value for the AVR and ω is the rotor angle of the machine that passes through a washout filter (to eliminate any control contribution under steady conditions) before being applied to the PSS. The washout filter is frequently used with power system damping controllers and, in this work, every PSS input signal pass through a washout filter. The hat symbol is used to represent the filtered signal as illustrated in Figure 2.5.

In this work, the data-driven VRFT method is adapted to cope with the power-system oscillation damping problem. The goal is to increase the damping ratio of

[6] Note that $y_d[n]$ is the output of the reference model $M_d[z]$ for the same input signal $u[n]$ that was applied to the system. Thus, it corresponds to the desired output for the closed-loop system. This interpretation is discussed in Section 3.1

electromechanical inter-area oscillation modes by designing Power Oscillation Damper (POD) controllers. Due to the global characteristics of the inter-area modes, the local damping controllers may not be sufficient to properly damp them. In those cases, the use of wide-area controllers, with remote measured signals, may be a suitable solution. Thus, the strategy is to design an extra damping controller using remote measurements, for systems were the existing PSS are not sufficient to achieve the desired performance. A remote PMU signal (or combination of signals) is used as the input to design a WAPSS, that is called remote input Power System Stabilizer (rPSS). The structure of the rPSS is illustrated in Figure 2.5, where $\hat{\gamma}$ represents the remote signal filtered by the washout.

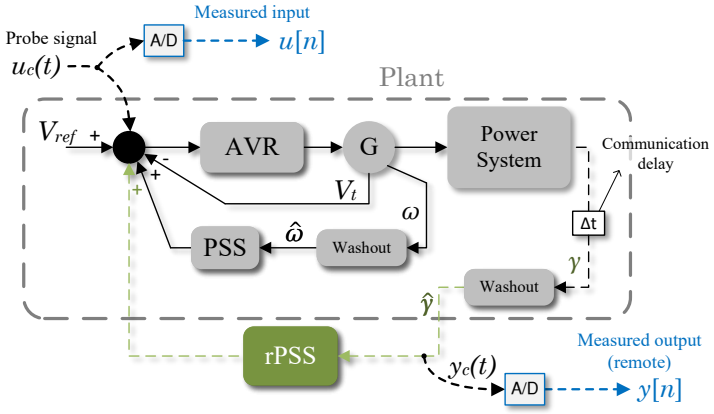

Figure 2.5 – Control Structure - Remote Input PSS ($rPSS$).

2.4.4.1 Control Signal for the $rPSS$

In the context of WADC, the selection of the remote measurements and placement of the extra damping control input are crucial steps. One strategy may be the use of a complete hierarchical control, as the one presented in Dotta, Silva and Decker (2009), where the rotor angular velocities of all generators are measured and a global MIMO controller provides an extra stabilizing signal for each PSS of the system. However, a simpler approach is adopted in this work. The rPSS is an extra SISO controller, designed to increase the damping ratio of a specific inter-area mode.

In the application proposed in this work, the input of the rPSS is the filtered difference between two bus frequencies, one of them being remotely measured and the other being the frequency of the terminal bus of the generator where the rPSS is installed. To achieve the goal of damping the inter-area mode, the generator at which the rPSS will be installed must have influence over this mode, also, the measured signal (filtered frequency difference) must contain sufficient information about it. That is, the remotely measured frequency should be selected to assure a high observability over the inter-area mode of interest, while the generator where the rPSS is placed must have a high controllability over the mode. The controllability/observability information is usually taken from the

modal analysis of linearized models of the power system. However, those models are not available considering the data-driven approach proposed in this work.

Still, the identification of the oscillatory mode as well as its controllability/observability information can be taken from a data-driven mode meter (LEANDRO, 2015; DOSIEK, 2018; ZHOU, 2018; LIU, 2014), what is generally available in power system control rooms (ZHANG, 2014). In this work, it is considered that the information about the inter-area oscillation modes, the bus frequency measurements at which those modes are better observed, and the generators that have the greatest influence on those modes are prior knowledge of the operator and that the low damping condition is already detected by the mode meter. Also, the efficiency of the method do not depend on the precise knowledge of controllability/observability. This is shown in the results presented Section 4.2, where the generator selected to have the rPSS installed is not the one with the highest controllability index.

2.4.4.2 Communication delay

The communication time-delay is an intrinsic characteristic of the WADC, due to the large distances covered by the measured signals. In this work, a fixed time-delay of 150 ms is considered during the data acquisition experiment. This value is compatible with traditional WAMS applications (NADUVATHUPARAMBIL, 2002; WU, 2004; LIU, 2021) and corresponds to total time needed to measure, synchronize, transmit and treat all data used. In this work, the duration of this time-delay is consider to be known by the system operator. Even though a fixed time-delay is considered during the data-driven control design procedure, the performance of the rPSS is tested for different values of time-delay.

3 VRFT adapted to cope with the PSS design

In order to be applied to the power-systems oscillation damping, the VRFT method needs to be adapted to cope with some particularities of the oscillation damping problem. The VRFT method (CAMPI, 2002a) is a data-driven method formulated to design controllers for the reference tracking problem. However, the POD controllers are designed to improve the damping-ratio of electromechanical oscillation without interfering in the steady-state response of the system. More specifically, the PSS is usually designed as compensator installed at feedback loop of the voltage control of a selected generator.

To adapt the VRFT method to the proposed application, the first step is to change the control-loop structure from the one in Figure 2.3 to the one presented in Figure 3.1, where $G[z]$ represents the plant, $u[n]$ is the perturbation input and $y[n]$ is the output of the system for the input $u[n]$. Supposing the ideal controller $C_i[z]$ exists, $\bar{r}[n]$ is the *virtual* reference signal that produces the same output $y[n]$ and $\bar{f}[n]$ is the *virtual* control output. Again, a transfer function $M_d[z]$ is considered to be the reference model that represents the dynamics of the closed-loop system with the ideal controller. Thus, as in the traditional VRFT approach, the *virtual* reference signal $\bar{r}[n]$ can be defined in function of the reference model, as described in Equation (2.15).

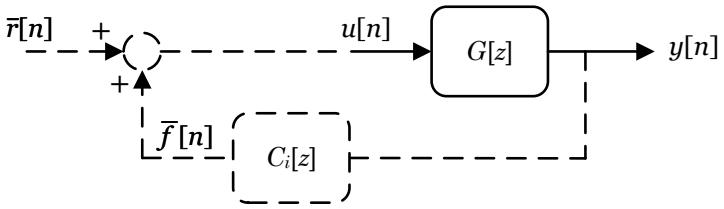

Figure 3.1 – Modified virtual closed-loop system.

Considering the ideal scenario, where the ideal parameterizable controller $C_i[z] = C[z, \rho_i]$ exists and the closed-loop dynamics matches $M_d[z]$ exactly, the *virtual* output of the controller $\bar{f}[n]$ can be computed by

$$\bar{f}[n] = \mathcal{Z}^{-1}\{C_i[z]Y[z]\} \tag{3.1}$$

and the sum of the *virtual* reference and *virtual* control output signals equals the input signal, that is,

$$u[n] - \left(\bar{r}[n] + \bar{f}[n]\right) = 0. \tag{3.2}$$

The modified VRFT method follows a procedure similar to the original one. Given a set of data arrays $\left(\mathbf{u} \in \mathbb{R}^{1\times N}, \mathbf{y} \in \mathbb{R}^{1\times N}\right)$, where each array is composed of N samples of the input and output signals of the system, respectively, i.e. $\mathbf{u} = \{u[1], \ldots, u[N]\}$

and $\mathbf{y} = \{y[1], \ldots, y[N]\}$, if $M_d[z]$ is known, the *virtual* reference data array $\bar{\mathbf{r}} = \{\bar{r}[1], \ldots, \bar{r}[N]\}$ can be computed with Equation (2.15) and *virtual* control output data array $\bar{\mathbf{f}} = \left\{\bar{f}[1], \ldots, \bar{f}[N]\right\}$ can be computed with Equation (3.1). Thus, the same procedure used in the original VRFT strategy can be applied here. That is, to assume that the controller is linearly parameterizable $C[z, \rho_i] = \rho_i^\top \bar{C}[z]$, impose a structure to $\bar{C}[z]$ and find the array of parameter ρ that minimizes the error array $\boldsymbol{\varepsilon}$, defined as

$$\boldsymbol{\varepsilon} = \mathbf{u} - \left(\bar{\mathbf{r}} + \rho^\top \boldsymbol{\Theta}\right), \tag{3.3}$$

where $\boldsymbol{\Theta} \in \mathbb{R}^{p \times N}$ and is defined as $\boldsymbol{\Theta} = \{\Theta[1], \ldots, \Theta[N]\}$, where $\Theta[n] = \mathcal{Z}^{-1}\left\{\bar{C}[z]Y[z]\right\}$. Once again the VRFT criterion is a prediction error identification criterion, formulated as the square of the 2-norm of the prediction error as follows,

$$J_N^{VR,POD}(\rho) = \frac{1}{2}\left\|\mathbf{u} - \bar{\mathbf{r}} - \rho^\top \boldsymbol{\Theta}\right\|_2^2 = \frac{1}{2}\left\|\boldsymbol{\Theta}^\top \rho - (\mathbf{u} - \bar{\mathbf{r}})^\top\right\|_2^2. \tag{3.4}$$

Then, the control tuning problem consists of a least-square problem; the value of ρ that optimally solves it is

$$\rho^* = \arg\min_{\rho} J_N^{VR,POD}(\rho) = (\boldsymbol{\Theta}\boldsymbol{\Theta}^\top)^{-1}\boldsymbol{\Theta}\,(\mathbf{u} - \bar{\mathbf{r}})^\top. \tag{3.5}$$

As describe in Section 2.4.3, it can be convenient to use an alternative cost function to avoid calculating the inverse $(M_d[z])^{-1}$, needed to compute $\bar{r}$. By applying the transfer function $M_d[z]$ as a filter in the signals $u[n]$ and $y[n]$, a new cost function, with the same optimum solution, is obtained

$$J_N^{VR,POD2}(\rho) = \frac{1}{2}\left\|\mathbf{y_d} - \left(\mathbf{y} + \rho^\top \boldsymbol{\Phi}\right)\right\|_2^2 = \frac{1}{2}\left\|\boldsymbol{\Phi}^\top \rho - (\mathbf{y_d} - \mathbf{y})\right\|_2^2, \tag{3.6}$$

where $\mathbf{y_d} \in \mathbb{R}^{1 \times N}$ and $\boldsymbol{\Phi} \in \mathbb{R}^{p \times N}$ and are defined as $\mathbf{y_d} = \{y_d[1], \ldots, y_d[N]\}$ and $\boldsymbol{\Phi} = \{\Phi[1], \ldots, \Phi[N]\}$, where $\Phi[n] = \mathcal{Z}^{-1}\left\{\bar{C}[z]M_d[z]Y[z]\right\}$ and $y_d[n] = \mathcal{Z}^{-1}\{M_d[z]U[z]\}$. The value of ρ that optimally solves the problem is

$$\rho^* = \arg\min_{\rho} J_N^{VR,POD2}(\rho) = (\boldsymbol{\Phi}\boldsymbol{\Phi}^\top)^{-1}\boldsymbol{\Phi}(\mathbf{y_d} - \mathbf{y})^\top. \tag{3.7}$$

3.1 Predicted Output

The signal $y_d[n]$ is the output of the reference model $M_d[z]$ for the same input signal $u[n]$ used to collect $y[n]$ from the plant. Since $M_d[z]$ represents the desired dynamics of the closed-loop system, the performance requirements are embedded in $y_d[n]$, which represents the desired output of the closed-loop system for the input $u[n]$. That is, the array $\mathbf{y_d}$ corresponds to samples of the desired output for the closed-loop system for the same input samples in the array $\mathbf{u}$.

In the ideal case, the value of cost function (3.6) evaluated at the optimum solution ρ^* is zero. However, in a realistic application this is unlikely to happen. Thus, if $\mathbf{y_d}$

is the ideal desired output, the difference between it and the remaining term $\left(\mathbf{y} + \rho^\top \mathbf{\Phi}\right)$ inside the cost function is an indication of how far from the ideal result the designed controller is. Defining this remaining term as

$$\mathbf{y_p} = \mathbf{y} + \rho^\top \mathbf{\Phi}, \tag{3.8}$$

one can interpret this data array as prediction samples of the closed-loop system output signal with the designed controller. Regarding the signal definition, $y_p[n]$ is a predicted output signal defined as

$$y_p[n] = \mathcal{L}^{-1}\left\{Y[z] + \rho^\top \bar{C}[z] M_d[z] Y[z]\right\} \tag{3.9}$$

and those prediction samples are $\mathbf{y_p} = \{y_p[1], \ldots, y_p[N]\}$. This signal can be used as a beforehand diagnosis for the controller performance, as $\mathbf{y_p}$ can be computed before installing the new controller in the system. In other words, $\mathbf{y_d}$ is the desired dynamic response and $\mathbf{y_p}$ is the best response possible with the controller $C[z, \rho]$, where ρ is computed with (3.7). If the dynamic response contained in the samples of $\mathbf{y_p}$ is close to the desired one ($\mathbf{y_d}$), it is an indication that the controller may achieve the performance requirements, but there is no guarantee. However, if the response $\mathbf{y_p}$ is far $\mathbf{y_d}$, the design procedure was not successful and the designed controller can be rejected without requiring any testing in the real system.

3.2 Application on continuous time systems

The VRFT is a data-driven method and, therefore, it is formulated considering discrete-time LTI systems. However, power systems are usually modeled using continuous-time equations, with the controllers being described by continuous-time transfer functions. So, in this work, the plant and the controller are considered in continuous-time and the data arrays used in the VRFT method are considered to be sequences of samples of continuous-time signals.

Let the diagram of the Figure 3.2 represent the closed-loop system with *virtual* controller and signals. The VRFT method described in Section 3 can be applied to this system by considering that $u[n] = u(nT)$ and $y[n] = y(nT)$ are sequences of samples of $u(t)$ and $y(t)$. The reference model is also considered to be a continuous-time system represented by a transfer-function $M_d(s)$, as presented in Figure 3.3. So, the *virtual* reference signal $\bar{r}[n] = \bar{r}(nT)$ is a sequence of samples of the continuous-time signal $\bar{r}(t)$, but, defining $M_d[z]$ as the discretized version[1] of $M_d(s)$, $\bar{r}[n]$ can still be defined in function of the reference model using Equation (2.15). The same is valid for $\bar{f}[n] = \bar{f}(nT)$ that can be computed with Equation(3.1), considering that $C_i[z]$ is the discretized version of $C_i(s)$.

[1] In this work, the conversions between continuous-time and discrete-time functions are done internally by the function lsim (The MathWorks, Inc, 2021c) of the Matlab software, with a combination of zero-order hold or first-order hold methods, as mentioned in Section 3.6.

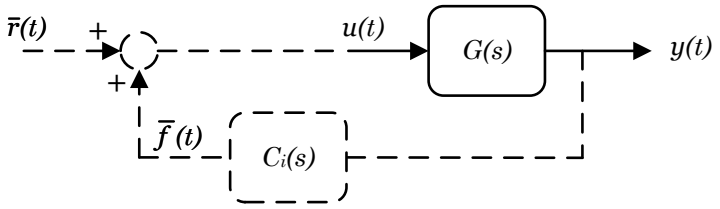

Figure 3.2 – Modified virtual closed-loop system (continuous-time).

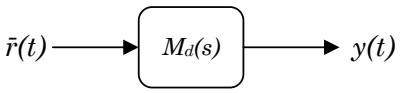

Figure 3.3 – Reference Model (continuous-time).

3.3 Using a Performance Output Signal

As described in Section 2.4.3, the transfer function $M_d[z]$ (or $M_d(s)$ for continuous-time systems) is the reference model that represents the desired dynamics for the closed-loop plant. The VRFT procedure presented here follows a SISO formulation, thus $M_d(s)$ must be a SISO transfer function. However, it is not necessary for the performance output signal, used to build $M_d(s)$, to be the same as the control output of the system. It is possible to have two different signals, one for the performance and one for the control (Figure 3.4). Even though this strategy is not used in the results presented in this document, it was used in Bernado, do Nascimento and Dotta (2020), therefore the author believes it is worth mentioning.

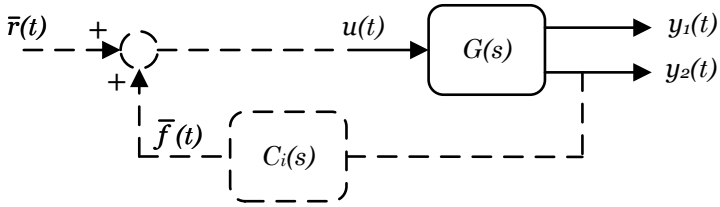

Figure 3.4 – Modified virtual closed-loop system, with two outputs.

Let the diagram of the Figure 3.4 represent the closed-loop system with *virtual* controller and two output signals. The output signal $y_1(t)$ represents the performance output, while the signal $y_2(t)$ is the control output. Considering that $u[n] = u(nT)$, $y_1[n] = y_1(nT)$ and $y_2[n] = y_2(nT)$ are sequences of samples of $u(t)$, $y_1(t)$ and $y_2(t)$, respectively, the VRFT method described in Section 3 can also be applied to this system. The main difference is that $M_d[z]$ (the discretized version of $M_d(s)$) should be build considering the performance output $y_1(t)$. It means that the *virtual* reference signal $\bar{r}[n] = \bar{r}(nT)$ should be defined in function of the reference model and the performance output, as follows,

$$\bar{r}[n] = \mathcal{Z}^{-1}\left\{(M_d[z])^{-1}\, Y_1[z]\right\}, \tag{3.10}$$

where $Y_1[z]$ is the z-transform of the output signal $y_1[n]$. Although, the *virtual* output of the controller $\bar{f}[n] = \bar{f}(nT)$ must be defined in function of the control output. That is,

$$\bar{f}[n] = \mathcal{Z}^{-1}\left\{C_i[z]Y_2[z]\right\}, \tag{3.11}$$

where $Y_2[z]$ is the z-transform of the output signal $y_2[n]$.

Following the procedure described in Section 3, the cost function of the VRFT problem with separate performance and control outputs is

$$J_N^{VR,POD3}(\rho) = \frac{1}{2}\left\|\mathbf{y_d} - \left(\mathbf{y_1} + \rho^\top \mathbf{\Phi_2}\right)\right\|_2^2 = \frac{1}{2}\left\|\mathbf{\Phi_2}^\top \rho - (\mathbf{y_d} - \mathbf{y_1})\right\|_2^2, \tag{3.12}$$

where $\mathbf{y_1} = \{y_1[1], \ldots, y_1[N]\}$, $\mathbf{y_d} = \{y_d[1], \ldots, y_d[N]\}$, $\mathbf{\Phi_2} = \{\Phi_2[1], \ldots, \Phi_2[N]\}$, $\Phi_2[n] = \mathcal{Z}^{-1}\left\{\bar{C}[z]M_d[z]Y_2[z]\right\}$ and $y_d[n] = \mathcal{Z}^{-1}\left\{M_d[z]U[z]\right\}$. The value of ρ that optimally solves the problem is

$$\rho^* = \arg\min_{\rho} J_N^{VR,POD3}(\rho) = (\mathbf{\Phi_2}\mathbf{\Phi_2}^\top)^{-1}\mathbf{\Phi_2}(\mathbf{y_d} - \mathbf{y_1})^\top. \tag{3.13}$$

3.4 Controller Parameterization

The VRFT criterion is a prediction error identification criterion, formulated as a least-squares problem. To accomplish this formulation it is mandatory that the controller fulfills the Assumption 3, presented in Section 2.4.3. That is, the controller must be linearly parameterizable. For example, let $C_{PID}(s)$ be the transfer function of a PID (proportional–integral–derivative) controller, it can be linearly parameterizable as follows

$$C_{PID}(s) = \rho^\top \bar{C}_{PID}(s) = \begin{bmatrix} \rho_1 & \rho_2 & \rho_3 \end{bmatrix} \begin{bmatrix} 1 \\ 1/s \\ s \end{bmatrix}, \tag{3.14}$$

where ρ_1, ρ_2 and ρ_3 are the proportional, integral and derivative gains, respectively. However, POD controllers are usually formulated as lead-lag compensators or rational transfer functions. So, a complete parameterization as in the PID case is not viable. The solution found to accomplish a parameterization that comply with the VRFT method was to use a fixed denominator for the controller transfer function. By fixing the denominator, the numerator of the controller transfer function can be linearly parameterized. This strategy is used on both control structures explored in this work.

Consider the following rational polynomial transfer function, that represents a traditional PSS already installed in a given power system[2]

$$PSS(s) = \frac{n_1 s^2 + n_2 s + n_3}{as^2 + bs + c}. \tag{3.15}$$

In both formulations used to parameterize the controller, it is assumed that (3.15) is known. These formulations are presented as follows.

[2] A high order transfer functions may be used depending on the power system

3.4.1 New PSS design ($rPSS$)

Consider that the transfer function defined in Equation (3.15) represents an already installed regular PSS of the power system. In order to design a new PSS for the system, the remote signal WAPSS for instance, it is necessary that the transfer function of this new PSS is parameterized linearly (assumption 3). To comply with this assumption, the structure of $\bar{C}(s)$ is defined using the same denominator of the original PSS transfer function of Equation (3.15)

$$\bar{C}(s) = \frac{1}{as^2 + bs + c} \begin{bmatrix} s^2 & s & 1 \end{bmatrix}^\top. \tag{3.16}$$

By defining $\bar{C}[z]$ as a discretized version of $\bar{C}(s)$ and using (3.16) to compute the cost function (3.6), the resulting array of parameters ρ is the numerator coefficients of the new controller, represented by

$$rPSS(s) = \frac{\rho_1 s^2 + \rho_2 s + \rho_3}{as^2 + bs + c}. \tag{3.17}$$

3.4.2 PSS Re-tuning

In the proposed application, the PSS re-tuning consists of finding new coefficients for the numerator of a selected PSS transfer function. Thus, the structure of $\bar{C}(s)$ is defined using the same denominator of the original PSS transfer function of Equation (3.16). By defining $\bar{C}[z]$ as a discretized version of $\bar{C}(s)$ and using (3.16) to compute the cost function (3.6), the resulting array of parameters ρ is the numerator coefficients of a controller that is virtually connected in parallel to the original PSS, as illustrated in Figure 3.5. So, the re-tuning procedure is done by adjusting the numerator of the selected PSS transfer function, according to (3.18). Note that re-tuning procedure can be applied to any PSS of the system, including the WAPSS ($rPSS$) explored in this work.

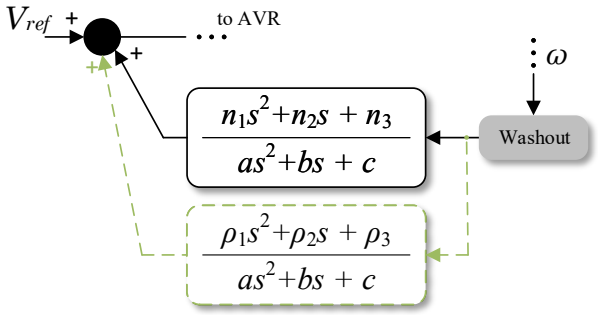

Figure 3.5 – Virtual connection of the tuned controller.

$$PSS_{retuned}(s) = \frac{(\rho_1 + n_1)s^2 + (\rho_2 + n_2)s + (\rho_3 + n_3)}{as^2 + bs + c} \tag{3.18}$$

3.5 Methods for building the reference model

In the data-driven control framework, the measured input and output data is directly used to find the controller parameters. That is, during the control design procedure, the dynamic model of the plant is unknown. And still, the design procedure must somehow consider the dynamic performance requirements for the closed-loop system. One way of approaching this problem is to use a Model Reference control method. The VRFT method explored in this work is a Model Reference control method, where a predefined reference model is needed for computing the *virtual* signals, as presented in Section 2.4.3. This model, referred here by $M_d(s)$, represents the dynamics of the closed-loop system with the controller that will be designed, i.e., it represents the desired dynamics or the performance requirements for the closed-loop system. In a practical application, the model $M_d(s)$ is usually unknown and its construction becomes a critical step on the VRFT procedure.

Considering the proposed power system application, the well damped oscillation performance must be included in the reference model $M_d(s)$, but it must still represent a reachable dynamics. That is, if the damping requirements are too ambitious, one of the following may happen: the solution will result in a high valued cost function ($J_N^{VR,POD2}(\rho^*) \gg 0$); or, even if the cost function value is low, the controller $C(s, \rho^*)$ may not be able to make $G(s)$ reach $M_d(s)$ dynamics, because the reference model does not represent a feasible dynamics for the power system plant. In the worst case, $C(s, \rho^*)$ may lead the plant to instability.

Until the research proposed in this thesis, the VRFT method had not yet been applied to the problem of damping oscillations in electrical power systems. Hence, the literature lacks reference methodologies for building the reference model for the proposed application. In this work, two methods are proposed for building the reference model, considering the power systems oscillation damping application. The first one is based on the analysis of the dominant oscillation mode of the measured output signal. Once this mode is identified, a second order transfer function is build based on classical linear system analysis. The second method is based on a black-box system identification method.

> "A black-box model of a system is one that does not use any particular prior knowledge of the character or physics of the relationships involved. It is therefore more a question of *curve-fitting* than *modeling*" (LJUNG, 2001).

After identifying a transfer function that fits the input/output data, a pole-placement restriction is used so the reference model attends to the desired oscillation damping performance.

Before detailing the two method proposed, it is important to address two constraints usually related with Model Reference control methods. According to Silva,

Bazanella and Campestrini (2019), during the definition of a SISO reference model, the designer must take the following two precautions: *i)* The relative degree of the reference model transfer function must be greater or equal to the relative degree of the plant, so that the ideal controller is causal; *ii)* The Non-Minimum Phase (NMP) zeros of the plant must be included in the reference model, to avoid internal instability problems. The first restriction is related with the causality of the *ideal* controller. If the relative degree of the reference model $M_d(s)$ is smaller than the one of the plant $G(s)$, the *ideal* controller that exactly meets the desired closed-loop dynamics is non-causal. Making it impossible to be used in a physical system application. The second restriction is related with the internal stability of the closed-loop system. If the plant has NMP zeros and the reference model does not, the NMP zeros of the plant must be canceled out by the *ideal* controller, so the closed-loop system meets the reference model dynamics. Thus, the *ideal* controller must have unstable poles.

Both restrictions are related with the structure of the controller and, therefore, are not a problem for the application proposed in this work. Here, a fixed structure with a proper transfer function is used for the controller, with fixed poles. Thus, the designed controller is always causal and have stable poles. Also, those restrictions are meant for the scenario where the *ideal* controller is designed. The *ideal* controller is the one that meets the reference model dynamics exactly, that is, is the one for which the value of the cost function is zero. This is not the case of the proposed application, it is not expected to obtain the ideal controller, in the sense that the closed loop dynamics is not expected to correspond exactly to the reference model. The objective of the proposed method is to improve the oscillation damping performance of the power system by designing a controller to approximate the reference model dynamics. That should be kept in mind when applying the following methods for building the reference model.

3.5.1 Building the reference model as a second order transfer function - Method 1

The first method proposed is based on the analysis of the dominant oscillation mode presented in the output signal measured in the data acquisition process. The goal of the method is to build a reference model that produces a similar time response but with an improved damping ratio, using a second order transfer function. For the applications proposed in this work, the input signal is a step of small amplitude (0.1pu) applied to the voltage regulator reference input of a selected generator. And the measured output signal is the difference between two bus frequency measurements. Thus, the reference model is built based on the step response of a second order system.

Consider the step response illustrated in Figure 3.6a. This signal is an example of bus frequency difference, filtered by a washout filter, after a step applied in the voltage

regulator reference of a generator at 1 s. A noiseless case is considered. The frequency $\hat{f}_b$ is the filtered frequency at the terminal bus of the generator and $\hat{f}_a$ is the filtered frequency of a remote bus of the system. This is the dynamic response expected for the proposed application, i.e., a poorly damped low frequency oscillatory response around the zero axis. So, a second order transfer function is built to resemble this step response.

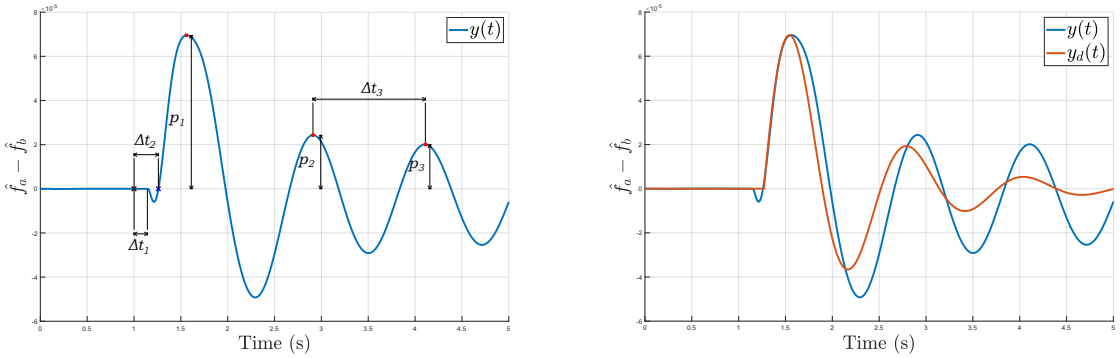

(a) Measured output signal. (b) Response of a second order reference model.

Figure 3.6 – Example of reference model response, with Method 1.

A generic representation of a second order transfer function is presented as follows

$$G_{2\text{nd}}(s) = \frac{\omega_n^2}{s^2 + 2\zeta\omega_n s + \omega_n^2}, \tag{3.19}$$

where ω_n is the natural frequency and ζ is the damping ratio of the oscillation mode. The damping ratio of the signal can be approximated using the following logarithm decrement formula for any two adjacent peaks

$$\zeta_0 = \frac{1}{\sqrt{1 + \left(\frac{2\pi}{\ln\left(\frac{p_2}{p_3}\right)}\right)}}. \tag{3.20}$$

The second and third peaks are chosen to avoid the transient dynamics of the first swing. Then, the natural frequency of the dominant oscillation mode can be estimated by

$$\omega_n = \frac{\omega}{\sqrt{1 - \zeta_0^2}}, \tag{3.21}$$

where ω is the damped frequency that can also be estimated from the signal as

$$\omega = 2\pi\frac{1}{\Delta t_3}. \tag{3.22}$$

However, for poorly damped oscillation modes one has that $\omega_n \approx \omega$. So it is not even necessary to compute ζ_0.

Note that, for a stable system, the step response resented in Figure 3.6a will eventually converge to zero, due to the characteristics of the chosen output signal and the

washout filter. This dynamics can be modeled by adding a zero to the transfer function, in the origin of the complex-plane. Also, note that there is a delay between the control action and the response of the system. The step input starts at 1 s and the output response starts a few milliseconds later, this time delay is indicated by Δt_1 in the figure. A NMP zero dynamics can also be observed in the output response. Before starting to rise, the signal decreases until it reaches a negative peak. Nevertheless, as this negative peak is small compared to the rest of the output response, it will be neglected in the reference model. This is done by considering Δt_2 as the time delay, i.e., the time between the start of the step input and the beginning of the positive response of the system. The transfer function of a second order system with a zero at the origin and a input/output time delay is

$$M_0(s) = e^{-T_d s} \frac{\omega_n^2 s}{s^2 + 2\zeta\omega_n s + \omega_n^2}. \tag{3.23}$$

However, a final adjustment is needed so the amplitude of the step response of $M_0(s)$ is comparable to the amplitudes of the measured output signal. This adjustment is the inclusion of a gain K so the first peak of the response of $M_0(s)$ is close to p_1 (amplitude of the first peak of the measured output). One can demonstrate that for a given step input of amplitude u_s, the first peak of the step response of $M_0(s)$ is

$$y_{M,p1} = u_s \omega_n e^{\frac{-\zeta\theta}{\sqrt{1-\zeta^2}}}, \tag{3.24}$$

where $\theta = \sin^{-1}(\sqrt{1-\zeta^2})$. Then, the adjustment gain K is

$$K = \frac{p_1}{y_{M,p1}}. \tag{3.25}$$

Thus, the reference model transfer function, considering the time delay, the zero at the origin, and the adjustment gain is

$$M_d(s) = e^{-T_d s} K \frac{\omega_n^2 s}{s^2 + 2\zeta\omega_n s + \omega_n^2}, \tag{3.26}$$

where $T_d = \Delta t_2$ and ζ is the desired damping ratio. The output response of a reference model built with Equation (3.26), using $\zeta = 0.15$, is presented in Figure 3.6b, for the same step input used to measure $y(t)$.

The following procedure can be applied to design a second order reference model for the data-driven oscillation damping control design proposed in this work.

1. Identify the time delay between the step input and the start of the positive response of the system, Δt_2 in Figure 3.6a.
2. Identify the frequency of the dominant oscillation mode ω_n with Equation (3.22) and compute ω_n with (3.20) and (3.21).
3. Define the desired damping ratio ζ.

4. Compute the gain K to adjust the amplitude of the reference model output with Equation (3.25).

5. Build the reference model $M_d(s)$ using Equation (3.26).

3.5.2 Building the reference model using a identification method - Method 2

The second method proposed to build the reference model is based on a black-box identification method. The idea behind this approach is to extract from the measure data (same data that will be used in the data-driven design procedure) as much information as possible to build the reference model. The goal is to reduce the necessity of previous knowledge of the plant, but still build a reference model with a more realistic dynamics than in the previous method.

The proposed method consists of two stages, as illustrated in Figure 3.7, and uses the same measured data arrays $(\mathbf{u}, \mathbf{y})$ used in the control design procedure. The first stage corresponds to a model estimation step using the Maltab function tfest (The MathWorks, Inc, 2021a). This black-box process starts by initializing the estimable parameters using the Instrument Variable (IV) method (YOUNG; JAKEMAN, 1980), then a combination of line search algorithms is performed in sequence (Gauss-Newton least squares search, adaptive subspace Gauss-Newton search, Levenberg-Marquardt least squares search and steepest descent least squares search) and the first descent direction leading to a reduction in estimation cost is selected (The MathWorks, Inc, 2021b). The output of the estimation process is a continuous-time transfer function based on the measured data, the number of poles and time-delay, defined by the user[3].

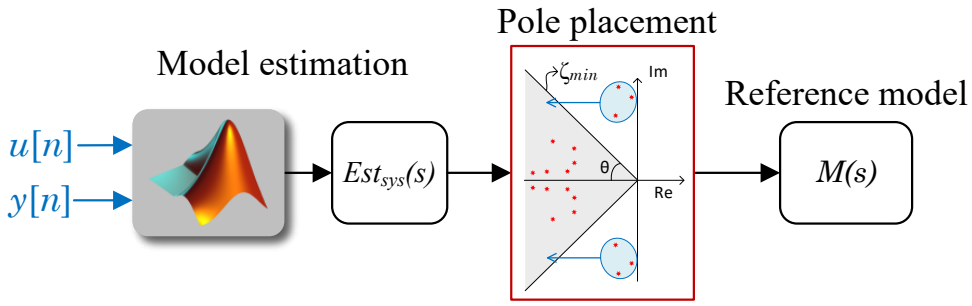

Figure 3.7 – Diagram of the reference model building process.

The second stage modifies the estimated model to cope with the minimum damping performance requirement, defined by the user as a desired minimum damping ratio ζ_{min}. Once the estimated transfer function is computed, its poles are shifted so the minimum damping of the system is greater or equal to the desired one (pole placement

[3] *A priori* knowledge of the plant may be used to define the number of poles. In this work, the estimation was performed for multiple number of poles and the estimation with the best fit was selected.

stage). For a given pole $\lambda = \sigma \pm j\omega$, its damping ratio is defined as

$$\zeta(\lambda) \triangleq \frac{-\sigma}{\sqrt{\sigma^2 + \omega^2}}.$$

So, for the same frequency ω and the desired minimum damping $\zeta_{min} = d$, the real part of the pole must be

$$\sigma_d = -\frac{d\omega}{\sqrt{1 - d^2}}.$$

The reference model $M_d(s)$ corresponds to the estimated model transfer function with shifted poles to reach the minimum damping ratio. That is, replacing σ by σ_d for every pole where $\zeta(\lambda) < \zeta_{min}$. Then, the model is multiplied by a gain to correct the steady state value. An example of a reference model output is presented in Figure 3.8. The model was built using the measured output $y(t)$ data and considering a minimum damping ratio of 10%. The blue continuous line corresponds to the output signal of the plant (filtered bus frequency difference), the red dashed line is the output response of the estimated system $Est_{sys}(s)$, and the yellow line is the response of the reference model for the same step input signal, i.e., the desired output $y_d(t)$ for the closed-loop system.

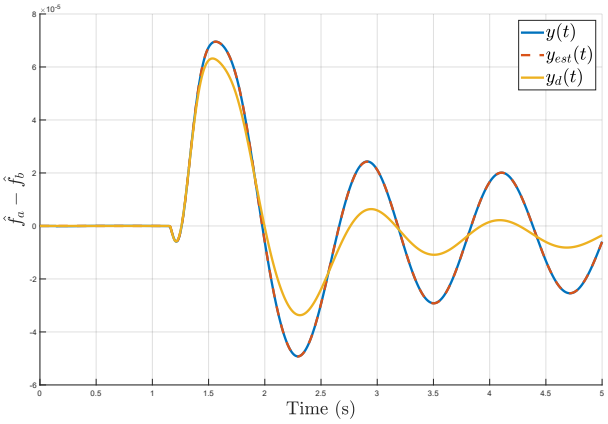

Figure 3.8 – Example of reference model response, with Method 2.

Even though a model estimation step is usually undesired in a data-driven control framework, its benefits justify its application in the proposed problem. The estimated model has the same (or very similar) NMP characteristic of the plant, so the model $M_d(s)$ has NMP zeros equal or very close to the ones of the plant. Besides contributing to build a reachable desired closed-loop dynamics, the inclusion of those NMP zeros on the reference model avoids internal instability problems caused by pole and zero cancellation (BAZANELLA, 2011). Specifically for the rPSS proposed in this work, the internal instability problem is already prevented by the fixed stable poles of the controller. So, including NMP zeros on the reference model is an appropriate strategy, since the NMP dynamics of the plant cannot be canceled out by the controller anyway, due to its fixed pole characteristics.

3.6 Application discussion

Even though the design procedure is data-based and, therefore, a discrete-time procedure, the plant G and the controller rPSS are considered in continuous-time. This is done to simplify the interface between the software used in the controller design (Matlab) and the power systems simulation software (ANATEM). The ANATEM (CEPEL; ELETROBRAS, 2020a) is a software for the analysis of electromechanical transitory events in power systems and it is based on nonlinear continuous-time models, i.e., the controllers are defined with continuous-time transfer functions. To minimize the errors of the conversions between continuous and discrete-time representations, those conversions are performed internally by the function lsim (The MathWorks, Inc, 2021c) of the Matlab software. The sample time is set to the spacing between the user-supplied time samples and the conversion method (zero-order hold or first-order hold) is automatically selected based on the smoothness of the input signal (The MathWorks, Inc, 2021c). Also, all formulation is done using transfer functions, thus, the initial condition is assumed to be zero. However, in a practical power systems application, the measured signals will probably have a non-zero value. To overcome this issue, it is considered that the power system is operating near a steady-state condition, and the values of the measured signals before the application of the probe input are considered to be the initial condition and are subtracted from the signals.

As mentioned in Section 2.4.4.1, it is assumed that the inter-area modes of the system are known, as well as the proper control input/output that can be used to include an extra damping controller. Thus, the strategy presented in this document is a proof of concept of applying a simple and fast offline data-driven control design procedure to include an extra damping controller in power systems.

Consider the scenario where the damping ratio of an inter-area mode is deteriorated by some variation on the operating condition of the system, e.g., power flow variations caused by the intermittence of renewable sources. Once this poorly damped condition is detected[4], depending on the characteristics of the power system a PSS can be re-tuned or an extra damping controller can be designed by means of the proposed data-driven procedure, without needing the dynamic model of the system. For that, a data set $(\mathbf{u}, \mathbf{y})$ is constructed through a data collecting experiment, then the reference model $M_d(s)$ is built. Lastly, the parameters for the controller are found by solving (3.7), using predefined poles (the same of the already installed regular PSS, for instance). Note that the proposed method is a procedure performed offline. That is, the data-set is collected at one time and the controller design takes place without interfering in the dynamics of the system, except by the probe signal of the data collecting experiment. Due to the offline feature of the method and considering the time-scale of the data collecting experiment (few seconds), the computation time (milliseconds) needed to build the reference model

[4] Note that the detection of such condition is out of the scope of this work.

and to solve the VRFT problem (3.7) are not a concern. However, due to the variability of the power systems with high penetration of renewable sources, the operating conditions will continue to change after the re-tuning of the PSS or inclusion of the rPSS. Those variations may deteriorate the damping ratio of the inter-area mode again. In this case, the re-tuning of the controller is possible, by re-applying the VRFT procedure. Note that in a re-tuning scenario, the aforementioned initial condition approximation should be carefully applied, since the system is in a transient condition.

4 Results

This chapter presents the simulation results of the proposed VRFT method applied to two benchmark power system models. The simulations were performed with the time-domain nonlinear model and all control limiters of the benchmark models were included. Note that the VRFT method was formulated considering LTI systems, but nonlinear power system models are used in this work. Before the results presented in this section were obtained, a preliminary test was done to evaluate the impacts of this nonlinearities and to validate the proposed method. This test is presented in Appendix A.

Even though no model information is used during the controller design, a minimum knowledge of the system dynamics is expected in a practical control application. In this work, that previous knowledge corresponds to information about the inter-area oscillation modes, as the bus frequency measurements at which those modes are better observed and the generators that have the greatest influence on those modes. The proposed VRFT algorithm was applied to two power system models that belong to a set of benchmark models for the analysis and control of small-signal oscillatory dynamics in power systems (CANIZARES, 2017). Both systems were implemented in a software for nonlinear time-domain power systems simulation (CEPEL; ELETROBRAS, 2020a).

4.1 Brazilian 7 bus equivalent system

The Brazilian 7-Bus Equivalent System (Figure 4.1) is a reduced model of the South-Southeastern Brazilian system configuration in the 1990s. The system is composed of five generators, one of them being an equivalent machine of the Brazilian southeast system, installed at bus 7 and used as the angular reference of the model. Fifth order models are used to represent all five generators that are equipped with first order AVRs. The generators 1 to 4 are also equipped with second order traditional PSS.

Concerning the small-signal angular stability, this system is well damped at its original load condition. The less damped oscillation mode is an inter-area mode with a damping ratio of 6.38%, that corresponds to the oscillation between the SE Equivalent (G5) and the southern system (generators 1 to 4). The damping of this inter-area mode is considerably deteriorated, decreasing to around 3.10%, if the load of Bus 1 is reduced by 700MW at the initial conditions of the system (power flow). This load reduction corresponds to approximately 15% of the total load of the southern system. The goal of applying the proposed VRFT method is to improve the system damping performance at this modified operating point. To achieve that goal, a new PSS using a remote measured signal is designed for the Itaipu generator (bus 4). The linear analysis of the system model,

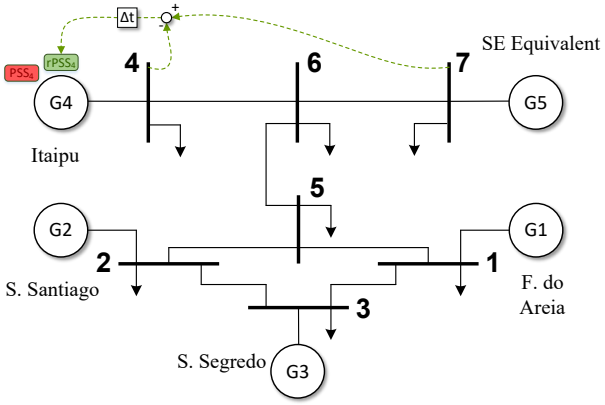

Figure 4.1 – Single-line diagram of the Brazilian 7-Bus Equivalent System.

presented in Appendix B.1, shows that this generator has the greater controllability factor over the inter-area mode. Although this is a model-based information, it is reasonable to consider it as basic knowledge of the power system operator.

4.1.1 Including a remote PSS

The adapted VRFT procedure is used to design an extra damping controller (rPSS) for the Itaipu generator (G4) using the difference between the frequencies of bus 7 and 4 as a remote input ($f_{7-4} = f_7 - f_4$). Those bus frequencies and generator were selected due to the characteristics of the inter-area mode.

Before being connected to the rPSS input, the remote signal passes through a washout filter, so the output signal of the data acquisition experiment is the filtered frequency difference, represented here by $y[n] = \hat{f}_{7-4}$. A fixed time-delay of 150 ms was considered. The input signal $u[n]$ is a 0.01 p.u. step applied to AVR reference input, at instant 1 s, and the data is collected for 5 seconds with a sampling time of 0.01 s.

As described in Section 3.5, two strategies are proposed to build the reference model needed for the VRFT procedure. The results obtained with both strategies are presented as follows.

4.1.1.1 Reference model using Method 1

The reference model $M_d(s)$ is built using the method described in Section 3.5.1. Analyzing the measured output signal $y[n]$, presented in Figure 4.2, it is possible to identify a predominant oscillation mode of approximately 0.8Hz. Using this frequency and a user-defined damping ratio of $\zeta_{min} = 20\%$, the natural frequency of the reference model is $\omega_n = 5.138$ rad/s. As described in Section 3.5.1, the NMP zero dynamics is neglected and replaced by a time delay of $\Delta t = 0.27\ s$. This time delay contains the NMP zero dynamics and the actual communication delay of 150 ms. Then, the transfer function of

the reference model is

$$M_d(s) = e^{-0.27s}\frac{0.04725s}{s^2 + 2.055s + 26.4}. \tag{4.1}$$

The controller was parameterized according to Equation (3.16), where the denominator of the transfer function is the same as the PSS already installed at generator 4. The solution to the VRFT problem was computed with Equation (3.7), using the measured data and is presented as follows

$$\rho = [\rho_1 \ \rho_2 \ \rho_3]' = [-253.25 \ \ -1181.79 \ \ -7040.86]'. \tag{4.2}$$

The resulting rPSS transfer function is

$$rPSS_4(s) = \frac{-253.25s^2 - 1181.79s - 7040.86}{s^2 + 30.77s + 236.7}. \tag{4.3}$$

The measured output signal $y[n]$ (filtered frequency difference) for the input signal $u[n]$ (step on the AVR of gen. 4) is presented in Figure 4.2, together with reference model output $y_d[n]$ (desired response) for the same input signal. The predicted output $y_p[n]$, computed with Equation (3.8), is also presented. Finally, the closed-loop response of the system $y_{CL}[n]$, obtained after inserting the $rPSS_4$ (4.5) in the power system model, is also presented, indicated by the red dashed line.

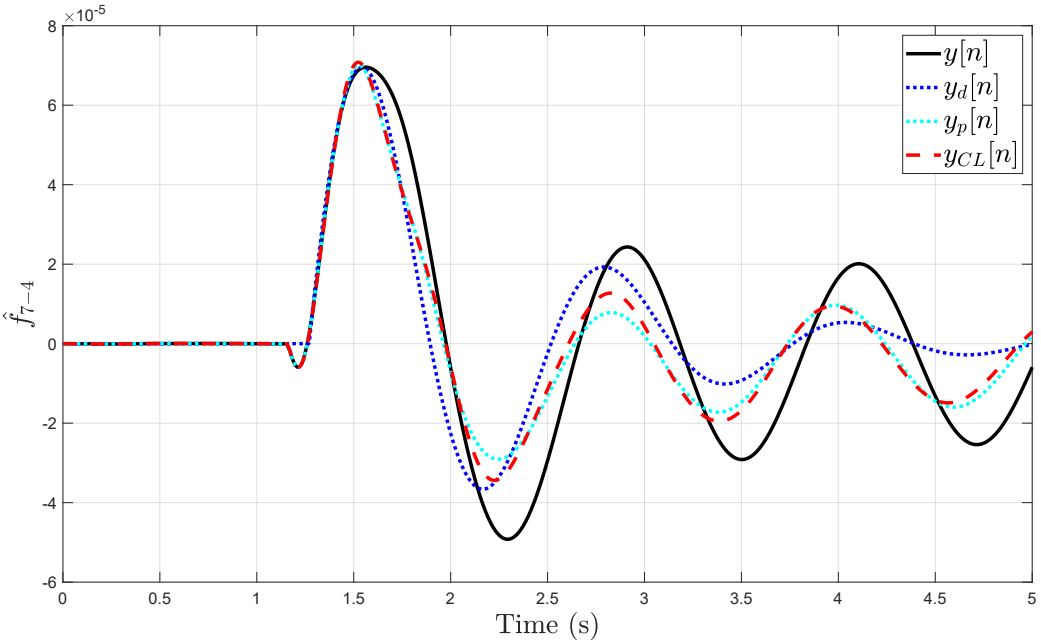

Figure 4.2 – Brazilian 7-bus system response to a step in the voltage regulator: filtered frequency difference between buses 4 and 7. Reference model built with Method 1.

The performance of the new controller was tested over a more severe scenario: a three-phase short-circuit was applied at bus 6 at instant 10 s and cleared after 30 ms. The

full nonlinear continuous-time simulation result (probe signal and short-circuit response) is presented in Figure 4.3a and Figure 4.3b, where the rotor angle of generator 4 and the non-filtered difference between frequencies of bus 7 and bus 4 are displayed, respectively. The inter-area mode corresponds to the oscillation between generators 1 to 4 and the SE Equivalent, but it is more evident at G4. Therefore the rotor angle of generator 4 is presented, using the equivalent machine as angular reference. The response without the rPSS is also presented for comparison.

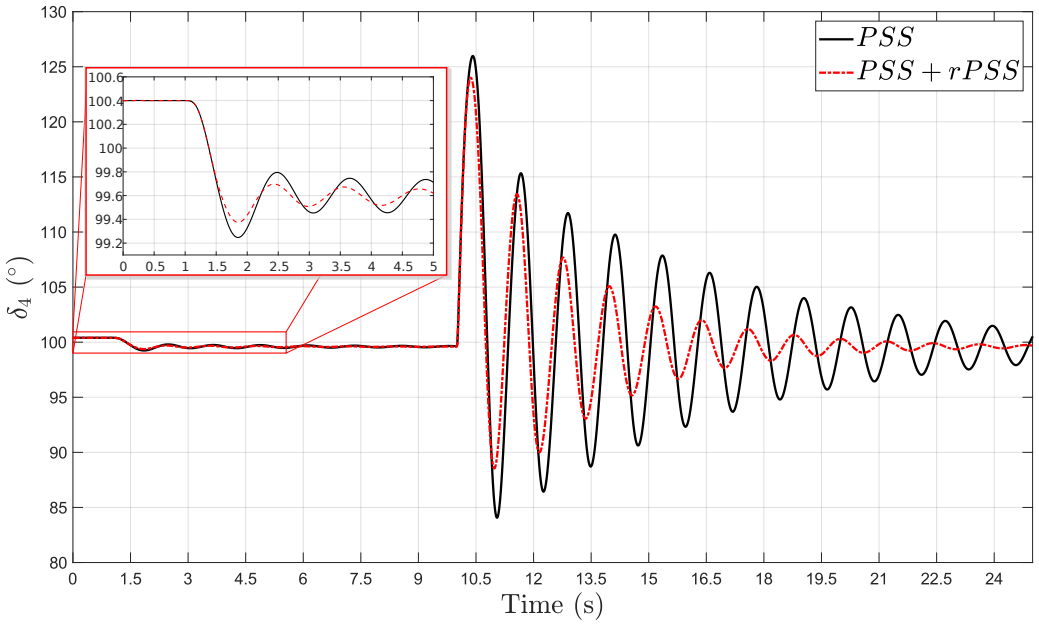

(a) Gen. 4 rotor angle.

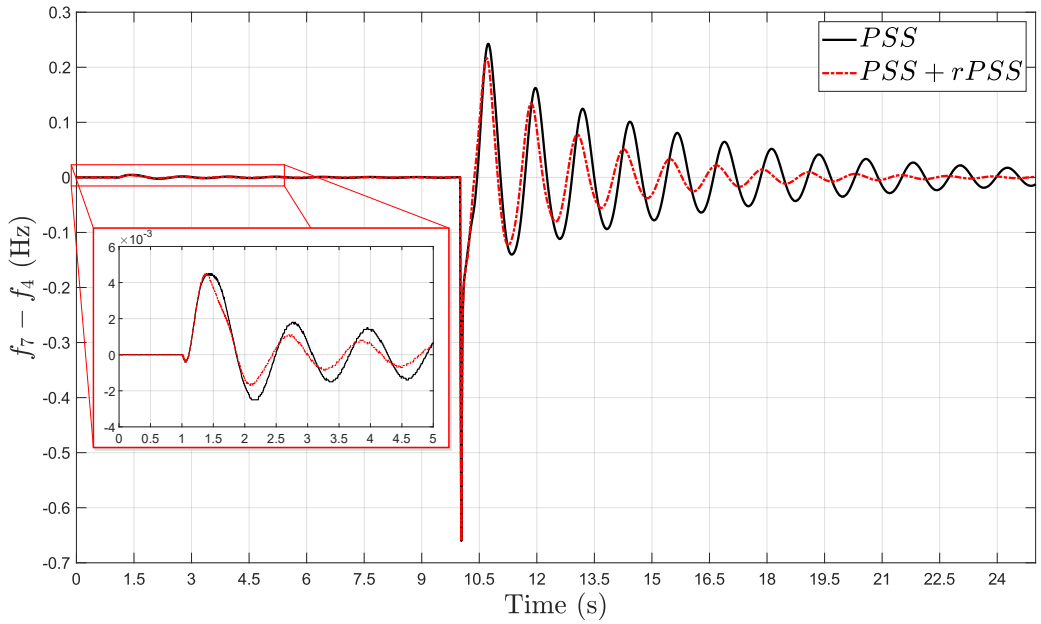

(b) Bus 7 and bus 4 frequency difference.

Figure 4.3 – Performance of the rPSS with $M_d[z]$ built with Method 1. Brazilian 7-bus system response to a step in the voltage regulator followed by a short-circuit.

The dynamic response presented in Figures 4.3a and 4.3b indicates that the

damping ratio of the inter-area mode was improved by the rPSS. Also, the closed-loop system output $y_{CL}[n]$ is similar to the predicted output $y_p[n]$, as shown in Figure 4.2, indicating that, even with a simple second order transfer function, it was possible to estimate the closed-loop performance of the system with the rPSS. The linear analysis of the system indicates that the damping ratio of the inter-area mode was increased to 5.64%.

4.1.1.2 Reference model using Method 2

The reference model $M_d(s)$ is built using the method described in Section 3.5.2. The estimated model has 9 poles and 8 zeros, with a 99.85% fit to estimation data, and a minimum damping of $\zeta_{min} = 10\%$ was used. The transfer function of the resulting reference model is presented in Appendix C.1.

As for the previous case, the controller was parameterized according to (3.16) and using the denominator of the PSS of the generator 4. The solution to the VRFT problem (Equation (3.7)) is

$$\rho = [\rho_1 \ \rho_2 \ \rho_3]' = [-201.27 \ \ -955.43 \ \ 227.13]' \tag{4.4}$$

and rPSS transfer function is

$$rPSS_4(s) = \frac{-201.27s^2 - 955.43s + 227.13}{s^2 + 30.77s + 236.7}. \tag{4.5}$$

The measured output signal $y[n]$ (filtered frequency difference) for the input signal $u[n]$ (step on the AVR of gen. 4) is presented in Figure 4.4, together with estimated system output $y_{est}[n]$ and reference model output $y_d[n]$ (desired response) for the same input signal. The signal $y_{est}[n]$ is the output of the estimated system before the minimum damping requirement is imposed. The predicted output $y_p[n]$, computed with Equation (3.8), is also presented. Finally, the closed-loop response of the system $y_{CL}[n]$, obtained after inserting the $rPSS_4$ (4.5) in the power system model, is also presented, indicated by the red dashed line.

As for the previous strategy, the performance of the new controller was tested over a more severe scenario and the same fault was considered: a three-phase short-circuit applied at bus 6 at instant 10 s and cleared after 30 ms. The full nonlinear continuous-time simulation result (probe signal and short-circuit response) is presented in Figure 4.5a and Figure 4.5b, where the rotor angle of generator 4 and the non-filtered difference between frequencies of bus 7 and bus 4 are displayed, respectively.

The closed-loop system output $y_{CL}[n]$ is very similar to the predicted output $y_p[n]$, as shown in Figure 4.4, indicating that the controller was successfully tuned. The inclusion of the rPSS improved the damping performance of the system significantly. The

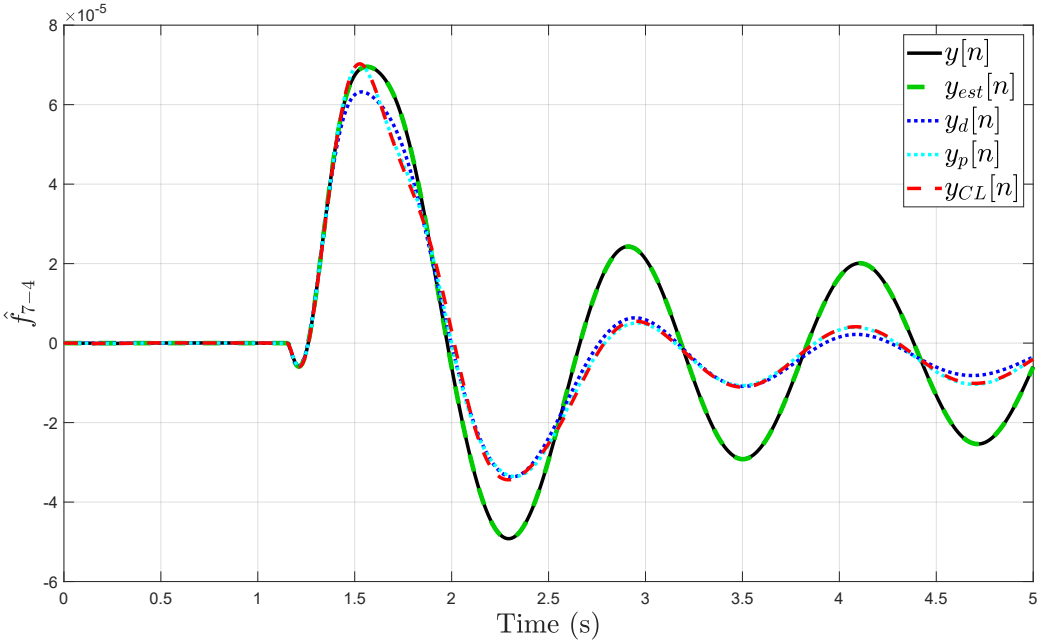

Figure 4.4 – Brazilian 7-bus system response to a step in the voltage regulator: bus 7 and bus 4 filtered frequency difference (collected at bus 4). Reference model built with Method 2.

linear analysis of the system indicates that the damping ratio of the inter-area mode was increased to 7.36%.

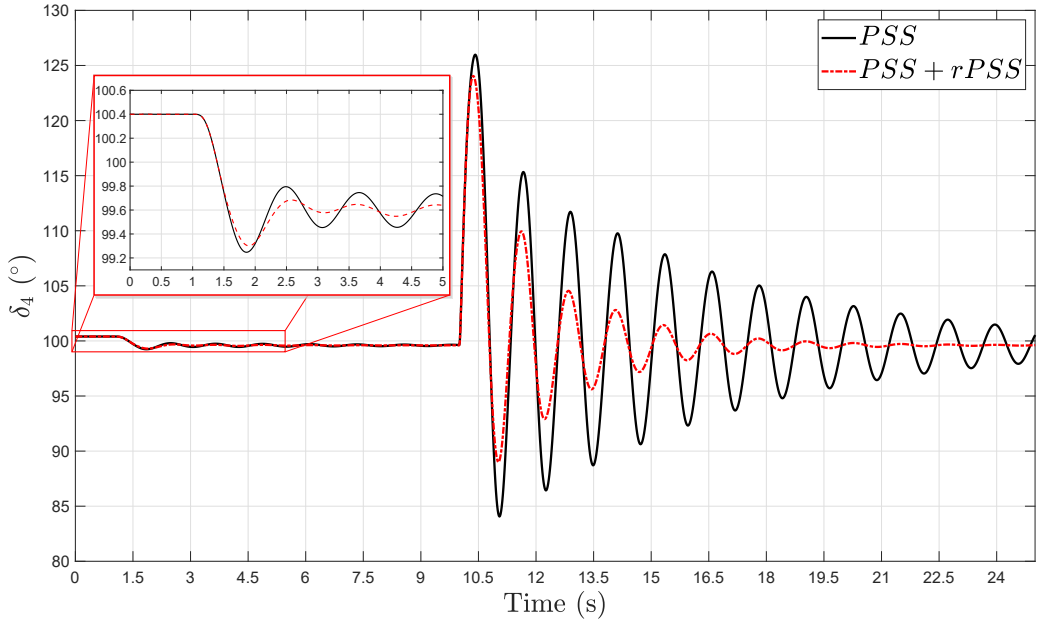

(a) Gen. 4 rotor angle.

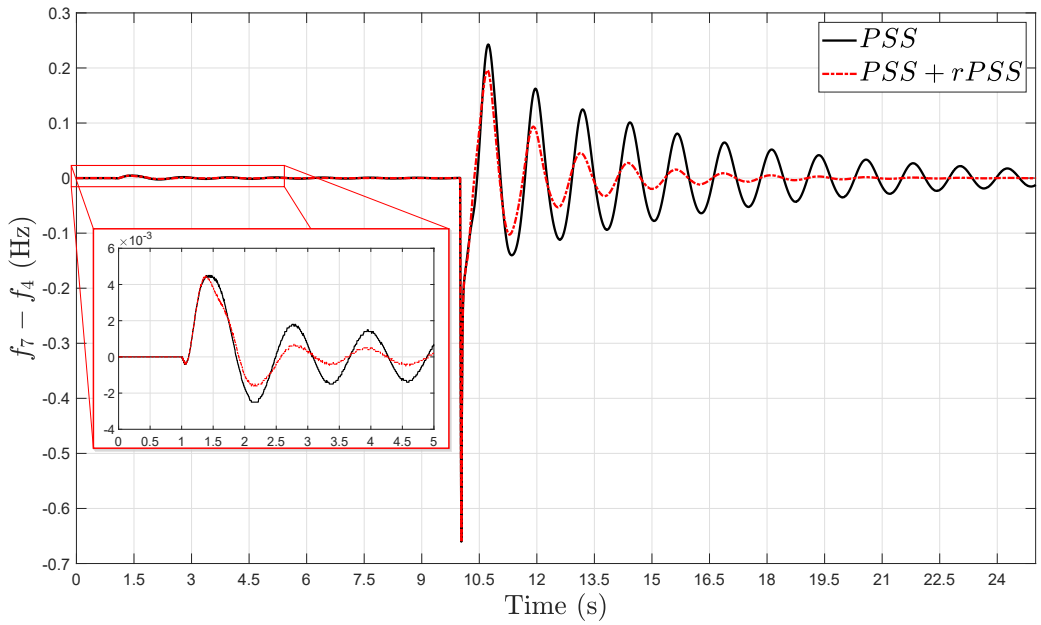

(b) Bus 7 and bus 4 frequency difference.

Figure 4.5 – Performance of the rPSS with $M_d[z]$ built with Method 2. Brazilian 7-bus system response to a step in the voltage regulator followed by a short-circuit.

4.2 The 39-Bus New-England Test System

First presented in Athay, Podmore and Virmani (1979), the 39-Bus New-England Test System (NETS) is a ten machine system that models the New England region of the US power system and its connection to the New York power system, that is represented by an equivalent generator (G1). All 10 generators are equipped with second order traditional PSS that efficiently damp all oscillation modes of the system. At its normal operating point, this system has one inter-area oscillation mode with a damping

ratio of 12.08% and observed as the oscillation of generators 2 to 10 against generator 1. The damping ratio of this inter-area mode was reduced by making the following modifications on the system. First, each bus load was increased by 13%, what reduced the damping ratio to 6.69%. Then, generators G4 and G10 were replaced by wind power plants (Figure 4.6), deteriorating the damping ratio considerably, to around 1.45%.

The wind power plants are modeled by variable speed synchronous generators connected to the grid via a voltage source converter and a transformer (same used for the original generators). They are included in the power system model using the built-in model for wind generation of the simulation software (CEPEL; ELETROBRAS, 2020a) and are equipped with first-order voltage regulators. Each wind turbine is considered to be operating at 0.75 pu capacity of a nominal 850 kW, in a constant power factor control mode. The wind power plants are introduced here to model the reduction of damping performance caused by a high penetration of IBS generation, without interfering in the power flow condition of the system. To keep the original power generation of the NETS, the wind power plants are composed of 392 (bus 30) and 991 (bus 33) wind turbines in parallel.

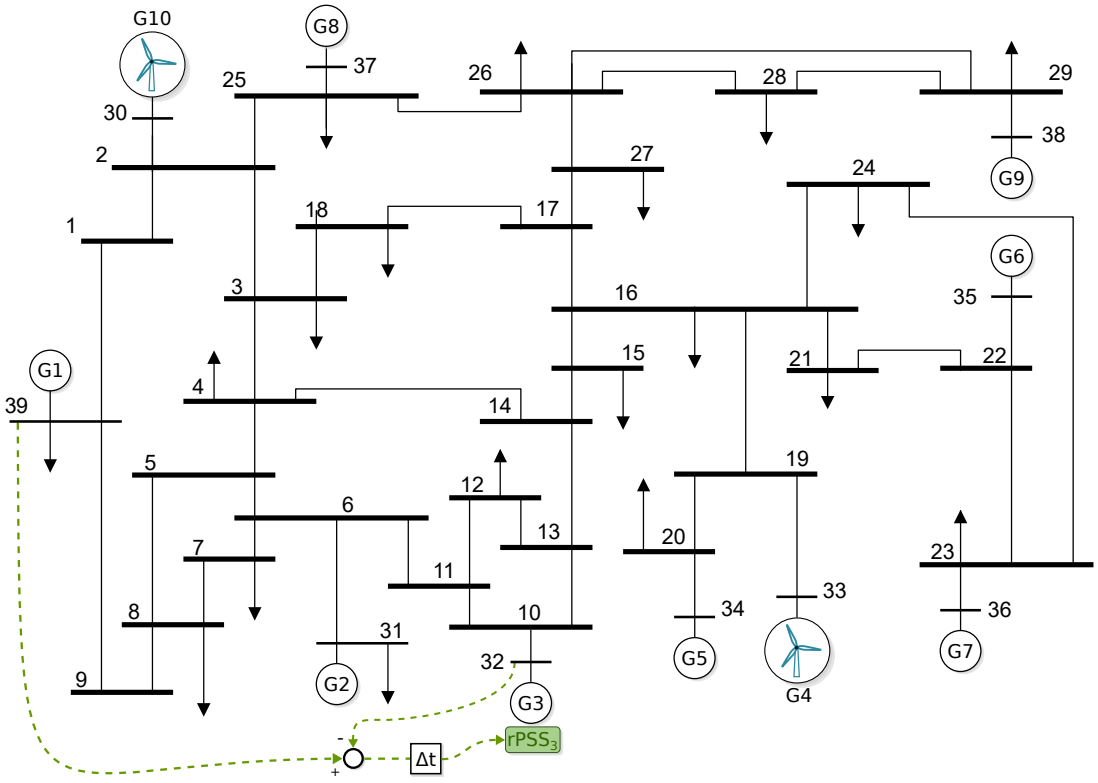

Figure 4.6 – Single-line diagram of the modified 39-Bus New-England Test System.

The proposed VRFT method is applied to this system to improve the damping ratio of the inter-area oscillation mode. As for the previous test system, a generator with a high controllability factor over the inter-area mode is selected to receive the extra damping controller. Since this is a model-based information, it is not expected that the exactly

controllability factors are known. It is only necessary to know that if the selected generator has sufficient influence over the oscillation mode. And it is reasonable to consider it as basic knowledge of the power system operator. To simulate this scenario where the controllability factors are not precisely known, the generator with the second highest controllability factor was selected to receive the rPSS, instead of the highest one. Therefore, the rPSS is installed at G3 (bus 32), as illustrated in Figure 4.6. The controllability and observability factors of the inter-area mode are presented in Appendix B.2. Then, once the goal of the rPSS is to improve the damping ratio of the inter-area mode, the remote frequency is measured at bus 39. This is the natural choice since it is known that the mode corresponds to an oscillation between G1 (bus39) and the rest of the system.

4.2.1 Including a remote PSS

As described in Section 4.2, the generation characteristics and operating point modifications deteriorated the damping ratio of the inter-area mode of the NETS. Under this condition, the adapted VRFT procedure was applied to design a rPSS to be installed at the voltage control loop of the generator 3 (higher influence over the inter-area mode). As for the previous system, a difference between bus frequencies remotely measured is used as input for this new PSS. Bus 39 and 32 were selected based on the inter-area characteristics of the oscillation mode and a fixed time-delay of 150 ms was considered. Before being connected to the rPSS input, the remote signal passes through a washout filter and it is denoted by $y[n] = \hat{f}_{39-32}$. The input signal $u[n]$ is a 0.01 p.u. step applied to reference input of the generator 3 AVR, at instant 1 s, and the data is collected for 5 seconds with a sampling time of 0.01 s.

4.2.1.1 Reference model using Method 1

The reference model $M_d(s)$ is built using the method described in Section 3.5.2. From the measured signal $y[n]$, presented in Figure 4.7, it is possible to detect a 0.6Hz predominant oscillation mode. Then, considering the damping ratio of $\zeta_{min} = 20\%$, the natural frequency of the reference model is $\omega_n = 3.84$ rad/s, which results in the following transfer function

$$M_d(s) = e^{-0.33s}\frac{0.0254s}{s^2 + 1.537s + 14.76}. \tag{4.6}$$

The same denominator of the already installed PSS of the generator 3 was used to parameterize the rPSS, according to (3.16). The solution to the VRFT problem, computed with Equation (3.7), and the resulting transfer function are

$$\rho = [\rho_1 \ \rho_2 \ \rho_3]' = [143.0 \ \ -441.70 \ \ -2534.08]' \tag{4.7}$$

and

$$rPSS_3(s) = \frac{143s^2 - 441.7s - 2534.08}{s^2 + 10s + 25}. \tag{4.8}$$

The measured output signal $y[n]$ and reference model output $y_d[n]$ (desired response) are presented in Figure 4.7, for the input signal $u[n]$. The predicted output $y_p[n]$, computed with Equation (3.8), and the closed-loop response $y_{CL}[n]$ are also presented. This last one is the simulated response after inserting the rPSS (4.8) in the power system model.

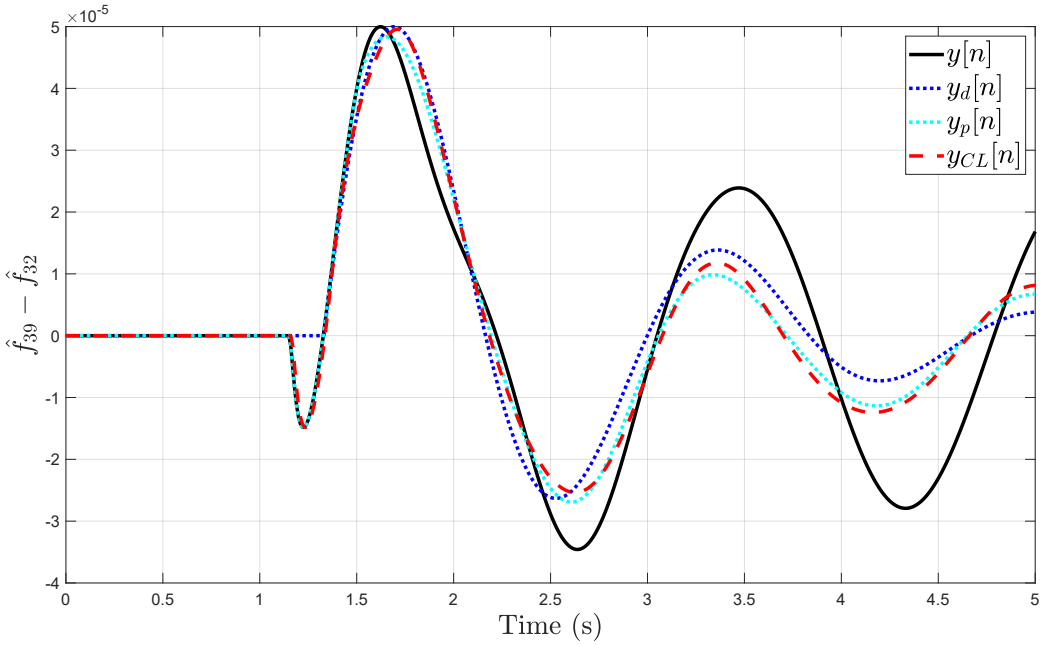

Figure 4.7 – NETS response to a step in the voltage regulator: bus 39 and bus 34 filtered frequency difference (collected at bus 34). Reference model built with Method 1.

A more severe disturbance was applied to evaluate the improvement on the damping performance. A three-phase short-circuit was applied at the middle of line 1-2 at instant 10 s and cleared after 30 ms, without any control action. The full nonlinear continuous-time simulation result (probe signal and short-circuit response) is presented in Figures 4.8a and 4.8b, where the rotor angle of G3 in respect to G1 and the non-filtered frequency difference between bus 39 and 32 are displayed. The response without the rPSS is also presented for comparison.

The inclusion of the rPSS at generator 3 had a positive impact over the damping performance of the system. As presented in Figures 4.8a and 4.8b, the damping ratio of the inter-area oscillation mode is grater in the case with the $rPSS_3$. The predicted output $y_p[n]$ turned out to be a good estimation of the closed-loop response $y_{CL}[n]$, as shown in Figure 4.7. The improvement in the damping performance is supported by the linear analysis of the model, that indicates a damping ratio of 6.8% for the inter-area mode, after the inclusion of the rPSS.

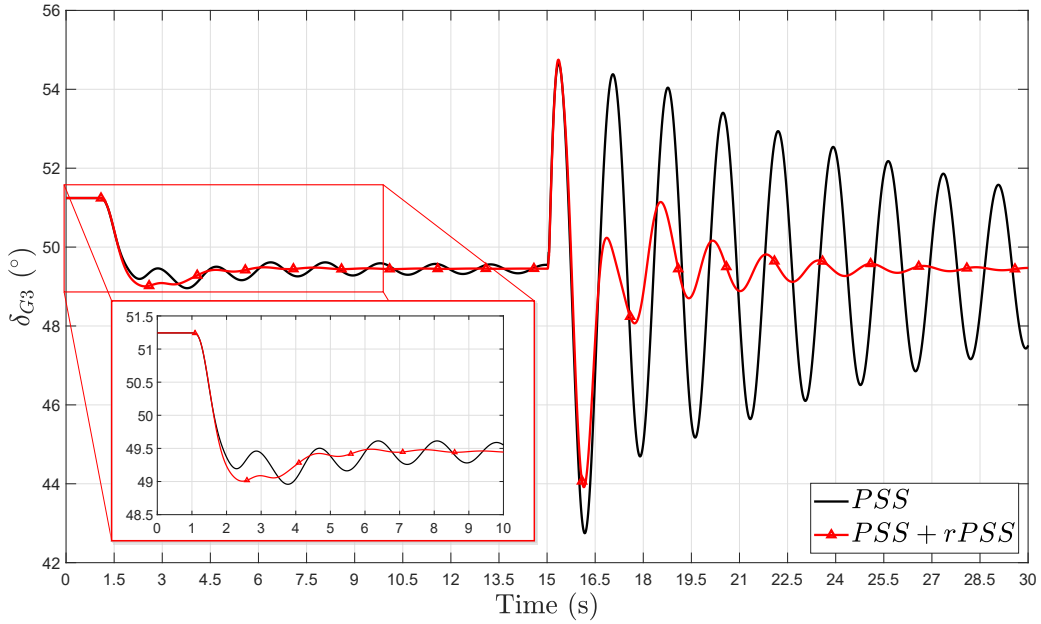

(a) Gen. 3 rotor angle.

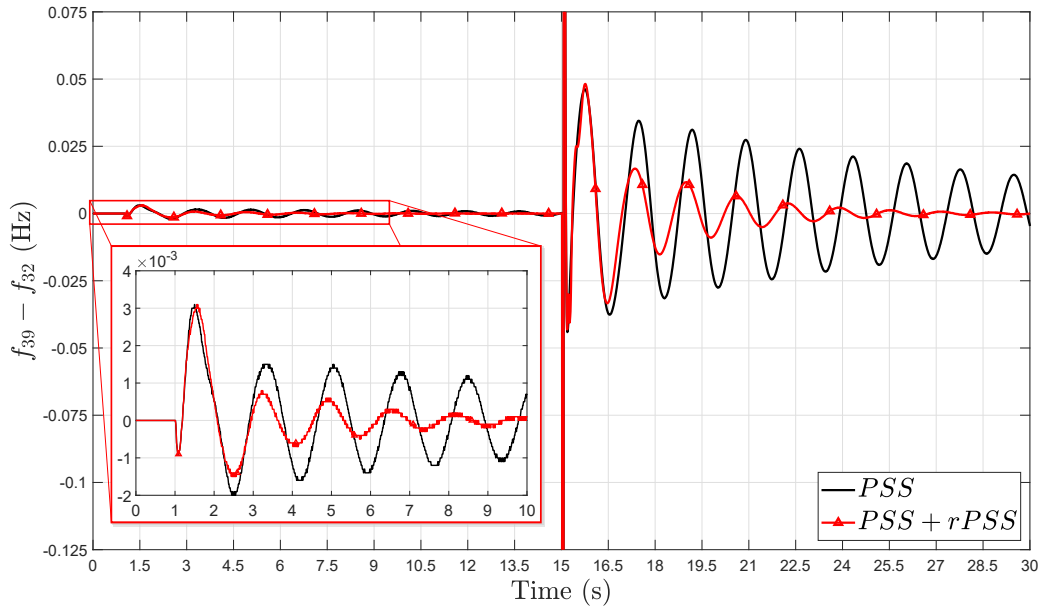

(b) Bus 39 and bus 32 frequency difference.

Figure 4.8 – Performance of the rPSS with $M_d[z]$ built with Method 1. NETS response to a step in the voltage regulator followed by a short-circuit.

4.2.1.2 Reference model using Method 2

The reference model $M_d(s)$ is built using the method described in Section 3.5.2. A model with 12 poles and 11 zeros was identified using the measured data, with a 99.99% fit to estimation data. And the reference model was built considering a minimum damping ratio of $\zeta_{min} = 10\%$. The transfer function of the reference model is presented in the Appendix C.2.

The controller was parameterized using the denominator of the PSS installed at generator 3, according to (3.16). The solution to the VRFT problem, Equation (3.7),

and rPSS transfer function are

$$\rho = [\rho_1 \ \rho_2 \ \rho_3]' = [-19.90 \ \ -392.55 \ \ 1255.50]' \tag{4.9}$$

and

$$rPSS_3(s) = \frac{-19.90s^2 - 392.55s + 1255.50}{s^2 + 10s + 25}. \tag{4.10}$$

The measured output signal $y[n]$, estimated system output $y_{est}[n]$ and reference model output $y_d[n]$ (desired response) are presented in Figure 4.9, for the input signal $u[n]$. The predicted output $y_p[n]$, computed with Equation (3.8), and the closed-loop response $y_{CL}[n]$ are also presented. This last one is the simulated response after inserting the rPSS (4.10) in the power system model.

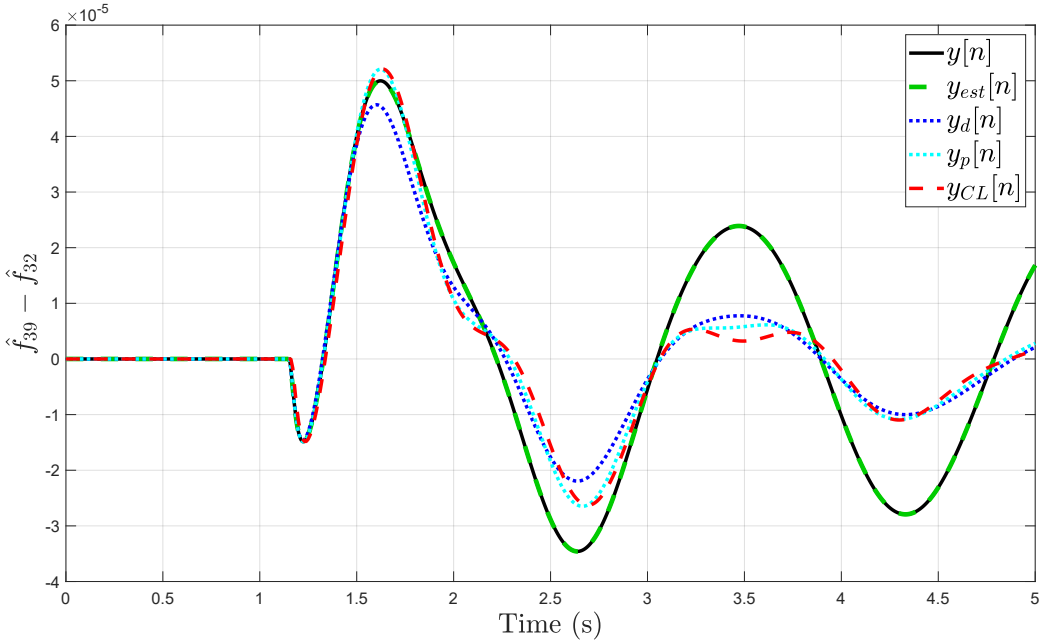

Figure 4.9 – NETS response to a step in the voltage regulator: bus 39 and bus 34 filtered frequency difference (collected at bus 34). Reference model built with Method 2.

As for the previous case, a more severe disturbance was also applied to evaluate the improvement on the damping performance. The same disturbance was considered, a three-phase short-circuit was applied at the middle of line 1-2 at instant 10 s and cleared after 30 ms, without any control action. The full nonlinear continuous-time simulation result (probe signal and short-circuit response) is presented in Figures 4.10a and 4.10b, where the rotor angle of G3 in respect to G1 and the non-filtered frequency difference between bus 39 and 32 are displayed. The response without the rPSS is also presented for comparison. The closed-loop response is presented for three values of fixed communication delay to evaluate its influence on the rPSS performance.

The dynamic response presented in Figures 4.10a and 4.10b shows a notable improvement on the oscillation damping performance of the system. This is confirmed by the linear analysis of the model that indicates that the inclusion of the rPSS increased the damping ratio of the inter-area mode to 9.50%. As in the previous case, the closed-loop system output $y_{CL}[n]$ is very similar to the predicted output $y_p[n]$, as shown in Figure 4.9, endorsing the consistency of the method. And, even though a fixed delay of 150 ms was considered during the data collecting simulation and design procedure, the $\pm$100 ms variation had no major impact on the damping performance. This small impact was expected because, since the communication delay is in the order of dozens of milliseconds, it has a small influence over the electromechanical dynamics of the system, especially in the inter-area oscillation modes.

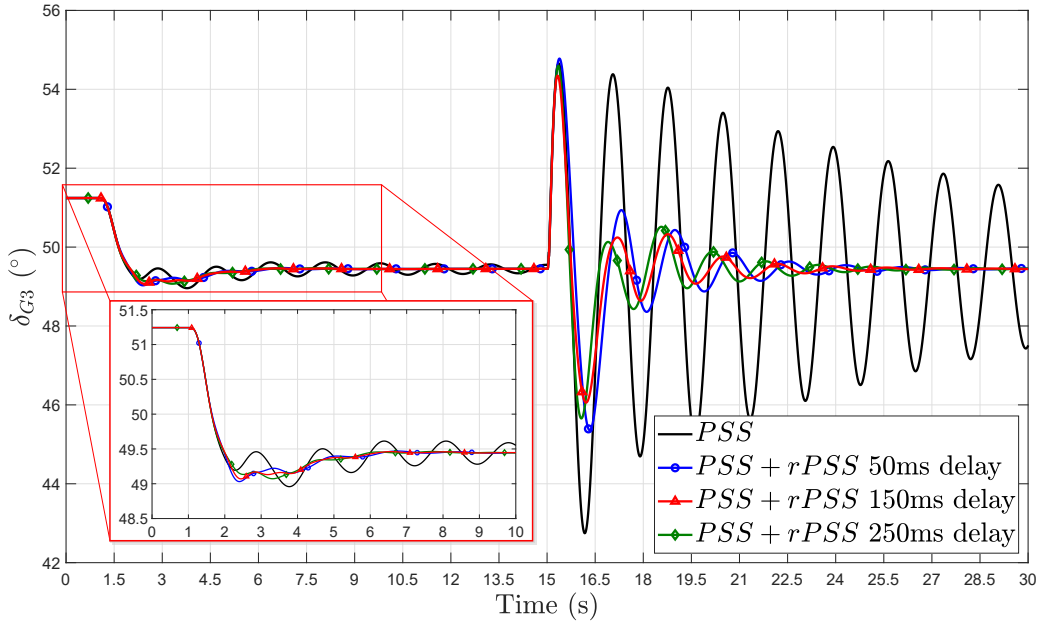

(a) Gen. 3 rotor angle.

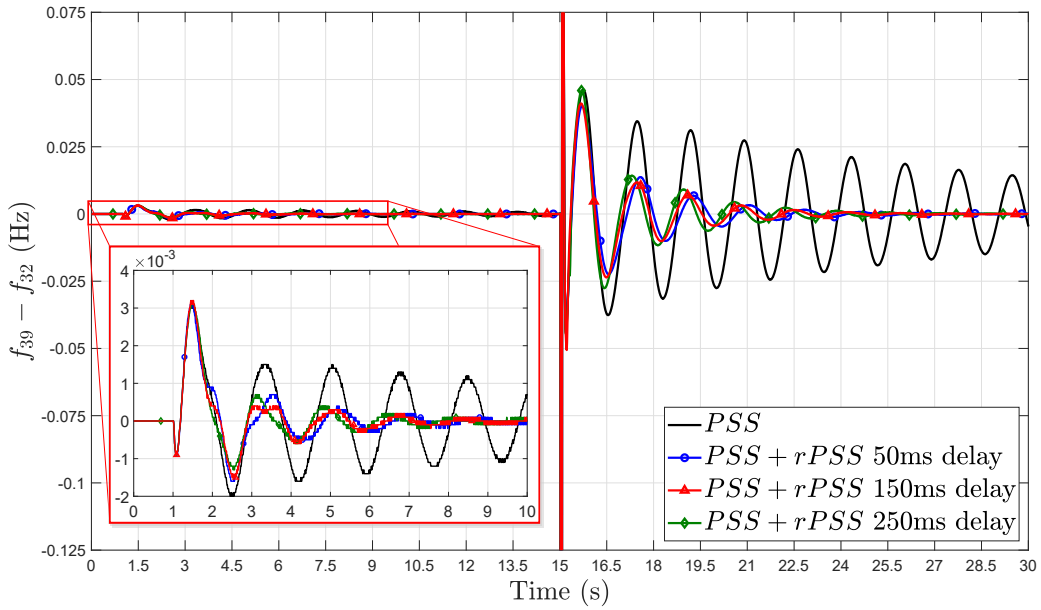

(b) Bus 39 and bus 32 frequency difference.

Figure 4.10 – Performance of the rPSS with $M_d[z]$ built with Method 2. NETS response to a step in the voltage regulator followed by a short-circuit.

4.2.2 Retuning the remote PSS

To demonstrate the versatility of the method over variations in the operating condition a new scenario was tested using the 39-Bus New-England Test System. Consider the system described in Section 4.2 equipped with the remote controller presented in (4.10). Variations in the operating conditions of the system may lead to an operating point at which the damping controllers, even with the $rPSS_3$ included, may not guarantee an appropriate damping performance. In this scenario the PSS retuning approach, described in Section 3.4.2, can be applied to adjust a selected PSS and improve the damping

performance of the system. To emulate that scenario, a series of load variations were simulated to lead the system to an poorly damped operating condition and an *online* procedure is applied to update the $rPSS_3$.

As in the previous scenario, the input of the remote controller is the difference between bus frequencies 39 and 32. A fixed time-delay of 150 ms was considered. Before being connected to the rPSS input, the remote signal passes through a washout filter and it is denoted by $y[n] = \hat{f}_{39-32}$. Before the data acquisition experiment a series of load variations is applied as follows:

- t=0.1 s - increase of 10% in the load of bus 39.
- t=2.0 s - reduction of 15% in the load of bus 20.
- t=5.0 s - increase of 15% in the load of bus 39.
- t=6.0 s - reduction of 15% in the load of bus 20.
- t=10.0 s - increase of 5% in the load of bus 39.
- t=11.0 s - reduction of 15% in the load of bus 20.

The input signal $u[n]$ is a 0.01 p.u. step applied to reference input of the generator 3 AVR, at instant t=26.0 s, and the data is collected for 5 seconds with a sampling time of 0.01 s. The reference model $M_d(s)$ is built using the method described in Section 3.5.2, with $\zeta_{min} = 10\%$, and the identified model has 12 poles and 11 zeros, with a 86.23% fit to estimation data. The transfer function of the reference model is presented in the Appendix C.3.

The controller was parameterized using the denominator of the $rPSS_3$, according to (3.16), and the VRFT criterion (3.6) was minimized using the measured data. The array of parameters ρ computed with Equation (3.7) is

$$\rho = [\rho_1 \ \rho_2 \ \rho_3]' = [-21.74 \ \ -121.92 \ \ 460.06]' \tag{4.11}$$

and the retuned rPSS transfer function, according with Equation (3.18), is

$$rPSS_{3-retuned}(s) = \frac{-41.64s^2 - 514.47s + 1715,56}{s^2 + 10s + 25}. \tag{4.12}$$

The measured output signal $y[n]$, estimated system output $y_{est}[n]$ and reference model output $y_d[n]$ (desired response) are presented in Figure 4.11, for the input signal $u[n]$. The predicted output $y_p[n]$, computed with Equation (3.8), and the closed-loop response $y_{CL}[n]$ are also presented. Note that this closed-loop response is the one obtained considering that the $rPSS_{3-retuned}$ of Equation (4.12) is installed in the system since the beginning of

the simulation, i.e., the updating of the parameters (switching) was not simulated in the response presented in this figure.

The probe signal $u[n]$ and the data acquisition process occurred with the system already running, that is the reason why the signal $y[n]$ do not start at zero in Figure 4.11. Still, the value of $y[n]$ immediately before the probe signal is applied is considered to be the initial condition of the system. In a real online implementation of the method, the $rPSS_{3-retuned}$ is included after the time window of the data acquisition process. A more realistic scenario is presented in Figure 4.12, where a full nonlinear continuous-time simulation is presented. The updating of the $rPSS_3$ to $rPSS_{3-retuned}$ occurs at instant t=30.2 s, 200 ms after the data-acquisition experiment ends. As for the previous scenarios, a more severe disturbance was also applied to evaluate the improvement on the damping performance. A three-phase short-circuit was applied at the middle of line 16-19 at instant t=40.0 s and cleared after 30 ms, without any control action. The rotor angle of G3 in respect to G1 is presented in Figure 4.12a and the non-filtered frequency difference between bus 39 and 32 is displayed in Figure 4.12b. The response with the initial rPSS is also presented for comparison.

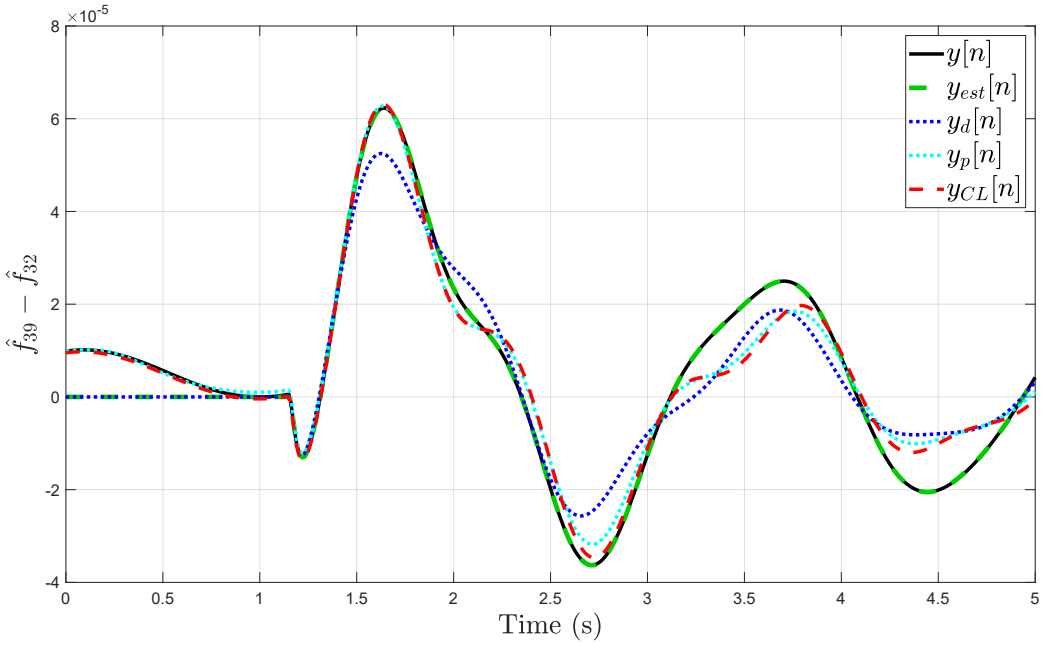

Figure 4.11 – NETS response to a step in the voltage regulator: bus 39 and bus 34 filtered frequency difference (collected at bus 34). Retuning procedure with reference model built with Method 2.

The dynamic response presented in Figures 4.12a and 4.12b shows that the retuning process was successful to achieve a suitable damping performance after the variation of the operating condition.

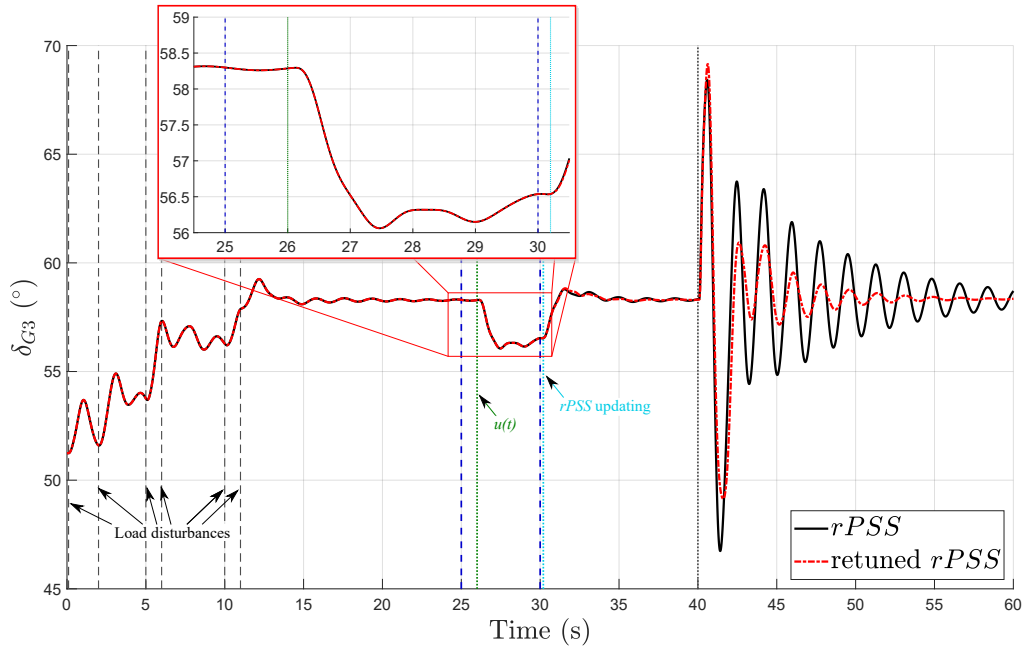

(a) Gen. 3 rotor angle.

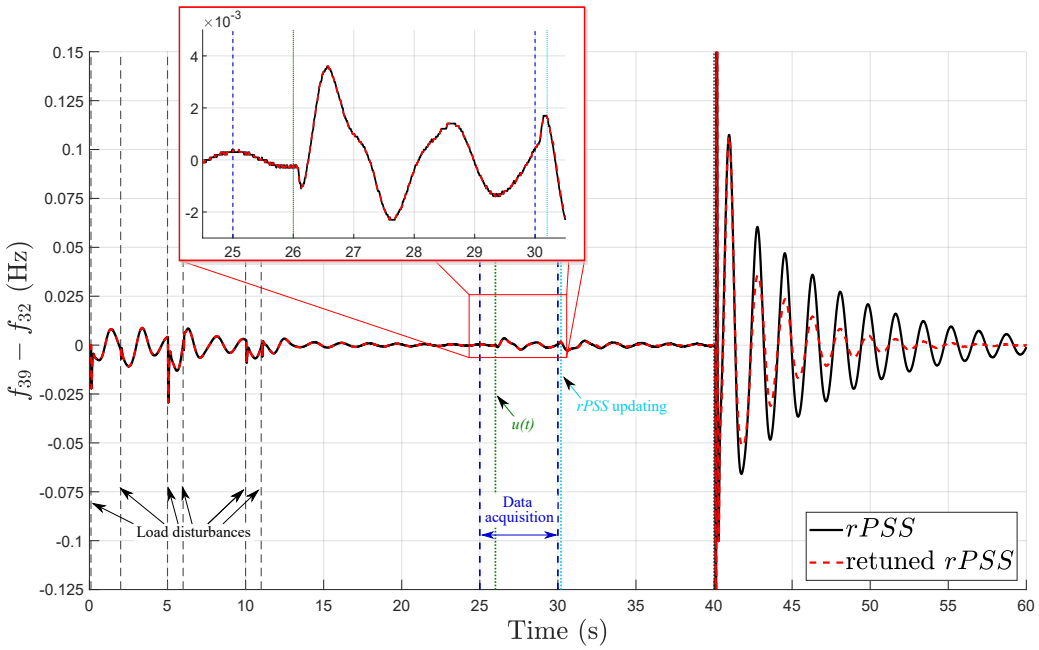

(b) Bus 39 and bus 32 frequency difference.

Figure 4.12 – Performance of the retuned rPSS with $M_d[z]$ built with Method 2. NETS response to a step in the voltage regulator followed by a short-circuit.

4.3 Comments

This chapter presented the results obtained with the proposed data-driven procedure to design SISO power system damping controllers. The explored technique consists on an adaptation of data-driven control, design method called VRFT, to design a PSS-like controller using remote measurements as inputs. The controller, called remote PSS (rPSS), is a WADC designed to improve the damping performance of the power system,

focusing on inter-area oscillation modes. A procedure to re-tune the already designed rPSS is also presented, so the controller can be adapted to variations in the operating condition. The method was successfully applied to two benchmark power systems.

The VRFT procedure is a model reference method, where the controller is tuned so the closed-loop dynamics matches, as closely as possible, the dynamics of the reference model. Two procedures are proposed to build such reference models, considering the power system oscillation problem. The first one is based on the identification of the predominant inter-area oscillation mode and uses a classical second-order transfer function structure. The second one is based on traditional techniques of identification and pole placement to build a transfer function that approximates the measured input/output dynamics. Those procedures made the task of building the reference model, considering the damping performance requirement, much easier.

The method was applied to design damping controllers for two benchmark systems, the Brazilian 7-bus test system and the 39-Bus New-England Test System. Critical operating points were considered for the test systems, where load variations and the high penetration of IBS generation deteriorated the damping ratio of the inter-area modes. The proposed rPSS controllers were able to successfully increase the damping ratio of the inter-area modes to secure levels, guaranteeing the small-signal stability of the system, in both test systems. Positive results were obtained with both strategies proposed to build the reference model. The strategy based on a classical second-order transfer function structure is simpler and faster, since it does not need a curve-fitting stage. However, the predicted closed-loop responses, computed beforehand, were more accurate when the second strategy was applied. Also, the closed-loop responses were closer to the desired ones when the reference models were built using the second strategy. Furthermore, variations in the communication time delay were tested and had no significant impact on the performance of the proposed controller. At last, a a second feature of the method was tested, where the previously designed rPSS for the 39-bus NETS were re-tuned to improve the damping performance of the system after variation in the operating condition. An online control design procedure was simulated and the damping performance was successfully improved without needing to include an extra controller.

5 Further discussion and applications of the VRFT method to WADC

This chapter presents a further discussion about the VRFT method in the power system oscillation damping context. A preliminary methodology for expanding the formulation for the MIMO case is proposed. Also, a different control design strategy is explored in a coordinated control approach. The method is tested with the same power system models presented in Chapter 4 and some preliminary results are presented.

The MIMO case

The VRFT is data-driven method conceived for the design of reference tracking SISO controllers. However, its formulation has been expanded to deal with MIMO control design already. In Nakamoto (2004) the SISO formulation is directly expanded for the MIMO case, but with a strong restriction over the reference model. It needs to be a diagonal transfer function matrix, where all nonzero elements are the same, so the filter structure is satisfied. A similar formulation is presented in Formentin, Savaresi and Re (2012), with the addition of a 'optimal prefiltering' formulation. In Campestrini, Eckhard, Chía and Boeira (2016), a new formulation is proposed to reduce the bias of the designed controller, where the bias is defined as the error between the ideal controller and the estimated one. The formulation presented in these works have two characteristics in common that impede the direct application of the method to the power system damping application as proposed in this work. The first one is the reference tracking formulation, as for the SISO case the formulation needs to be adjusted to cope with the PSS design, i.e., place the controller in the feedback loop instead of the direct loop. The second one is the reference model structure. All three works use a diagonal transfer function matrix as the reference model. Thus, the full transfer function matrix MIMO controller is designed so the closed-loop system has a decoupled dynamics. In a interconnected power system, an inter-area oscillation can affect a large group of generators and the goal of the POD controllers is to assure that those oscillations are properly damped. By definition, an inter-area oscillation is a global phenomenon, thus, it is not reasonable to impose a decoupled dynamics to the closed-loop system. On the contrary, a coupled dynamics is expected, with various generators oscillating after a disturbance, but with an acceptable damping ratio.

One common approach to improve the inter-area damping performance of power systems using traditional PSS is to perform a coordinated design. That is, tune a group of PSSs simultaneously to achieve a global performance. Since the inter-area modes have impact over large areas of the power system, the coordinated design of multiple PSSs is an intuitive and cost-effective approach and has been widely explored in the literature

(RAMOS, 2004; RAMOS, 2005; BERNARDO, 2018). In this section, the VRFT procedure adapted to cope with the PSS design, presented in Section 3, is expanded for the MIMO case. But, instead of designing WAPSS, the method is applied to re-tune a group of PSSs simultaneously, in a coordinated design approach. For that, the controller is defined as a MIMO decentralized controller (diagonal transfer function mantrix). The multiple PSSs control structure as well as the measured signals are illustrated in Figure 5.1.

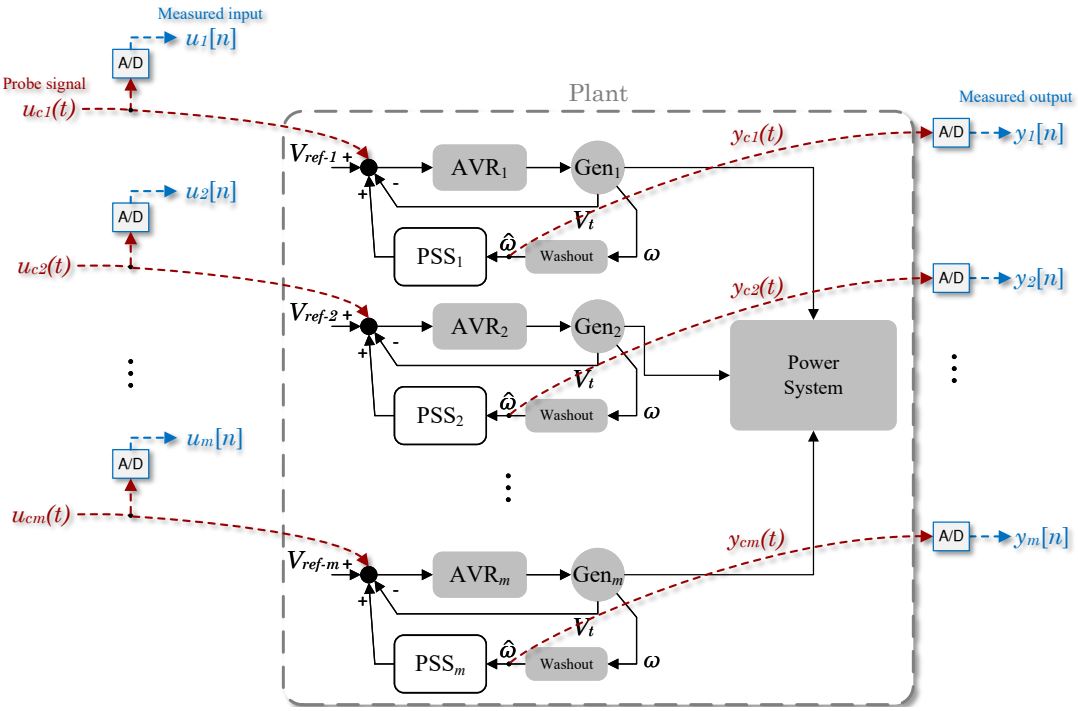

Figure 5.1 – Control Structure - Traditional MIMO PSS

5.1 MIMO Formulation

The MIMO VRFT procedure proposed in this work follows the control structure presented in Figure 5.2, where $G[z]$ represents the discrete-time version of the MIMO plant with m inputs and m outputs and $C_i[z]$ represents the discrete-time MIMO ideal controller. The signals $u_1[n], u_2[n], \ldots, u_m[n]$ are the perturbation inputs and $y_1[n], y_2[n], \ldots, y_m[n]$ are the outputs of the system. Supposing the ideal controller $C_i[z]$ exists, $\bar{r}_1[n], \bar{r}_2[n], \ldots, \bar{r}_m[n]$ are the *virtual* reference signals that produce the same outputs $y_1[n], y_2[n], \ldots, y_m[n]$ and $\bar{f}_1[n], \bar{f}_2[n], \ldots, \bar{f}_m[n]$ are the *virtual* control outputs.

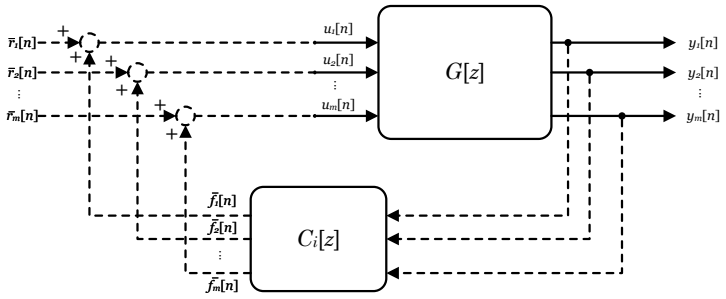

Figure 5.2 – Modified virtual closed-loop MIMO system

To match the control structure of Figure 5.1 it is necessary to impose a diagonal structure to the controller $C_i[z]$, so each diagonal element is a transfer function associated with one PSS of the power system, as follows

$$C_i[z] = \begin{bmatrix} C_{i1}[z] & 0 & \dots & 0 \\ 0 & C_{i2}[z] & \dots & 0 \\ \vdots & \vdots & \ddots & \vdots \\ 0 & 0 & \dots & C_{im}[z] \end{bmatrix}. \tag{5.1}$$

A $m \times m$ transfer function matrix $M_d[z]$ is considered to be the reference model that represents the dynamics of the closed-loop system with the ideal controller. So, $M_d[z]$ is a full transfer function matrix where each element corresponds the transfer function that models each input/output pair of the reference model, as follows.

$$M_d[z] = \begin{bmatrix} M_{d_{11}}[z] & M_{d_{12}}[z] & \dots & M_{d_{1m}}[z] \\ M_{d_{21}}[z] & M_{d_{22}}[z] & \dots & M_{d_{2m}}[z] \\ \vdots & \vdots & \ddots & \vdots \\ M_{d_{m1}}[z] & M_{d_{m2}}[z] & \dots & M_{d_{mm}}[z] \end{bmatrix}. \tag{5.2}$$

Let $U[n] = [u_1[n], u_2[n], \dots, u_m[n]]^\top$ and $Y[n] = [y_1[n], y_2[n], \dots, y_m[n]]^\top$ be the arrays of measured inputs and outputs, respectively. As in the traditional VRFT approach, the array of *virtual* reference signals $\bar{R}[n] = [\bar{r}_1[n], \bar{r}_2[n], \dots, \bar{r}_m[n]]^\top$ can be defined in function of the reference model,

$$\bar{R}[n] = \mathcal{Z}^{-1}\left\{\bar{R}[z]\right\} = \mathcal{Z}^{-1}\left\{(M_d[z])^{-1} Y[z]\right\}, \tag{5.3}$$

where $Y[z]$ is the z-transform of $Y[n]$.

Considering the ideal scenario, where the ideal parameterizable controller $C_i[z] = C[z, \rho_i]$ exists and the closed-loop dynamics matches $M_d[z]$ exactly, the array of *virtual* outputs of the controller $\bar{F}[n] = [\bar{f}_1[n], \bar{f}_2[n], \dots, \bar{f}_m[n]]^\top$ can be computed by

$$\bar{F}[n, \rho_i] = \mathcal{Z}^{-1}\left\{\bar{F}[z, \rho_i]\right\} = \mathcal{Z}^{-1}\left\{C[z, \rho_i] Y[z]\right\} \tag{5.4}$$

and the sum of the *virtual* references and *virtual* control output signals equals the input signals, that is,

$$U[n] - \left(\bar{R}[n] + \bar{F}[n, \rho_i]\right) = 0. \tag{5.5}$$

Thus, the MIMO VRFT method follows a procedure similar to the SISO one presented in Section 3, that is to impose a parameterized structure to the controller and find the array of parameters ρ that minimizes the following prediction error

$$\mathcal{E}[n,\rho] = U[n] - \bar{R}[n] - \bar{F}[n,\rho]. \tag{5.6}$$

As for the SISO case, an alternative formulation is possible by applying a filter to the signals used to compute the error $\mathcal{E}[n,\rho]$. Let $L[z]$ be a $m \times m$ transfer function matrix of a filter, the alternative prediction error is

$$\mathcal{E}_f[n,\rho] = U_f[n] - \bar{R}_f[n] - \bar{F}_f[n,\rho], \tag{5.7}$$

where $U_f[n] = \mathcal{Z}^{-1}\{L[z]U[z]\}$, $\bar{R}_f[n] = \mathcal{Z}^{-1}\left\{L[z]\bar{R}[z]\right\}$, and $\bar{F}_f[n,\rho] = \mathcal{Z}^{-1}\left\{L[z]\bar{F}[z,\rho]\right\}$.

A convenient choice of filter is $L[z] = M_d[z]$, by doing so, the necessity of computing inverse of the reference model transfer matrix $(M_d[z])^{-1}$ is eliminated and resulting signals used to compute the error become

$$\begin{aligned} U_f[n] =& \mathcal{Z}^{-1}\{M_d[z]U[z]\} = Y_d[n] \\ \bar{R}_f[n] =& \mathcal{Z}^{-1}\left\{M_d[z]\left(M_d[z]\right)^{-1}Y[z]\right\} = Y[n] \\ \bar{F}_f[n,\rho] =& \mathcal{Z}^{-1}\{M_d[z]C[z,\rho]Y[z]\} = \mathcal{Z}^{-1}\{Q[z,\rho]Y[z]\}, \end{aligned} \tag{5.8}$$

where

$$Y_d[n] = [y_{d1}[n], \ldots, y_{dm}[n]]^\top, \tag{5.9}$$

is the array of output signals of the reference model $M_d[z]$ for the set of inputs $U[n]$, called desired output. And, for a diagonal $C[z,\rho]$, the transfer function matrix $Q[z,\rho]$ is defined as follows

$$\begin{aligned} Q[z,\rho] = M_d[z]C[z,\rho] &= \begin{bmatrix} M_{d_{11}}[z]C_1[z,\rho_1] & M_{d_{12}}[z]C_2[z,\rho_2] & \ldots & M_{d_{1m}}[z]C_m[z,\rho_m] \\ M_{d_{21}}[z]C_1[z,\rho_1] & M_{d_{22}}[z]C_2[z,\rho_2] & \ldots & M_{d_{2m}}[z]C_m[z,\rho_m] \\ \vdots & \vdots & \ddots & \vdots \\ M_{d_{m1}}[z]C_1[z,\rho_1] & M_{d_{m2}}[z]C_2[z,\rho_2] & \ldots & M_{d_{mm}}[z]C_m[z,\rho_m] \end{bmatrix} \\ &= \begin{bmatrix} C_1[z,\rho_1]M_{d_{11}}[z] & C_2[z,\rho_2]M_{d_{12}}[z] & \ldots & C_m[z,\rho_m]M_{d_{1m}}[z] \\ C_1[z,\rho_1]M_{d_{21}}[z] & C_2[z,\rho_2]M_{d_{22}}[z] & \ldots & C_m[z,\rho_m]M_{d_{2m}}[z] \\ \vdots & \vdots & \ddots & \vdots \\ C_1[z,\rho_1]M_{d_{m1}}[z] & C_2[z,\rho_2]M_{d_{m2}}[z] & \ldots & C_m[z,\rho_m]M_{d_{mm}}[z] \end{bmatrix}, \end{aligned} \tag{5.10}$$

where $\rho = [\rho_1^\top, \ldots, \rho_m^\top]^\top$. If each element of the controller transfer function matrix is linearly parameterizable, that is,

$$C[z,\rho] = \begin{bmatrix} \rho_1^\top \bar{C}_1[z] & 0 & \ldots & 0 \\ 0 & \rho_2^\top \bar{C}_2[z] & \ldots & 0 \\ \vdots & \vdots & \ddots & \vdots \\ 0 & 0 & \ldots & \rho_m^\top \bar{C}_m[z] \end{bmatrix}, \tag{5.11}$$

where $\rho_k \in \mathbb{R}^p$, for $k = 1, \ldots, m$, the transfer function matrix $Q[z, \rho]$ becomes

$$Q[z,\rho] = \begin{bmatrix} \rho^\top \bar{Q}_1[z] \\ \vdots \\ \rho^\top \bar{Q}_m[z] \end{bmatrix} = \begin{bmatrix} \begin{bmatrix} \rho_1^\top, \ldots, \rho_m^\top \end{bmatrix} \begin{bmatrix} \bar{C}_1[z] M_{d_{11}}[z] & \ldots & 0 \\ \vdots & \ddots & \vdots \\ 0 & \ldots & \bar{C}_m[z] M_{d_{1m}}[z] \end{bmatrix} \\ \vdots \\ \begin{bmatrix} \rho_1^\top, \ldots, \rho_m^\top \end{bmatrix} \begin{bmatrix} \bar{C}_1[z] M_{d_{m1}}[z] & \ldots & 0 \\ \vdots & \ddots & \vdots \\ 0 & \ldots & \bar{C}_m[z] M_{d_{mm}}[z] \end{bmatrix} \end{bmatrix}, \tag{5.12}$$

and $\bar{F}_f[n, \rho]$ becomes

$$\bar{F}_f[n,\rho] = \begin{bmatrix} \rho^\top \Phi_1[n] \\ \rho^\top \Phi_2[n] \\ \vdots \\ \rho^\top \Phi_m[n] \end{bmatrix} \tag{5.13}$$

where

$$\Phi_k[n] = \mathcal{Z}^{-1} \left\{ \begin{bmatrix} \bar{C}_1[z] M_{d_{k1}}[z] & \ldots & 0 \\ \vdots & \ddots & \vdots \\ 0 & \ldots & \bar{C}_m[z] M_{d_{km}}[z] \end{bmatrix} \begin{bmatrix} Y_1[z] \\ \vdots \\ Y_m[z] \end{bmatrix} \right\}, \tag{5.14}$$

for $k = 1, \ldots, m$, or, in a more compact form,

$$\Phi_k[n] = \mathcal{Z}^{-1} \left\{ \mathrm{diag}(\bar{C}_1[z] M_{d_{k1}}[z], \ldots, \bar{C}_m[z] M_{d_{km}}[z]) Y[z] \right\}. \tag{5.15}$$

The proposed MIMO VRFT procedure

For a given set of data matrices $\left(\mathbf{U} \in \mathbb{R}^{m \times N}, \mathbf{Y} \in \mathbb{R}^{m \times N}\right)$, where each matrix is a set of data arrays $\mathbf{U} = [\mathbf{u_1}^\top \ \ldots \ \mathbf{u_m}^\top]^\top$ and $\mathbf{Y} = [\mathbf{y_1}^\top \ \ldots \ \mathbf{y_m}^\top]^\top$, where each array is composed of N samples of the arrays of measured inputs and outputs, respectively, i.e., $\mathbf{u_1} = \{u_1[1], \ldots, u_1[N]\}$, $\mathbf{u_2} = \{u_2[1], \ldots, u_2[N]\}$, $\mathbf{y_1} = \{y_1[1], \ldots, y_1[N]\}$, $\mathbf{y_2} = \{y_2[1], \ldots, y_2[N]\}$, and so on. The MIMO VRFT procedure consists on finding the array of parameters ρ that minimizes a prediction error identification criterion. This criterion is formulated as the square of the 2-norm of the prediction error defined in Equation (5.7) and, if the proposed filter $L[z] = M_d[z]$ is used, the MIMO VRFT criterion is

$$J^{MIMO}(\rho) = \left\| \mathbf{Y_d}^\top - \mathbf{Y}^\top - \begin{bmatrix} \rho^\top \mathbf{\Phi}_1 \\ \vdots \\ \rho^\top \mathbf{\Phi}_m \end{bmatrix}^\top \right\|_2^2, \tag{5.16}$$

where $\mathbf{Y_d} \in \mathbb{R}^{m \times N}$ is the set of arrays composed of N samples of the desired output signals $Y_d[n]$ and $\mathbf{\Phi}_k \in \mathbb{R}^{pm \times N}$ is composed of N samples of $\Phi_k[n]$, for $k = 1, \ldots, m$. That is, $\mathbf{Y_d} = [\mathbf{y_{d1}}^\top \ \ldots \ \mathbf{y_{dm}}^\top]^\top$, where $\mathbf{y_{dk}} = \{y_{dk}[1], \ldots, y_{dk}[N]\}$, and $\mathbf{\Phi_k} = \{\Phi_k[1], \ldots, \Phi_k[N]\}$, for $k = 1, \ldots, m$.

Defining $\mathbf{V} = \mathbf{Y_d} - \mathbf{Y} = [\mathbf{v}_1^\top \ \dots \ \mathbf{v}_m^\top]^\top$, the MIMO VRFT criterion can be written as

$$J^{MIMO}(\rho) = \left\| \begin{bmatrix} \mathbf{v}_1 \\ \vdots \\ \mathbf{v}_m \end{bmatrix}^\top - \begin{bmatrix} \rho^\top \mathbf{\Phi}_1 \\ \vdots \\ \rho^\top \mathbf{\Phi}_m \end{bmatrix}^\top \right\|_2^2, \tag{5.17}$$

where $\rho \in \mathbb{R}^{pm\times 1}$, $\mathbf{v}_k \in \mathbb{R}^{1\times N}$, and $\mathbf{\Phi}_k \in \mathbb{R}^{pm\times N}$, for $k = 1, \dots, m$. The cost function of Equation (5.17) can be seen as a set of m least-squares problems, then, it can be rearranged to match the formulation of the equally weighted sum least squares problem

$$J_{LS}^{MIMO}(\rho) = \left\| \begin{bmatrix} \mathbf{\Phi}_1^\top \\ \vdots \\ \mathbf{\Phi}_m^\top \end{bmatrix} \rho - \begin{bmatrix} \mathbf{v}_1^\top \\ \vdots \\ \mathbf{v}_m^\top \end{bmatrix} \right\|_2^2 = \left\| \tilde{\mathbf{A}}\rho - \tilde{\mathbf{b}} \right\|_2^2, \tag{5.18}$$

where $\tilde{\mathbf{A}} \in \mathbb{R}^{Nm\times pm}$ and $\tilde{\mathbf{b}} \in \mathbb{R}^{Nm\times 1}$. Thus, the array of parameters ρ that minimizes the cost function (5.18) is (BOYD; VANDENBERGHE, 2018)

$$\rho^* = \arg\min_{\rho} \ J_{LS}^{MIMO}(\rho) = (\tilde{\mathbf{A}}^\top \tilde{\mathbf{A}})^{-1} \tilde{\mathbf{A}}^\top \tilde{\mathbf{b}}. \tag{5.19}$$

5.2 Results

The results obtained with the proposed MIMO formulation are presented in this section, divided in three subsections. First, a numerical example is presented. Then, the method is applied to the Brazilian 7-bus Equivalent System to retune the four PSSs of the system. Lastly, the method is tested with the 39-Bus New-England Test System, where two PSSs are simultaneously retuned.

5.2.1 Numerical example

A numerical example is presented in this section as a didactic application example of the proposed MIMO VRFT procedure described in the previous section. Consider the LTI continuous-time MIMO system described by

$$G(s) = \begin{bmatrix} G_{11}(s) & G_{12}(s) \\ G_{21}(s) & G_{22}(s) \end{bmatrix} = \begin{bmatrix} \frac{-18.57s}{s^2+0.2463s+12.38} & \frac{-8.451s}{s^2+0.278s+12.07} \\ \frac{-9.693s}{s^2+0.2785s+12.12} & \frac{-28.78s}{s^2+0.2239s+11.51} \end{bmatrix}, \tag{5.20}$$

where $G_{ji}(s)$ indicates the transfer function from input i to output j. The closed-loop reference model is

$$M_d(s) = \begin{bmatrix} M_{d_{11}}(s) & M_{d_{12}}(s) \\ M_{d_{21}}(s) & M_{d_{22}}(s) \end{bmatrix}, \tag{5.21}$$

where

$$
\begin{aligned}
M_{d_{11}}(s) &= \frac{-18.571s(s+54.28)(s+40)(s^2+0.3007s+6.333)(s^2+0.2344s+12.11)(s^2+0.3363s+12.14)}{(s+137.8)(s+53.52)(s^2+0.4407s+3.48)(s^2+0.3114s+6.63)(s^2+0.2342s+12.11)(s^2+0.3366s+12.14)},\\
M_{d_{12}}(s) &= \frac{-9.6932s(s+40)(s+30)(s^2+0.2239s+11.51)(s^2+0.278s+12.07)(s^2+0.2463s+12.38)}{(s+137.8)(s+53.52)(s^2+0.4407s+3.48)(s^2+0.3114s+6.63)(s^2+0.2342s+12.11)(s^2+0.3366s+12.14)},\\
M_{d_{21}}(s) &= \frac{-8.451s(s+40)(s+30)(s^2+0.2239s+11.51)(s^2+0.2785s+12.12)(s^2+0.2463s+12.38)}{(s+137.8)(s+53.52)(s^2+0.4407s+3.48)(s^2+0.3114s+6.63)(s^2+0.2342s+12.11)(s^2+0.3366s+12.14)},\\
M_{d_{22}}(s) &= \frac{-28.78s(s+118.4)(s+30)(s^2+0.4522s+4.162)(s^2+0.2331s+12.11)(s^2+0.339s+12.14)}{(s+137.8)(s+53.52)(s^2+0.4407s+3.48)(s^2+0.3114s+6.63)(s^2+0.2342s+12.11)(s^2+0.3366s+12.14)}.
\end{aligned}
\tag{5.22}
$$

The ideal MIMO controller $C_i(s)$ with which the closed-loop system exactly matches the reference model is

$$
C_i(s) = \begin{bmatrix} C_{i1}(s) & 0 \\ 0 & C_{i2}(s) \end{bmatrix} = \begin{bmatrix} \frac{5s+2.3}{s+40} & 0 \\ 0 & \frac{s+0.2}{s+30} \end{bmatrix}. \tag{5.23}
$$

The ideal controller is a decentralized controller (diagonal structure) composed of two SISO controllers that can be linearly parameterized as follows

$$
C_i(s,\rho_i) = \begin{bmatrix} \rho_{i1}^{\top}\bar{C}_1(s) & 0 \\ 0 & \rho_{i1}^{\top}\bar{C}_2(s) \end{bmatrix} = \begin{bmatrix} \begin{bmatrix} 5 & 2.3 \end{bmatrix} \begin{bmatrix} \frac{s}{s+40} \\ \frac{1}{s+40} \end{bmatrix} & 0 \\ 0 & \begin{bmatrix} 1 & 0.2 \end{bmatrix} \begin{bmatrix} \frac{s}{s+30} \\ \frac{1}{s+30} \end{bmatrix} \end{bmatrix}. \tag{5.24}
$$

Then, the ideal array of parameters is

$$
\rho_i = [5.0 \;\; 2.3 \;\; 1.0 \;\; 0.20]^{\top}. \tag{5.25}
$$

A 10 s data acquisition experiment[1] was performed using a sampling time of $T_s = 0.001$ s, thus $N = 10001$. A unitary step was applied to the first input of the system at instant $t = 1$ s, then, at instant $t = 5$ s, a second unitary step was applied to the second input. The data set is composed of two data matrices $(\mathbf{U}, \mathbf{Y})$, where each matrix is composed of two data arrays associated to the measured inputs and outputs, respectively, $\mathbf{U} = [\mathbf{u_1}, \mathbf{u_2}]^{\top}$ and $\mathbf{Y} = [\mathbf{y_1}, \mathbf{y_2}]^{\top}$, where $\mathbf{u_1}$,$\mathbf{u_2}$,$\mathbf{y_1}$ and $\mathbf{y_2} \in \mathbb{R}^{1\times 10001}$.

Let $\mathbf{Y_d} = [\mathbf{y_{d1}}, \mathbf{y_{d2}}]^{\top}$ be the desired closed-loop output for the same inputs used in the data acquisition experiment, that is, $\mathbf{Y_d}$ is a $2 \times N$ array containing the simulated response of the reference model $M(s)$ for the input $\mathbf{U}$. The MIMO VRFT criterion is formulated according to Equation (5.18), as follows

$$
J_{LS}^{MIMO}(\rho) = \left\| \begin{bmatrix} \mathbf{\Phi}_1^{\top} \\ \mathbf{\Phi}_2^{\top} \end{bmatrix} \rho - \begin{bmatrix} \mathbf{v}_1^{\top} \\ \mathbf{v}_2^{\top} \end{bmatrix} \right\|_2^2 = \left\| \tilde{\mathbf{A}}\rho - \tilde{\mathbf{b}} \right\|_2^2, \tag{5.26}
$$

where $\mathbf{v}_1 = \mathbf{y_{d1}} - \mathbf{y_1}$, $\mathbf{v}_2 = \mathbf{y_{d2}} - \mathbf{y_2}$ and $\mathbf{\Phi}_1$ and $\mathbf{\Phi}_2$ are the simulated responses of the transfer matrices $\bar{Q}_1(s)$ and $\bar{Q}_2(s)$, respectively, for the input $\mathbf{Y}$, where

[1] As described in Section 3.6, the simulations are done using the function lsim of the Matlab software, where all continuous to discrete-time conversions and data sampling are performed automatically by the software.

$$\bar{Q}_1(s) = \begin{bmatrix} \bar{C}_1(s)M_{11}(s) & 0 \\ 0 & \bar{C}_2(s)M_{12}(s) \end{bmatrix} \tag{5.27}$$

and

$$\bar{Q}_2(s) = \begin{bmatrix} \bar{C}_1(s)M_{21}(s) & 0 \\ 0 & \bar{C}_2(s)M_{22}(s) \end{bmatrix}. \tag{5.28}$$

The solution to the MIMO VRFT problem, computed with Equation (5.19), is

$$\rho = [5.00000519165561 \quad 2.30000145445418 \quad 1.00000097098053 \quad 0.200000009285679]^\top. \tag{5.29}$$

The result (5.29) is very close to the ideal solution (5.25), with every element being equal to the ideal one for at least five decimal places. Thus, the resulting controller is practically identical to the ideal one

$$C_{VRFT}(s) = \begin{bmatrix} \frac{5s+2.3}{s+40} & 0 \\ 0 & \frac{s+0.2}{s+30} \end{bmatrix}. \tag{5.30}$$

The dynamic response of the system for the input signal **U** is presented in Figure 5.3. The black continuous lines corresponds to the input signals, the blue lines are the measured outputs, the red lines are the desired outputs (reference model outputs) and the dashed yellow lines are the closed-loop response with the controller designed with the MIMO VRFT procedure.

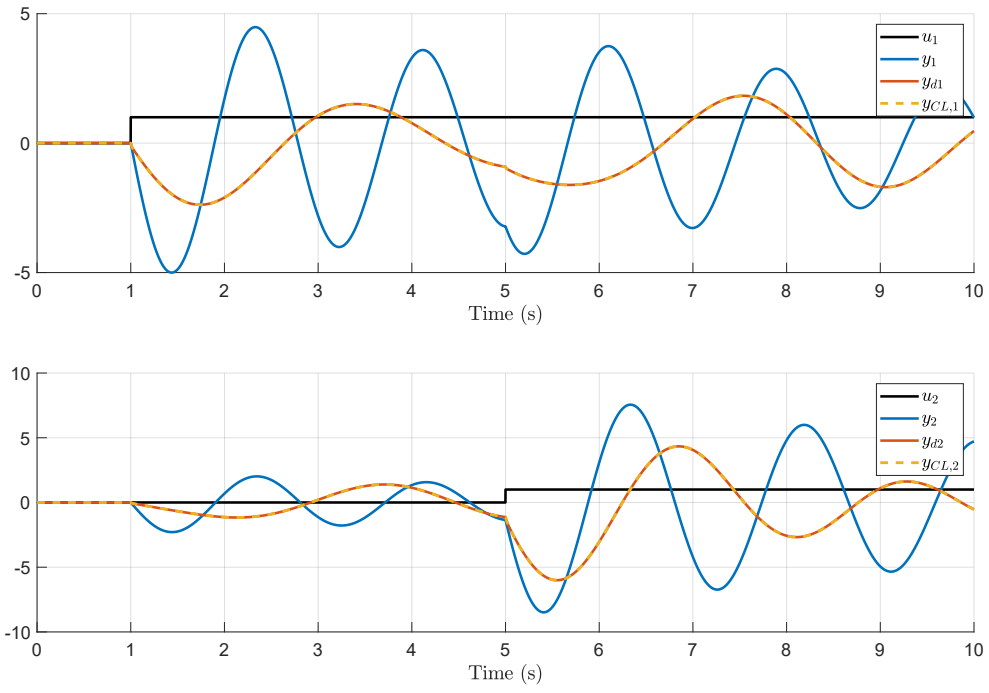

Figure 5.3 – Example MIMO system: response to the probe signal (unitary step). Measured input and output signals, reference model and closed-loop responses.

The numerical example presented here is a proof of concept to show that the proposed MIMO VRFT procedure is capable of finding the optimum solution to the problem, even with a limited time experiment. The method was tested in a very controlled setting, the test system is an LTI system, where the linearly parameterizable controller was known to exist and the data were collected with a small sampling time (high sampling frequency). The result is very promising, justifying the test in a more complex scenario.

5.2.2 Coordinated PSS design - Brazilian 7 bus equivalent system

The proposed MIMO VRFT procedure was applied to design POD controllers for the Brazilian 7-bus equivalent system, described in Section 4.1. This system has an inter-area mode that corresponds to the oscillation between the SE Equivalent (G5) and the southern system (generators 1 to 4). And the damping ratio of this mode is deteriorated to around 3.10% if the load of Bus 1 is reduced by 700MW at the initial condition (power flow). This is the operating point considered here. However, a different approach is proposed, instead of designing new WAPSSs, the VRFT procedure is applied to simultaneously re-tune the four PSSs of the system in a coordinated control design strategy. The original four PSSs of the system are

$$\begin{aligned} PSS_1(s) = PSS_2(s) = PSS_3(s) = 10\left(\frac{0.3s+1}{0.075s+1}\right)^2 = \frac{160s^2+1067s+1778}{s^2+26.67s+177.8}, \\ PSS_4(s) = 16\left(\frac{0.52s+1}{0.065s+1}\right)^2 = \frac{1024s^2+3938s+3787}{s^2+30.77s+236.7}. \end{aligned} \tag{5.31}$$

In order to perform the re-tuning of the four PSSs, the controller is defined as a 4×4 MIMO diagonal transfer function matrix, Equation (5.11), where each diagonal element represents one of the four PSSs.

The definition of the reference model $M_d(s)$ that was already a challenging task for the SISO case, now becomes a even more complex task. The power system is a 4×4 MIMO system and a diagonal (decoupled) reference model is not viable. A full 4×4 MIMO transfer function matrix needs to be build to represent the reference model $M(s)$, for this application. That is, for every input of the plant, it is necessary to build four SISO reference models, one for each output. Which means a total of 16 SISO transfer functions, as follows

$$M_d(s) = \begin{bmatrix} M_{d_{11}}(s) & M_{d_{12}}(s) & M_{d_{13}}(s) & M_{d_{14}}(s) \\ M_{d_{21}}(s) & M_{d_{22}}(s) & M_{d_{23}}(s) & M_{d_{24}}(s) \\ M_{d_{31}}(s) & M_{d_{32}}(s) & M_{d_{33}}(s) & M_{d_{34}}(s) \\ M_{d_{41}}(s) & M_{d_{42}}(s) & M_{d_{44}}(s) & M_{d_{44}}(s) \end{bmatrix}, \tag{5.32}$$

where $M_{d_{ji}}(s)$ indicates the transfer function from input i to output j. Each transfer function of the reference model $M_d(s)$ was built using the method described in Section 3.5.2. Four experiments were performed separately, where a 0.01 pu step input was applied to a generator AVR reference input, at instant 1 s, and the data was collected for 5

seconds with a sampling time of 0.01 s. The transfer functions related with the output 1 ($M_{d_{11}}(s), \ldots, M_{d_{14}}(s)$) were built with 9 poles and 7 zeros, the remaining models were built with 9 poles and 8 zeros. All estimated models have a fit to estimation data of at least 99.84% and a minimum damping of $\zeta_{min} = 15\%$ was used to convert the estimated models to the reference ones. The transfer functions of the reference model are presented in the Appendix C.4. The dynamic response of each transfer function of the reference model is presented in Figures 5.4 to 5.7, where the black continuous lines indicates the measured outputs, the dashed green lines are the estimated models responses and the dashed blue lines are the reference models outputs (desired outputs), for each input.

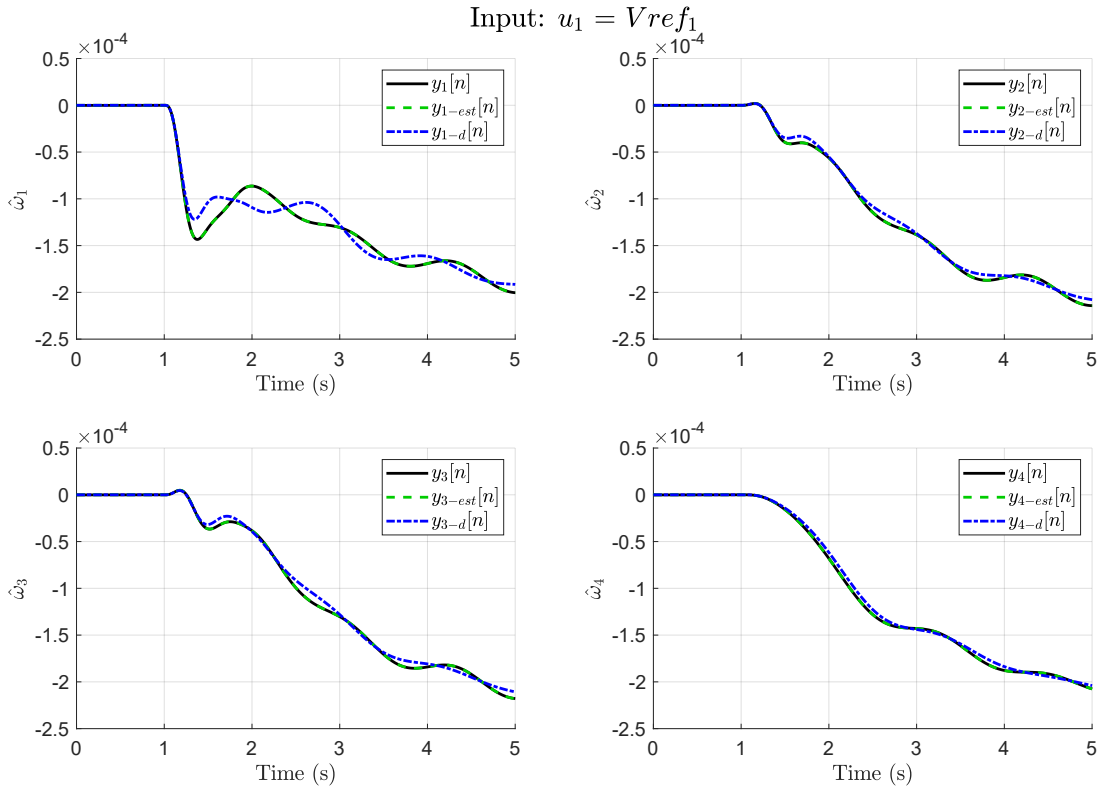

Figure 5.4 – Brazilian 7-bus MIMO system: filtered angular velocity response to a step in the voltage regulator of generator 1. Measured signal, estimated model and reference model responses.

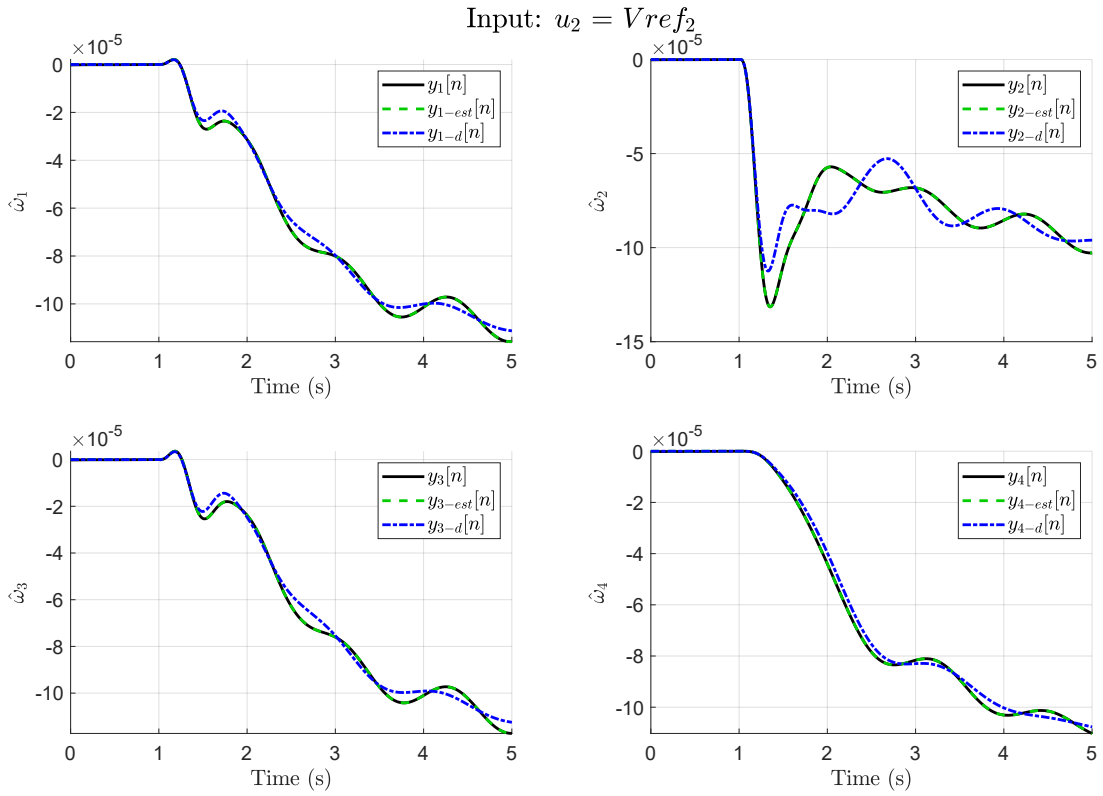

Figure 5.5 – Brazilian 7-bus MIMO system: filtered angular velocity response to a step in the voltage regulator of generator 2. Measured signal, estimated model and reference model responses.

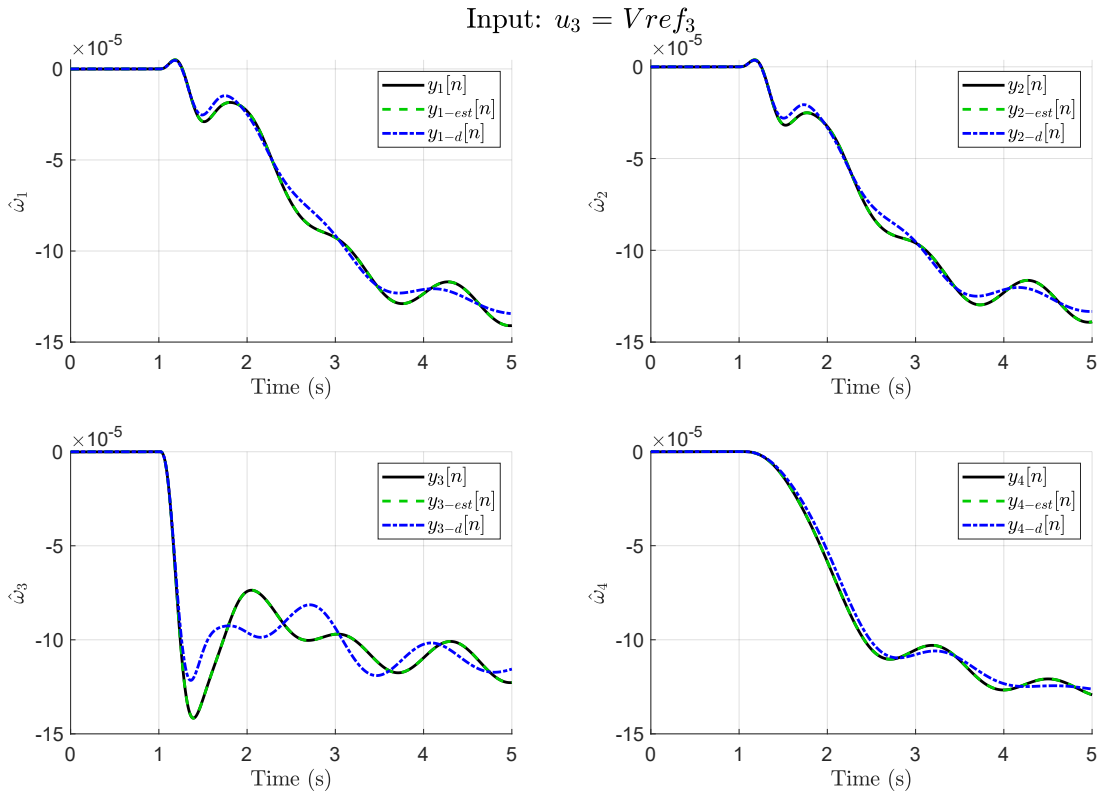

Figure 5.6 – Brazilian 7-bus MIMO system: filtered angular velocity response to a step in the voltage regulator of generator 3. Measured signal, estimated model and reference model responses.

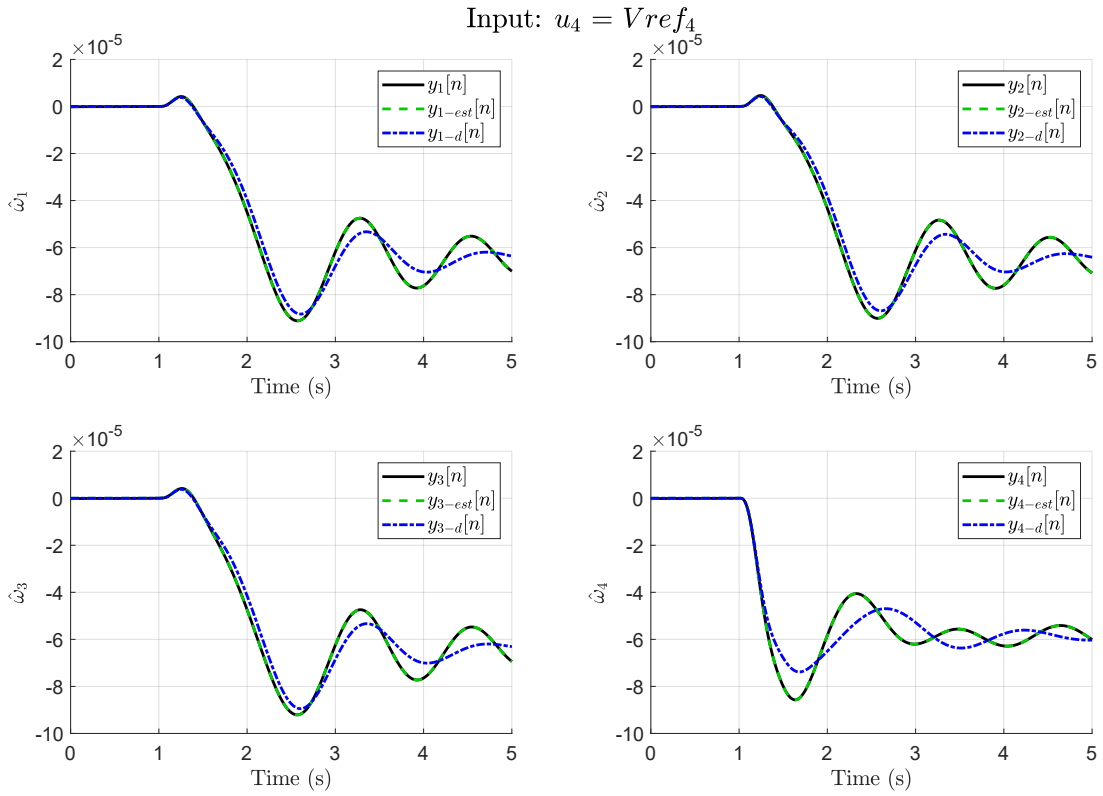

Figure 5.7 – Brazilian 7-bus MIMO system: filtered angular velocity response to a step in the voltage regulator of generator 4. Measured signal, estimated model and reference model responses.

However, considering the scenario where the PSSs need to be retuned, it is not reasonable to assume that it will be possible to perform four independent experiments to collect the data. So, it is assumed that the reference model was already built, with a previous set of experiments. If the damping performance of the system is deteriorated and the PSS retuning is needed, a new experiment is done to collect the data for the VRFT procedure only. The experiment used here is a sequence of step input applied to the inputs of the system, as follows.

1. Instant t=1.0 s: 0.01pu step is at the AVR reference input of gen. 1 (u_1);
2. Instant t=5.0 s: 0.01pu step is at the AVR reference input of gen. 2 (u_2);
3. Instant t=9.0 s: 0.01pu step is at the AVR reference input of gen. 3 (u_3);
4. Instant t=13.0 s: 0.01pu step is at the AVR reference input of gen. 4 (u_4).

The data was collected for 17 seconds with a sampling time of 0.01 s. This data is presented in Figure 5.8 together with the desired output, predicted output (using the same logic described in Section 3.1) and closed-loop response (after retuning the four PSS).

The controller was parameterized according to Equation (5.11), using the denominator of the PSSs presented in (5.31) to build $\bar{C}_1(s), \ldots, \bar{C}_4(s)$. The solution to the MIMO VRFT problem (Equation (3.7)) is

$$\rho = \begin{bmatrix} \rho_1 \\ \rho_2 \\ \rho_3 \\ \rho_4 \end{bmatrix} = \begin{bmatrix} \left.\begin{matrix} -49.6056555919157 \\ 674.51624682303 \\ 202.332221539901 \end{matrix}\right\} \rho_1 \\ \left.\begin{matrix} -39.4047912361761 \\ 750.808302317477 \\ -357.903668962698 \end{matrix}\right\} \rho_2 \\ \left.\begin{matrix} -30.7155934163161 \\ 664.028214433017 \\ 450.655106144045 \end{matrix}\right\} \rho_3 \\ \left.\begin{matrix} 102.08811308384 \\ 208.759811706327 \\ -2594.69700221884 \end{matrix}\right\} \rho_4 \end{bmatrix} \tag{5.33}$$

and the transfer functions of the re-tuned PSSs are

$$\begin{aligned} PSS_1(s) &= \frac{110.4s^2 + 1741s + 1980}{s^2 + 26.67s + 177.8}, \quad PSS_2(s) = \frac{120.6s^2 + 1817s + 1420}{s^2 + 26.67s + 177.8}, \\ PSS_3(s) &= \frac{129.3s^2 + 1731s + 2228}{s^2 + 26.67s + 177.8}, \quad PSS_4(s) = \frac{1126s^2 + 4147s + 1192}{s^2 + 30.77s + 236.7}. \end{aligned} \tag{5.34}$$

where each PSS was re-tuned following the procedure described in Section 3.4.2. The performance of the re-tuned controllers was tested over a more severe scenario where a

three-phase short-circuit was applied at bus 6 at instant 10 s and cleared after 30 ms. The full nonlinear continuous-time simulation result (0.1 pu step in the AVR reference signal of gen. 4 followed by the short-circuit) is presented in Figure 5.9.

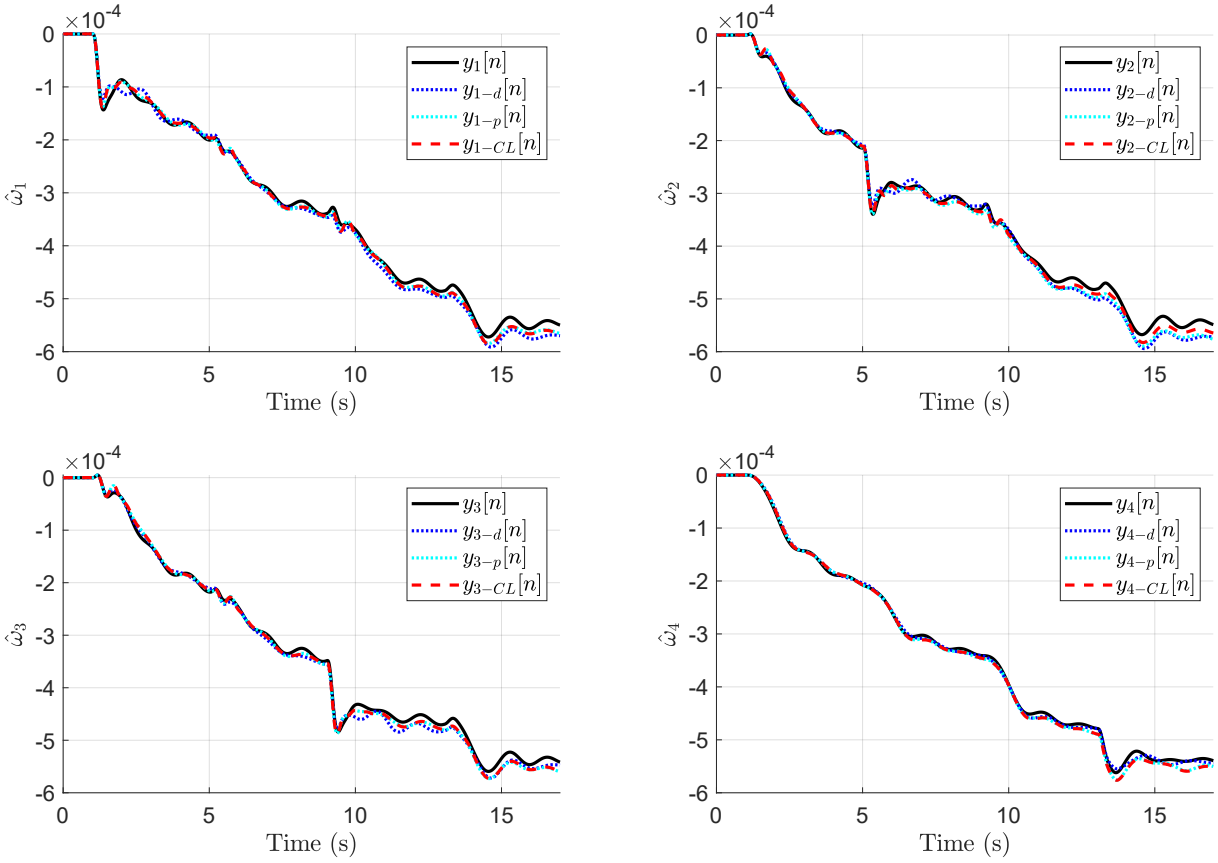

Figure 5.8 – Brazilian 7-bus MIMO system: filtered angular velocity response to the sequence of steps on the voltage regulators. Measured signal, reference model response, predicted output and retuned PSS response.

The dynamic responses presented in Figure 5.9 shows that the damping performance of the system was improved by the re-tuning procedure. The linear analysis of the closed-loop system model also confirms this result, indicating that the damping ratio of the inter-area mode was increased to around 4.89%. Even though the damping performance was improved, the damping ratio of the inter-area mode after the re-tuning procedure is below 5%. The analysis of the measured signals used to build the reference model suggests that maybe the re-tuning of all four PSS is not a good strategy for this system. The inter-area oscillation mode is not very evident in most of the signals measured. That is, in some of the generators, the voltage reference step is not sufficient to properly excite the mode and the measured angular velocities do not capture the poorly damped dynamics. Thus, for some of the input/output pairs of the reference model, the desired dynamics is very close to the measured ones, indicating that the re-tuning is not actually needed. The measured signals where the oscillation is more evident are the ones related with G_4 that has the higher controllability factor over the inter-area mode.

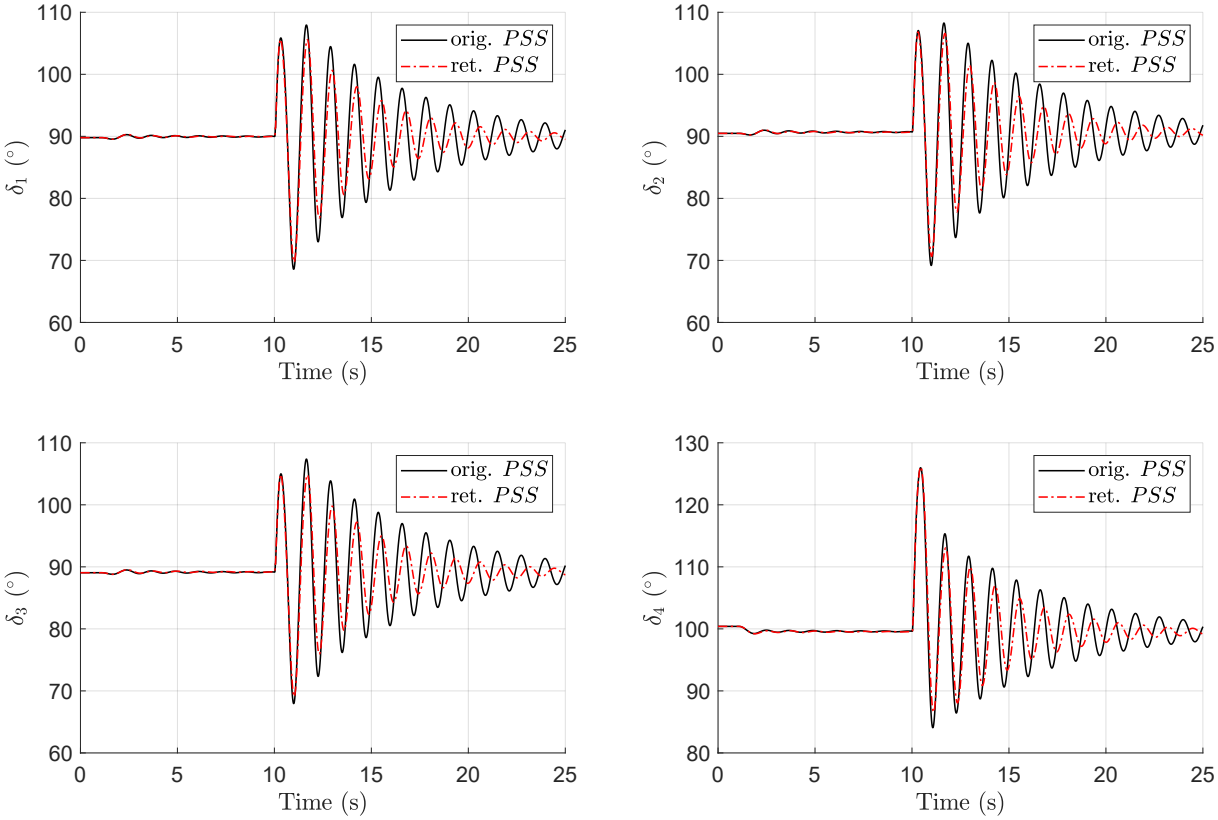

Figure 5.9 – Brazilian 7-bus MIMO system: rotor angle response to a step on the voltage regulator of generator 4, followed by a short-circuit. Original PSSs and retuned PSSs comparison.

5.2.3 Coordinated PSS design - 39-Bus New England Test System

The proposed MIMO VRFT procedure was also applied to design POD controllers for the 39-Bus NETS. As for the SISO application presented in Chapter 4, the modified operating condition was used. As it was described in Section 4.2, the operating point (initial condition) of the system was changed and two synchronous generators were replaced by wind power plants. Those modifications caused a significantly reduction in the inter-area mode damping ratio, to around 1.45%. As for the previous test system, the proposed MIMO VRFT procedure was applied to simultaneously retune multiple PSSs of the system, in a coordinated control design. However, instead of retuning all PSSs, only two of them were selected to be retuned. The NETS originally has ten PSSs, one for each synchronous generator. After the proposed modifications, the total number of PSSs is eight (no POD were included in the wind power plants). That is, the simultaneous retuning of all PSSs of the system implies on designing an 8×8 MIMO controller. To do so, with the proposed method, it is necessary to build an 8×8 MIMO reference model for the desired closed-loop dynamics, what can be challenging. The complexity of the problem is reduced by selecting fewer controllers to be retuned. Thus, the two PSSs with greater controllability over the inter-area mode (PSSs of G2 and G3) were selected to be retuned.

The original transfer function of those two PSSs are

$$\begin{aligned} PSS_2(s) &= 0.5\frac{5s+1}{0.4s+1}\frac{1s+1}{0.1s+1} = \frac{62.5s^2+75s+12.5}{s^2+12.5s+25}, \\ PSS_3(s) &= 0.5\frac{3s+1}{0.2s+1}\frac{2s+1}{0.2s+1} = \frac{75s^2+62.5s+12.5}{s^2+10s+25}. \end{aligned} \tag{5.35}$$

In order to perform the retuning of the four PSSs, the controller is defined as a 2×2 MIMO diagonal transfer function matrix, Equation (5.11), where each diagonal element represents one PSS.

The reference model $M(s)$ is built as 2×2 MIMO transfer function matrix, where the inputs are AVR reference signals and the outputs are filtered angular velocities, as illustrated in Figure 5.1. Thus, for each input, it is necessary to build two SISO reference models, resulting in a total of four SISO transfer functions, as follows

$$M(s) = \begin{bmatrix} M_{11}(s) & M_{12}(s) \\ M_{21}(s) & M_{22}(s) \end{bmatrix}, \tag{5.36}$$

where $M_{ji}(s)$ indicates the transfer function from input i to output j. Each transfer function of the reference model $M(s)$ was built using the method describe in Section 3.5.2. Two experiments were performed separately, where a 0.01 pu step input was applied to a generator AVR reference input, at instant 1 s, and the data was collected for 5 seconds with a sampling time of 0.01 s. The transfer functions $M_{11}(s)$ and $M_{12}(s)$ were built with 9 poles and 7 zeros, the transfer function $M_{21}(s)$ with with 9 poles and 8 zeros, and $M_{22}(s)$ with 10 poles and 8 zeros. All estimated models have a fit to estimation data of at least 99.99% and a minimum damping of $\zeta_{min} = 15\%$ was used to convert the estimated models to the reference ones. The dynamic response of each transfer function of the reference model is presented in Figures 5.10 and 5.11, where the black continuous lines indicates the measured outputs, the dashed green lines are the estimated models responses and the dashed blue lines are the reference models outputs (desired outputs), for each input. The transfer function of each reference model of (5.36) is presented in the Appendix C.5.

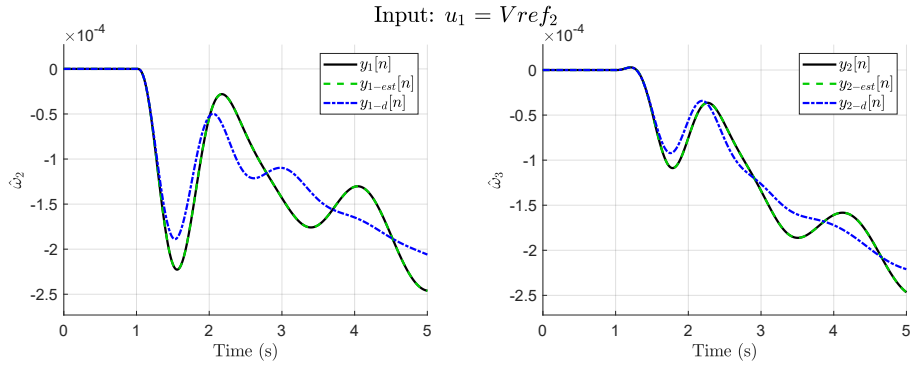

Figure 5.10 – 39-bus NETS MIMO: filtered angular velocity response to a step in the voltage regulator of generator 2. Measured signals and estimated model and reference model responses.

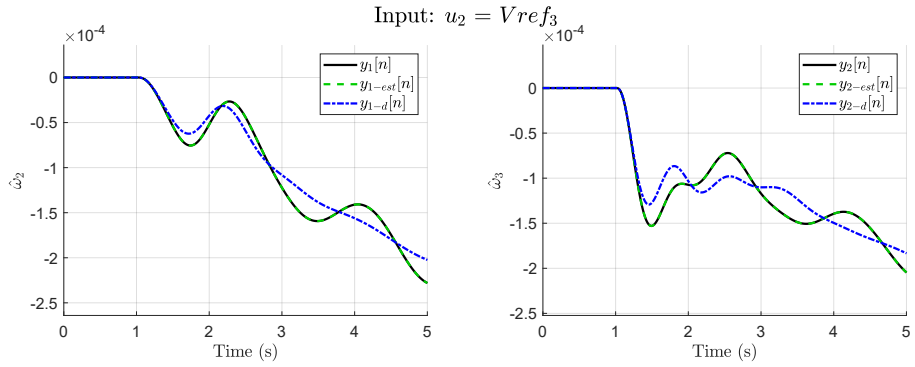

Figure 5.11 – 39-bus NETS MIMO: filtered angular velocity response to a step in the voltage regulator of generator 3. Measured signals and estimated model and reference model responses.

As for the previous test system it is considered that the experiment used to build the reference model is different from the data acquisition experiment for the VRFT procedure. That is, it is considered that the reference model is known before the PSS retuning procedure. Once it is decided that the PSSs need to be retuned, a new experiment is done to collect the data for the VRFT procedure. The experiment used here is a sequence of steps applied to the inputs of the system, as follows.

1. Instant t=1.0 s: 0.01pu step is at the AVR reference input of gen. 2 (u_1);
2. Instant t=5.0 s: 0.01pu step is at the AVR reference input of gen. 3 (u_2).

The data was collected for 9 seconds with a sampling time of 0.01 s. This data is presented in Figure 5.12 together with the desired output, predicted output (using the same logic described in Section 3.1) and closed-loop response (after retuning the four PSS).

The controller was parameterized according to Equation (5.11), using the denominator of the PSSs presented in (5.35) to build $\bar{C}_1(s)$ and $\bar{C}_2(s)$. The solution to

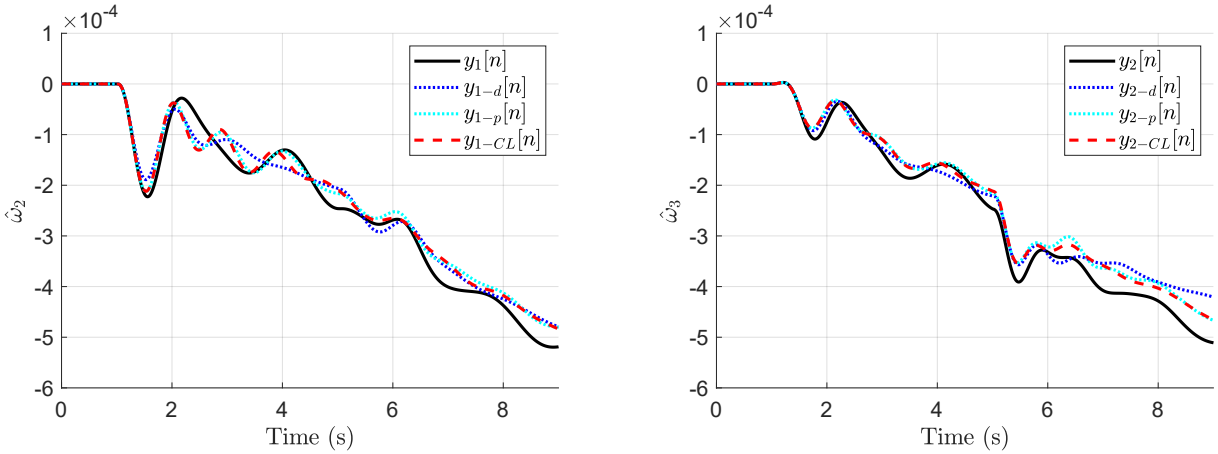

Figure 5.12 – 39-bus NETS MIMO: filtered angular velocity response to the sequence of steps on the voltage regulators. Measured signal, reference model responses, predicted outputs and retuned PSS responses.

the MIMO VRFT problem (3.7) is

$$\rho = \begin{bmatrix} \rho_1 \\ \rho_2 \end{bmatrix} = \begin{bmatrix} -14.2155403034276 \\ 223.700025541719 \\ -308.793637019887 \\ 43.0535043943878 \\ 127.518854710537 \\ 355.35148376218 \end{bmatrix} \begin{matrix} \} \rho_1 \\ \\ \\ \} \rho_2 \\ \\ \end{matrix} \tag{5.37}$$

and the transfer functions of the retuned PSSs are

$$PSS_2(s) = \frac{48.28s^2 + 298.7s - 296.3}{s^2 + 12.5s + 25}, \quad PSS_3(s) = \frac{118.1s^2 + 190s + 367.9}{s^2 + 10s + 25}, \tag{5.38}$$

where each PSS was retuned following the procedure described in Section 3.4.2. The performance of the retuned controllers was tested over a more severe scenario where a three-phase short-circuit was applied at the middle of line 1-2 at instant 10 s and cleared after 30 ms, without any control action. The full nonlinear continuous-time simulation result, 0.1 pu step in the AVR reference signal of gen. 4, followed by the short-circuit, is presented in Figure 5.13.

The inter-area oscillation mode of the system was successfully damped, as shown in the dynamic responses of Figure 5.13. The linear analysis of the closed-loop model indicates that the damping ratio of the mode was increased to around 7.19%. However, an undesired characteristic is also observed in the dynamic response. The steady-state condition of the system was slightly changed. One can observe that after the step on the voltage regulator of generator 2, the rotor angles of the generators converge to a slightly different value (around 15 s). Even though this difference is small and do not have a significant impact of the performance of the system, it is worth mentioning, since this phenomenon was not observed in the SISO implementation of the method. This difference

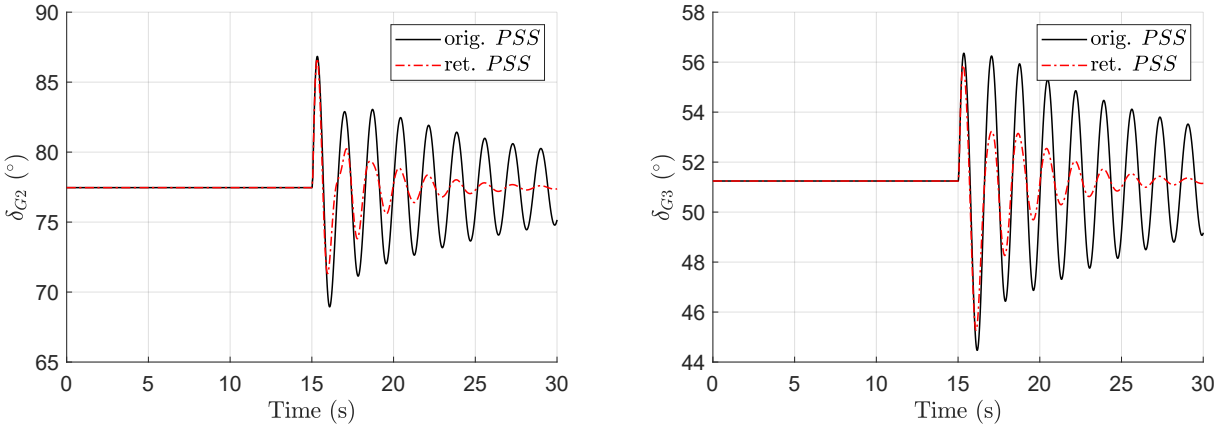

Figure 5.13 – 39-bus NETS MIMO: rotor angle response to a step on the voltage regulator of generator 2, followed by a short-circuit. Original PSSs and retuned PSSs comparison.

in the steady-state condition is probably related with the use of a MIMO linear reference model. This model was build as four separate transfer functions, combined in a MIMO model. Each SISO transfer function was build considering that the initial condition of the system was zero and the identified models response match the measured ones, as presented in Figures 5.10 and 5.11. However, the data collected for the MIMO VRFT is the response of the system for a sequence of two steps, one at each input of the system. Thus, when the second step is applied the system is no longer in the zero state condition. For this combined input perturbation, the outputs of the MIMO identified model do not match the measured responses exactly. Although this response is not presented here, this difference can be observed in the outputs of the reference model (dashed blue line) in Figure 5.12. Note that after the second step (at 5 s) the desired output of the system (reference model output) tends to a slightly different steady-state condition. That is, the reference model has a different steady-state value than the power system, for the same combined input (sequence of steps). Therefore, the retuned PSSs lead the system to a slightly different steady-state condition. The same phenomenon is observed if the order of the steps is inverted.

5.3 Comments

In this chapter, a further discussion about the VRFT applications to the proposed power system damping problem is presented. The method proposed for the SISO case is expanded to a MIMO application, where the MIMO controller that minimizes the prediction error criterion is computed using the multi-objective least-squares formulation. The proposed VRFT MIMO formulation is applied to retune multiple PSS of two benchmark power system models in a coordinated control approach. This strategy has a cost-effective appeal since no extra controllers are needed and the results are promising. However, from

a practical point of view, the MIMO application is more challenging as a MIMO reference model is required. Also, the practical limitations of performing the MIMO data acquisition experiment were not taken into consideration.

The damping ratio of the inter-area mode of interest was increased in both test systems considered. However, for the Brazilian 7-Bus Test System, where the four PSSs were re-tuned, the damping ratio stayed bellow the 5% mark. Even though, the results are considered to be positive, since they bring valuable information about the use of the proposed MIMO formulation of the VRFT method. For the 39-Bus NETS, the damping ratio of the inter-area mode was successfully increased to around 7.19%, which is a positive result, especially considering that only two PSSs were re-tuned. The re-tuned controllers changed the steady-state condition of the system. Even though such influence is undesired, the magnitude of the changes are small and did not impact the performance of the system. From the implementation point of view, the re-tuning of two controllers is much simpler than the four PSSs re-tuning strategy that was adopted for the first test system. Also, for the 39-Bus NETS, the inter-area mode was evident in the measured signals, what contributed for the positive results obtained.

Part II

Transient stability assurance with a generator-rejection control for parallel AC and DC transmission systems

6 Introduction

The limitations of building new transmission infrastructure for a scenario of ever-increasing demand bring the necessity of using the power transmission system at its highest capacity. A cost-effective solution adopted for some countries with fast growing demand is the introduction of long distance HVDC technologies to move large amount of power from remote areas of generation to dense load centers (SCHONLEBER, 2020). The integration of WAMS and control techniques based on power electronics induces new opportunities to improve the use of existing assets (MARTíNEZ-PARRALES; FUERTE-ESQUIVEL, 2018; LI; VANFRETTI, 2015), and to unlock additional transfer capability and assure system security (BALLAL, 2021). However, from the point of view of system security and Special Protection System (SPS), there is a clear need of new analytical methods to evaluate the effects of these embedded HVDC transmission systems over the power system transient stability. This lack of accurate methods for transient dynamic analysis together with the high amount of data available (increasing number of installed PMUs) motivates the development of new data-driven control and protection schemes to improve the power systems dynamics and security.

In this chapter, a new on-line Generation Rejection Scheme (GRS) for power systems with parallel AC and DC transmission lines is proposed. The goal of the method is to compute the amount of generation that must be rejected after a forced outage of the HVDC transmission. To reach this goal, a new mathematical model for the transient stability analysis based on the principle of equal-area criterion for parallel AC and DC transmission systems is developed. The proposed methodology can be used to evaluate if a predetermined fault (HVDC transmission loss) will cause instability and to compute the control action (generation rejection) needed to avoid such outcome. Those functionalities are usually known as *arming* and *operational calculation*, of a more complex scheme called System Integrity Protection Scheme (SIPS).

6.1 Review of Literature

Direct methods for the study on the impact of HVDC lines on the transient stability of power systems are introduced in the seminal work in Pai, Padiyar and Radhakrishna (1981). The work extends the direct method in transient stability analysis from AC systems to parallel AC/DC systems. The analysis approach uses the energy function method with internal node representation and one HVDC link. The author's goal was to estimate the critical clearing time by integrating the equations until reaching the critical energy value. In DeMarco and Cañizares (1992), the authors introduce two

separate energy functions for the AC and the DC systems whose weighted sum produces a single expression for the integrated AC/DC system. In Fernandopulle and Alden (2003) is introduced an energy function for AC/DC systems which includes the dynamics of a DC damping controller. In Fernandopulle and Alden (2005), the energy function for AC/DC systems considers the dynamics of the rectifier controller, the inverter controller, the master controller, and the VDCOLs (Voltage Dependent Current Order Limiters). In Jiang and Chiang (2013), the authors represented the DC link as equivalent loads at converter buses, where the load dynamics is a function of the AC voltages of the converter buses and DC line current. As a result, the proposed energy function assumes constant converter bus voltage, converter load, or voltage ratio. More recent works such as Eriksson (2013) and Gonzalez-Torres, Damm, Costan, Benchaib and Lamnabhi-Lagarrigue (2020) proposed new control design methods that modulate the active reference of the HVDC, providing synchronizing and damping power to the system based on energy functions for hybrid systems. Note that the studies conducted using energy functions work over numerical simulations.

As well as direct methods, reports on analytical methods are found in the literature. The base strategy is the adaptation of the EAC to cope with simultaneous AC-DC power transmission systems. In Tang, Xu and Zhou (2014), the authors analyze the impacts of HVDC faults on the transient stability of power systems for three configurations of MMC-HVDC (modular multilevel converter based high voltage direct current). The EAC is used to propose an index of critical AC transmitted power that determines if the DC line fault will cause instability, considering that the faulted DC line returns to normal operating condition after a predefined fault clearance time. A similar study is presented in Gonzalez-Torres, Costan, Damm, Benchaib, Bertinato, Poullain, Luscan and Lamnabhi-Lagarrigue (2018), where a simplified two-area hybrid system is used to develop a transient stability assessment methodology for DC faults. The authors present an analysis based on the EAC for critical time required to return to operation for DC contingencies. Finally, in Alam and Ahsan (2017), the authors developed a mathematical model based on the EAC to facilitate a comprehensive and generalized analysis of hybrid transmission systems. This model is derived from graphical analyses with some parameters computed using numerical methods. In general, those methods based on the EAC consider the power flow contribution of the DC link to be constant, and the transient stability analysis is done by adding this constant to the power-angle curve of a traditional SMIB system. Moreover, in those approaches, the validation of the method is done with two-area system models disregarding the equivalent impedance between the generators and the transmission system.

6.2 Problem Statement

The HVDC transmission systems have become a common part of modern power systems. Due to the physical characteristic of HVDC transmission, it has some advantages over the traditional AC systems, depending on the situation. Common applications of HVDC transmission are (KUNDUR, 1994):

- Long underwater lines, where the capacitance of traditional AC lines is too high.
- Connection between two asynchronous AC systems, where the use of AC ties is not feasible.
- Bulk power transmission over long distances. The HVDC transmission becomes a more cost-effective solution for distances above 600 km.

In addition, due to the growth of offshore wind farms in the recent years, HVDC systems have been used for transmission of offshore wind energy (CHOW; SANCHEZ-GASCA, 2020). The case of study of the present work belongs to the third situation. That is, the focus of this work is the transient stability analysis of large two-areas power systems, where HVDC links are responsible for a large power transmission between those areas. However, the case of interest is the one where there are also AC lines interconnecting the two areas, in parallel with the DC lines, making the transient stability analysis much more challenging.

In the Brazilian National Interconnected System (SIN) (from the Portuguese *Sistema Interligado Nacional*), the power transmissions between generation and load centers are done by both traditional AC lines and HVDC transmission lines. According to the National Operator of the System (ONS)(from the Portuguese *Operador Nacional do Sistema*), the total extension of the HVDC lines is 22020 km, almost 15% of the extension of HVAC lines, for the year 2021 (ONS, 2022c). From the perspective of transient stability, one of the most critical conditions occurs when the northern region (large generation center) is exporting power to the southeastern area (largest load center). Most of the power transmission goes through the two HVDC systems between *Xingu-Estreito* and *Xingu-Terminal Rio*, illustrated in Figure 6.1. Therefore, contingencies on those DC lines may have severe consequences. The blocking of one pole (or bipole) is seen by the rectifier side of the DC line as instantaneous load reduction, while the inverter side of the system observes an input power reduction. It causes the generators near the rectifier side to accelerate and the generators on the inverter side to decelerate and may lead to a loss of synchronization (ONS, 2018a; ONS, 2018c). Once this type of fault has the potential to affect the whole system and lead it to collapse, it is very important to have a SIPS operating to assure stability. According to the IEEE Guide for Engineering, Implementation, and Management of System Integrity Protection Schemes, the definition of SIPS is:

> "**System Integrity Protection Scheme** (SIPS): serves to enhance security and prevent propagation of disturbances for severe system emergencies caused by unacceptable operating conditions and is used to stabilize the power system by taking control action to mitigate those system conditions. It also encompasses Special Protection Systems (SPS) and Remedial Action Schemes (RAS) as well as underfrequency (UF), undervoltage (UV), and out-of-step (OOS) protection schemes"(IEEE, 2020).

Considering the Brazilian power system, the *Xingu-Estreito* and *Xingu-Terminal Rio* are two HVDC bipoles of ±800 kV (9000 MW) based on Line-Commutated Converter (LCC) technology (ONS, 2017; ONS, 2018b). Among the various control logics present on the HVDC systems of *Xingu-Estreito* and *Xingu-Terminal Rio*, there is a master control logic that acts on both bipoles as a high level of hierarchical control (acts as a SIPS). This master control is responsible for an SPS that monitors events that may affect the bipoles and executes control actions to guarantee the system stability. In case of faults that leads to the blocking of a HVDC pole or bipole, on of the control logics of the master control applies run-ups to the remaining bipoles and also commands the generator-rejection of the *Belo Monte* power plant (largest northern power plant in Brazil). Currently, this generator-rejection control is based on numerical simulations that feed a decision table and takes into account the amount of DC power lost and the power flow on the AC lines connecting the northern and the southeastern regions before the contingency (ONS, 2018b). The table needs to be very conservative to compensate for the uncertainties not covered in numerical simulations, as load variations, number of generator in operation, amount of wind and solar generation, etc. That is, the generator-rejection is defined considering the worst case scenario, and, therefore, may be excessive (disconnecting more generators than needed) depending on the current operating condition of the system.

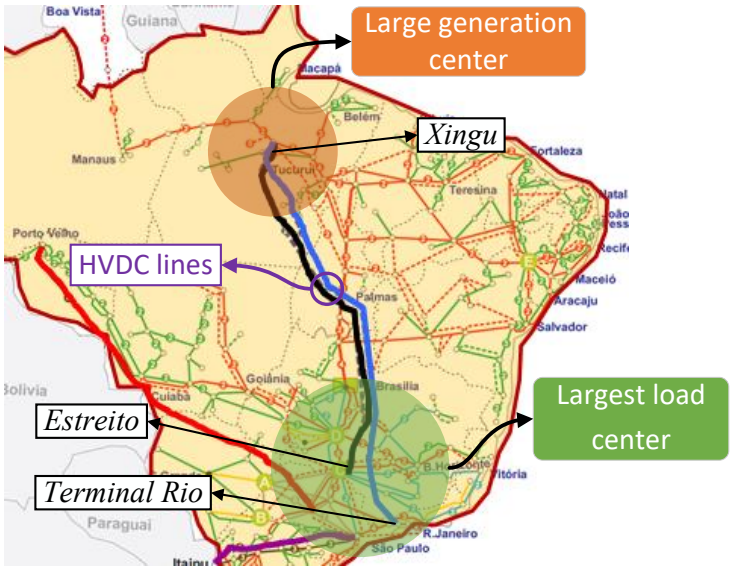

Figure 6.1 – Brazilian HVDC systems of *Xingu-Estreito* and *Xingu-Terminal Rio*.

Consider a generic two-area system, as the one shown in Figure 6.2, with two HVDC bipoles in parallel with an equivalent AC transmission corridor. Severe faults at the DC system may lead to permanent blocking of a pole or bipole and a consequent instantaneous reduction of active power flow between the two areas. Depending on the power system condition, the excess of generation in Area 1 can lead to a transient stability problem. One possible approach to assure the transient stability in cases of forced outage of the HVDC transmission is to implement an SPS, based on a predefined decision table as the one presented in the Brazilian power system, to reject the generation at Area 1. Now, suppose that is possible to capture the transient dynamics of this system using a simplified model. That is, suppose that knowing some equivalent parameters of this system and using some key measurements (like power flows, current and voltage levels) it is possible to build a reduced model and that this model can emulate the transient dynamics of the real system sufficiently enough so an stability analysis can be performed. Thus, it is not expected for the reduced model to accurately represent the dynamic response of the system. It is only expected that: *i)* it can capture the interaction between the HVDC system and the equivalent generators; and *ii)* that it is able to model whether the system will lose stability or not in cases of forced outage of the HVDC transmission. So, the following questions are addressed in this part of the work.

- If such reduced model exists, is it possible to perform a transient stability analysis using traditional techniques, such as the EAC?
- What is a suitable method for modeling the HVDC system in order to perform such analysis?
- Is it possible to design a generator rejection based SPS for this reduced model, using the EAC instead of a predefined decision table?

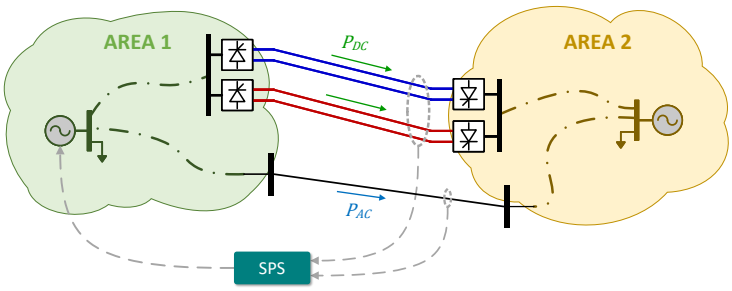

Figure 6.2 – Representation of a generic two-area system with parallel AC and DC transmission.

A simplified two-area reduced power system model is built and, supposing that it can sufficiently represent the transient stability of the power system, an SPS based on the EAC is proposed. The goal of the SPS is to reject the exact amount of generation in AREA 1 to avoid the collapse of the system due to transient instability, in cases of

forced outage of the HVDC transmission (blocking of a pole or a bipole). The structure of this special protection scheme is illustrated in Figure 6.3, which consists on using PMU data to monitor the HVDC transmission and constantly update the reduced model and an approximated power-angle curve of the system. At the core of the SPS is an algorithm for generator-rejection control that uses the EAC and the two-area reduced model to determine the number of Generator Units (GUs) that should be rejected in case of a forced outage of the HVDC transmission.

The first challenge to accomplish an SPS of this type is to build a model simple enough to be constantly updated, but that still contemplates the HVDC transmission influence on the transient stability. However, this is not the focus of this work. Assuming that such model exists, the next challenge is how to perform a transient stability analysis of a system with parallel AC and DC transmission. Taking the EAC as a main tool, this challenge translates to how to trace the power-angle curve of a power system with parallel AC and DC transmission. This work presents a new approach to build this power-angle expression and a generator-rejection algorithm using the proposed formulation.

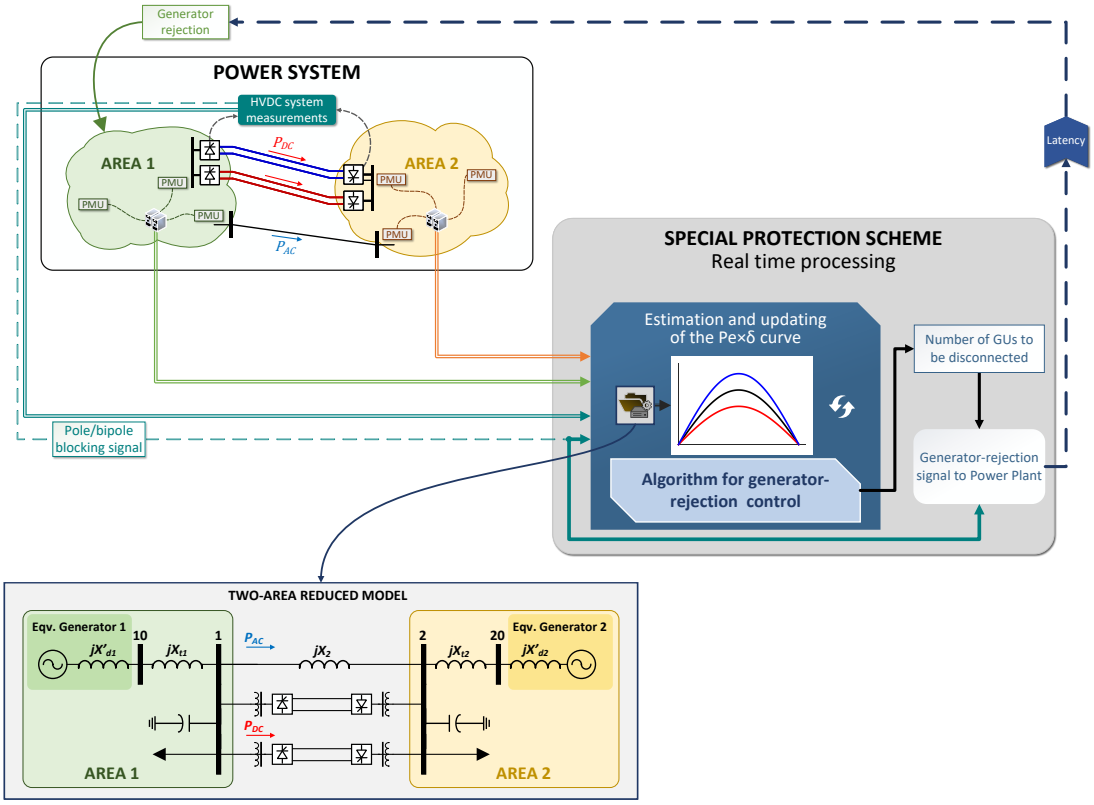

Figure 6.3 – Special Protection Scheme for a two-area system with parallel AC and DC transmission.

6.3 Contribution

In this work, an algorithm for an on-line generator-rejection control for power systems with parallel AC and DC transmission under contingencies on the HVDC system is proposed. The goal of the proposed method is to use an analytical approach to determine the generation-rejection instead of a predefined decision table. By doing so, it is expected that the method can be more easily adapted for different operating conditions. To reach this goal an analytical expression is proposed to approximate the power-angle dynamics of two-area systems with parallel AC and DC transmission lines. Using this proposed equation, the transient stability analysis is performed and the EAC is applied to determine the minimum generation rejection needed to assure the transient stability of the system in cases of forced outage of part of the HVDC transmission. The main advantage of the proposed method is that, if the key quantities related with system dynamics are known (initial condition measurements and equivalent network parameters), it is possible to perform the transient stability analysis and determine the control action beforehand (SIPS arming). Then, if those key quantities change, the model can be updated and a new transient stability analysis can be performed. That is, by constantly updating the model, the proposed method can regularly adapt to variations in the operational conditions and anticipate the control action needed to assure the transient stability, before the fault in the HVDC transmission occurs. Additionally, differently from the works in the literature (TANG, 2014; ALAM; AHSAN, 2017; GONZALEZ-TORRES, 2018), the methodology applied to model the HVDC system is based on the current drained by the converters, instead of the DC power flow. By doing so, a more precise power-angle dynamics is obtained. Also, the formulation is developed so the equivalent impedance of the second area of system (large load area), as well as shunt bank of capacitors/filters, and active loads are taken into account during the analysis.

The development of the methodology starts with an SMIB system, where the proof of concept is presented. Then, the two area system model is expanded to include a second equivalent machine. Lastly, shunt capacitor banks/filters and loads are included in the system and in the proposed formulation.

6.4 Fundamentals

This section presents a summary of the theoretical background necessary to understand the phenomenon of interest and to develop the proposed control method.

6.4.1 HVDC Converters

A brief description of the HVDC converters is presented in this section. The objective here is not to give a detailed explanation of the operation of such converters,

but to give an overview of the AC/DC conversion focusing on the characteristics that may impact on the transient stability analysis proposed in this work.

There are two common types of HVDC systems that differ in the technology on which the converters are built, the VSC (voltage-sourced converters) and the LCC based systems. The first one is built by coupling the DC buses of shunt VSCs and are usually called VSC HVDC systems (CHOW; SANCHEZ-GASCA, 2020). The second type is built using thyristor technology and is the type of HVDC system considered in this work. The structure of an HVDC system can also vary and the most common ones are the monopolar link, the bipolar link an the homopolar link (KUNDUR, 1994). The structure considered in this work is the bipolar one, illustrated in Figure 6.4, where there are two sets of converters of equal rated voltage at each terminal and two conductors, one positive and one negative. The junctions between the converters are grounded so that the DC voltage on one line is positive and that on the other line is negative. Normally, the current on each line is equal, so the ground current is zero. However, a bipolar system can operate in a single-pole mode, in case of a fault on one of the conductors for instance. In that case, the remaining pole operates with a ground current. A third connector can be used as a neutral connector in cases where ground currents are not tolerable or not feasible. A current can also flow to the third connector in case of power imbalance during bipolar operation (KUNDUR, 1994).

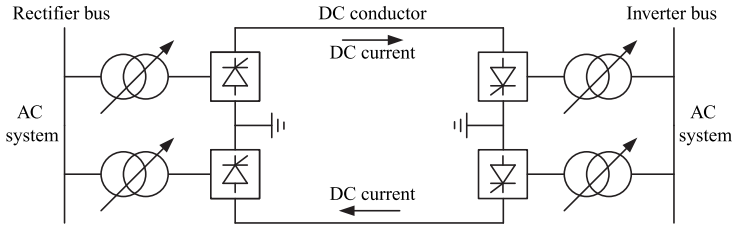

Figure 6.4 – Schematics of two-terminal HVDC bipolar link (CHOW; SANCHEZ-GASCA, 2020).

In an LCC HVDC system, a switching circuit is responsible for the AC/DC conversions. A common type of switching circuit is the three-phase full-wave bridge converter, where six valves (thyristors) are fired in such manner so that the three-phase sinusoidal voltages are converted to a DC voltage. This switching circuit is illustrated in Figure 6.5, where L is the smoothing reactor that limits variations in current I_d. Note that at any given instant it is necessary to have two valves conducting to complete the circuit and have current flow. In an ideal circuit, this switching can be synchronized with the voltage frequency with each upper valve (1, 3 and 5) conducting where the voltage at its phase is higher than the other two and each lower valve (2, 4 and 6) conducting where the voltage at its phase is lower than the other two. However, in a practical application, the thyristor switching is delayed to assure that the phase voltage is either sufficiently larger or sufficiently smaller than the other two phases. This is called the ignition delay and it

is represented by a delay angle α. One consequence of the ignition delay is the reactive power consumption at the converters, that is zero at the ideal case with $\alpha = 0$ (CHOW; SANCHEZ-GASCA, 2020). The adjustment of this firing instant allows the HVDC power transfer to be regulated and it is a key factor for the proposed transient stability analysis.

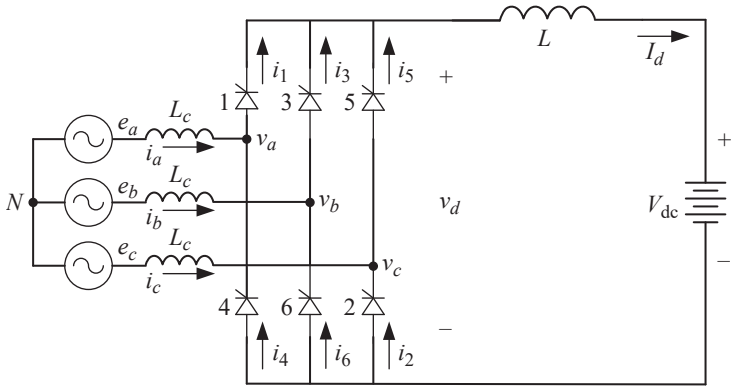

Figure 6.5 – Three-phase full-wave bridge rectifier circuit (CHOW; SANCHEZ-GASCA, 2020).

Another characteristic of the LCC is the commutation overlap. Since it is impossible to instantaneously switch the current between two valves, there is a current overlap during this switching period. As for the ignition delay, the overlap period also corresponds to an angle (a portion of the operation cycle of a valve) usually represented by μ. The sum of the ignition and overlap angles is the extinction angle of that valve, represented by δ. At the rectifier side of the HVDC system, the three-phase AC voltages and currents are converted to DC voltage and current and the delay angle α controls the level of the DC voltages. At the inverter side, the DC voltage level is controlled by the extinction advance angle γ and the DC voltage and current are converted back to three-phase AC voltages and currents (CHOW; SANCHEZ-GASCA, 2020). The extinction advance angle is the extinction angle of the valve defined by it advance with the instant where the commutating voltage is zero and decreasing, that is, $\gamma = \pi - \delta$ (KUNDUR, 1994).

The power flow at the HVDC system is controlled by the thyristors switching at the converters and by the transformer tap adjustment at the converter buses. According to Chow and Sanchez-Gasca (2020), the control objectives of an HVDC system can be summarized as follows:

1. Maintain the DC voltage at the inverter terminal, current order at the rectifier terminal, and DC power flow at the rated or desired values.

2. Maintain the power factor at preset values at both the rectifier and inverter terminals.

3. Maintain the ignition and extinction angles and the transformer taps within limits.

The tap adjustment is a mechanical operation and therefore much slower then the thyristors switching. Considering the time scale of power systems transient stability analysis, the transformer tap can be considered constant, thus, the transient performance of the HVDC system depends only on the dynamics of the converters. The operation of such converters depends on the voltage support capability of the AC system and three control modes are possible, depending on the operating condition (CHOW; SANCHEZ-GASCA, 2020). At *normal operation* (**Mode 1**), the rectifier maintains the DC current constant at the rated value and the inverter operates with a constant extinction angle, maintaining adequate commutation margin. There is, the firing angle at the inverter side is controlled to keep its extinction angle constant and the firing angle at the rectifier converters is adjusted to regulate the DC voltage difference and thus control the DC current. This operating mode is also called CC (constant current) operation. If a disturbance causes the voltage levels to drop, the firing angle α at the rectifier side is reduced to increase the DC voltage level at the rectifier and maintain the DC current at the desired value. But the firing angle control is limited by its minimum value (α_{min}). If such limit is reached, the rectifier DC voltage level may drop and, if so, the inverter will reduce the current by the current margin value to avoid an unfeasible condition (inverter DC voltage greater than the rectifier one). This is known as *reduced-voltage operation* (**Mode 2**), where the DC voltage at the inverter is determined by the voltage at the rectifier. A third operating mode known as the *transitional mode* (**Mode 3**) is also possible. In this mode, as the HVDC system transitions from Mode 1 to Mode 2, a constant ignition advance angle control is applied to avoid undesired operating conditions (CHOW; SANCHEZ-GASCA, 2020).

The transient stability analysis and generator-rejection control proposed in this work is based on the premise that the DC current at the HVDC system is approximately constant during the period of analysis. That is, the AC system can provide enough voltage support so the HVDC system operates at normal operating mode. Simulation results are presented in Chapter 8 to support this premise and the impact of not having enough voltage support is also presented.

6.4.2 Transient stability and the equal-area criterion

This section presents the analytical framework used to analyze the transient stability of two-area power systems, after large disturbances. First, an SMIB formulation is presented, then, the infinite-bus is replaced by a second machine, resulting in a two-machine system. Also, the fundamental idea behind the generation-rejection control proposed in this work is presented.

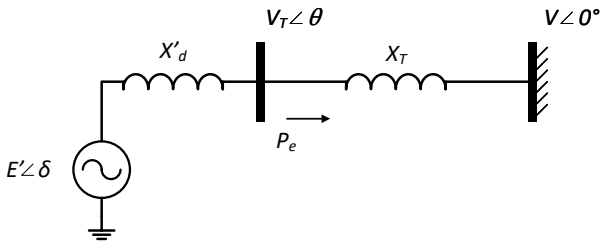

Figure 6.6 – Single-Machine Infinite-Bus System.

6.4.2.1 Single-machine infinite-bus system

Consider the Single-Machine Infinite-Bus system represented by Figure 6.6, if all damping effects are neglected, the dynamics of this system is modeled by the following swing equation (SAADAT, 1999)

$$\frac{d\delta}{dt} = \omega, \quad \frac{2H}{\omega_0}\frac{d\omega}{dt} = Pm - Pe, \tag{6.1}$$

where $\delta = \delta_{gen} - \delta_{ref}$ is the angular position of the rotor (in electrical radians) with respect to a synchronously rotating reference, ω is the angular velocity of the rotor (in electric radians per second), ω_0 is the rated velocity (in electric radians per second), H is the machine rotor inertia (in seconds), Pm is the mechanical input power of the machine (in pu), and Pe is the electrical output power (in pu). As the angular reference of the system is the infinite-bus, the reference angle is zero, therefore $\delta = \delta_{gen}$. The electric power output is given by

$$Pe(\delta) = \frac{E'V}{X_{eq}} \sin\delta, \tag{6.2}$$

where E' is the generator internal voltage (behind the transient reactance), V is the infinite-bus voltage, and X_{eq} is the equivalent reactance between them. For the system represented in Figure 6.6, the equivalent reactance is given by

$$X_{eq} = X'_d + X_T, \tag{6.3}$$

where X'_d is the direct-axis transient reactance of the generator and X_T is the transformer reactance. As the values of E', V, and X_{eq} are constant, the maximum output power occurs when $\sin\delta = 1$, there is

$$P_{max} = \frac{E'V}{X_{eq}}. \tag{6.4}$$

So Equation (6.2) can also be written as

$$Pe(\delta) = P_{max} \sin\delta. \tag{6.5}$$

Consider that this system is operating at steady-state with an electric power output of Pe_0, then the rotor angle is given by

$$\delta_{ep}^{sta} = \sin^{-1}\left(\frac{Pe_0}{P_{max}}\right), \tag{6.6}$$

and δ_{ep}^{sta} is known as the stable equilibrium point. As the rotor velocity is constant at steady-state, we have that $Pm = Pe_0$, so the mechanical input power applied to the generator is

$$Pm = \frac{E'V}{X_{eq}} \sin \delta_{ep}^{sta}. \tag{6.7}$$

The variation of the electric output versus the rotor angle ($Pe \times \delta$) is called the power-angle curve an it is displayed in Figure 6.7. The stable equilibrium point and the mechanical power are also presented. The angle δ_{ep}^{uns} represents the rotor angle at the unstable equilibrium point, given by $\delta_{ep}^{uns} = \pi - \delta_{ep}^{sta}$. If a perturbation is applied to the system, the rotor angle will change and also the electric power output, obeying Equation (6.2). Lets assume that a disturbance leads the rotor angle to the point a in the power-angle curve of Figure 6.7. At point a we have $Pm > Pe$, so the rotor angle will accelerate ($d^2\delta/dt^2 > 0$) and increase its value. When the rotor angle reaches δ_{ep}^{sta}, its acceleration is zero because $Pm = Pe$, but its velocity still is greater than zero, so the angle continues to increase. However, after crossing δ_{ep}^{sta}, we have $Pm < Pe$, what implies a negative acceleration. Assuming that this system is stable, the negative acceleration will slow down δ making it eventually stop and start to decrease, this point where ($d\delta/dt = 0$) is represented as δ_b in Figure 6.7. So, after the disturbance, the rotor angle will oscillate between δ_a and δ_b and, if a damping factor is considered, the rotor angle will return to δ_{ep}^{sta}.

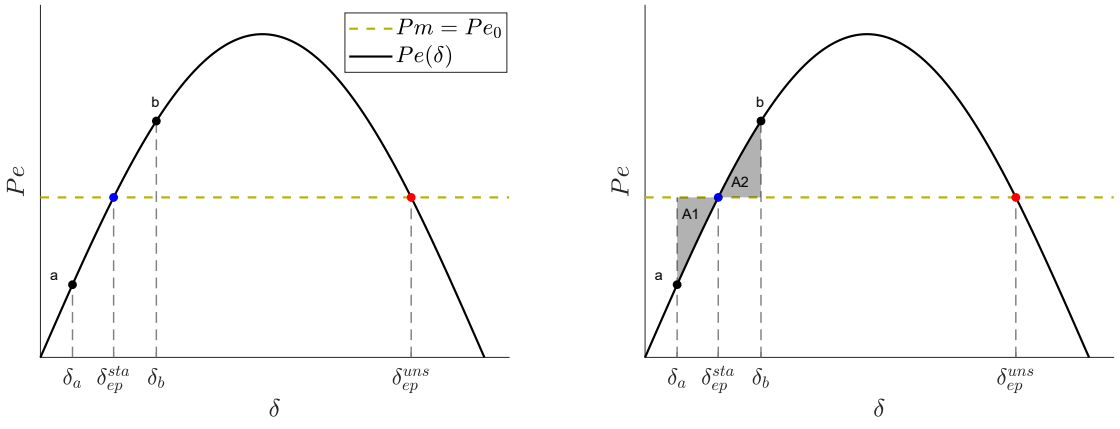

(a) (b)

Figure 6.7 – Power-angle curve of an SMIB system.

During the acceleration, the rotor is gaining energy that must be dissipated by the system in order to maintain stability. If the energy is dissipated before the rotor angle reaches the unstable equilibrium point, the system is stable from a transient stability perspective. That is, areas $A1$ and $A2$ are strongly related to the capability of the system maintain its stability after the disturbance. Considering the rotor angle excursion, area $A1$ corresponds to the portion where it is accelerating and area $A2$ is the portion where it is

decelerating. One can demonstrate that $A1 = A2$, that is

$$\begin{gathered} A1 = A2, \\ \int_{\delta_a}^{\delta_{ep}^{sta}} (Pm - Pe(\delta))\, d\delta = \int_{\delta_{ep}^{sta}}^{\delta_b} (Pe(\delta) - Pm)\, d\delta. \end{gathered} \tag{6.8}$$

Note that there is a maximum deceleration area, delimited by the equilibrium points δ_{ep}^{sta} and δ_{ep}^{uns}. So, if the acceleration area ($A1$) is greater than this maximum deceleration area, the rotor angle will cross the unstable equilibrium point and the machine will lose synchronism. This is known as the EAC.

6.4.2.2 Two-machine system

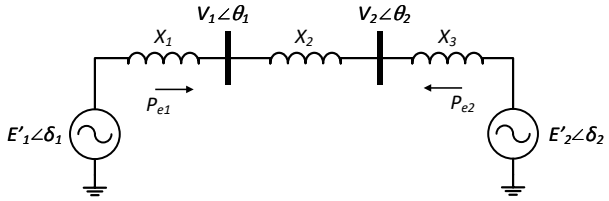

Figure 6.8 – Two-machine system

Suppose that instead of an infinite-bus, a second machine is used to model the load area, as illustrated in Figure 6.8. Each machine is representing an equivalent generator, where E_1' and E_2' are their internal voltages. The reactances X_1 and X_3 represent the total reactance between the internal voltage and terminal bus of each generator (direct-axis transient reactance plus transformer reactance). The two machines are connected by a transmission line represented by the reactance X_2. The transient stability of this two finite machines system can be studied using the same approach presented in the previous section by means of an equivalent SMIB system.

> "A system having two finite machines may be replaced by an equivalent system having one finite machine and an infinite-bus, so that the swing equations and swing curves of angular displacement between the two machines are the same for both systems." (KIMBARK, 1995).

To build this equivalent system it is necessary to use equivalent values of inertia, mechanical power input and electric power output. The swing equations of the two-machines system are

$$\begin{aligned} \frac{d\delta_1}{dt} &= \omega_1, \quad \frac{2H_1}{\omega_0}\frac{d\omega_1}{dt} = Pm_1 - Pe_1, \\ \frac{d\delta_2}{dt} &= \omega_2, \quad \frac{2H_2}{\omega_0}\frac{d\omega_2}{dt} = Pm_2 - Pe_2, \end{aligned} \tag{6.9}$$

where δ_1 and δ_2 are the rotor angles (measured in radians), ω_1 and ω_2 are the rotor speed deviation from the nominal value (in radians per second), H_1 and H_2 are the rotor inertia constant (in seconds), Pm_1 and Pm_2 are the mechanical input power of each machine (in

pu), and Pe_1 and Pe_2 are their electrical output power (in pu). Defining $M_1 = 2H_1/\omega_0$ and $M_2 = 2H_2/\omega_0$ and the relative angle as $\delta_r = \delta_1 - \delta_2$, one has that (KIMBARK, 1995)

$$M\frac{d^2\delta_r}{dt^2} = Pm_{eqv} - Pe_{eqv}, \tag{6.10}$$

where

$$M = \frac{M_1 M_2}{M_1 + M_2}, \tag{6.11}$$

$$Pm_{eqv} = \frac{M_2 Pm_1 - M_1 Pm_2}{M_1 + M_2}, \tag{6.12}$$

$$Pe_{eqv} = \frac{M_2 Pe_1 - M_1 Pe_2}{M_1 + M_2}. \tag{6.13}$$

If the network that connects the two-machines is purely reactive (contains only reactances), as the one in Figure 6.8, the electric power output of the generators are equal and opposite $Pe_1 = -Pe_2$. In other words, one machine is acting as a generator while the other one is acting as a synchronous motor. Thus, the equivalent electric power output, in function of the relative angle, is

$$Pe_{eqv}(\delta_r) = Pe_1 = \frac{E'_1 E'_2}{X_{eq}} \sin\delta_r, \tag{6.14}$$

where $X_{eq} = X_1 + X_2 + X_3$. This equivalent electric power equation is essentially the same as the Equation (6.2). Therefore, the same transient stability analysis based on the power-angle curve and the EAC can be performed here.

6.4.2.3 Fault and control action

The purpose of this part of the work is to study the possibility of using the EAC to compute a generator-rejection control action for systems with parallel AC and DC transmission lines, after a forced outage of the HVDC transmission. The fundamental logic behind the proposed method is presented here, but without including the HVDC transmission to the problem. A forced outage of the HVDC transmission leads to an almost instantaneous electric power reduction, that is, a negative step in electric power output of the generator. Numerical simulations are presented to illustrate this phenomenon in the further chapters of this work. For now, let us consider a system without HVDC transmission, as the one in Figure 6.8, and focus only in the type of disturbance.

Consider the two-machine system of Figure 6.8, its power-angle curve can be traced with Equation (6.14). Suppose that the system is at equilibrium ($Pm_{eqv} = Pe_{eqv}$) and a severe perturbation instantaneously reduces the electric power flowing from generator 1 to generator 2, an instantaneous increase of the equivalent reactance, for instance. After this reduction in electric power, the system is unbalanced, i.e., there is an excess of mechanical power at generator 1. Thus, it will accelerate in relation to generator 2. The same analysis presented in Section 6.4.2.1 can be used here. That is, if the energy

accumulated in the rotor of the generator 1 is dissipated before the angular difference between the generators reaches the unstable equilibrium point, the system is stable from a transient stability perspective. Otherwise, if this energy is not completely dissipated, the angular difference between the generators will increase indefinitely until stability is lost. This phenomenon is illustrated in Figure 6.9a, where the yellow dot indicates the initial condition of the system (pre-fault equilibrium point), the dotted gray curve is the power-angle curve of the system before the fault and the dashed green curve is the power-angle curve after the disturbance (change in X_{eq}), the black line is equivalent mechanical input at the initial condition, and the blue continuous curve is the dynamic response of the system. Note that the fault causes the system response to instantaneously jump from one power-angle curve to the other. The system is unstable because the excess of power at the generator 1 is too great to be dissipated by the rest of the system. Analyzing it graphically, there is not enough deceleration area at the post-fault power-angle curve of Figure 6.9a.

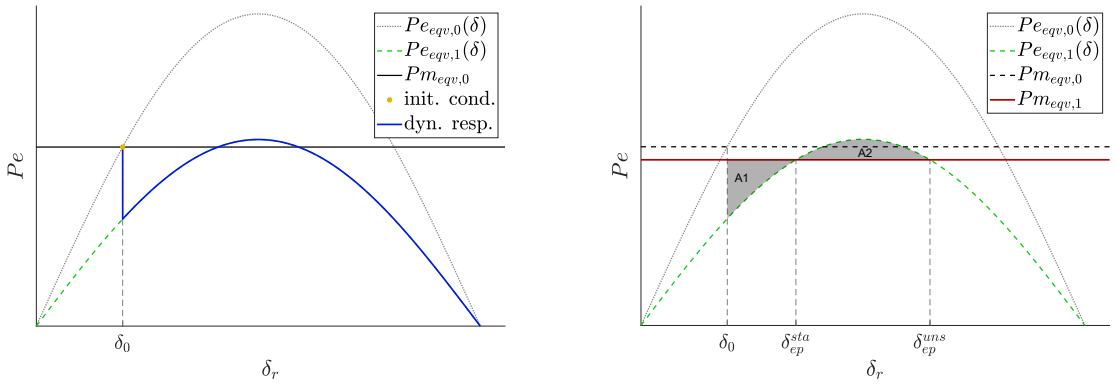

(a) Dynamic response

(b) EAC and the maximum mechanical power input.

Figure 6.9 – Post-fault power-angle curve of an equivalent SMIB system.

One possible strategy to avoid the loss of stability is to reduce the mechanical power input (equivalent mechanical input in this case). By doing so, depending of the operating condition of the system, it may be possible to guarantee that the energy accumulated in the rotor of the generator 1 is dissipated before the angular difference reaches the unstable equilibrium point. Following the EAC, the mechanical power input must be reduced so the deceleration area of the power-angle curve is greater or equal to the acceleration area, $A2 \geq A1$ in Figure 6.9b. So, the maximum mechanical input that can be applied to the system after the fault $Pm_{eqv,1}$ can be computed as follows.

$$\int_{\delta_0}^{\delta_{ep}^{sta}} \left(Pm_{eqv,1} - Pe_{eqv,1}(\delta)\right) d\delta = \int_{\delta_{ep}^{sta}}^{\delta_{ep}^{uns}} \left(Pe_{eqv,1}(\delta) - Pm_{eqv,1}\right) d\delta. \tag{6.15}$$

Solving the integrals of Equation (6.15), the resulting simplified equation is

$$Pm_{eqv,1}\left(\delta_{ep}^{uns} - \delta_0\right) + Pe_{max,1}\left(\cos\delta_{ep}^{uns} - \cos\delta_0\right) = 0, \tag{6.16}$$

where

$$Pe_{max,1} = \frac{E'_1 E'_2}{X_{eq,1}}, \tag{6.17}$$

and $X_{eq,1}$ is the post-fault equivalent reactance of the system. The unstable equilibrium point δ_{ep}^{uns} is also a function of the mechanical power

$$\delta_{ep}^{uns} = \pi - \sin^{-1}\left(\frac{Pm_{eqv,1}}{Pe_{max,1}}\right). \tag{6.18}$$

If $Pe_{max,1}$ and δ_0 are known, Equation (6.15) can be numerically solved to find $Pm_{eqv,1}$. Then, supposing that it is possible to reduce the mechanical input of the system without changing the power-angle curve[1], the minimum mechanical power step that should be applied to the system to assure its transient stability is $\Delta Pm_{eqv} = Pm_{eqv,1} - Pm_{eqv,0}$. Note that this mechanical power step refers to the equivalent mechanical power input. If the step is applied to only one of the two generators, it should be adjusted using the definition of Pm_{eqv} in Equation (6.12).

6.4.2.4 Delayed control action

At the scenario illustrated in Figure 6.9b, the mechanical power is reduced to $Pm_{eqv,1}$ when the relative angle is $\delta_r = \delta_0$. This is not a realistic situation because it implies that the control action occurs simultaneously with the fault. In a practical application there will always be a time window between the fault and the control action, this time window depends on the fault-detection period and the time delays inherent of the control structure (data acquisition, signal processing and transmission, control action calculations, interrupting time of the circuit breakers). In this work, the sum of all these delays from various sources is referred to simply as the *delay between the fault and the control action*. Considering the same system of Figure 6.8, and the same fault (increase in X_{eq}), the post-fault power angle curve considering the delay between the fault and the control action is presented in Figure 6.10. The angle δ_a corresponds to the relative angle value at the instant the control action takes place (the mechanical input is switched from $Pm_{eqv,0}$ to $Pm_{eqv,1}$), that is, δ_a is the relative angle after the time delay. During the interval between the fault and the control action, the accelerating power depends on $Pm_{eqv,0}$ (the initial value of mechanical input), after the control action the acceleration depends on $Pm_{eqv,1}$. This difference must be accounted for when applying the EAC.

Applying the EAC to the scenario illustrated in Figure 6.10 one has that the maximum mechanical input that can be applied to the system after the fault $Pm_{eqv,1}$,

[1] This fast reduction in the mechanical power is achieved by disconnecting generator units (generator-rejection control). This control action impacts on the total reactance of the system and, therefore, impacts on the power-angle curve. This problem is addressed in Chapter 7.

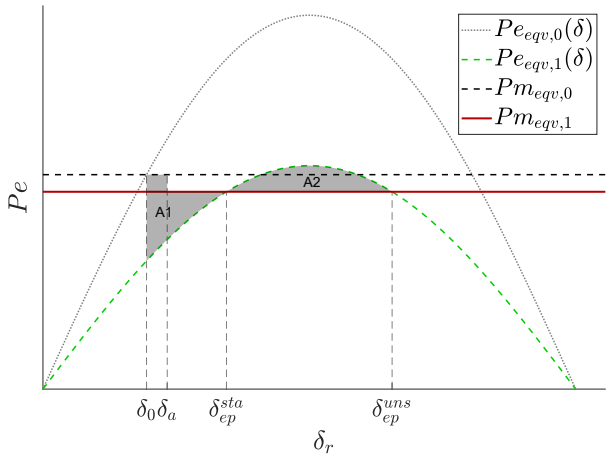

Figure 6.10 – EAC and the maximum mechanical power input for an equivalent SMIB system, considering the delay between the fault and the control action.

considering the delay between the fault and the control action, computed as follows.

$$\int_{\delta_0}^{\delta_a} \left(Pm_{eqv,0} - Pe_{eqv,1}(\delta)\right) d\delta + \int_{\delta_a}^{\delta_{ep}^{sta}} \left(Pm_{eqv,1} - Pe_{eqv,1}(\delta)\right) d\delta = \int_{\delta_{ep}^{sta}}^{\delta_{ep}^{uns}} \left(Pe_{eqv,1}(\delta) - Pm_{eqv,1}\right) d\delta. \tag{6.19}$$

Solving the integrals of Equation (6.19), the resulting simplified equation is

$$Pm_{eqv,0}\left(\delta_a - \delta_0\right) + Pm_{eqv,1}\left(\delta_{ep}^{uns} - \delta_a\right) + Pe_{max,1}\left(\cos\delta_{ep}^{uns} - \cos\delta_0\right) = 0, \tag{6.20}$$

where, δ_a is the relative angle after the time delay, $Pe_{max,1}$ is defined in (6.17), and δ_{ep}^{uns} is defined in (6.18). The relative angle after the time delay δ_a depends on the system dynamics. If $Pe_{max,1}$ and the inertia constants of the two equivalent generators are known, this angle can be computed by integrating the Equation (6.10) for a given period of time (time delay). Then, Equation (6.19) can be solved numerically to find $Pm_{eqv,1}$. Hence, the minimum mechanical power step that should be applied to the system to assure its transient stability is $\Delta Pm_{eqv} = Pm_{eqv,1} - Pm_{eqv,0}$, supposing that this control action does not change the power-angle curve of the system.

6.4.3 Using the DC power flow to build the power-angle curve

As mentioned in Section 6.1, there are some works in the literature that explored the power-angle curve for the transient stability analysis of systems with AC and DC transmission lines (TANG, 2014; ALAM; AHSAN, 2017; GONZALEZ-TORRES, 2018). In those works, the strategy adopted is to shift the power-angle curve of a traditional AC system by a constant factor, defined by the DC power flow at the HVDC links.

Consider the SMIB system with parallel AC and DC lines illustrated in Figure 6.11. If the DC line is removed, the power angle curve of the system is defined by Equation (6.5), with $X_{eq} = X_1 + X_2 + X_3$. Now, supposing that the contribution of the

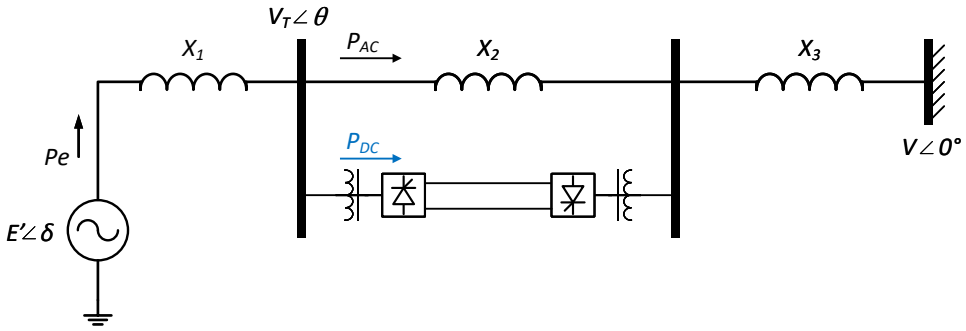

Figure 6.11 – SMIB system with parallel AC and DC transmission.

HVDC system to this power-angle dynamics is a constant factor (P_{DC}), the power-angle curve is given by

$$Pe(\delta) = P_{AC}(\delta) + Pe_{DC} = \frac{E'V}{X_{eq}} \sin\delta + P_{DC}. \tag{6.21}$$

A power-angle curve traced with Equation (6.21) is illustrated in Figure 6.12. In the present thesis, a different and more precise approach is proposed to model the contribution of the HVDC system to the power-angle response.

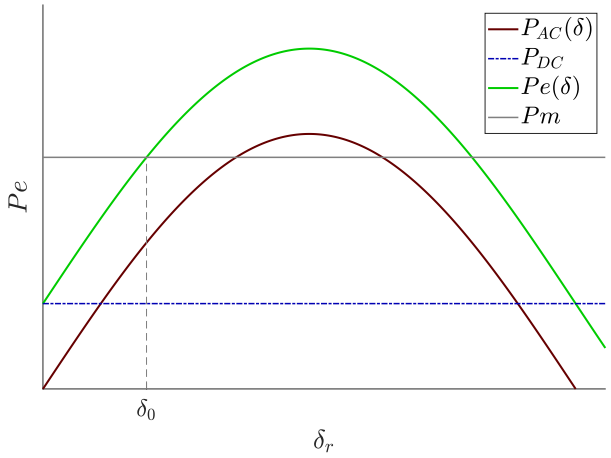

Figure 6.12 – Power-angle curve of an SMIB system with parallel AC and DC lines, considering P_{DC} as a constant factor.

7 Transient Stability Analysis and Generator-Rejection Control for Two-area Systems with Parallel AC and DC Transmission

In order to study the impact of embedded HVDC transmission systems in the angular transient stability problem, a simple scenario is proposed: a two-area system interconnected by parallel AC and DC transmission lines. Each area of the system is modeled by an equivalent generator, with one area representing a large generation area and the other one representing a large load area. The power flow between this two areas is done by means of a HVDC system in parallel with a traditional AC transmission line. Using the concepts introduced in the fundamentals section (Section 6.4), this two-area system can be represented by an equivalent SMIB system, for which an approach for building the power-angle curve is proposed. The methodology is based on the premise that the HVDC links can be modeled by constant current sources and, holding to that premise, an equation to model the electric output power of the equivalent generators is proposed. By means of a series of assumptions, this equation is simplified so it can be used to approximate the power-angle curve of the proposed system. The generator-rejection control for transient stability assurance, in case of forced outage of the HVDC transmission, is proposed using the EAC and the approximated power-angle equation.

7.1 Electric power equation

This section presents the development of the strategy used to model the electric power of a two-machines systems with parallel AC and DC transmission. It is considered that the system is at a steady-state condition and the HVDC system is operating at constant current control mode. Note that, at normal operation, the controllers of the HVDC system regulates the DC power being transferred, however the current control loop of those controllers is much faster (smaller time constants) than the power control loop. Therefore, a current control operation is suitable for a transient stability analysis (KUNDUR, 1994). So, the premise is to combine the current drained by all AC/DC converters in the system and replace each side of the HVDC system by an equivalent current source. The magnitude and phase of each current source is defined based on the total power consumed by the converters. That is, $I_{\mathrm{rec},t}$ represents the current drained by the converters at rectifier side and $I_{\mathrm{inv},t}$ represents the current drained at the inverter side,

computed as follows

$$\begin{aligned} I_{\text{rec},t} &= \left(\frac{S_{\text{rec},t}}{V_{1,t}}\right)^* = \frac{|S_{\text{rec},t}|}{|V_{1,t}|}\angle(\theta_{1,t} - \varphi_{\text{rec},t}) = |I_{\text{rec},t}|\angle\varphi_{1,t} \\ I_{\text{inv},t} &= \left(\frac{S_{\text{inv},t}}{V_{2,t}}\right)^* = \frac{|S_{\text{inv},t}|}{|V_{2,t}|}\angle(\theta_{2,t} - \varphi_{\text{inv},t}) = |I_{\text{inv},t}|\angle\varphi_{2,t}, \end{aligned} \tag{7.1}$$

where $S_{\text{rec},t}$ and $S_{\text{inv},t}$ are the apparent power drained by all converters at the rectifier side and inverter side respectively, defined as

$$\begin{aligned} S_{\text{rec},t} &= P_{\text{rec},t} + jQ_{\text{rec},t} = |S_{\text{rec},t}|\angle\varphi_{\text{rec},t}, \\ S_{\text{inv},t} &= P_{\text{inv},t} + jQ_{\text{inv},t} = |S_{\text{inv},t}|\angle\varphi_{\text{inv},t}, \end{aligned} \tag{7.2}$$

and $|V_{1,t}|\angle\theta_{1,t}$ and $|V_{2,t}|\angle\theta_{2,t}$ are the rectifier bus and inverter bus voltage phasors. The subscript notation "$_{,t}$" is used herein to indicate a time-varying parameter. Note that at Equation (7.1) the complex current is a function of time, because the power drained by the converters and the bus voltages are time-varying parameters. The constant current assumption is applied further, in Section 7.2.

Consider a two-machine system with parallel AC and DC transmission, as the one illustrated in Figure 7.1. Even though the system has two machines, it can be replaced by an equivalent SMIB system. To do that, it is necessary to consider an equivalent inertia constant, an equivalent mechanical power input and an equivalent electrical power output for the equivalent generator, as presented in Section 6.4.2.2.

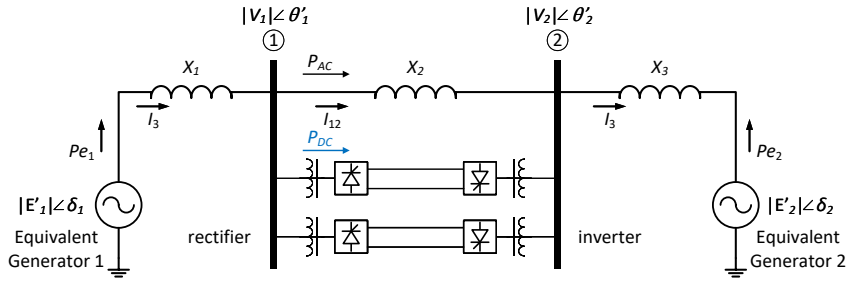

Figure 7.1 – Two machine system with parallel AC and DC transmission.

Let $Pm_{1,t}$ and $Pm_{2,t}$ be the mechanical power input of generators 1 and 2, $Pe_{1,t}$ and $Pe_{2,t}$ be the electrical power output of each generator and $\delta_{r,t} = \delta_{1,t} - \delta_{2,t}$ be the relative angle. The swing equation for this equivalent SMIB system is

$$M\frac{d^2\delta_{r,t}}{dt^2} = P_{a,t} = Pm_{eqv,t} - Pe_{eqv,t}, \tag{7.3}$$

where

$$M = \frac{M_1 M_2}{M_1 + M_2}, \tag{7.4}$$

$$Pm_{eqv,t} = \frac{M_2 Pm_{1,t} - M_1 Pm_{2,t}}{M_1 + M_2}, \tag{7.5}$$

$$Pe_{eqv,t} = \frac{M_2 Pe_{1,t} - M_1 Pe_{2,t}}{M_1 + M_2}, \tag{7.6}$$

and M_1 and M_2 are the inertia constants of generators 1 and 2, respectively.

Each side of the bipole is replaced by a current source, were the magnitude of the current is equivalent to the one consumed by the original AC/DC converters as defined in Equation (7.1). The diagram of the equivalent system with the current sources replacing the HVDC system is presented in Figure 7.2a. The next step is to replace the two generators by an equivalent one and an infinite bus, as illustrated in Figure 7.2b, where $\delta_r = \delta_1 - \delta_2$ is the relative angle between the two machines[1].

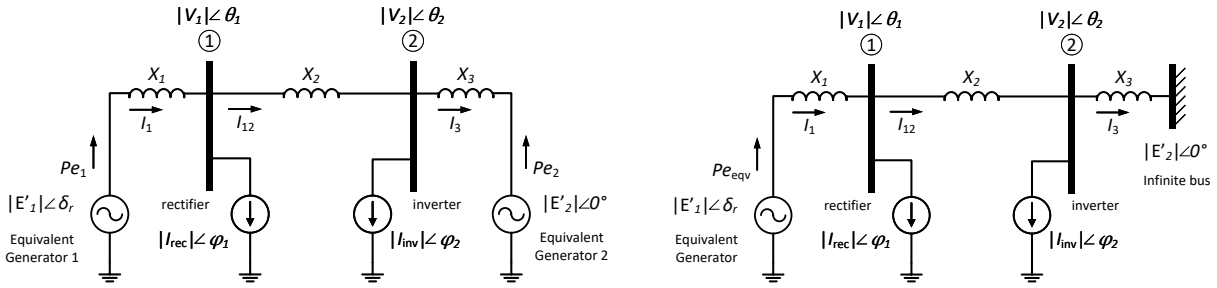

(a) Two machine system. (b) SMIB system.

Figure 7.2 – Equivalent system using current sources to model the HVDC system.

From the circuit analysis theory one can demonstrate[2] that the apparent electric power output of the equivalent generator 1 of Figure 7.2a is

$$\begin{aligned} S_{1,t} = & \frac{|E'_1|^2}{X_1 + X_2 + X_3} \angle 90^\circ - \frac{|E'_1||E'_2|}{X_1 + X_2 + X_3} \angle (90^\circ + \delta_{r,t} - \delta_{2,t}) \\ & + \frac{(X_2 + X_3)|E'_1||I_{\text{rec},t}|}{X_1 + X_2 + X_3} \angle (\delta_{r,t} - \theta_{1,t} + \varphi_{\text{rec},t}) \\ & + \frac{(X_3)|E'_1||I_{\text{inv},t}|}{X_1 + X_2 + X_3} \angle (\delta_{r,t} - \theta_{2,t} + \varphi_{\text{inv},t}). \end{aligned} \tag{7.7}$$

Separating the real component of (7.7), the following expression for the active power output Pe_1 is obtained

$$Pe_{1,t} = P_1 \sin(\delta_{r,t}) + P_2 |I_{\text{rec},t}| \cos(\delta_{r,t} - \theta_{1,t} + \varphi_{\text{rec},t}) + P_3 |I_{\text{inv},t}| \cos(\delta_{r,t} - \theta_{2,t} + \varphi_{\text{inv},t}), \tag{7.8}$$

where

$$P_1 = \frac{|E'_1||E'_2|}{X_1 + X_2 + X_3}, \quad P_2 = \frac{(X_2 + X_3)|E'_1|}{X_1 + X_2 + X_3}, \quad P_3 = \frac{X_3 |E'_1|}{X_1 + X_2 + X_3}. \tag{7.9}$$

A similar approach can be applied to the equivalent generator 2 to obtain $Pe_{2,t}$ and the equivalent electric power output $Pe_{eqv,t}$ can be computed with Equation (7.6). However,

[1] The angles θ_1 and θ_2 in Figure 7.2 corresponds to the voltage phasor angles in respect to the new angular reference, the rotor angle of the equivalent generator 2. In Figure 7.1 an angular reference is not specified, therefore, $\theta_1 \neq \theta'_1$ and $\theta_2 \neq \theta'_2$.

[2] This demonstration is presented in Appendix D.

depending on the characteristics of the system and the assumptions considered, it may not be necessary to compute $Pe_{2,t}$. Those assumptions are discussed in the following section.

7.2 Assumptions and approximated power-angle curve

One of the goals of defining an expression for the electric power output of power systems with parallel AC and DC transmission is to be able to perform transient stability analysis using the power-angle curve. To accomplish that, the electric power expression must be a function of $\delta_{r,t}$, with fixed parameters related to the initial condition of the system, so the power-angle curve can be traced by varying $\delta_{r,t}$ in the desired range. An approach to build expressions for the electric power of parallel AC and DC transmission systems is presented in Section 7.1. However, the equation obtained is a function of time, since it depends on time-varying parameters. Thus, it cannot be used to compute the power-angle curve beforehand without knowing the complete dynamics of the system. In the present section, a series of assumptions and approximations are proposed to build an expression that computes the output active power in function of the relative rotor angle only, so the power-angle curve can be used for the proposed transient stability analysis.

The following assumptions, regarding the power system and mainly the AC/DC converters dynamics, are considered to simplify the electric power equation (7.8). Note that the time window related with transient stability phenomena is a key factor for some of those assumptions. The fundamental assumption (**Assumption 0**) is that the remaining part (pole/bipole) of the HVDC system continues at normal operating mode, that is, the rectifier is able to maintain constant DC current (CHOW; SANCHEZ-GASCA, 2020). Starting at this particular operating condition and considering the transient stability analysis time scale, the following assumptions are considered.

Assumption 1. *The resistive loss of the transmission lines and the HVDC system are neglected. So, assuming that the system has a purely reactive network, one has that the total active electric power provided by the equivalent generator 1 is drained by the infinite-bus ($Pe_{2,t} \approx -Pe_{1,t}$).*

Assumption 2. *It is assumed that the magnitude of the AC current drained by the converters is constant, such that,*

$$\begin{aligned} |I_{rec,t}| = |I_{rec,0}| \;\rightarrow\; |I_{rec,t}| = \frac{|S_{rec,t}|}{|V_{1,t}|} = \frac{|S_{rec,0}|}{|V_{1,0}|}, \\ |I_{inv,t}| = |I_{inv,0}| \;\rightarrow\; |I_{inv,t}| = \frac{|S_{inv,t}|}{|V_{2,t}|} = \frac{|S_{inv,0}|}{|V_{2,0}|}. \end{aligned} \tag{7.10}$$

where $|S_{rec,0}|$, $|S_{inv,0}|$, $|V_{1,0}|$ and $|V_{2,0}|$ are the total apparent power drained by the rectifier converters, the total apparent power drained by the inverter converters, the magnitude

of the rectifier bus voltage and the magnitude of the inverter bus voltage at the initial condition[3].

Assumption 3. *There is no change on the power order of the converters during the time window considered, so the ratio between the active and reactive power drained by the converters is approximately constant. That is, the power factor of each apparent power drained by the converters is considered to be constant, i.e.* $\varphi_{rec,t} = \varphi_{rec,0}$ *and* $\varphi_{inv,t} = \varphi_{inv,0}$.

Assumption 4. *The inductance* X_3 *is considered to be small compared to the rest of the system, so the voltage angle of bus 2 is close to the reference angle (infinite-bus angle or equivalent generator 2 rotor angle), that is,* $\theta_2 \approx 0°$.

Assumption 5. *The inductance* X_1 *is considered to be small compared to* X_2 *(large* X_2/X_1 *ratio), so the difference between the relative rotor angle and the voltage angle of bus 1 is considered to be constant, i.e.* $\delta_{r,t} - \theta_{1,t} \approx \delta_{r,0} - \theta_{1,0}$.

Assumption 6. *The power loss on the HVDC system is considered to be small enough so almost the same amount of active power drained on the rectifier is transferred to the inverter. Also, the converters on the rectifier and inverter sides are considered to be similar, consuming the same amount of reactive power (ARRILLAGA, 1998). That is,* $P_{inv,t} \approx -P_{rec,t}$ *and* $Q_{inv,t} \approx Q_{rec,t}$. *Under this condition,* $|S_{inv,0}| \approx |S_{rec,0}|$ *and* $\varphi_{inv} \approx 180° - \varphi_{rec}$.

Assumption 7. *The magnitude of the voltage of buses 1 and 2 are approximately equal at the initial condition,* $|V_{1,0}| \approx |V_{2,0}|$. *This assumption combined with assumptions 1 and 5 leads to the equivalence* $|I_{rec}| \approx |I_{inv}|$. *That is, it is assumed that the magnitude of the current drained by the converters at the rectifier side has the same magnitude as the one drained by the converters at the inverter side.*

Note that with Assumptions 3 and 5, the term $\delta_{1,t} - \theta_{1,t} + \varphi_{\mathrm{rec},t}$, in Equation (7.8), becomes $\delta_{1,0} - \theta_{1,0} + \varphi_{\mathrm{rec},0}$. The angle difference $\theta_{1,t} - \varphi_{\mathrm{rec},t}$ corresponds to the phase-angle of the current drained by the rectifier converters, as defined in Equation (7.1). Thus, Assumptions 3 and 5 are equivalent to the assumption that the angular difference between the current drained by the rectifier converters and rotor angle of the equivalent generator 1 is constant.

7.2.1 Approximated power-angle equation

From assumptions 1 to 4, all time-varying parameters of Equation (7.8) are replaced by initial condition parameters (except for the relative rotor angle). These assumptions are sufficient to build a power-angle curve for the system and perform the

[3] For the generator-rejection control, the power-angle curve is computed considering the power being transmitted by the remaining poles/bipole of the HVDC system after the forced outage. This is done by properly defining the values of $|S_{\mathrm{rec},0}|$ and $|S_{\mathrm{inv},0}|$ as presented in Sections 7.3 and 7.4.

transient stabilty analysis. However, the power-angle expression can be further simplified. With assumptions 5 and 6 the power-angle equation becomes independent of the parameters of the inverter bus or converter. The power-angle equation resulting from applying assumptions 1 to 6 to Equation (7.8) is

$$\bar{P}e(\delta_{r,t}) = \mathsf{P}_1 \sin(\delta_{r,t}) + \mathsf{P}_2 - \mathsf{P}_3 \cos\left(\delta_{r,t} - \varphi_{\text{rec},0}\right), \tag{7.11}$$

where

$$\begin{aligned} \mathsf{P}_1 &= \frac{|E_1'||E_2'|}{X_1 + X_2 + X_3}, \quad \mathsf{P}_2 = \frac{(X_2 + X_3)|E_1'||I_{\text{rec},0}|}{X_1 + X_2 + X_3} \cos\left(\delta_{1,0} - \theta_{1,0} + \varphi_{\text{rec},0}\right), \\ \mathsf{P}_3 &= \frac{X_3|E_1'||I_{\text{rec},0}|}{X_1 + X_2 + X_3}, \end{aligned} \tag{7.12}$$

and $\delta_{1,0}$ and $\theta_{1,0}$ are the initial condition values (pre-fault values) of the rotor angle and bus 1 voltage angle. In order to apply the EAC it is necessary to know the equilibrium points of the system, i.e. the relative rotor angle at which the electric power output equals the mechanical input power. The equilibrium points considering Equation (7.11) are

$$\begin{aligned} \delta_{ep}^1 = \sin^{-1}\Bigg(& \frac{\left(\mathsf{P}_3 \sin\varphi_{\text{rec},0} - \mathsf{P}_1\right)\left(\mathsf{P}_2 - Pm_{eqv,1}\right)}{\mathsf{P}_1^2 - 2\mathsf{P}_1\mathsf{P}_3 \sin(\varphi_{\text{rec},0}) + \mathsf{P}_3^2} + \\ & + \frac{\mathsf{P}_3 \cos(\varphi_{\text{rec},0})\sqrt{\mathsf{P}_1^2 - 2\mathsf{P}_1\mathsf{P}_3 \sin(\varphi_{\text{rec},0}) + \mathsf{P}_3^2 - \left(\mathsf{P}_2 - Pm_{eqv,1}\right)^2}}{\mathsf{P}_1^2 - 2\mathsf{P}_1\mathsf{P}_3 \sin(\varphi_{\text{rec},0}) + \mathsf{P}_3^2} \Bigg), \end{aligned} \tag{7.13}$$

and

$$\begin{aligned} \delta_{ep}^2 = \sin^{-1}\Bigg(& \frac{\left(\mathsf{P}_3 \sin(\varphi_{\text{rec},0}) - \mathsf{P}_1\right)\left(\mathsf{P}_2 - Pm_{eqv,1}\right)}{\mathsf{P}_1^2 - 2\mathsf{P}_1\mathsf{P}_3 \sin(\varphi_{\text{rec},0}) + \mathsf{P}_3^2} - \\ & - \frac{\mathsf{P}_3 \cos(\varphi_{\text{rec},0})\sqrt{\mathsf{P}_1^2 - 2\mathsf{P}_1\mathsf{P}_3 \sin(\varphi_{\text{rec},0}) + \mathsf{P}_3^2 - \left(\mathsf{P}_2 - Pm_{eqv,1}\right)^2}}{\mathsf{P}_1^2 - 2\mathsf{P}_1\mathsf{P}_3 \sin(\varphi_{\text{rec},0}) + \mathsf{P}_3^2} \Bigg), \end{aligned} \tag{7.14}$$

where $Pm_{eqv,1}$ is the equivalent mechanical input power. The procedure to find the equations for the equilibrium points can be found in the Appendix D.1.1.

7.3 Equal-Area criterion for DC transmission forced outage

Faults in the HVDC transmission system may produce the blocking of a pole or even the blocking of a bipole. An instantaneous change in the value of the power flow causes a step in the electric power output of the generators and affects the transient stability of the system. Considering two-area systems, as the one presented in Figure 7.1, if the total HVDC transmission is lost (blocking of the two bipoles), the system is reduced to a traditional two-machine system (that can be reduced to an equivalent SMIB system). In that case, the power-angle curve is known and the equal-area criterion can be applied to verify if the system will lose stability. However, if only a portion of the HVDC transmission

is lost (blocking of one pole or bipole), the system will continue to operate with parallel AC and DC transmission lines. In that scenario, the Equation (7.11) provides an approximation to the power-angle dynamics of the system. Therefore, it is a tool for the transient stability assessment for scenarios of pole (or bipole) blocking for such parallel AC and DC systems.

To analyze the transient stability of the system after the blocking of a pole/bipole, the amount of HVDC power transmission lost needs to be taken into account. This is done by adjusting the value of $|I_{\text{rec},0}|$ used to compute the weights P_2 and P_3 of Equation (7.11). That is, the value of power consumed only by the remaining converters at the rectifier side (after the pole/bipole blocking) is used to define $|I_{\text{rec},0}|$ with Equation (7.10). If a portion of the power of the blocked pole/bipole is transmitted to the remaining ones (by a run-up on the remaining poles), this power needs to be accounted for by adjusting the value of $|S_{\text{rec},0}|$ accordingly. Assuming that the pre-fault parameters needed for Equation (7.10) are known, the post-fault power-angle curve can be estimated beforehand for any given amount of remaining HVDC transmission, needing only to adjust the value of $|I_{\text{rec},0}|$ properly.

Figure 7.3a shows the effect of a partial HVDC transmission blocking in the power-angle curve of a system with parallel AC and DC transmission. The gray line indicates the equivalent mechanical power input and the yellow circle indicates the initial condition. After the partial blocking of the HVDC transmission, for the case illustrated in Figure 7.3a, the dynamic response does not even reach the equivalent mechanical power line. Thus, there is no deceleration area to dissipate the post-fault surplus energy. The EAC can be used to determine the maximum value of equivalent mechanical power that can be applied to the system in order to guarantee the angular transient stability after the fault, following the idea presented in Section 6.4.2.3. The EAC, disregarding any delay between the forced outage and the control action, is illustrated in Figure 7.3b, where $Pm_{eqv,1}$ represents the maximum post-fault equivalent mechanical power the system can handle.

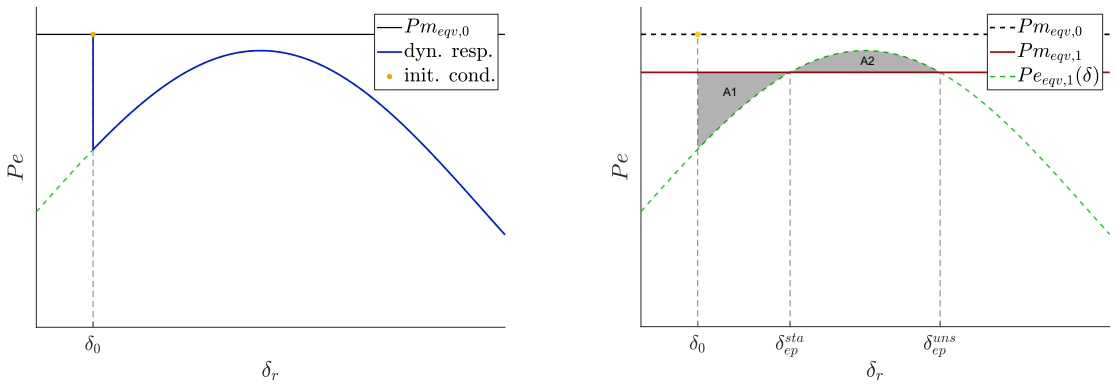

(a) Partial HVDC transmission blocking.

(b) EAC.

Figure 7.3 – Power-angle curve of an SMIB system with parallel AC and DC transmission, using current sources.

The following equation corresponds to the EAC applied for the partial HVDC blocking, using Equation (7.11).

$$\int_{\delta_0}^{\delta_{ep}^{sta}} \left(Pm_{eqv,1} - \bar{P}e(\delta)\right) d\delta = \int_{\delta_{ep}^{sta}}^{\delta_{ep}^{uns}} \left(\bar{P}e(\delta) - Pm_{eqv,1}\right) d\delta. \tag{7.15}$$

Solving the integrals of Equation (7.15), the resulting simplified expression is

$$\begin{aligned}(Pm_{eqv,1} - \mathsf{P}_2)\,(\delta_{ep}^{uns} - \delta_{r,0}) - \mathsf{P}_1(\cos\delta_{r,0} - \cos\delta_{ep}^{uns}) \\ -\mathsf{P}_3(\sin(\delta_{r,0} - \varphi_{\text{rec}}) - \sin(\delta_{ep}^{uns} - \varphi_{\text{rec}})) = 0,\end{aligned} \tag{7.16}$$

where $\delta_{ep}^{uns} = \pi - \delta_{ep}^{2}$ and δ_{ep}^{2} is defined by Equation (7.14), which depends on $Pm_{eqv,1}$, and $|I_{\text{rec}}|$ is computed with Equation (7.1) for the total consumed power by the remaining converters. Thus, the maximum value that the equivalent mechanical input can assume after the electric power step (caused by the HVDC transmission blocking) is the value $Pm_{eqv,1}$ that solves Equation (7.16). This value can be computed numerically by means of a Newton search algorithm.

The proposed generator-rejection control consists on disconnecting generator units of an equivalent generation area to guarantee the transient stability of the system after a forced outage of the HVDC transmission. The amount of mechanical power that must be removed (number of GUs disconnected) is computed with Equation (7.16). However, before applying Equation (7.16) one application problem must be addressed. The maximum mechanical power $Pm_{eqv,1}$ calculated directly with Equation (7.16) depends on the weights P_1, P_2 and P_3, and, therefore, it depends on the equivalent impedance of the system. The generator-rejection control is carried out by disconnecting GUs of the equivalent generator 1 group. As the impedance X_1 corresponds to the parallel equivalent of the impedances (transitory impedance and transformer impedance) of all GUs in the equivalent generator 1 group, it depends on the number of GUs currently connected at that generator, so do the weights P_1, P_2 and P_3 of Equation (7.16). Therefore, the generator-rejection control must take this dependence into consideration during the calculation of the maximum equivalent mechanical input. Also, the value $Pm_{eqv,1}$ corresponds to the equivalent mechanical power, but the control action (generator-rejection) is applied to the equivalent generator 1. That is, the mechanical power reduction happens at generator 1, so the reduction in Pm_1 must be the one such that the resulting $Pm_{eqv,1}$ meets the EAC.

One possible solution, instead of computing $Pm_{eqv,1}$ to then compute the generator-rejection, is to compute the number of GU to be rejected N_{Tr} directly. This can be done by applying the following change in variables. Let $X_{1,0}$, $H_{1,0}$ and $Pm_{1,0}$ be the initial condition values of the inductance between generator 1 and the rectifier bus (bus 1), the constant of inertia of the generator 1 group and the mechanical power input of generator 1, respectively. Defining

$$X_1(x) = \frac{X_{1,0}N_{GU1}}{N_{GU1} - x}, \tag{7.17}$$

$$H_1(x) = (N_{GU1} - x)\frac{H_{1,0}}{N_{GU1}}, \tag{7.18}$$

$$Pm_1(x) = (N_{GU1} - x)\frac{Pm_{1,0}}{N_{GU1}}, \tag{7.19}$$

where $x \in \mathbb{R}$ and N_{GU1} is the number of GUs in parallel at generator 1 at the initial condition. The equivalent mechanical power becomes

$$Pm_{eqv,1}(x) = \frac{H_2 Pm_1(x) - H_1(x)Pm_2}{H_1(x) + H_2}, \tag{7.20}$$

where H_2 and Pm_2 are the constant of inertia and the mechanical power input of generator 2, respectively. Once $X_1(x)$ becomes a function of x, so do the weights P_1, P_2 and P_3 and the equilibrium point δ_{ep}^{uns} of Equation (7.16). So, one has that the number of generators to be rejected N_{Tr} in order to achieve an equivalent mechanical input lower or equal to $Pm_{eqv,1}$ is the next integer greater than x, that is,

$$N_{Tr} = \min n \in \mathbb{N} \mid n \geq x, \tag{7.21}$$

where x is the solution to Equation (7.16) with the change of variables (7.17) to (7.20).

7.3.1 Algorithm for generator-rejection control

The proposed method to compute the generator-rejection control in order to assure the transient stability of a two-machine system with parallel AC and DC transmission is summarized as follows.

Algorithm 1. ***Generator-rejection control:*** *Number of GUs to be disconnected in order to assure the transient stability in case of HVDC transmission blocking on an SMIB system with parallel AC and DC transmission*

Step 1 Define the values N_{GU1}, $X_{1,0}$, X_2, X_3, $H_{1,0}$, H_2, $Pm_{1,0}$, Pm_2, $\theta_{1,0}$, $\delta_{r,0}$, $|V_{1,0}|$, $|E_1'|$ and $|E_2'|$ using the initial condition parameters (pre-fault) of the system.

Step 2 Define $S_{\text{rec},0}$ as the total remaining apparent power drained at the rectifier side after the HVDC transmission blocking using Equation (7.2).

Step 3 Define $|I_{\text{rec},0}|$ with Equation (7.10), for the remaining HVDC transmission after the fault.

Step 4 Using the value $X_{1,0}$, define P_1, P_2 and P_3 with Equation (7.12), using the change of variable (7.17).

Step 5 Define $H_1(x)$, $Pm_1(x)$ and $Pm_{eqv,1}(x)$, using equations (7.18) to (7.20)

Step 6 Solve Equation (7.16) numerically, for $x \in \mathbb{R}$.

Step 7 Compute the number of GUs to be rejected at the generator group 1 as $N_{Tr} = \min n \in \mathbb{N} \mid n \geq x$.

7.4 Equal-area criterion for DC transmission forced outage with delayed control action

The method to compute the generator-rejection control described in Section 7.3.1 is based on the EAC applied to the power-angle curve of the system, as illustrated in Figure 7.3b. The maximum post-fault equivalent mechanical power $Pm_{eqv,1}$ is computed considering that the control action (generator-rejection) occurs simultaneously with the fault (forced outage of the HVDC transmission). However, in a practical application, there is a delay between the fault occurrence and the control action. The contingency considered here is the short-circuit at a DC line followed by the blocking of the pole/bipole by the protection (forced outage), that stays disconnected after the fault clearance. During the short-circuit, the DC power flow on the faulted line is approximately zero. Therefore, for the transient analysis based on the power-angle curve proposed here, the effect of the short-circuit is equivalent to the instantaneous disconnection of the HVDC pole/bipole. Thence, the fault clearance (interrupting time of the circuit breakers) and control (data acquisition, signal processing and transmission, calculation of the control action) delays can be combined in a total time delay. Once there is a delay between the fault and the control action, the acceleration area expected in a real application is greater that the one illustrated in Figure 7.3b. The EAC for the forced outage of the HVDC transmission, considering the delay between the fault and the control action is illustrated in Figure 7.4.

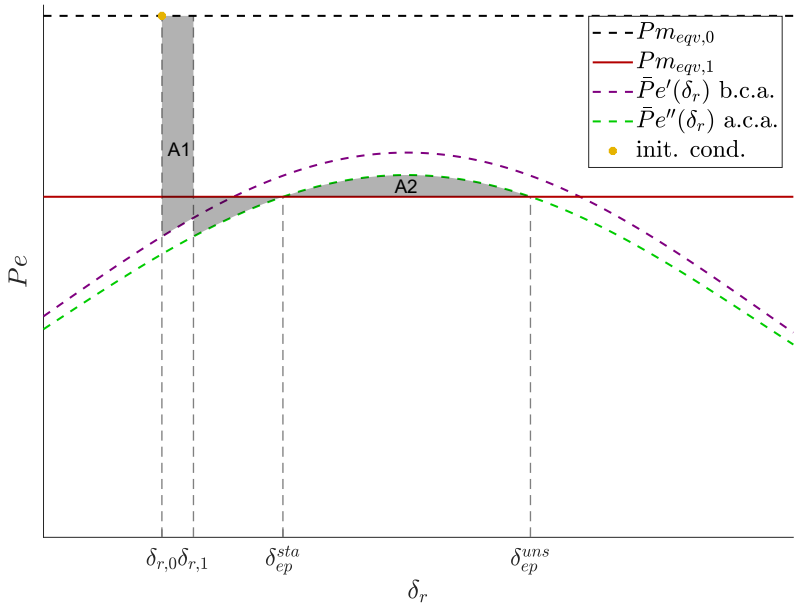

Figure 7.4 – EAC considering the delay between the fault and the control action.

The parameter X_1 used to compute the weights of the power-angle equation (7.11) is the total equivalent reactance between the equivalent generator and the rectifier bus (transient reactance + transformer reactance), therefore it depends directly on the

number of GUs currently operating at the equivalent generator 1. Thus, the power-angle curve of the system is different before control action (**b.c.a.**) and after the control action (**a.c.a.**). This difference is illustrated in Figure 7.4 and must be taken into account during the computation of the control action, i.e. the number of GUs to be rejected.

Let $\bar{P}e^{'}(\delta_r)$ and $\bar{P}e^{''}(\delta_r)$ be the approximations for the power-angle curve of a two-area system with parallel AC and DC transmission, for the **b.c.a.** and **a.c.a.** scenarios, respectively. Applying the EAC to the curves of Figure 7.4 one has that

$$\int_{\delta_0}^{\delta_1} \left(Pm_{eqv,0} - \bar{P}e^{'}(\delta)\right) d\delta + \int_{\delta_1}^{\delta_{ep}^{sta}} \left(Pm_{eqv,1} - \bar{P}e^{''}(\delta)\right) d\delta = \int_{\delta_{ep}^{sta}}^{\delta_{ep}^{uns}} \left(\bar{P}e^{''}(\delta) - Pm_{eqv,1}\right) d\delta, \tag{7.22}$$

where $Pm_{eqv,0}$ is the initial value of the equivalent mechanical power input and $Pm_{eqv,1}$ is the equivalent mechanical power input for which the acceleration and deceleration areas are equal. Solving the integrals of Equation (7.22), the resulting simplified expression is

$$\begin{aligned} Pm_{eqv,0}(\delta_{r,1} - \delta_{r,0}) + Pm_{eqv,1}(\delta_{ep}^{uns} - \delta_{r,1}) + \mathsf{P}_1'(\cos\delta_{r,1} - \cos\delta_{r,0}) + \mathsf{P}_2'(\delta_{r,0} - \delta_{r,1}) \\ + \mathsf{P}_3' \left(\sin(\varphi_{\text{rec}} - \delta_{r,0}) - \sin(\varphi_{\text{rec}} - \delta_{r,1})\right) + \mathsf{P}_1''(\cos\delta_{ep}^{uns} - \cos\delta_{r,1}) + \mathsf{P}_2''(\delta_{r,1} - \delta_{ep}^{uns}) \\ + \mathsf{P}_3'' \left(\sin(\varphi_{\text{rec}} - \delta_{r,1}) - \sin(\varphi_{\text{rec}} - \delta_{ep}^{uns})\right) = 0, \end{aligned} \tag{7.23}$$

where P_1', P_2' and P_3' are the weights of the power-angle curve approximation, computed with Equation (7.12) for the **b.c.a.** scenario and P_1'', P_2'' and P_3'' are the weights computed for the **a.c.a.** scenario. With the $|I_{\text{rec},0}|$ corresponding to the current drained by the remaining converters after the forced outage of HVDC transmission, including any power transmission to the remaining poles (run-up action). Also, $\delta_{ep}^{uns} = \pi - \delta_{ep}^{2}$ is the unstable equilibrium point for the $\bar{P}e^{''}(\delta_r)$ curve, where δ_{ep}^{2} is computed using Equation (7.14). However, the parameters P_1'', P_2'' and P_3'' are unknown, since the amount of generation that should be rejected was not computed yet. Therefore, the same change in variables used for the case without time delay is used here. That is, the **a.c.a.** value of X_1 is defined as a function of a variable $x \in \mathrm{R}$, that will be later used to compute N_{Tr} (the number of GUs to be rejected). Then, the number of generators to be rejected N_{Tr} in order to achieve an equivalent mechanical input lower or equal to $Pm_{eqv,1}(x)$ is the next integer greater than x, that is,

$$N_{Tr} = \min n \in \mathbb{N} \mid n \geq x, \tag{7.24}$$

where x is the solution to Equation (7.23) with the change of variables (7.17) to (7.20). However, to solve Equation (7.20), the value $\delta_{r,1}$ (relative rotor angle at the instant of the control action) must be known. As this value is a dynamic variable of the system and not a pre-defined parameter, an estimation procedures is needed. The approach chosen to find $\delta_{r,1}$ is to integrate the swing equation of the system for a pre-defined time delay value, using the approximated power-angle equation (7.11) to model the equivalent electric power output of the system.

Using Equation (7.11), computed with **b.c.a.** parameters, to model the equivalent electric output, the swing equation of the two-area system is

$$M\frac{d\omega_{r,t}}{dt} = Pm_{eqv,0} - \bar{P}e'(\delta_{r,t}), \tag{7.25}$$

where $\omega_{r,t} = d\delta_{r,t}/dt$. So, knowing the initial condition of the system, for a fixed time delay of Δt, one can integrate Equation (7.25) to estimate the relative rotor angle $\delta_{r,1}$ at the instant $t_1 = t_0 + \Delta t$.

7.4.1 Algorithm for generator-rejection control with time delay

The proposed method to compute the generator-rejection control in order to assure the transient stability of a two-machine system with parallel AC and DC transmission, considering a fixed time delay, is summarized as follows.

Algorithm 2. ***Generator-rejection control with time delay:*** *Number of GUs to be disconnected to maintain stability after a HVDC transmission blocking, considering the delay between fault and control action*

Step 1 Define the values $X_{1,0}$, X_2, X_3, $H_{1,0}$, H_2, $Pm_{1,0}$, Pm_2, $\theta_{1,0}$, $\delta_{r,0}$, $|V_{1,0}|$, $|E_1'|$ and $|E_2'|$ using the initial condition parameters (pre-fault) of the system.

Step 2 Define $S_{\text{rec},0}$ as the total remaining apparent power drained at the rectifier side after the HVDC transmission blocking, Equation (7.2).

Step 3 Define $|I_{\text{rec},0}|$ with Equation (7.10), for the remaining HVDC transmission after the fault.

Step 4 Using the value $X_{1,0}$, define P_1', P_2' and P_3' with Equation (7.12) and build the approximated power-angle equation $\bar{P}e'(\delta_{r,t})$ for the **b.c.a.** scenario, using (7.11).

Step 5 Compute the estimated relative rotor angle $\delta_{r,1}$ by integrating Equation (7.25), for the expected time-delay Δt, using $\bar{P}e'(\delta_{r,t})$.

Step 6 Using the change of variable (7.17), define the weights P_1'', P_2'' and P_3'' for **a.c.a.** scenario, using Equation (7.12). And define δ_{ep}^2 using Equation (7.14).

Step 7 Define $H_1(x)$, $Pm_1(x)$ and $Pm_{eqv,1}(x)$, using equations (7.18) to (7.20)

Step 8 Solve Equation (7.23) numerically, for $x \in \mathbb{R}$.

Step 9 Compute the number of GUs to be rejected at the generator group 1 as $N_{Tr} = \min n \in \mathbb{N} \mid n \geq x$.

8 Proof of concept and preliminary results

The goal of the proposed methodology is to provide tools for the transient stability analysis and control of systems with parallel AC and DC transmission in cases of partial forced outage of the DC transmission. This chapter presents the preliminary results obtained with the algorithms for generator-rejection control proposed in Chapter 7.

As described in Section 6.2, in the Brazilian power system there is a large power transmission from the northern region to the southeastern region and this transmission goes through two HVDC systems (two HVDC bipoles) in parallel with 500 kV AC transmission lines. Inspired by the Brazilian system, a simple scenario is proposed to test the methodology. The system follows the structure illustrated in Figure 6.2, a two-area system connected by parallel AC and DC lines. In the first approach, Area 1 is modeled by an equivalent generator, while Area 2 is modeled as an infinite-bus. Then, the infinite-bus is replaced by a second equivalent generator resulting in a two-machine test system. The purpose of the analysis presented here is to test the proposed methodology in a proof of concept scenario. Therefore, the test system is as simple as possible. Resistive losses are neglected (except for the HVDC system) and neither loads nor any shunt devices are considered. However, the power flow condition is inspired by a real condition of the Brazilian HVDC system of interest. Among the various operating conditions considered for the test system, the power flow values of the most loaded operating point is based on a typical condition of the Brazilian test system, with the HVDC system transmitting 8000 MW while the AC line is transmitting 1000 MW.

The intention of performing the preliminary tests presented in this chapter is to test the methodology, especially the proposed assumptions used to simplify the power-angle expression, and investigate the transient dynamic response of two-area systems interconnected by bulk DC transmission lines in parallel with a traditional AC line.

8.1 SMIB system

8.1.1 Test System

The test system used is a simplified two-area system with parallel AC and DC transmission network presented in Figure 8.1, where Area 1 consists of a equivalent generator that is providing electric power to Area 2, that represents a load center with a high equivalent inertia, modeled as an infinite-bus. All reactance values are presented in Table 8.1 in percentage values in respect to a 100 MVA power base. The transmission network consists of two HVDC bipoles in parallel with an AC transmission line. The HVDC

system is built using the Model 01[1] of the software ANATEM (CEPEL; ELETROBRAS, 2020a), with 5 Ω line resistances ($R_{dc1} = R_{dc2} = R_{dc3} = R_{dc4} = 5\ \Omega$), and it is configured to operate at current control mode. Four different operating conditions are considered where the amount of power being transmitted by the two bipoles varies from 2000 MW to 8000 MW. The active power flow in the AC line is fixed in 1000 MW, for all scenarios tested. The classical model (voltage source behind a transient direct-axis inductance) is used to represent the equivalent generator and its parameters are presented in Table 8.2. The active power flow configuration of the transmission lines at each operating point is presented in Table 8.3. The initial condition parameters of the system, needed to build the approximated power-angle curve with Equation (7.11) is presented in Table 8.4. More details about the power flow of each operating point is presented in the Appendix F.1.

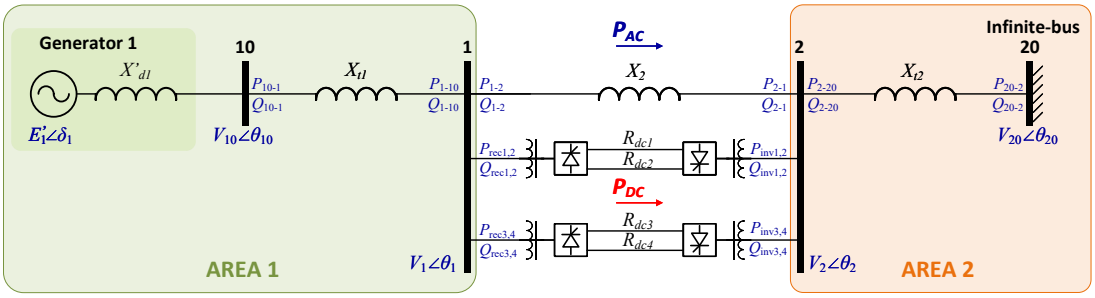

Figure 8.1 – SMIB test system with parallel AC and DC transmission.

Table 8.1 – Reactances of the system.

$X'_{d1}(\%)$	$X_{t1}(\%)$	$X_2(\%)$	$X_{t2}(\%)$
0.18851	0.125	4.0	0.1

Table 8.2 – Equivalent generator parameters.

Num. of GUs	$X'_{d1}(\%)$/GU	H(s)/GU	Base(MVA)
25	32.0	4.8	679

As there are no loads in the system, all power generated by the equivalent generator 1 is transmitted to the infinite-bus. There is, the total active electric power output of generator 1 at the initial condition is the sum of the transmitted active power ($Pe_{1,0} = P_{AC,0} + P_{DC,0}$). The operating point 4 is based on a critical operating condition of the Brazilian power system (Belo Monte's HVDC system in the north exporting configuration) and the other operating points are hypothetical scenarios with reduced

[1] The system was simulated using the ANATEM software and the parameters of the HVDC converters and control model are presented in Apendix G.

Table 8.3 – DC and AC active power flow at each operating point.

Operating Point	P_{DC}(MW) Pole 1	Pole 2	Pole 3	Pole 4	P_{AC}(MW)
1	500	500	500	500	1000
2	1000	1000	1000	1000	1000
3	1500	1500	1500	1500	1000
4	2000	2000	2000	2000	1000

Table 8.4 – Initial condition parameters.

Operating Point	$\lvert E_1' \rvert$(pu)	$\lvert V_{20} \rvert$(pu)	$\delta_{r,0}(^\circ)$	$\lvert V_{1,0} \rvert$(pu)	$\theta_{1,0}(^\circ)$	$\lvert S_{\text{rec},0} \rvert$(pu)	$\varphi_{\text{rec},0}(^\circ)$
1	1.0427	1.01	30.148	1.0099	25.024	21.159	19.052
2	1.0791	1.02	34.397	1.0101	26.129	43.195	22.177
3	1.1246	1.033	38.31	1.0103	27.173	66.089	24.788
4	1.1774	1.048	41.919	1.0097	28.19	89.832	27.057

HVDC transmission. From Tables 8.2 and 8.3 one has that dispatch at operating point 4 is 360 MW/GU. This value is lower than the usual dispatch for the Belo Monte's power plant (around 530 MW/GU in north exporting configuration) (ONS, 2020). However, the equivalent generator 1 is modeling the entire Area 1, that represents the north and northeast regions of Brazil. Therefore, the number of GUs is chosen based on the short-circuit level of those regions and not in the actual dispatch of Belo Monte's power plant (ONS, 2022a).

The simulation results are presented in two stages. First the impact of the disconnection of HVDC lines over the transient stability of the test system is presented for different operating conditions and the proposed approximation for the power-angle curve is validated. Then, the algorithm for generator-rejection control is applied to determine the minimum number of GUs to be disconnected in order to guarantee the transient stability.

8.1.1.1 Transient stability analysis using the proposed power-angle curve

Consider the test system represented by Figure 8.1, if one pole or bipole is blocked, the system will continue to operate with a parallel AC and DC transmission. In that scenario, Area 1 will suffer an instantaneous reduction of electric power consumption, while Area 2 will suffer an instantaneous increase of load. This power imbalance may lead the system to instability.

This section presents the transient stability analysis of the SMIB test system, for the forced outage of part of the HVDC transmission, using the proposed approximated power-angle equation. Two contingencies were simulated, the blocking of one pole and the blocking of one bipole, with no power transfer to the remaining poles, what causes a 25%

and 50% reduction in the HVDC transmission[2].

The effect of the forced outage of part of the HVDC transmission over the power-angle dynamics of the system is presented in Figures 8.2a to 8.2d, for the four operating points considered. The blue continuous line corresponds to the dynamic response obtained via nonlinear simulation, for the blocking of one pole (indicated by the "1P"). The green continuous line is the dynamic response for the blocking of the bipole (indicated by the "2P"). The power-angle curve approximation computed with Equation (7.11) is presented as a dash-dot red line, for the one pole blocking case, and as a black dash-dot line for the bipole blocking. Note that there is no second generator in this scenario, then the electric power output is computed in reference to the infinite-bus (bus 20) using the values $V_{20}\angle\theta_{20}$ instead of $E'_2\angle\delta_2$, and the relative angle is $\delta_r = \delta_1 - \theta_{20}$. All initial condition parameters needed for Equation (7.11) are presented in the Table 8.4. The brown continuous line indicates the mechanical power input of generator 1 and the yellow circle indicates the initial steady-state condition, before the pole/bipole blocking. As expected, the power imbalance caused generator 1 to accelerate in relation to the infinite-bus.

At operating point 1, the blocking of one pole was not sufficient to cause instability, what was expected considering the large deceleration area that can be observed in Figure 8.2a for the pole blocking case. For the remaining cases, as no control action was taken, the rotor angle difference between the equivalent generator and the infinite-bus increases until the stability is lost. The analysis of the power-angle curve endorse these results, because it is clear that, except for operating point 1, there is no deceleration area to dissipate the surplus energy accumulated in the rotor. In the results presented in Figures 8.2a to 8.2d, the dynamic response follows a path very similar to the approximated curve, what indicates that the assumptions used to build the approximated expression are reasonable. However, a divergence between the curves is observed for the cases where the system became unstable. This divergence starts with a discontinuity caused by a sudden change in electric power and it happens after the peak of the power-angle curve. This is related with the HVDC converters reaching their operating limits, what strongly reduces their capability of maintaining constant current after the fault. This issue is addressed further in Section 8.2.3.1. For this particular test system and operating points, this divergences in the power-angle curve did not impact the results. Since they occurred in the cases were the loss of synchronism was expected anyway.

[2] The power transfer to the remaining poles (run-up) can be taken into account by including the transferred power when defining $S_{sec,0}$ at the initialization of the generator-rejection control algorithm. However, this strategy implies that the power transfer to the remaining poles is instantaneous.

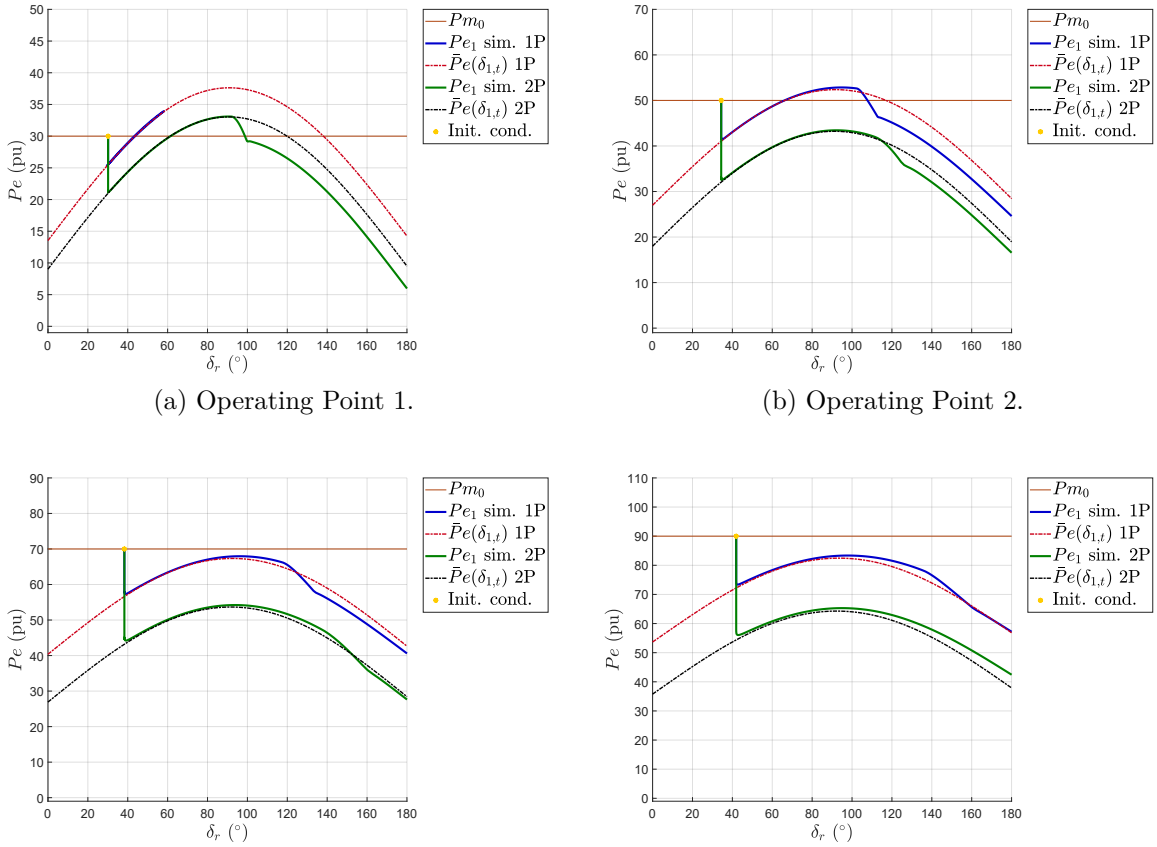

(a) Operating Point 1.

(b) Operating Point 2.

(c) Operating Point 3.

(d) Operating Point 4.

Figure 8.2 – Power-angle curve after the blocking of one (1P) or two (2P) HVDC poles. No control action.

8.1.1.2 Comparison with the constant P_{DC} factor approach

As described in Section 6.4.3, a traditional approach to model the contribution of the HVDC transmission into the power-angle dynamics is to add a constant factor (P_{DC}) to the power-angle curve of the system without the HVDC transmission. The methodology proposed in Chapter 7 is considerably different. The propose formulation, based on modeling of the HVDC transmission with current-sources, resulted in a more complex, and also more precise, equation for the approximation of the power-angle dynamics of two-area systems with parallel AC and DC transmission. This improved precision is illustrated in Figure 8.3, where the power-angle dynamics after the forced outage of part of the HVDC transmission is presented, for operating point 4. This is the same case illustrated in Figure 8.2d, but now the approximated power-angle curves computed with the method described in Section 6.4.3 are also presented (indicated by the $[P_{DC}^{const}]$ in the legend).

Note that, differently from the curves computed with the proposed method, the curves computed with the traditional approach of adding P_{DC} as a constant factor are not good approximations of the simulated dynamics of the system. Thus, computing the control-action (generator-rejection) with such curves is not recommended.

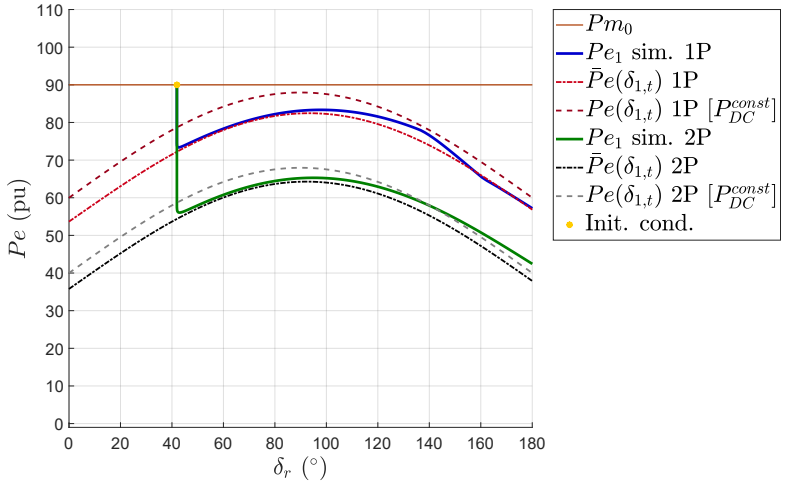

Figure 8.3 – Power-angle curve after the blocking of one (1P) or two (2P) HVDC poles. No control action. Comparison with the constant P_{DC} approach.

8.1.2 Applying the generator-rejection control to the SMIB system

Once it was verified that the curve computed with Equation (7.11) is a satisfactory approximation for the power-angle response of the system, the proposed algorithm for generator-rejection control can be applied. The different operating points presented in Table 8.3 were considered and the algorithm presented in Section 7.3.1 was applied for the forced outage of part of the HVDC transmission (blocking of a pole and a bipole). Again, as the system has only one equivalent generator group, the angular reference is the infinite-bus. Also, there is no need to consider an equivalent mechanical power, so, the change of variables of Equation (7.20) is not used and the Equation (7.16) is solved for $Pm^1_{eqv}(x) = Pm_1(x)$. The results are summarized in Table 8.5, where the number of disconnected generator units computed with the algorithm is presented, as well as the effect of the control action over the transient stability. The last column of Table 8.5 indicates the minimum number of GUs that needs to be disconnected to assure transient stability, obtained by simulation.

Table 8.5 – Results of the generator-rejection control.

Poles Blocked	Operating Point	GUs disconnected	Stable	Minimum gen. rejection
1 Pole	1	0	yes	0
	2	1	yes	1
	3	3	yes	3
	4	4	yes	3
2 Poles	1	1	yes	1
	2	6	yes	6
	3	8	yes	8
	4	9	yes	9

The number of GU to be rejected in order to assure the transient stability computed with the proposed algorithm was exactly the minimum, for almost all scenarios considered. Except for the one pole blocking at operating point 4, where the generator-rejection computed with algorithm was 1 GU greater than the minimum. Note that the number of GUs to be disconnected computed for the one pole blocking at the operating point 1 is 0. That is, the algorithm, based on the EAC, was capable of identifying that no control action was needed. Thus, the number of GUs computed by algorithm is a valuable information that can avoid unnecessary generator-rejection.

The power-angle curve of the system at operating points 1 to 4, with the respective generator-rejection of Table 8.5, are presented in Figures 8.4a to 8.4d, for the blocking of one pole (1P) and one bipole (2P). The blue and green continuous lines corresponds to the simulated response of the system for the pole and bipole blocking, respectively. The dash-dot red line corresponds to the approximated curve computed with Equation (7.11), for the pole (1P) blocking scenario. And the dash-dot black line is the approximated power-angle curve computed with Equation (7.11) for the bipole (2P) blocking case. The brown continuous line indicates the mechanical power input before the generator-rejection. And the light blue and purple continuous lines indicate the mechanical input after the generator-rejection control, for the one pole and bipole blocking cases, respectively. Lastly, the yellow circle indicates the initial condition of the system.

As it was presented in Section 8.1.1.2, the strategy of approximating the power-angle curve by just adding a constant P_{DC} factor to a traditional SMIB power-angle curve is not as precise as using Equation (7.11). To demonstrate that, the generation-rejection was also computed using the constant P_{DC} factor approach, described in Section 6.4.3. The same four operating points presented in Table 8.3 were considered and the same algorithm was used, but using Equation (6.21) instead of Equation (7.11). For the one pole blocking cases, the resulting generation-rejection is 0 GUs, 0 GUs, 1 GU, and 2 GUs, and for the bipole blocking cases, the generator-rejection computed is 0 GUs, 5 GUs, 6 GUs, and 7 GUs, for operating points 1 to 4, respectively. The dynamic responses with those generation-rejections are not presented here, but the comparison with Table 8.5 is sufficient to verify that, except for the one pole blocking case at operating point 1, the number of GUs disconnected is less than the minimum necessary to guarantee the transient stability of the system.

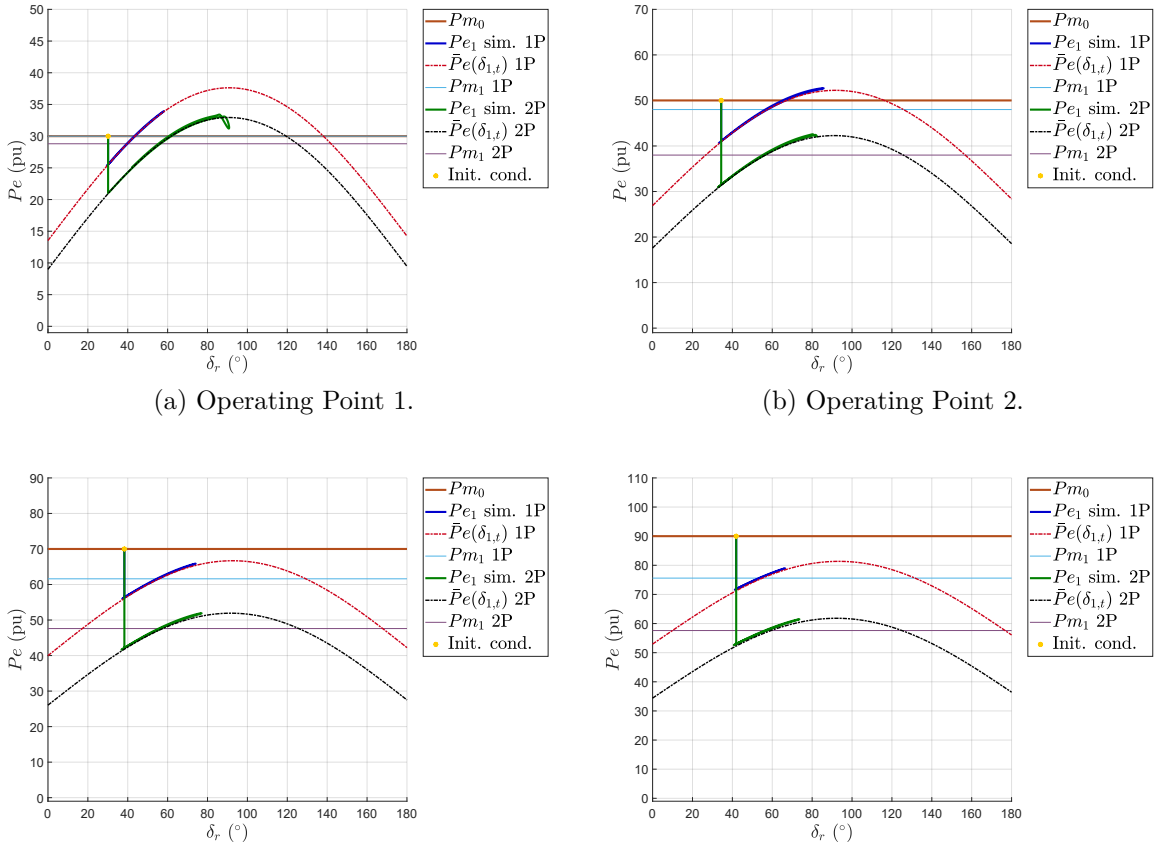

(a) Operating Point 1.

(b) Operating Point 2.

(c) Operating Point 3.

(d) Operating Point 4.

Figure 8.4 – Power-angle curve after the blocking of one (1P) or two (2P) HVDC poles, with simultaneous generator-rejection.

8.2 Two Machine system

Once the results with the SMIB system were very promising, the next step was to include the second generator in the system, replacing the infinite-bus. Also, a delay between fault and control action was considered to test second algorithm proposed. The results obtained with this new configuration are presented in this section.

8.2.1 Test System

The test system is the same one presented in Section 8.1.1, but with a second equivalent generator modeling the load area, instead of the infinite-bus, as presented in Figure 8.5. Area 1 consists of an equivalent generator that is providing electric power to Area 2, that represents a load center with a high equivalent inertia. The transmission network consists of two HVDC bipoles in parallel with an AC transmission line. The HVDC system is the Model 01 of the software ANATEM (CEPEL; ELETROBRAS, 2020a) and the current control configuration is used[3]. The system has no loads, so all of the power

[3] The system was simulated using the ANATEM software and the parameters of the HVDC converters and control model are presented in Apendix G.

provided by the equivalent generator 1 is being transmitted to the equivalent generator 2.

The line reactance parameters are presented in Table 8.6 and the same values of line resistance is used for the HVDC system, $R_{dc} = 5\ \Omega$. The same four operating conditions are considered, with DC power flow varying from 2000 MW to 8000 MW and the active power flow in the AC line fixed in 1000 MW. The classical model (voltage source behind a transient direct-axis inductance) is used to represent both equivalent generators and their parameters are presented in Table 8.7. The active power transmission of each operating point is presented in Table 8.3. The initial condition parameters of the system, needed to build the approximated power-angle curve with Equation (7.11) is presented in Table 8.4 and more details about the power flow condition of the system are presented in the Appendix F.2. As for the previous scenario, the number of GUs of Area 1 is selected based on the short-circuit level of the north and northeast areas and not in the usual dispatch value for the Belo Monte's power plant.

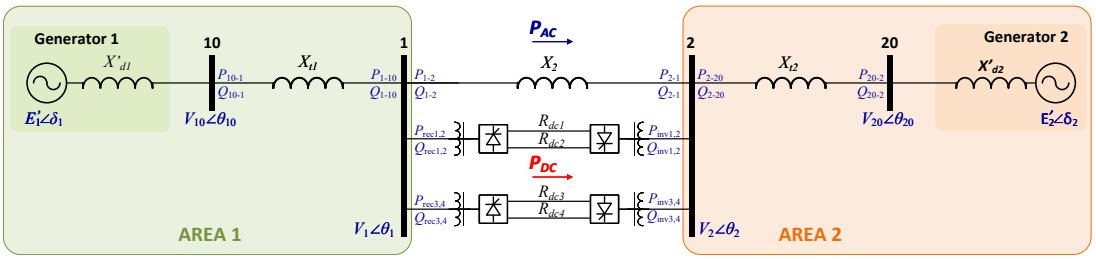

Figure 8.5 – Two-machine system with parallel AC and DC transmission.

Table 8.6 – Reactances of the system.

$X'_{d1}(\%)$	$X_{t1}(\%)$	$X_2(\%)$	$X_{t2}(\%)$	$X'_{d2}(\%)$
0.18851	0.125	4.0	0.03	0.07

Table 8.7 – Equivalent generator parameters - Two-machine system.

	Num. of GUs	$X'_d(\%)$/GU	H(s)/GU	Base(MVA)
Eq. gen. 1	25	32.0	4.8	679
Eq. gen. 2	1	35.0	3.5	50000

The results for the two-machine system are presented in two stages. First the impact of the disconnection of HVDC lines over the transient stability of the test system is presented for the different operating conditions, where the simulated response is compared with the one obtained with the proposed equation for the approximation of the power-angle curve. Then, the algorithm for generator-rejection control is applied to determine the minimum number of GUs to be disconnected in order to guarantee the transient stability.

Table 8.8 – DC and AC active power flow at each operating point - Two-machine system.

Operating Point	P_{DC}(MW)				P_{AC}(MW)
	Pole 1	Pole 2	Pole 3	Pole 4	
1	500	500	500	500	1000
2	1000	1000	1000	1000	1000
3	1500	1500	1500	1500	1000
4	2000	2000	2000	2000	1000

Table 8.9 – Initial condition parameters - Two-machine system.

Operating Point	$\|E'_1\|$(pu)	$\|E'_2\|$(pu)	$\delta_{r,0}(^\circ)$*	$\|V_{1,0}\|$(pu)	$\theta_{1,0}(^\circ)$*	$\|S_{\text{rec},0}\|$(pu)	$\varphi_{\text{rec},0}(^\circ)$
1	1.0427	1.00992	30.1492	1.00992	25.02486	21.1591	19.0523
2	1.07912	1.02046	34.383	1.01011	26.11458	43.1954	22.1766
3	1.12467	1.03264	38.3218	1.01025	27.185	66.0893	24.7883
4	1.1774	1.04825	41.9102	1.00975	28.1809	89.8317	27.0570

*In reference to the rotor angle of the eq. gen 2.

8.2.2 Transient Stability analysis using the proposed power-angle curve

This section presents the transient stability analysis of the two-machine test system, for the forced outage of part of the HVDC transmission. Two contingencies were simulated, the blocking of one pole and the blocking of one bipole, with no power transfer to the remaining poles, what causes a 25% and 50% reduction in the HVDC transmission. The forced outage of the HVDC transmission is usually caused by a short-circuit on the DC line. But, since the effect of this short-circuit is an almost instantaneous reduction of the DC power flow to approximately zero, on the faulted line, it was not necessary to include the short-circuit in the simulations. Instead, the HVDC pole/bipole is permanently disconnected, what causes the same effect over the DC power flow.

The effect of the forced outage of part of the HVDC transmission over the power-angle dynamics of the system is presented in Figures 8.6a to 8.6d, for the four operating points considered, where the simulated response and approximated one are presented. The blue continuous line corresponds to the dynamic response obtained via nonlinear simulation, for the blocking of one pole (indicated by the "1P"). The green continuous line is the dynamic response for the blocking of the bipole (indicated by the "2P"). The power-angle curve approximation computed with Equation (7.11) is presented as a dash-dot red line, for the one pole blocking case, and as a black dash-dot line for the bipole blocking. All initial condition parameters needed for Equation (7.11) are presented in Table 8.9. The brown continuous line indicates the equivalent mechanical power input of generators 1 and 2 and the yellow circle indicates the initial steady-state condition, before the pole/bipole blocking. As expected, the power imbalance caused the equivalent

generator 1 to accelerate in relation to the equivalent generator 2.

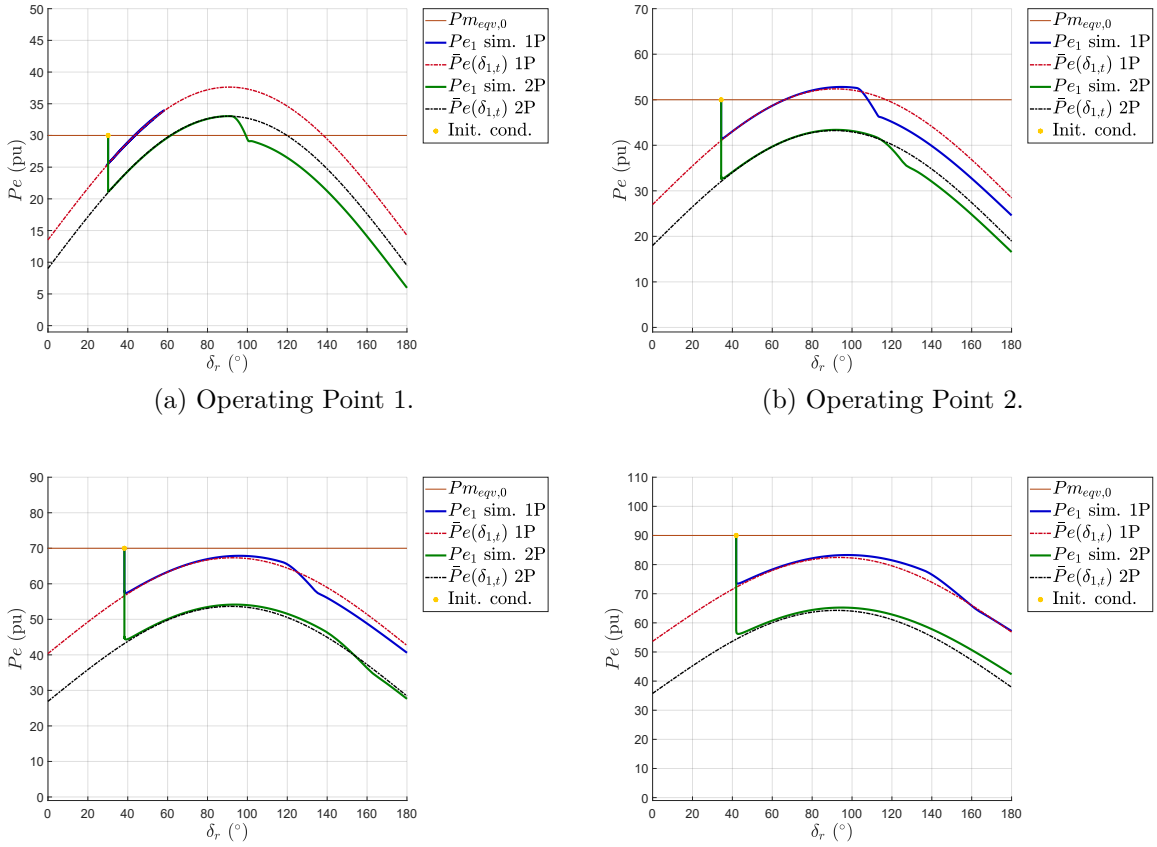

(a) Operating Point 1.

(b) Operating Point 2.

(c) Operating Point 3.

(d) Operating Point 4.

Figure 8.6 – Power-angle curve after the blocking of one (1P) or two (2P) HVDC poles. Two-machine system, with no control action.

The results for the two-machine system are very similar to the SMIB system. That is, the blocking of one pole at the operating point 1 was not sufficient to cause instability. In the remaining scenarios, the fault (blocking of one pole or bipole) caused the rotor of generator 1 to accelerate in relation to generator 2 until stability is lost. Once again, the approximated power-angle curve, computed beforehand using pre-fault parameters, endorse these results. At operating points 2 to 4, it is clear that there is no deceleration area to dissipates the surplus energy accumulated in the rotor.

However, the same divergences related with the HVDC converters reaching their operating limits were observed. Thus, it is important to evaluate the impact of such limits in the proposed methodology. This is discussed in the following section, where the generator-rejection algorithm is tested.

8.2.3 Applying the generator-rejection control to the Two Machine System

As it is shown in Figures 8.6a to 8.6d, a forced outage of the DC transmission may have a severe impact on the transient stability of the system. The generator-rejection control Algorithm 2 described in Section 7.4.1 was applied to the two-machine system to compute the minimum amount of generation that should be disconnected in order to avoid the angular instability. Differently from the method used in the SMIB system, the Algorithm 2 takes the delay between the fault and the control action into consideration. The value considered for the delay is 250 ms. As mentioned in Section 7.4, the delay corresponds to the time window that comprises fault detection, data acquisition, signal processing and transmission, and control action calculations. In this work, it is considered that the fault is cleared after 100 ms and the control action occurs 150 ms after the fault clearance. This are typical values for this type of fault and control action (FILHO, 2022; NOHARA, 2017). The different operating points presented in Table 8.8 were considered and the results are summarized in Table 8.10, where the number of disconnected generator units computed with the algorithm is presented together with effect over the transient stability. The last column of Table 8.10 indicates the minimum number of GUs that needs to be disconnected to assure transient stability, obtained by simulation.

Table 8.10 – Results of the generator-rejection control. Two-machine system.

Poles Blocked	Operating Point	GUs disconnected	Stable	Minimum gen. rejection
1 Pole	1	0	yes	0
	2	1	yes	1
	3	4	yes	4
	4	5	no	6
2 Poles	1	1	no	2
	2	9	yes	9
	3	12	no	11
	4	14	no	13

The power-angle curve of the system at operating points 1 to 4, with the respective generator-rejection of Table 8.10, are presented in Figures 8.7a to 8.7d, for the blocking of one pole (1P) and in Figures 8.8a to 8.8d for the blocking of one bipole (2P). As explained in Section 7.4, there is a difference between the approximated power angle curves before and after the control action, due to the variation in the X_1 inductance caused by the disconnection of the GUs. As a time delay was considered, this difference can be noted in the power-angle curves. That is, before the control action the system is operating with the initial condition inductance ($X_{1,0}$) and after the control action, that happens at $\delta_{r,1}$, the system is operating with an increased X_1 inductance. The approximated power-angle curve before the control action ($\bar{P}e'(\delta)$) corresponds to the dashed green line in the figures, the approximated power-angle curve after the control action ($\bar{P}e''(\delta)$) and corresponds to

the dashed red line. The blue continuous line corresponds to the simulated response of the system. The brown continuous line indicates the equivalent mechanical power input before the generator-rejection. And the light blue continuous line indicate the equivalent mechanical input after the generator-rejection control. Lastly, the yellow circle indicates the initial condition of the system.

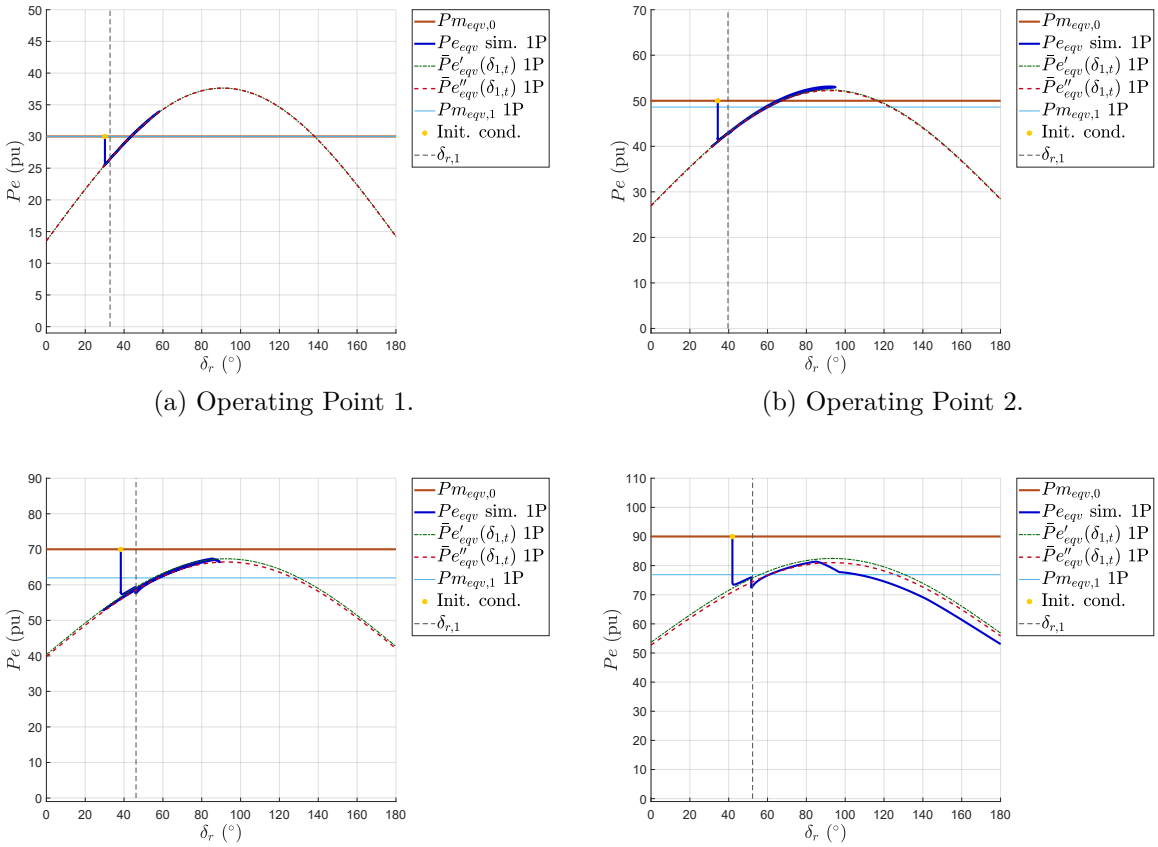

(a) Operating Point 1.

(b) Operating Point 2.

(c) Operating Point 3.

(d) Operating Point 4.

Figure 8.7 – Power-angle curve for the blocking of one HVDC pole followed by the generator-rejection (250ms time delay). Two-machine system.

The results for the two-machines system are very distinct from the ones obtained with the SMIB system. The number of GUs computed with Algorithm 2 are not sufficient to assure the transient stability in half of the scenarios tested. Note that the generator-rejection control used here is different from the previous one. A time delay between the fault and the control action is considered. Thus, in the instant where the generator-rejection occurs, the system is already experiencing the effects of the forced outage of the HVDC transmission. And it is known from the previous simulations that those effects are severe enough to cause instability if no control action is taken. Second, even though the generator-rejection is not sufficient to guarantee the stability, the number of GUs disconnected is close to the actual desired value. As displayed in the last column of the Table 8.10, for the cases where the system lost stability, the number of GUs disconnected is 1 unit bellow the desired one (minimum generator-rejection). Lastly, the dynamics of converters are having

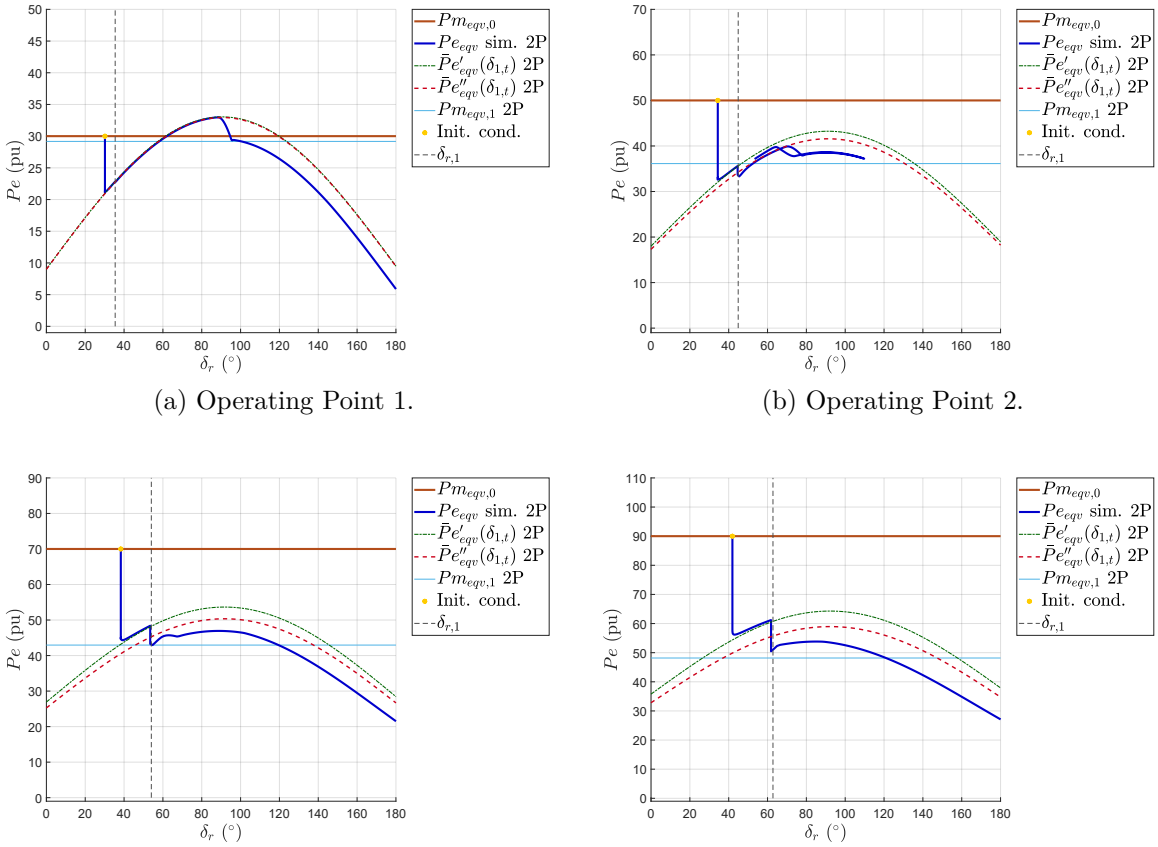

(a) Operating Point 1.

(b) Operating Point 2.

(c) Operating Point 3.

(d) Operating Point 4.

Figure 8.8 – Power-angle curve for the blocking of one HVDC bipole followed by the generator-rejection (250ms time delay). Two-machine system.

a larger influence than expected. This influence is related with the converters reaching their operating limits (minimum firing angle) and, therefore, not being able to provide the rated current value. The simulation data that supports this information are presented in the following section. An strategy to overcome this problem, by including shunt capacitors at the converter buses is presented in Chapter 9.

As for the SMIB case, the generation-rejection was also computed using the constant P_{DC} factor approach to trace the power-angle curve, as described in Section 6.4.3. That is, the Algorithm 2 was applied using Equation (6.21) instead of Equation (7.11). The same four operating points presented in Table 8.8 were considered and the results are: 0 GUs, 0 GUs, 1 GU, and 3 GUs, for the one pole blocking cases, and 0 GUs, 7 GUs, 10 GUs, and 12 GUs for the bipole blocking cases, for operating points 1 to 4, respectively. Comparing those generator-rejections to the minimum ones presented in Table 8.10 one can verify that, except for the one pole blocking case at operating point 1, the number of GUs disconnected is less than the minimum necessary to guarantee the transient stability of the system in all cases considered. Thus, the constant P_{DC} performed worse than the proposed methodology.

8.2.3.1 Voltage level and converter operation

The constant current operation of the HVDC link is the main premise of the methodology proposed in this work, as discussed in Section 7.2. However, this characteristic is expected for HVDC system as long as the converters do not reach any operational limit. It is known that the proper operation of an HVDC system requires sufficient voltage support at the converter terminals (CHOW, 2000), otherwise the commutation angles may reach their limits. And this is happening in the results presented in the previous section.

In order to simplify the transient stability analysis and study the specific influence of parallel AC and DC lines, the test system built is too simple. That is, no voltage support was considered. Let us evaluate the results of the operating point 4 (worst case). The bus voltage levels of this operating point are presented in Figure 8.9a, the electric power output of the equivalent generator 1 is presented in Figure 8.9b, the DC currents on each HVDC pole are presented in Figure 8.9c, and, lastly, the firing angles of the rectifier converters of the remaining bipole are presented in Figure 8.9d, for the bipole blocking case. The vertical dashed lines indicate the instants of bipole blocking, the generator-rejection and the instant at which the firing angle of the converters reach the minimum limit. Note that the minimum firing angle is reached right after the control action. Thus, the HVDC system is not able to maintain the constant current value that was considered during the computation of the generator-rejection.

The firing angle reaches its minimum because the converter control is compensating for the sudden reduction in the voltage level of the rectifier bus, suggesting that it is a voltage compensation problem. To verify this hypothesis, a simulation test were performed where a shunt capacitor was switched simultaneously with the generator-rejection. The size of the capacitor were selected to be the minimum value so the rectifier converters firing angle did not reach their minimum limit. Those values are 210 Mvar, 510 Mvar, 1030 Mvar, and 1710 Mvar, for the operating points 1, 2, 3 and 4, respectively, for the bipole blocking case. The bus voltage levels, electric power output of the equivalent generator 1, DC currents on each HVDC pole, and the firing angles of the rectifier converters are presented in the Figures 8.10a to 8.10d, for the operating point 4. Note that the voltage levels do not have a significant decrease as in the case without the shunt capacitor. Then, the current level is kept close to the initial condition, as the firing angles do not reach their minimum limits. With the shunt capacitor switching, the generation-rejection is sufficient to assure the transient stability. The power-angle curves of the system for the bipole blocking followed by the simultaneous generator-rejection and capacitor switching are presented in Figures 8.11a to 8.11d, for each operating point. Note that the system is stable, but the approximated curve for the **a.c.a.** moment is offset from the simulated response. This difference exists because the shunt capacitor changes the total reactance of the system, and, as the proposed equation is strongly dependent of the reactance parameters, the

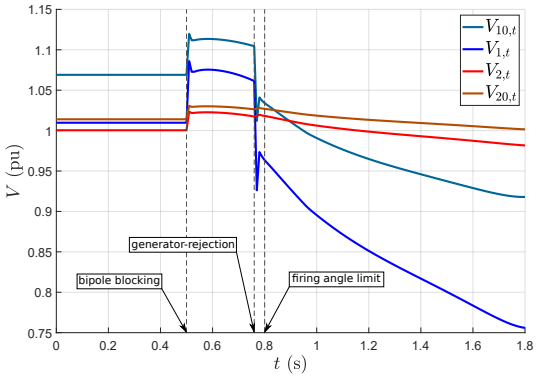

(a) Bus voltages.

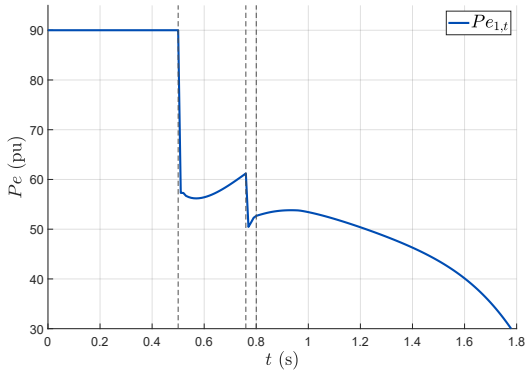

(b) Eq. gen. 1 electric power output.

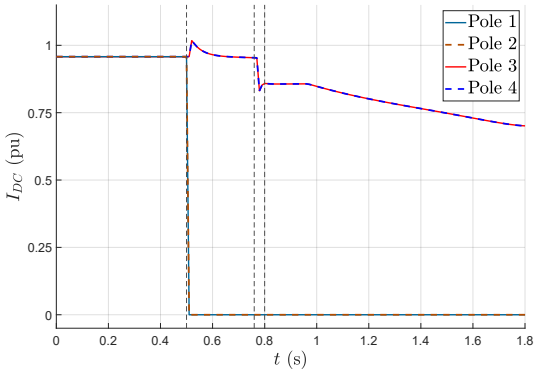

(c) DC current.

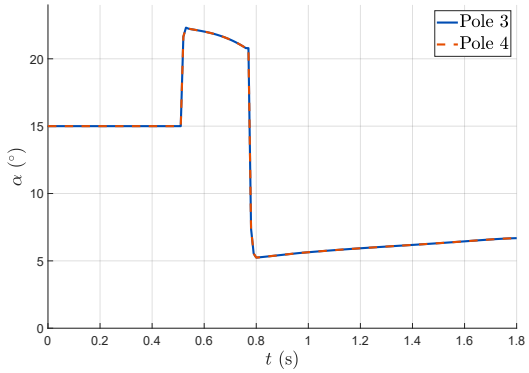

(d) Rectifier converter firing angle.

Figure 8.9 – Dynamic response of the two-machine system for the blocking of one HVDC bipole followed by the generator-rejection (250ms time delay), at operating point 4.

approximated curve is distant from the simulated one. A new formulation to account for shunt capacitor banks/filters in the system is presented in Chapter 9.

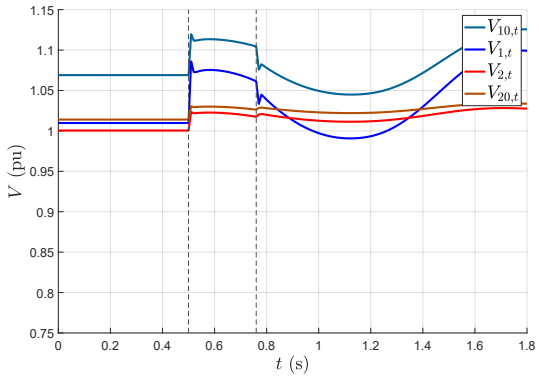

(a) Bus voltages.

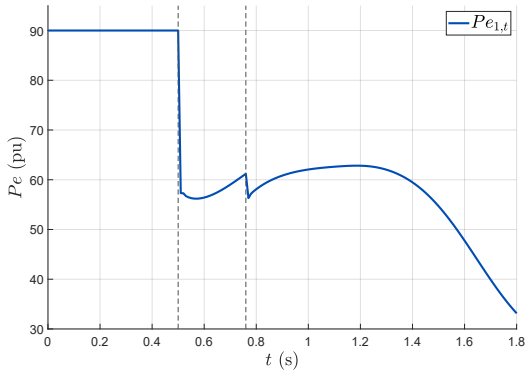

(b) Eq. gen. 1 electric power output.

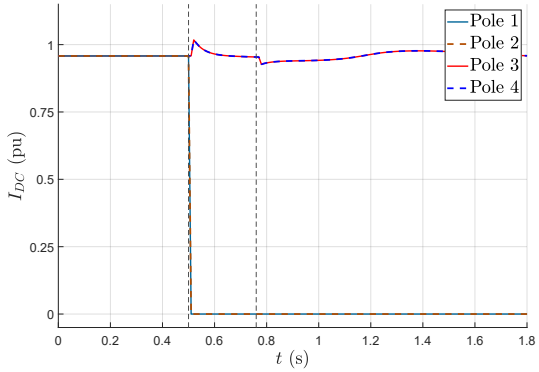

(c) DC current.

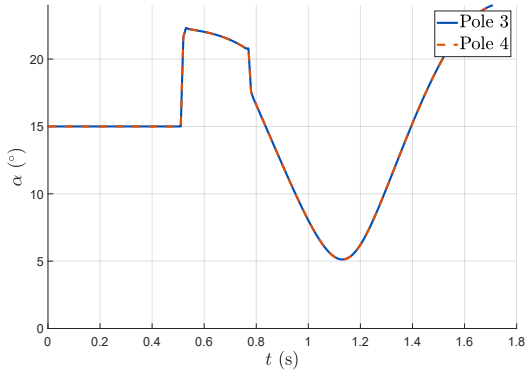

(d) Rectifier converter firing angle.

Figure 8.10 – Dynamic response of the two-machine system for the blocking of one HVDC bipole followed by the generator-rejection (250ms time delay) with a shunt capacitor switching, at operating point 4.

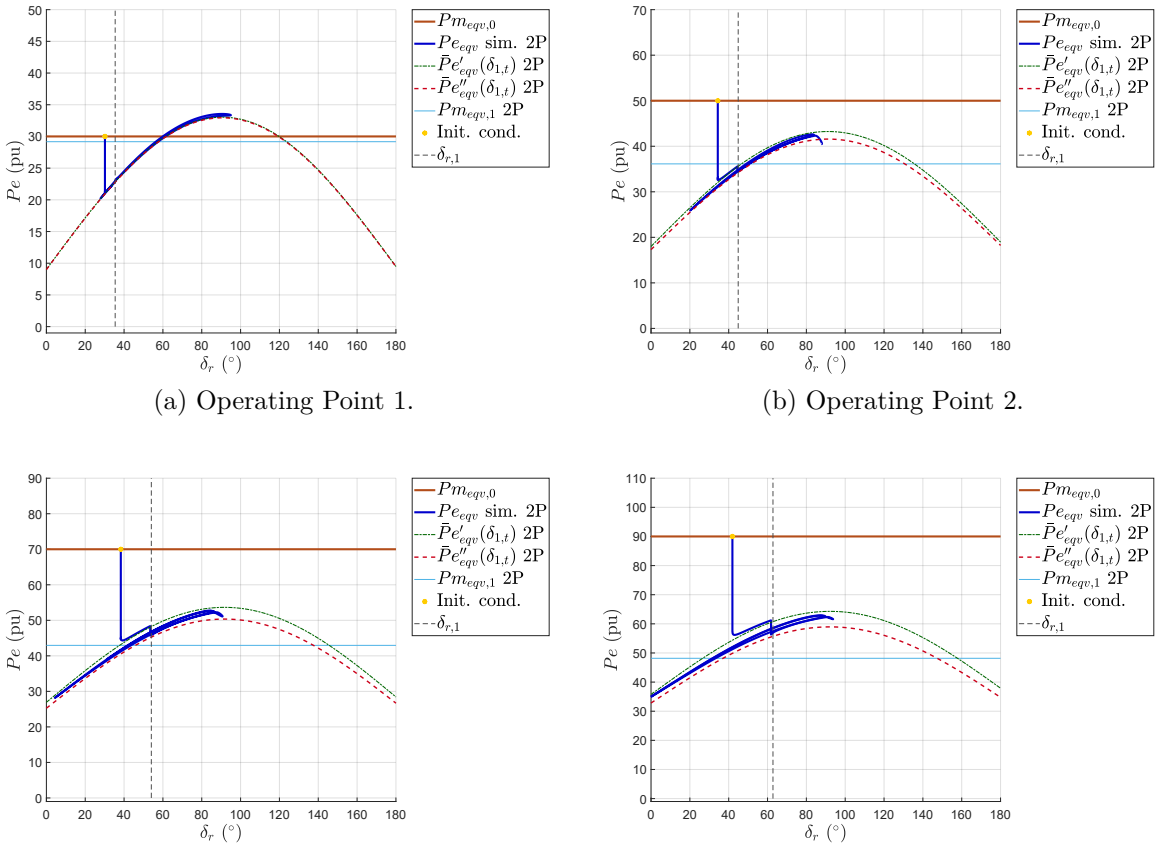

(a) Operating Point 1.

(b) Operating Point 2.

(c) Operating Point 3.

(d) Operating Point 4.

Figure 8.11 – Power-angle curve for the blocking of one HVDC bipole followed by the generator-rejection (250ms time delay) with a shunt capacitor switching. Two-machine system.

8.2.3.2 Reference simulations with a complete model

The results presented in the previous section suggests that the two-area test system is subject to a voltage stability problem, causing the converters of the HVDC system to reach their limit operating condition. This dynamic response is related with the simplicity of the proposed test system and not with the actual phenomenon of interest. A real life power system, interconnected by bulk HVDC transmission lines, is expected to be much more robust to voltage disturbances that the proposed test system. Common power system devices such as AVR, filters, SVCs, synchronous compensators are not considered in the simplified test system. Also, the total power generated at Area 1 is being transmitted to Area-2. Thus, the bipole blocking represents a 44.4% reduction in the total load of the equivalent generator 1. What is not a realistic condition, since generator 1 models a whole area of the system.

To support the hypothesis that this dynamic response is not expected in a real system, a simulation test was performed with a much more complex model. The test system used is the complete model of the transmission system of the Brazilian power system, with 7291 AC buses and 5 HVDC transmission systems (ONS, 2020). The study was performed focusing in the two HVDC systems of *Belo Monte's* power plant, mentioned in Section 6.2. A bipole blocking was simulated followed by the minimum amount of generator-rejection necessary to guarantee the transient stability of the system, without transferring any power to the remaining bipole. The operating condition of the system corresponds to the second third (May to August) of the year 2020, where the two HVDC bipoles were transmitting 8000 MW from the north region to the southeast region of Brazil, while a 937 MW FNS (AC North to South Flow, from the Portuguese *Fluxo Norte Sul*) was being transmitted by the AC lines.

The *Xingu-Estreito* bipole was blocked without any previous fault, and, after 250 ms, 6 GUs were disconnected at the *Belo Monte's* power plant[4]. The SPS of the HVDC systems were turned off to prevent any extra GU disconnection or power transfer to the *Xingu-Terminal Rio* bipole (remaining bipole). The bus voltages, electric power output, HVDC current and rectifier converter firing angles are presented in Figures 8.12a to 8.12d. The voltage level V_{10} corresponds to *Belo Monte* 500 kV bus, V_1 is the *Xingu* 500 kV bus (rectifier bus), V_2 is the *Terminal Rio* 500 kV bus (inverter bus of the remaining bipole), and V_{20} is the *Ilha Solteira* 500 kV bus. The electric power output in Figure 8.12b is the sum of the outputs of the three generator groups of *Belo Monte's* power plant, with a total of 17 GUs. Poles 1 and 2 corresponds to the *Xingu-Estreito* bipole, while poles 3 and 4 corresponds to the *Xingu-Terminal Rio* bipole.

[4] Similar results are obtained by applying a 100 ms short-circuit to the DC lines, followed by the generator-rejection after 150 ms. Since the short-circuit drops the DC power to zero at the faulting lines, for the proposed analysis, its effect is equivalent to the bipole blocking.

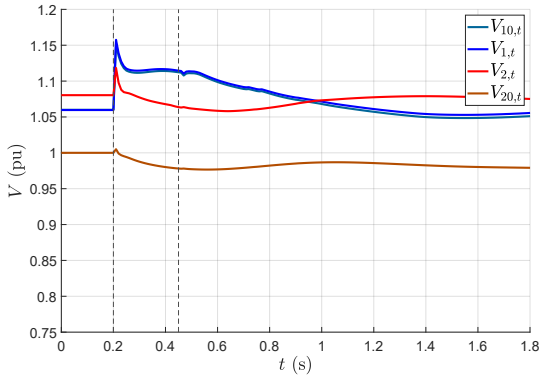

(a) Bus voltages.

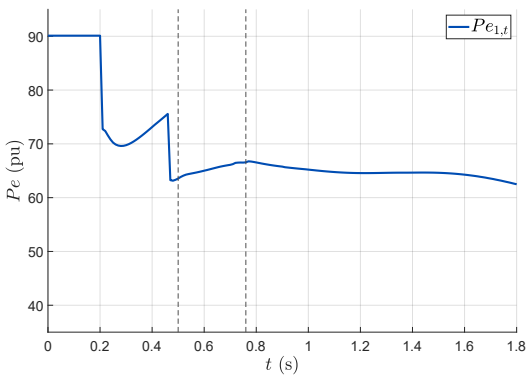

(b) Electric power output.

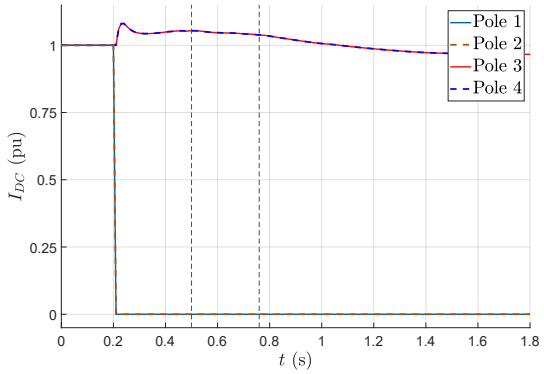

(c) DC current.

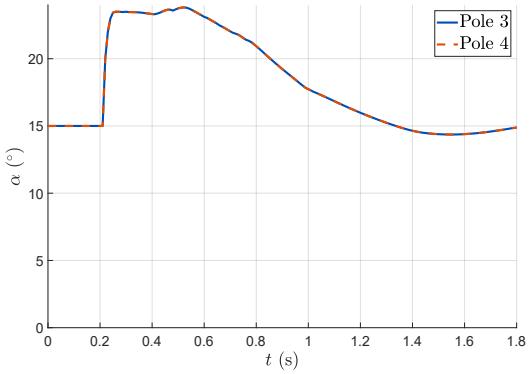

(d) Rectifier converter firing angle.

Figure 8.12 – Dynamic response of model of the Brazilian interconnected system for the blocking of one HVDC bipole (*Xingu-Estreito*) followed by the generator-rejection (250ms time delay).

The dynamic response of the complete model of the system shows that it is more robust to voltages disturbances than the two-area test system. There is no voltage level drops and the firing angles of the converters stay far from their limits. These results suggests that the proposed two-area test system has a limitation regarding the voltage stability. However, it is still a tool for better understanding the phenomenon of interest. In Chapter 9 a modification of the test-system is proposed to improve its voltage dynamic response, approaching a more realistic scenario.

8.3 Comments

This chapter presented the validation of the proposed method for the transient stability assurance of two-area systems with parallel AC and DC transmission, in case of forced outage of the HVDC transmission. The validation is presented in two stages, first an SMIB system is proposed. Then, a second machine is introduced to build a two-machine test system.

The Section 8.1 presented the proof of concept of the proposed methodology. The proposed expression for approximating the power-angle curve of SMIB systems with parallel AC and DC transmission was validated with a simple test system. The power-angle curve of the system was traced, using the proposed equation, for multiple operating conditions and compared with the dynamic response of the system obtained via simulation. The results were promising supporting the next stage of investigation, that is to use the proposed equation to compute the minimum number of GUs to be disconnected in case of forced outage of the HVDC transmission. The proposed algorithm for generator-rejection control was applied to the system at same operating points and the exactly amount of generator-rejection needed to assure the transient stability was found, except for one scenario were the number of GUs computed was 1 GU above the minimum. The result was verified with nonlinear simulations using the ANATEM software.

The Section 8.2 presented the test of the proposed methodology for two-area systems with two equivalent machines. The second version of the proposed generator-rejection algorithm was used, to account for the time delay between the fault and the control action. The method was tested with a simplified two-machine system and the proposed equation for approximating the power-angle curve was applied to evaluate the transient stability of the system. It was possible to predict if the systems was going to lose stability with the proposed equation. However, the amount of generator-rejection computed with the proposed algorithm was not sufficient to assure the transient stability in all cases. The analysis of the results suggests that the stability was lost due to a lack of voltage support, that caused the converters to reach their limit operating condition. Some experiments were presented with shunt capacitor banks/filters providing voltage support to the rectifier bus and the results were promising. Also, a simulation with the Brazilian power system model was presented. The results suggest that the voltage stability problem is a characteristics of the proposed two-machines test system and it is an aspect for further investigation.

The simplicity of the proposed test system was intentional, so limitations were expected. Even though, the results are enlightening and help to understand the impact of a forced outage of the HVDC transmission in interconnected power systems. Even though the lack of voltage support is not expected in a practical application, it still need to be accounted for in the formulation. The voltage support is usually related with the presence of shunt capacitors/filters, that also impacts on the equivalent reactance of the system. In the proposed methodology, the equivalent reactance of the system is used to build the approximated power-angle curve and compute the generation-rejection. Therefore, it is not prudent to expect that the generation-rejection computed with the two-area system is adequate for a realistic system, once this generation-rejection was computed considering a different equivalent reactance. A more suitable strategy is to include those shunt capacitors/filters in the two-area reduced system and in the formulation, as presented

in the next chapter.

Lastly, the proposed methodology for approximating the power-angle curve was compared with a simpler approach, based on the modeling of the power-angle dynamics as a constant active power factor added to a traditional SMIB system curve. The resulting generator-rejection computed with both methods confirms that the new formulation proposed in this thesis is more precise in modeling the transient response of two-area systems with parallel AC and DC transmission.

9 Extending the methodology to include shunt capacitor banks/filters and loads

In Chapter 7, a methodology for the transient stability analysis in cases of forced outage of the HVDC transmission of two-machine systems with parallel AC and DC transmission was presented. The transient stability method is based in the EAC criterion and the formulation is based in the premise that the transient dynamic behavior of the HVDC links can be modeled by equivalent current sources. Also, an algorithm for a generator-rejection control was proposed, based on the same formulation. Some interesting preliminary results were obtained, as presented in Chapter 8. These results can be seen as a proof of concept, and helped understanding the phenomena and the limitations of the proposed two-area test system.

In the present chapter, modifications in the formulation as well as in the power system configuration are proposed to extend the methodology to a more complex scenario and overcome the limitations discovered in Chapter 8. The two-area test system is modified to include shunt capacitor banks/filters representing the filters of the HVDC system converters. Also a load is introduced to the generation area, so a better ratio between total generated power and transmitted power can be achieved. To cope with this new configuration, an extension of the formulation is proposed to include the influence of shunt capacitor banks/filters and complex loads in the power-angle curve of parallel AC and DC transmission systems.

Since it was already shown in Chapter 8 that the proposed methodology, based on current sources, is more precise to model the transient response of the system than the traditional method, based on adding a constant power factor to the power-angle curve of SMIB system, such comparison is omitted in the present chapter.

9.1 Two Machine system with shunt capacitor banks/filters and load

The proposed methodology for the transient stability assurance for systems with parallel AC and DC transmission is based on the premise that the HVDC system is capable of maintaining a constant current during the first swing of oscillation after the fault (time window of the transient stability analysis). As it was shown in the first results obtained with the two-area system, this capability is strongly dependent on the voltage support at the converter buses. The rectifier and inverter buses of an HVDC system are

usually equipped with filters in the form of shunt capacitor banks/filters (KUNDUR, 1994). Those bank of capacitors/filters have a direct impact on the methodology as they change the amount of reactive power generated at the equivalent generators. And, therefore, change the impact of the generator-rejection over the reactive power flow. Also, the filters have an impact over the voltage dynamics of the system, that influences on the converter dynamics, as presented in Section 8.2.3.1. So, it is important to include the shunt filters in the proposed methodology.

One of the goals of this work is to better understand the transient dynamics of systems with parallel AC and DC transmission such as the HVDC systems of the *Belo Monte's* power plant in the Brazilian power system, as mentioned in Section 6.2. In this Brazilian system, there is a large amount of power being generated in the North system (*Belo Monte's power plant* together with other power plants of the North system) and a great portion of this energy is being transmitted to the Southeastern system trough parallel AC and DC lines. However, some of the energy generated in the North system is also consumed by the North or Northeastern systems. Therefore, in order to better understand the phenomenon it is important to consider the impact of loads in the proposed two-area power system, specially at Area 1 (generation area). By including a load in Area 1, the total power generated by the equivalent generator 1 needs to be increased, thus the number of GUs at this generator group is also increased. Therefore, the total inertia of the area is increased. Also the proportion between the HVDC power flow and the total electric power output of the equivalent generator 1 is reduced. So, the proportion of electric power reduced after a disconnection of a pole or bipole is more realistic.

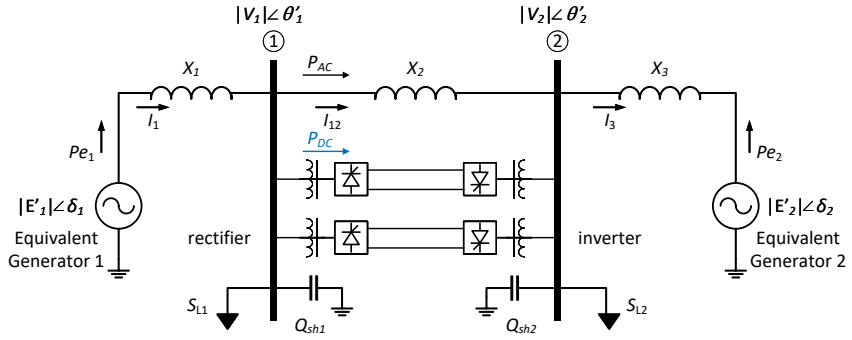

Figure 9.1 – Two machine system with parallel AC and DC transmission, shunt capacitor banks/filters and loads.

Consider the two machine system with parallel AC and DC transmission, shunt capacitor banks/filters, and loads illustrated in Figure 9.1. Let $S_{L1} = P_{L1} + jQ_{L1}$ and $S_{L2} = P_{L2} + jQ_{L2}$ be the complex loads and Q_{sh1} and Q_{sh2} be the capacitive reactive shunt power at the rectifier and inverter buses, respectively. Both shunt capacitor banks/filters and the loads are modeled as a single constant impedance load, as follows

$$\dot{Z}_{sh1} = \dot{Z}_{L1} + \dot{X}_{sh1} \quad \text{and} \quad \dot{Z}_{sh2} = \dot{Z}_{L2} + \dot{X}_{sh2}, \tag{9.1}$$

where $\dot{X}_{sh1}$ and $\dot{X}_{sh2}$ are the complex reactances of the capacitor banks/filters and $\dot{Z}_{L1}$ and $\dot{Z}_{L2}$ are the complex impedances of the loads, defined as[1]

$$\begin{aligned} \dot{X}_{sh1} &= -j\frac{|V_{1,0}|^2}{Q_{\text{sh1}}}, \quad \dot{X}_{sh2} = -\frac{|V_{2,0}|^2}{Q_{\text{sh2}}}, \\ \dot{Z}_{L1} &= \frac{|V_{1,0}|^2}{S^*_{L1}}, \qquad \dot{Z}_{L2} = \frac{|V_{2,0}|^2}{S^*_{L2}}. \end{aligned} \tag{9.2}$$

Each side of the HVDC system is replaced by an equivalent current source using Equation (7.1), then equations (7.3) to (7.6) are used to build an equivalent SMIB system. The diagram of the system with the current sources and equivalent shunt impedances is presented in Figure 9.2a and the equivalent SMIB system, after performing a $\Delta \rightarrow Y$ transformation, is present in Figure 9.2b, where $\delta_r = \delta_1 - \delta_2$ is the relative angle between the two machines[2],

$$\dot{Z}_a = \frac{\dot{Z}_{sh1}\dot{X}_2}{\dot{Z}_{sh1} + \dot{Z}_{sh2} + \dot{X}_2}, \quad \dot{Z}_b = \frac{\dot{Z}_{sh2}\dot{X}_2}{\dot{Z}_{sh1} + \dot{Z}_{sh2} + \dot{X}_2}, \quad \dot{Z}_c = \frac{\dot{Z}_{sh1}\dot{Z}_{sh2}}{\dot{Z}_{sh1} + \dot{Z}_{sh2} + \dot{X}_2}, \tag{9.3}$$

and $\dot{X}_2 = +jX_2$. Note that the system is no longer purely reactive, this is due to the presence of the loads. Since they are complex loads with active and reactive components, the load impedances are complex numbers with real and imaginary parts. Consequently, the **Assumption 1** is no longer valid in this scenario.

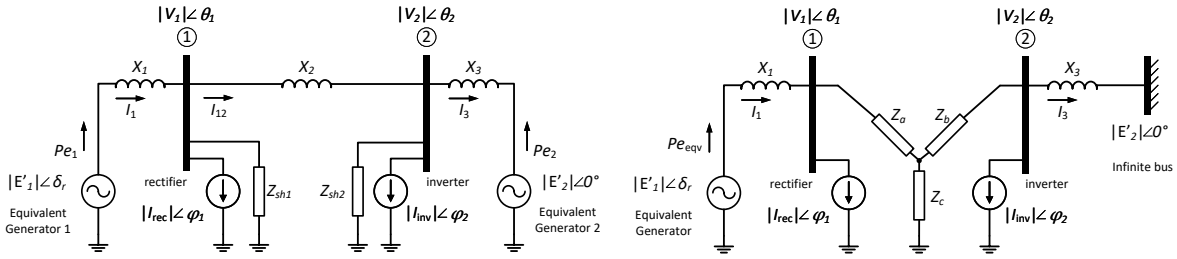

(a) Two machine system with shunt capacitor banks/filters and loads.

(b) SMIB system with shunt capacitor banks/filters and loads.

Figure 9.2 – Equivalent system using current sources to model the HVDC system, with shunt capacitor banks/filters and loads.

Performing a circuit analysis on the system of Figure 9.2a, one can prove[3] that the apparent electric power output of the generators 1 and 2 are

$$\begin{aligned} Se_{1,t} = &|Y_{A1}||E'_1|^2\angle(-\gamma_{A1}) - |Y_{B1}||E'_1||E'_2|\angle\left(-\gamma_{B1} + \delta_{1,t} - \delta_{2,t}\right) \\ &+ |Y_{C1}||E'_1||I_{\text{rec},t}|\angle\left(-\gamma_{C1} + \delta_{1,t} - \theta_{1,t} + \varphi_{\text{rec},t}\right) \\ &+ |Y_{D1}||E'_1||I_{\text{inv},t}|\angle\left(-\gamma_{D1} + \delta_{1,t} - \theta_{2,t} + \varphi_{\text{inv},t}\right), \end{aligned} \tag{9.4}$$

[1] As the capacitor banks/filters and loads are modeled as constant impedance loads, the value of the impedance is defined using the initial condition of the bus voltages.

[2] The angles θ_1 and θ_2 in Figure 9.2 corresponds to the voltage phasor angles in respect to the new angular reference, the rotor angle of the equivalent generator 2. In Figure 9.1 an angular reference is not specified, therefore, $\theta_1 \neq \theta'_1$ and $\theta_2 \neq \theta'_2$.

[3] This deduction is presented in the Appendix E.

and

$$\begin{aligned} Se_{2,t} = &|Y_{A2}||E_2'|^2\angle(-\gamma_{A2}) - |Y_{B2}||E_1'||E_2'|\angle\left(-\gamma_{B2}+\delta_{2,t}-\delta_{1,t}\right) \\ &+ |Y_{C2}||E_2'||I_{\text{inv}}|\angle\left(-\gamma_{C1}+\delta_{2,t}-\theta_{2,t}+\varphi_{\text{inv},t}\right) \\ &+ |Y_{D2}||E_2'||I_{\text{rec}}|\angle\left(-\gamma_{D2}+\delta_{2,t}-\theta_{1,t}+\varphi_{\text{rec},t}\right), \end{aligned} \tag{9.5}$$

where

$$\begin{aligned} \dot{Y}_{A1} &= |Y_{A1}|\angle\gamma_{A1} = \frac{\dot{Z}_b+\dot{Z}_c+\dot{X}_3}{(\dot{Z}_a+\dot{X}_1)(\dot{Z}_b+\dot{Z}_c+\dot{X}_3)+\dot{Z}_c(\dot{Z}_b+\dot{X}_3)}, \\ \dot{Y}_{B1} &= |Y_{B1}|\angle\gamma_{B1} = \frac{\dot{Z}_c}{(\dot{Z}_a+\dot{X}_1)(\dot{Z}_b+\dot{Z}_c+\dot{X}_3)+\dot{Z}_c(\dot{Z}_b+\dot{X}_3)}, \\ \dot{Y}_{C1} &= |Y_{C1}|\angle\gamma_{C1} = \frac{\dot{Z}_a(\dot{Z}_b+\dot{Z}_c+\dot{X}_3)+\dot{Z}_c(\dot{Z}_b+\dot{X}_3)}{(\dot{Z}_a+\dot{X}_1)(\dot{Z}_b+\dot{Z}_c+\dot{X}_3)+\dot{Z}_c(\dot{Z}_b+\dot{X}_3)}, \\ \dot{Y}_{D1} &= |Y_{D1}|\angle\gamma_{D1} = \frac{\dot{Z}_c\dot{X}_3}{(\dot{Z}_a+\dot{X}_1)(\dot{Z}_b+\dot{Z}_c+\dot{X}_3)+\dot{Z}_c(\dot{Z}_b+\dot{X}_3)}, \end{aligned} \tag{9.6}$$

and

$$\begin{aligned} \dot{Y}_{A2} &= |Y_{A2}|\angle\gamma_{A2} = \frac{\dot{Z}_a+\dot{Z}_c+\dot{X}_1}{(\dot{Z}_a+\dot{X}_1)(\dot{Z}_b+\dot{Z}_c+\dot{X}_3)+\dot{Z}_c(\dot{Z}_b+\dot{X}_3)}, \\ \dot{Y}_{B2} &= |Y_{B2}|\angle\gamma_{B2} = \frac{\dot{Z}_c}{(\dot{Z}_a+\dot{X}_1)(\dot{Z}_b+\dot{Z}_c+\dot{X}_3)+\dot{Z}_c(\dot{Z}_b+\dot{X}_3)} = \dot{Y}_{B1}, \\ \dot{Y}_{C2} &= |Y_{C2}|\angle\gamma_{C2} = \frac{\dot{Z}_b(\dot{Z}_a+\dot{Z}_c+\dot{X}_1)+\dot{Z}_c(\dot{Z}_a+\dot{X}_1)}{(\dot{Z}_a+\dot{X}_1)(\dot{Z}_b+\dot{Z}_c+\dot{X}_3)+\dot{Z}_c(\dot{Z}_b+\dot{X}_3)}, \\ \dot{Y}_{D2} &= |Y_{D2}|\angle\gamma_{D2} = \frac{\dot{Z}_c\dot{X}_1}{(\dot{Z}_a+\dot{X}_1)(\dot{Z}_b+\dot{Z}_c+\dot{X}_3)+\dot{Z}_c(\dot{Z}_b+\dot{X}_3)}. \end{aligned} \tag{9.7}$$

Separating the real component of (9.4) and (9.5) and assuming that the rotor angle of the equivalent generator 2 is the angular reference[4] of the system, that is $\delta_{2,t} = 0°$ and $\delta_{r,t} = \delta_{1,t} - 0$, the following expressions for the active power output of the generators 1 and 2 are obtained

$$\begin{aligned} Pe_{1,t} = &P_{10} + P_{11}\cos\left(\delta_{r,t}-\gamma_{B1}\right) + P_{12}|I_{\text{rec},t}|\cos\left(\delta_{1,t}-\theta_{1,t}+\varphi_{\text{rec},t}-\gamma_{C1}\right) \\ &+ P_{13}|I_{\text{inv},t}|\cos\left(\delta_{1,t}-\theta_{2,t}+\varphi_{\text{inv},t}-\gamma_{D1}\right), \end{aligned} \tag{9.8}$$

where

$$\begin{aligned} P_{10} &= |Y_{A1}||E_1'|^2\cos(\gamma_{A1}), \quad P_{11} = -|Y_{B1}||E_1'||E_2'|, \\ P_{12} &= |Y_{C1}||E_1'|, \qquad\qquad P_{13} = |Y_{D1}||E_1'|. \end{aligned} \tag{9.9}$$

and

$$\begin{aligned} Pe_{2,t} = &P_{20} + P_{21}\cos\left(-\delta_{1,t}-\gamma_{B2}\right) + P_{22}|I_{\text{inv},t}|\cos\left(-\theta_{2,t}+\varphi_{\text{inv},t}-\gamma_{C1}\right) \\ &+ P_{23}|I_{\text{rec},t}|\cos\left(-\theta_{1,t}+\varphi_{\text{rec},t}-\gamma_{D2}\right), \end{aligned} \tag{9.10}$$

where

$$\begin{aligned} P_{20} &= |Y_{A2}||E_2'|^2\cos(\gamma_{A2}), \quad P_{21} = -|Y_{B2}||E_1'||E_2'|, \\ P_{22} &= |Y_{C2}||E_2'|, \qquad\qquad P_{23} = |Y_{D2}||E_2'|. \end{aligned} \tag{9.11}$$

[4] The rotor angle of the equivalent generator 2 is the angular reference for all angle values, including the bus voltages.

Then, the equivalent electric power output of the system illustrated in Figure 9.2a is

$$Pe_{eqv,t} = \frac{M_2 Pe_{1,t} - M_1 Pe_{2,t}}{M_1 + M_2}, \tag{9.12}$$

where M_1 and M_2 are the inertia constants of the equivalent generators 1 and 2, as presented in Section 8.2, and $Pe_{1,t}$ and $Pe_{2,t}$ are defined by equations (9.8) and (9.10).

9.1.1 Approximated power-angle equation

Although Assumption 1 can not be applied to the system with loads, the remaining assumptions presented in Section 7.2 are still needed to simplify equations (9.8) and (9.10), replacing the time-varying parameter by initial condition ones. Although, Assumption 4 is not used either. Instead, as it is necessary to compute the equation for each generator, Assumption 5 is applied twice, that is, $\delta_{1,t} - \theta_{1,t} \approx \delta_{1,0} - \theta_{1,0}$ and $\delta_{2,t} - \theta_{2,t} \approx \delta_{2,0} - \theta_{2,0}$. The resulting equations for approximating the electric power output of equivalent generators 1 and 2 are

$$\bar{P}e_1(\delta_{r,t}) = \mathsf{P}_{10} + \mathsf{P}_{11}\cos\left(\delta_{r,t} - \gamma_{B1}\right) + \mathsf{P}_{12} + \mathsf{P}_{13}\cos\left(\delta_{r,t} + \beta_1\right), \tag{9.13}$$

where

$$\begin{aligned} \mathsf{P}_{10} &= |Y_{A1}||E_1'|^2\cos(\gamma_{A1}), & \mathsf{P}_{11} &= -|Y_{B1}||E_1'||E_2'|, \\ \mathsf{P}_{12} &= |Y_{C1}||E_1'||I_{\text{rec}}|\cos\left(\delta_{r,0} - \theta_{1,0} + \varphi_{\text{rec},0} - \gamma_{C1}\right), & \mathsf{P}_{13} &= -|Y_{D1}||E_1'||I_{\text{rec},0}|, \\ \beta_1 &= -\theta_{2,0} - \varphi_{\text{rec},0} - \gamma_{D1}, \end{aligned} \tag{9.14}$$

and

$$\bar{P}e_2(\delta_{r,t}) = \mathsf{P}_{20} + \mathsf{P}_{21}\cos\left(-\delta_{r,t} - \gamma_{B2}\right) + \mathsf{P}_{22} + \mathsf{P}_{23}\cos\left(-\delta_{r,t} + \beta_2\right), \tag{9.15}$$

where

$$\begin{aligned} \mathsf{P}_{20} &= |Y_{A2}||E_2'|^2\cos(\gamma_{A2}), & \mathsf{P}_{21} &= -|Y_{B2}||E_1'||E_2'|, \\ \mathsf{P}_{22} &= -|Y_{C2}||E_2'||I_{\text{rec}}|\cos\left(-\theta_{2,0} - \varphi_{\text{rec},0} - \gamma_{C2}\right), & \mathsf{P}_{23} &= -|Y_{D2}||E_2'||I_{\text{rec},0}|, \\ \beta_2 &= \delta_{r,0} - \theta_{1,0} + \varphi_{\text{rec},0} - \gamma_{D2}. \end{aligned} \tag{9.16}$$

Then, the approximated equation for the equivalent electrical power output (or the approximated power-angle equation) is

$$\begin{aligned} \bar{P}e_{eqv}(\delta_{r,t}) =& \frac{H_2\bar{P}e_1(\delta_{r,t}) - H_1\bar{P}e_2(\delta_{r,t})}{H_1 + H_2}, \\ \bar{P}e_{eqv}(\delta_{r,t}) =& \frac{1}{H_1 + H_2}\left(H_2\left(\mathsf{P}_{10} + \mathsf{P}_{11}\cos\left(\delta_{r,t} - \gamma_{B1}\right) + \mathsf{P}_{12} + \mathsf{P}_{13}\cos\left(\delta_{r,t} + \beta_1\right)\right)\right) + \\ & \frac{1}{H_1 + H_2}\left(-H_1\left(\mathsf{P}_{20} + \mathsf{P}_{21}\cos\left(-\delta_{r,t} - \gamma_{B2}\right) + \mathsf{P}_{22} + \mathsf{P}_{23}\cos\left(-\delta_{r,t} + \beta_2\right)\right)\right). \end{aligned} \tag{9.17}$$

To account for the change in the total reactance of the system caused by the disconnection of the GUs, a change in variable is proposed and two approximated

power-angle equations are defined. One for the **b.c.a.** (before control action) time interval and one for the **a.c.a.** (after control action) stage, as described in Section 7.4. Rearranging Equation (9.17), one can define those approximated power-angle equations as follows.

The **b.c.a.** approximated power-angle equation is

$$\begin{aligned}\bar{P}e'_{eqv}(\delta_{r,t}) = C' + N'_1\cos\left(\delta_{r,t}-\gamma'_{B1}\right) + N'_2\cos\left(\delta_{r,t}+\beta'_1\right) + N'_3\cos\left(\delta_{r,t}+\gamma'_{B2}\right) \\ + N'_4\cos\left(\delta_{r,t}-\beta'_2\right),\end{aligned} \tag{9.18}$$

where

$$\begin{aligned}C' &= \frac{H_2(\mathsf{P}'_{10}+\mathsf{P}'_{12}) - H'_1(\mathsf{P}'_{20}+\mathsf{P}'_{22})}{H'_1+H_2}, \\ N'_1 &= \frac{H_2\mathsf{P}'_{11}}{H'_1+H_2},\ N'_2 = \frac{H_2\mathsf{P}'_{13}}{H'_1+H_2},\ N'_3 = -\frac{H'_1\mathsf{P}'_{21}}{H'_1+H_2},\ N'_4 = -\frac{H'_1\mathsf{P}'_{23}}{H'_1+H_2},\end{aligned} \tag{9.19}$$

and P'_{10}, P'_{11}, P'_{12}, P'_{13}, P'_{20}, P'_{21}, P'_{22}, P'_{23}, β'_1, and β'_2 are the weights computed with equations (9.14) and (9.16) using the initial condition value of the reactance between the generator and the rectifier bus ($X_{1,0}$). And H'_1 is the inertia constant of the equivalent generator 1 at the initial condition, before disconnecting any GU.

The **a.c.a.** approximated power-angle equation is

$$\begin{aligned}\bar{P}e''_{eqv}(\delta_{r,t}) = C'' + N''_1\cos\left(\delta_{r,t}-\gamma''_{B1}\right) + N''_2\cos\left(\delta_{r,t}+\beta''_1\right) + N''_3\cos\left(\delta_{r,t}+\gamma''_{B2}\right) \\ + N''_4\cos\left(\delta_{r,t}-\beta''_2\right),\end{aligned} \tag{9.20}$$

where

$$\begin{aligned}C'' &= \frac{H_2(\mathsf{P}''_{10}+\mathsf{P}''_{12}) - H''_1(\mathsf{P}''_{20}+\mathsf{P}''_{22})}{H''_1+H_2}, \\ N''_1 &= \frac{H_2\mathsf{P}''_{11}}{H''_1+H_2},\ N''_2 = \frac{H_2\mathsf{P}''_{13}}{H''_1+H_2},\ N''_3 = -\frac{H''_1\mathsf{P}''_{21}}{H''_1+H_2},\ N''_4 = -\frac{H''_1\mathsf{P}''_{23}}{H''_1+H_2}.\end{aligned} \tag{9.21}$$

and P''_{10}, P''_{11}, P''_{12}, P''_{13}, P''_{20}, P''_{21}, P''_{22}, P''_{23}, β''_1, and β''_2 are the weights defined with equations (9.14) and (9.16), but using the change of variables (7.17). And H''_1 is inertia constant of the equivalent generator 1 after the disconnection of the GUs, defined using the change of variables (7.18). That is, the parameters of the Equation (9.20) are defined as functions of a variable $x \in \mathrm{R}$, that will be later used to compute N_{Tr} (the number of GUs to be rejected), as described in Section 7.4.

Applying the EAC to the curves of Figure 7.4, but using $\bar{P}e'_{eqv}(\delta_{r,t})$ and $\bar{P}e''_{eqv}(\delta_{r,t})$, one has that

$$\begin{aligned}\int_{\delta_0}^{\delta_1}\left(Pm_{eqv,0} - \bar{P}e'_{eqv}(\delta)\right)d\delta + \int_{\delta_1}^{\delta_{ep}^{sta}}\left(Pm_{eqv,1} - \bar{P}e''_{eqv}(\delta)\right)d\delta \\ = \int_{\delta_{ep}^{sta}}^{\delta_{ep}^{uns}}\left(\bar{P}e''_{eqv}(\delta) - Pm_{eqv,1}\right)d\delta,\end{aligned} \tag{9.22}$$

where $Pm_{eqv,0}$ is the initial value of the equivalent mechanical power input and $Pm_{eqv,1}$ is the equivalent mechanical power input for which the acceleration and deceleration areas are equal. Solving the integrals of Equation (9.22), the resulting simplified expression is

$$\begin{aligned} &Pm_{eqv,0}(\delta_{r,1}-\delta_{r,0})+Pm_{eqv,1}(\delta_{ep}^{uns}-\delta_{r,1})-C'(\delta_{r,1}-\delta_{r,0})-C''(\delta_{ep}^{uns}-\delta_{r,1}) \\ &-N_1'(\sin(\delta_{r,1}-\gamma_{B1}')-\sin(\delta_{r,0}-\gamma_{B1}'))-N_2'(\sin(\delta_{r,1}+\beta_1')-\sin(\delta_{r,0}+\beta_1')) \\ &-N_3'(\sin(\delta_{r,1}+\gamma_{B2}')-\sin(\delta_{r,0}+\gamma_{B2}'))-N_4'(\sin(\delta_{r,1}-\beta_2')-\sin(\delta_{r,0}-\beta_2')) \\ &-N_1''(\sin(\delta_{ep}^{uns}-\gamma_{B1}'')-\sin(\delta_{r,1}-\gamma_{B1}''))-N_2''(\sin(\delta_{ep}^{uns}+\beta_1'')-\sin(\delta_{r,1}+\beta_1'')) \\ &-N_3''(\sin(\delta_{ep}^{uns}+\gamma_{B2}'')-\sin(\delta_{r,1}+\gamma_{B2}''))-N_4''(\sin(\delta_{ep}^{uns}-\beta_2'')-\sin(\delta_{r,1}-\beta_2''))=0. \end{aligned} \tag{9.23}$$

The angle $\delta_{ep}^{uns}=\pi-\delta_{ep2}$ is the unstable equilibrium point of the curve $\bar{P}e_{eqv}''(\delta_{r,t})$ defined by Equation (9.20), and δ_{ep2} is defined as follows[5]

$$\delta_{ep2}=\sin^{-1}\left(\frac{-\mathsf{AC}+\mathsf{B}\sqrt{\mathsf{A}^2+\mathsf{B}^2-\mathsf{C}^2}}{\mathsf{A}^2+\mathsf{B}^2}\right). \tag{9.24}$$

where

$$\begin{aligned} \mathsf{A}&=N_1''\sin(\gamma_{B1}'')-N_2''\sin(\beta_1'')-N_3''\sin(\gamma_{B2}'')+N_4''\sin(\beta_2'') \\ \mathsf{B}&=N_1''\cos(\gamma_{B1}'')+N_2''\cos(\beta_1'')+N_3''\cos(\gamma_{B2}'')+N_4''\cos(\beta_2'') \\ \mathsf{C}&=C''-Pm_{eqv,1}. \end{aligned} \tag{9.25}$$

9.1.2 Algorithm for generator-rejection control with time delay, considering shunt capacitors and loads

The proposed method to compute the generator-rejection control in order to assure the transient stability of a two-machine system with parallel AC and DC transmission, with shunt capacitors/filters, loads, and considering a fixed time delay, is summarized as follows.

Algorithm 3. ***Generator-rejection control with time delay, for two area systems with shunt capacitors and loads:*** *Number of GUs to be disconnected to maintain stability after a HVDC transmission blocking, considering the delay between fault and control action*

Step 1 Define the values N_{GU1}, $X_{1,0}$, X_2, X_3, $H_{1,0}$, H_2, $Pm_{1,0}$, Pm_2, $\theta_{1,0}$, $\theta_{2,0}$, $\delta_{r,0}$, $|V_{1,0}|$, $|E_1'|$ and $|E_2'|$ using the initial condition parameters (pre-fault) of the system.

Step 2 Define $S_{\text{rec},0}$ as the total remaining apparent power drained at the rectifier side after the HVDC transmission blocking, Equation (7.2).

Step 3 Define $|I_{\text{rec},0}|$ with Equation (7.10), for the remaining HVDC transmission after the fault.

[5] The deduction of the equation for δ_{ep2} is presented in Appendix E.1.

Step 4 Using the value $X_{1,0}$, build the approximated power-angle equation $\bar{P}e'_{eqv}(\delta_{r,t})$ for the **b.c.a.** scenario, using (9.18).

Step 5 Compute the estimated relative rotor angle $\delta_{r,1}$ by integrating Equation (7.3), for the expected time-delay Δt, using $Pm_{eqv,t} = Pm_{eqv,0}$ and $Pe_{eqv,t} = \bar{P}e'_{eqv}(\delta_{r,t})$.

Step 6 Using the change of variables (7.17) and (7.18), define the weights P''_1, P''_2 and P''_3 for **a.c.a.** approximated power-angle equation $\bar{P}e''_{eqv}(\delta_{r,t})$, using Equation (9.21).

Step 7 Define $Pm_1(x)$ and $Pm_{eqv,1}(x)$ with the change of variables (7.19) and (7.20), and define the angle δ^2_{ep} using Equation (9.24).

Step 8 Solve Equation (9.23) numerically, for $x \in \mathbb{R}$.

Step 9 Compute the number of GUs to be rejected at the generator group 1 as $N_{Tr} = \min n \in \mathbb{N} \mid n \geq x$.

9.2 Results

This section presents the results obtained with the proposed algorithm for generator-rejection control and the two-machine test system with parallel AC and DC transmission, considering shunt capacitor banks/filters and loads.

9.2.1 Test System

The test system used in this section is the same two-machine system presented in Section 8.2.1, but with the addition of a shunt capacitor bank/filter at each converter bus and a load at the rectifier bus. The diagram of the resulting system is presented in Figure 9.3. The line reactance of the AC equivalent line is $X_2 = 4\%$ (100 MVA

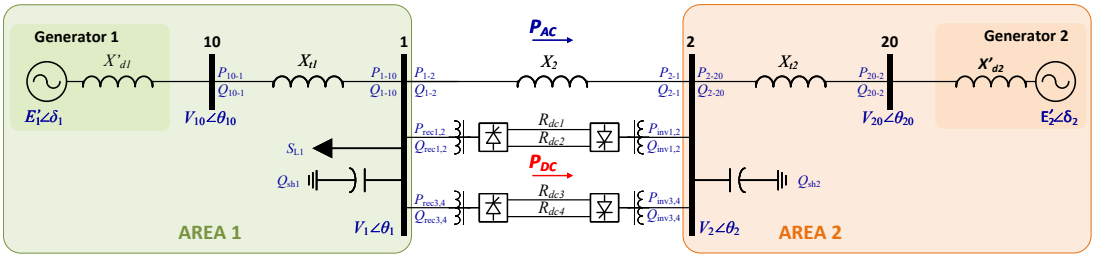

Figure 9.3 – Two-machine system with parallel AC and DC transmission, with shunt capacitor bank/filters and load.

power base) and the rest of the reactances is presented in Table 9.1, together with the parameters of the equivalent generators. The HVDC system is built using the Model 01 of the software ANATEM (CEPEL; ELETROBRAS, 2020a), with 5 Ω line resistances ($R_{dc1} = R_{dc2} = R_{dc3} = R_{dc4} = 5\ \Omega$), and it is configured to operate at current control mode.

The parameters of the HVDC converters and control model are presented in Apendix G. Five operating conditions are considered where the base case is the operating point 3 and the remaining cases were built by either reducing the DC transmission power or the load at Area 1. The number of GUs at the equivalent generator 1 is different at each operating point, so the dispatch of each GU is approximated equal for all cases. At the base case, the power flow values are similar to a typical condition of the Brazilian power system, more specifically the operating condition of May of 2020, where the two HVDC bipoles of the *Belo Monte's* power plant were transmitting 8000 MW from the north region to the southeast region of Brazil, while 937 MW were being transmitted by the AC lines (ONS, 2020). The load at Area 1 is 18000 MW, at the base case, modeling the north and northeast regions of Brazil at that period. The history of demand curves of the SIN is available at ONS (2022b). The DC and AC active power flows at each operating point are described in Table 9.2, together with the values of the load and the shunt capacitors/filters. It is known that, at steady state condition, the reactive power consumed by the converters is approximately 50% of the active power transferred by the HVDC system (KUNDUR, 1994). Here, this value is adjusted so the magnitude of the voltage at the rectifier bus is 1.010 pu while the bus voltage at the inverters is 1.00 pu at all operating points. Then, the initial condition parameters are presented in Table 9.3. More details about the power flow condition of each operating point is presented in the Appendix F.3.

Table 9.1 – Equivalent generator parameters - Two-machine system, with shunt capacitor banks/filters and load.

	Operating Point	Number of GUs	X'_d/GU (%)*	H/GU (s)	Base (MVA)	X'_d (%)$^\diamond$	X_t (%)$^\diamond$
Eq. gen. 1	1	39	32.0	4.8	679	0.12084	0.08013
	2	42	32.0	4.8	679	0.11221	0.0744
	3	50	32.0	4.8	679	0.09426	0.0625
	4	42	32.0	4.8	679	0.11221	0.0744
	5	39	32.0	4.8	679	0.12084	0.08013
Eq. gen. 2	1-5	1	35.0	3.5	50000	0.07	0.03

*at the generator power base.
$^\diamond$for a 100 MVA power base.

Table 9.2 – AC and DC power flow, load and shunt condition at each operating point - Two-machine system, with shunt capacitors/filters and load.

Operating Point	P_{DC}(MW) Pole 1	Pole 2	Pole 3	Pole 4	P_{AC} (MW)	P_{L1} (MW)	Q_{sh1} (MVar)	Q_{sh2} (MVar)
1	500	500	500	500	1000	18000	690.2	750.2
2	1000	1000	1000	1000	1000	18000	1629.8	1728.2
3	2000	2000	2000	2000	1000	18000	4085.3	4222.8
4	2000	2000	2000	2000	1000	14000	4088.4	4222.8
5	2000	2000	2000	2000	1000	12000	4083.5	4222.8

Table 9.3 – Initial condition parameters - Two-machine system, with shunt capacitor banks/filters and load.

Operating Point	$\lvert E_1' \rvert$ (pu)	$\lvert E_2' \rvert$ (pu)	$\delta_{r,0}$ (°)*	$\lvert V_{1,0} \rvert$ (pu)	$\theta_{1,0}$ (°)*	$\lvert S_{\text{rec},0} \rvert$ (pu)	$\varphi_{\text{rec},0}$ (°)	Q_{sh1} (pu)	Q_{sh2} (pu)	P_{L1} (pu)
1	1.0969	1.00269	47.4449	1.00953	25.04	21.16	19.05	6.90	7.50	180
2	1.09987	1.00339	48.8781	1.01021	26.15	43.19	22.18	16.30	17.28	180
3	1.0967	1.00585	50.8611	1.00985	28.39	89.83	27.06	40.85	42.23	180
4	1.09985	1.00584	51.108	1.01023	28.38	89.83	27.06	40.88	42.23	140
5	1.09694	1.00586	50.8053	1.00951	28.40	89.83	27.06	40.83	42.23	120

*In reference to the rotor angle of the eq. gen 2.

9.2.2 Transient Stability analysis using the proposed power-angle curve

The effect of the forced outage of HVDC transmission over the transient stability of the two-machine test system is tested for two different amounts of power loss: the blocking of one pole and the blocking of one bipole. As no power is transferred to the remaining poles, the HVDC transmission is instantly reduced by 25% and 50%, respectively. As for the previous chapter, it is considered that the forced outage of HVDC transmission is caused by a short-circuit at the DC line, but the short-circuit itself is not simulated since its effect over the power-angle dynamics is the same of the blocking of a pole/bipole (zero DC power flow at the faulted line).

The dynamic response of the system is compared with the one estimated with the proposed Equation (9.17) and the results are presented in Figures 9.4a to 9.4e, for the five operating points considered. The initial condition parameters needed for Equation (9.17) are presented in the Table 9.3. The blue continuous line corresponds to the dynamic response obtained via nonlinear simulation, for the blocking of one pole (indicated by the "1P"). The green continuous line is the dynamic response for the blocking of the bipole (indicated by the "2P"). The brown continuous line indicates the equivalent mechanical power input of generators 1 and 2 and the yellow circle indicates the initial steady-state condition, before the pole/bipole blocking. The estimated power-angle curve, computed with Equation (9.17), is presented as a dash-dot red line, for the one pole

blocking case, and as a black dash-dot line for the bipole blocking. As expected, the power imbalance caused the equivalent generator 1 to accelerate in relation to the equivalent generator 2.

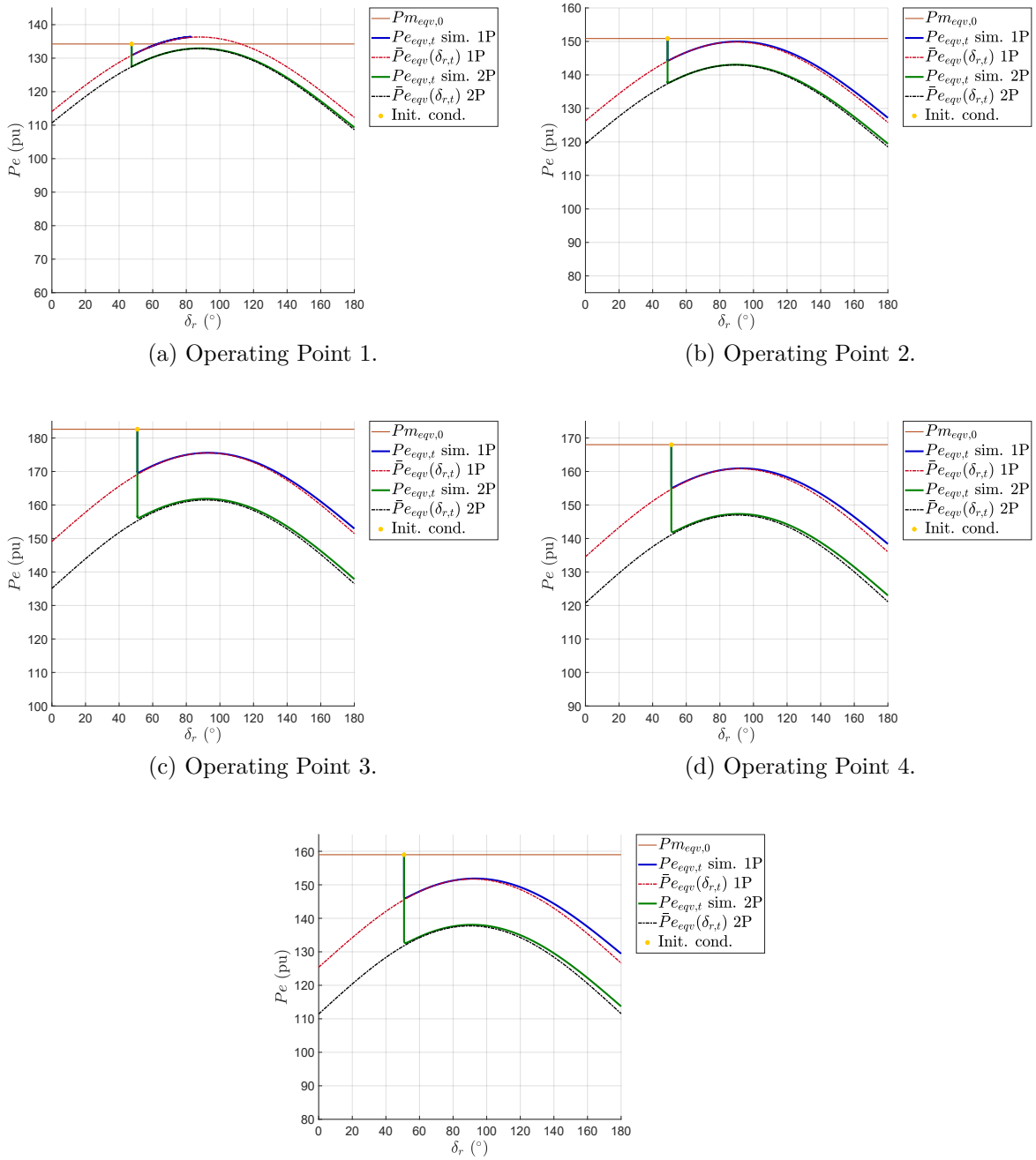

(a) Operating Point 1.

(b) Operating Point 2.

(c) Operating Point 3.

(d) Operating Point 4.

(e) Operating Point 5.

Figure 9.4 – Power-angle curve after the blocking of one (1P) or two (2P) HVDC poles. Two-machine system, with shunt capacitor banks/filters and load. No control action.

Note that the approximated power-angle curves, computed beforehand using initial condition parameters, are close to the actual dynamic response of the system. That is, it is possible to perform a transient stability analysis and use the EAC to predict

if the forced outage of the HVDC transmission will lead to the instability using those approximated curves.

9.2.3 Applying the generator-rejection control

The power-angle curves presented in Figures 9.4a to 9.4e confirms that the forced outage of the HVDC transmission simulated is sufficient to lead the system to instability, at almost all scenarios tested. Therefore, the generator-rejection algorithm, described in Section 9.1.2, is applied to determine the minimum number of GUs that should be disconnected in order to assure the transient stability of the system after the forced outage of the HVDC transmission. The Algorithm 3 was applied[6] using the equations (9.18) and (9.20) to model the equivalent electric power output before and after the control action, respectively. And a total time delay of 250 ms was considered between the fault and the control action (100 ms for the fault clearance plus 150 ms for the total control action). The results are summarized in Table 9.4.

Table 9.4 – Results of the generator-rejection control. Two-machine system with shunt capacitor banks/filters.

Poles Blocked	Operating Point	GUs disconnected	Stable	Minimum gen. rejection
1 Pole	1	0	**yes**	0
	2	2	**yes**	2
	3	5	**yes**	5
	4	4	**yes**	4
	5	4	**yes**	4
2 Poles	1	2	**yes**	2
	2	5	**yes**	5
	3	11	**yes**	11
	4	10	**yes**	10
	5	10	**yes**	10

The dynamic responses of the system (power-angle curve) at operating points 1 to 5, with the respective generator-rejection of Table 9.4, are presented in Figures 9.5a to 9.5e, for the blocking of one pole (1P) and in Figures 9.6a to 9.6e for the blocking of one bipole (2P). The dashed green line corresponds to the approximated power-angle curve before the control action ($\bar{P}e'_{eqv}(\delta)$) and the dashed red line is the approximated power-angle curve after the control action ($\bar{P}e''_{eqv}(\delta)$). The blue continuous line corresponds to the simulated response of the system. The brown continuous line indicates the equivalent mechanical power input before the generator-rejection. And the light blue continuous line

[6] The results (number of GUs to be disconnected) obtained disregarded the time delay are similar to the ones obtained with Algorithm 3 and are not presented in this document. The results considering the time delay were chosen to be presented since they represent a more realistic scenario.

indicate the equivalent mechanical input after the generator-rejection control. Lastly, the yellow circle indicates the initial condition of the system.

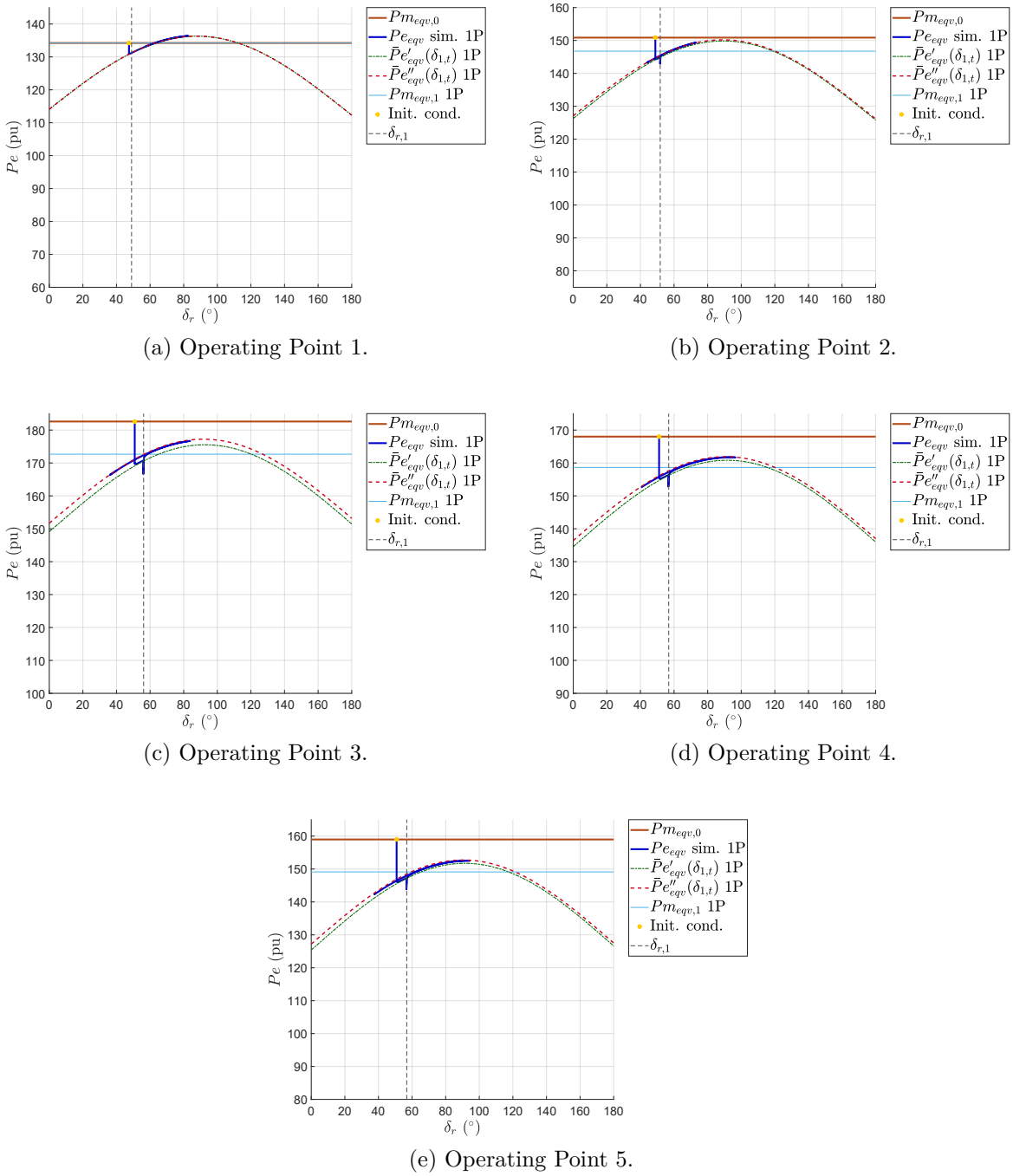

(a) Operating Point 1.

(b) Operating Point 2.

(c) Operating Point 3.

(d) Operating Point 4.

(e) Operating Point 5.

Figure 9.5 – Power-angle curve for the blocking of one HVDC pole followed by the generator-rejection (250 ms time delay). Two-machine system with shunt capacitor banks/filters and load.

The approximated power angle curves, before and after the control actions, proven to be good approximations of the actual dynamic response of the system at all cases simulated. At all ten cases, the number of GUs computed with the proposed algorithm is sufficient to assure the transient stability of the system after the forced outage of the

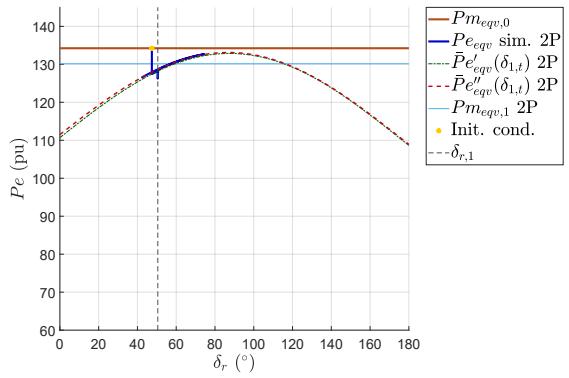

(a) Operating Point 1.

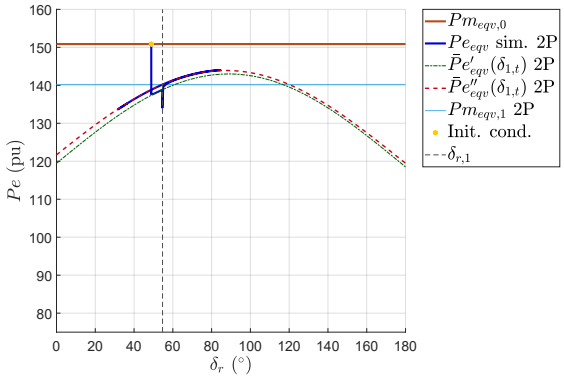

(b) Operating Point 2.

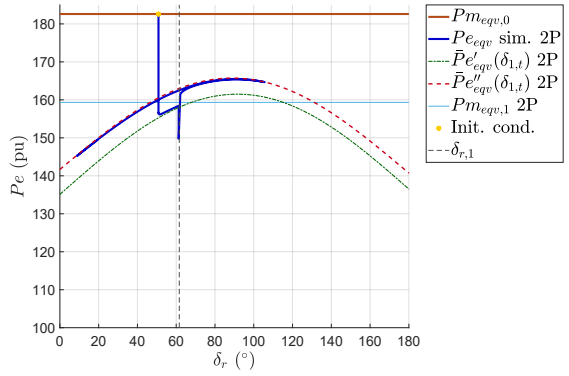

(c) Operating Point 3.

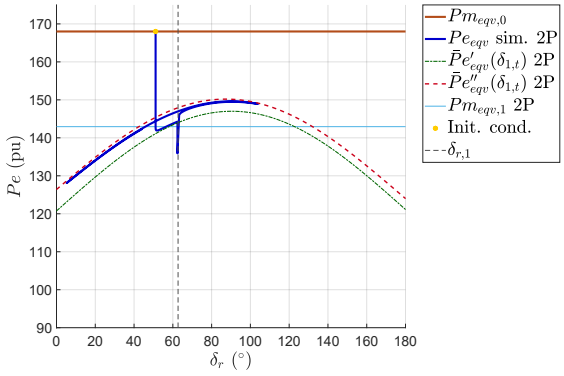

(d) Operating Point 4.

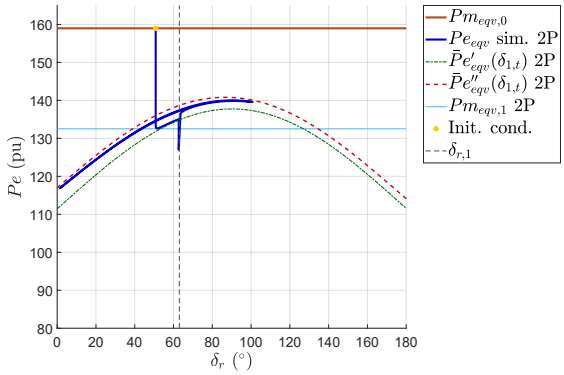

(e) Operating Point 5.

Figure 9.6 – Power-angle curve for the blocking of one HVDC bipole followed by the generator-rejection (250 ms time delay). Two-machine system with shunt capacitor banks/filters and load.

HVDC transmission. For the one pole blocking case at operating point 1, the number of GUs computed was zero. There is, the method correctly predicted that no control action was needed. At all cases, the number of GUs to be disconnected computed with the proposed algorithm is the minimum needed to assure the stability.

One may notice a different behavior when analyzing the dynamic response in Figures 9.5 and 9.6. In some cases, the equivalent electric power output of the system is

higher after the generator-rejection. This may seem counterintuitive, however it is due to the dynamic relation between the two equivalent generators of the system. Since the system network is not purely reactive, because of the loads, the active electric power output of the equivalent generators 1 and 2 are different. The responses presented in Figures 9.5 and 9.6 are the equivalent power of the system and, therefore, they are related with the inertia constant of the two equivalent generators, as defined in Equation (7.6). The disconnection of GUs at the equivalent generator 1 reduces its equivalent inertia. This change in the inertia constant may impact on the equivalent electric power output. So, even though the electric power output of the generator 1 is reduced, the equivalent electric power may be increased depending of the ratio between the inertia constants of the system. To illustrate this phenomenon, the electric power output of each equivalent generator is presented in Figure 9.7, for the bipole blocking case at the operating point 3 (base case), the approximated power-angle curves **b.c.a.** and **a.c.a.** of each equivalent generator are also presented. Note that the electric power output of generator 1 is reduced after the control action from approximately 250 pu to 240 pu, Figure 9.7a. The electric power output of generator 2 changes from approximately -56 pu to -53 pu, Figure 9.7b. However, while the inertia constant of the equivalent generator 2 stay constant at 1750 s, the inertia constant of the equivalent generator 1 is reduced from 1629.6 s to 1271.088 s. These values are computed in relation to a 100 MVA power base, as follows.

$$\begin{aligned} H_{1,0}^{\text{base}} &= \frac{N_{GU1} H_{1,GU} S_{\text{base}}^{G1}}{S_{\text{base}}} = \frac{50 \times 4.8 \times 679}{100} = 1629.6 \ s \\ H_{1,1}^{\text{base}} &= \frac{(N_{GU1} - N_{Tr}) H_{1,GU} S_{\text{base}}^{G1}}{S_{\text{base}}} = \frac{(50 - 11) \times 4.8 \times 679}{100} = 1271.088 \ s \\ H_{2}^{\text{base}} &= \frac{N_{GU2} H_{2,GU} S_{\text{base}}^{G2}}{S_{\text{base}}} = \frac{1 \times 3.5 \times 50000}{100} = 1750 \ s \end{aligned} \tag{9.26}$$

where N_{GU1} and N_{GU2} are the total number of GUs at the equivalent generator group 1 and 2, respectively. The value N_{Tr} is the number of GUs rejected at the equivalent generator 1, $H_{1,GU}$ is the inertia constant of each GU at the equivalent generator 1 at the 679 MVA power base, and $H_{2,GU}$ is the inertia constant of the GU of the equivalent generator 2 at the 50000 MVA power base. Then, the equivalent electric power output immediately before and immediately after the generator-rejection are

$$\begin{aligned} Pe_{eqv}^{\mathbf{b.c.a}} &= \frac{H_2^{\text{base}} Pe_1^{\mathbf{b.c.a}} - H_{1,0}^{\text{base}} Pe_2^{\mathbf{b.c.a}}}{H_{1,0}^{\text{base}} + H_2^{\text{base}}} = \frac{1750 \times 250 - 1629.6 \times (-56)}{1629.6 + 1750} = 156.46 \ pu, \\ Pe_{eqv}^{\mathbf{a.c.a}} &= \frac{H_2^{\text{base}} Pe_1^{\mathbf{a.c.a}} - H_{1,1}^{\text{base}} Pe_2^{\mathbf{a.c.a}}}{H_{1,1}^{\text{base}} + H_2^{\text{base}}} = \frac{1750 \times 240 - 1271.088 \times (-53)}{1271.088 + 1750} = 161.32 \ pu. \end{aligned} \tag{9.27}$$

Consequently, even though the electric power of each equivalent generator is reduced, the total equivalent electric power output is increased because the total inertia of the system is reduced.

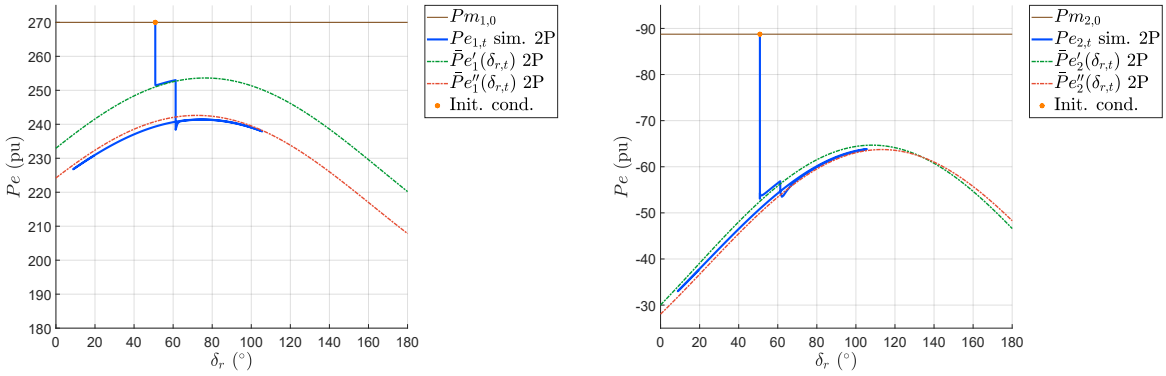

(a) Equivalent generator 1.

(b) Equivalent generator 2.

Figure 9.7 – Power-angle curves of each equivalent generator group of the two-machine system with shunt capacitor banks/filters and load, for the blocking of one HVDC bipole followed by the generator-rejection (250 ms time delay), at operating point 3.

9.3 Comments

In this section, an extension of the proposed methodology for the transient stability assurance for systems with parallel AC and DC transmission was presented, for cases where shunt capacitor banks/filters and loads are placed in the HVDC converter buses. The objective of including shunt capacitor banks/filters in the system is to provide the necessary voltage support to avoid reaching the limit operating conditions of the HVDC converters. The load, placed at the rectifier side of the system, have two purposes. First, to model a more realistic scenario, where the equivalent generators of Area 1 have to supply power to the HVDC system and still attend the local power consumption. Second, to reduce the ratio between the HVDC power transmission and the total AC power being generated, so the error introduced by the assumptions used to build the approximated power-angle equation is reduced. It was necessary to adapt the formulation so the proposed equation for the equivalent electric power output could cope with the presence of the shunt capacitor banks/filters and loads, both modeled as constant impedance loads.

The method was tested with the same two-machine test system investigated in Chapter 8, but with the addition of the shunt capacitor banks/filters and the load. The same two faults used with the initial two-machine test system were considered: the blocking of one pole and the blocking of one bipole, with no power transfer to the remaining poles. The comparison between the power-angle response built with the proposed equation and the simulated dynamic response of the system indicates that the influence of the shunt capacitor banks/filters and load in the transient dynamics was successfully modeled. It was possible to predict if the system was going to lose stability and the generator-rejection, computed with the proposed algorithm, was sufficient to assure the stability at all cases considered. The addition of the shunt capacitor banks/filters had a positive impact on

the voltage dynamics of the system, slowing the voltage drop so the system could pass the first swing of oscillation without exceeding the operating limits of the converters. The inclusion of the load had a significant impact on the formulation, since the simplifications related with a purely reactive network were not possible anymore. However, the results are very promising and, besides being more complex then in the previous cases, the proposed equation for the two-machine system with shunt capacitor banks/filters and loads proved to be adequate for the proposed transient stability assurance method.

Part III

Conclusions and final comments

10 Conclusions and final comments

10.1 Thesis Summary

The precise determination of the operating condition of modern power systems and the development of accurate dynamic models have become increasingly difficult tasks. The constant expansion of the systems, with distributed generation and IBS leads to high order and complex dynamic models. Also, the growing penetration of renewable sources increases the variability of the system and may cause the system to operate in conditions not considered during the modeling and control design stages. Therefore, power systems control and protection techniques must be constantly improved in order to maintain the desired performance and security of operation. The contributions of this thesis go in this direction, proposing new techniques to enhance the angular stability of power systems. The research was divided into two main branches, one focusing on the small-signal stability and other focusing on the transient stability of modern power system. Each branch of the research resulted in different contributions to the power systems angular stability field. The study of each topic was carried out in parallel during the research period of this thesis, however, each part of the research is presented separately in this document.

The first part of this work is named **data-driven control method for power system small-signal angular stability enhancement** and is dedicated to the development of a data-driven procedure to design power systems damping controllers using remotely measured signals as inputs. The strategy adopted is to adapt a well known offline data-driven control method for the proposed application. The method chosen is the VRFT, that is a one-shot data driven procedure formulated for the design of reference tracking controllers. The VRFT was chosen for its simple one-shot design characteristics and the lack of applications in the literature regarding the power system oscillation damping problem. The first contribution of this thesis is the adaptation of the VRFT formulation for the design of PSS-like controllers. Differently from the controllers of the reference tracking problem, PSSs are placed in the feedback path of the control loop and, therefore, a distinct formulation was necessary. The second contribution of this thesis regards the definition of reference models for the proposed application. The VRFT procedure is a model reference control method, where the controller is designed to reach a desired closed-loop performance based on a reference model. Considering the original VRFT application proposed in this thesis, the literature lacks of procedures for building such reference models. In this thesis, two simple solutions are proposed for building those models, taking into consideration the oscillation damping improvement without impacting the steady state response of the system, and using the same data measurements acquired for the control

design stage. The first method uses the predominant oscillation mode of the measured signal to build a second order transfer function, using classical concepts of control systems theory. The second one is based on a black-box identification method, where a transfer function is identified and then the damping performance criterion is introduced by means of a pole-placement restriction. Note that even though a dynamic model is estimated, no physical information of the system is used. The estimation consists of a curve-fitting procedure, where only the input/output relation between the measured signals is relevant.

The control structure mainly explored in this thesis consists of using a remote signal as input of an additional remote-input PSS (called rPSS) installed at the voltage loop control of a selected generator of the system. The remote signal used is the difference between the frequencies of two bus voltages of the system (usually available in WAMS, based on PMUs), selected according two the inter-area mode of interest. The proposed method is successfully applied to design damping controllers for two power system models that belong to a set of benchmark models for the analysis and control of small-signal oscillatory dynamics in power systems, the Brazilian 7-bus test system and the 39-Bus New-England Test System. The goal of the proposed methodology is to find a simple solution to improve the damping ratio of selected inter-area oscillation modes of power system. This is achieved for both test systems used, were the damping performance is successfully improved by including a SISO controller designed with the proposed data-driven strategy. Once these results were very promising, a complementary strategy was proposed. The VRFT is, by definition, an offline design technique. However, an online application is also presented in this thesis, where new measure data is used to re-tune the rPSS, simulating a real-time application. The re-tuned controller can re-establish the damping performance of the system after a change in operating condition.

The use of a remote measured signal to design a SISO rPSS for power systems, with a data-driven procedure, is the main result of Part I of the thesis (Chapter 4). But, a further discussion is proposed in Chapter 5, were interesting preliminary results are presented. The methodology is extended for the MIMO case and is applied to simultaneously re-tune the PSSs of the test systems, in a coordinate design strategy. With this different approach it is possible to improve the inter-area damping performance of the system without introducing new controllers or measured signals. The method is applied to simultaneously retune all four PSSs of the Brazilian 7-bus test system and two PSSs of the 39-Bus New-England Test System. The task of building the reference model for the MIMO case is significantly harder than for the SISO case, and the retuning of all PSSs of the system is a challenging task. The damping performance of the Brazilian 7-bus test system is improved, but the damping ratio of the inter-area mode stays bellow 5%. For the 39-Bus NETS, where only two PSSs are retuned, the result is much more promising, with a significant improvement of the damping performance.

The second part of this work is called **Transient stability assurance with a generator-rejection control for parallel AC and DC transmission systems** and is dedicated to improve the transient stability performance of power systems with parallel AC and DC transmission lines. The research was inspired by a practical challenge of the Brazilian power system, where an SPS is responsible for assuring the transient stability of the Brazilian system by rejecting generation at the north region (large generation center), in case of blocking of poles/bipoles of a critical HVDC system. The control logic behind this SPS is based on a decision table, previously defined. The construction of such tables is very time consuming as it depends on extensive simulation studies, with high order power system models at multiple operating conditions. The idea presented is to use a simple reduced model and analytical expressions to perform the transient stability analysis of the system and compute the ideal generator-rejection, before any forced outage of the HVDC transmission occurs (arming process of the SIPS). It is expected that the reduced model can be simple enough to be constantly updated using key measurements from the system. By doing so, the SPS can be constantly adjusted to the operating condition of the system. This strategy relies on the capability of the reduced model to capture the transient dynamic response of the system. Thus, the definition of such model is a critical step of the SPS. However, the focus of this thesis is not in the construction of such model. Instead, assuming that this model exists, the contributions of this part of the thesis are the analytical analysis of the reduced model, the conduction of simulations and related studies to better understand the phenomenon, a new approach to model the transient dynamics of two-area systems interconnected by AC and DC transmission lines, and the development of an algorithm for the generator-rejection control to assure the transient stability after a HVDC transmission blocking.

The proposed methodology consists of modeling the HVDC links as current sources and, by doing so, a new equation to model the dynamics of the electric power output of the equivalent generators is proposed. Based on the premise that DC current at LCC HVDC systems is approximately constant during the transient stability analysis time window, a series of approximations IS presented to simplify the proposed equation. The result is a fixed-parameters equation that depends only on the relative angle between the two generators of the system. Once this equation is built, it is possible to trace the power-angle curve of the system for different values of DC power flow and perform the transient stability analysis by means of the EAC. Another contribution of this thesis is the formalization of the proposed strategy in a form of an algorithm for the generator-rejection control, that takes into account the impact of the disconnection of the GUs into the transient dynamics to compute the control action.

The proposed method was first tested with an SMIB system and the results were very promising. The approximated power-angle curves computed with the proposed equation were close to the simulated responses. Also, the number of GUs to be rejected

computed with the proposed algorithm were the minimum necessary to assure the transient stability of the system. The next experiments were done with a two-machine system and the results revealed some limitations of the proposed method. It was possible to predict if the systems was going to lose stability with the proposed equation. However, the amount of generator-rejection computed with the proposed algorithm was not sufficient to assure the transient stability in all cases. This limited performance is related with the voltage dynamics of the reduced two-machine system. It was shown that the lack of voltage support caused the converters to reach their limits and, therefore, the constant current assumption was not valid anymore. However, reference simulations were presented to support the hypothesis that this lack of voltage support (in the intensity observed in the simulations with the reduced system) is not expected in a practical application.

The voltage support observed in the complete model of the Brazilian power system is related with the presence of shunt capacitors/filters. Those filters have an impact on the total reactance of the system, thus, also impact on the power-angle dynamics. In order to overcome the limitations discovered and obtain a more realistic scenario (sufficient voltage support), the methodology formulation was extended to include shunt capacitor banks/filters and loads. The results obtained with this extended methodology are the main results of this part of the thesis and are presented in Chapter 9. The two-area test system was adjusted to simulate a scenario closer to the Brazilian system condition and the results were positive. The inclusion of loads into the formulation increased complexity of the equations. However, the simulation results indicates that this was worth it. It was possible to evaluate the transient stability of the system e determine if it was going to lose stability or not, beforehand. Also, the amount of generator-rejection computed with the proposed algorithm was the minimum necessary, for all operating points considered.

10.2 Conclusions

The research contributions and knowledge acquired during the elaboration of this thesis can be summarized as follows.

Part I:

- The VRFT data-driven control design procedure was successfully adapted to an original application regarding the small-signal stability of power systems. The promising results obtained show that the adapted formulation of the VRFT procedure can be effectively applied to design power system damping controllers focusing on specific inter-area modes of oscillation. The proposed VRFT formulation combined with the adopted rPSS control structure, using remote measured bus-frequency signals, is well suited for inter-area oscillation damping problem. The proposed WADC, has shown to provide a significant improvement to the oscillation performance of two

IEEE benchmark power systems, the Brazilian 7-bus test system and the 39-Bus New-England Test System.

- Both methods proposed to build the reference model were suitable for the proposed application, resulting in an improved damping performance of the test systems. Method 1 is a simpler and faster solution, that converts the oscillation damping requirement into a second order transfer function. The reference model building with Method 2 is bit more time consuming since it depends on a identification/curve-fitting procedure. Even though the final damping performances were similar for both methods, the predicted closed-loop response of the cases where the reference models were built with Method 2 were more accurate. Also, Method 2 proved to be more efficient in getting closed-loop responses closer to the desired one (reference model response).

- Despite being designed for offline control design, the adapted VRFT procedure was successfully applied in a online control design scenario. It was possible to re-tune the previously designed rPSS using a new set of measured data, acquired after a series of disturbances that changed the operating condition of the 39-Bus New-England Test System. The new parameters of the controller were updated during the simulation, proving that an online application is also possible.

- A MIMO application with the proposed method is possible by formulating the problem as an equally weighted sum least squares problem. By doing so, the one-shot characteristic of the VRFT procedure is preserved. Also, the method can be applied to simultaneously design multiple SISO controllers in a coordinate design approach. However, as the number of input/output increases, the difficulty of building the reference model also increases. Due to the physical characteristics of the system, the usual diagonal structure adopted for the reference model in the literature is not viable. The solution adopted was to build the reference model as a full transfer function matrix. Even though the results were promising, the strategy applied to build the reference model, by means of a series of data acquisition experiments, may impede practical applications. In a scenario were the building of the MIMO reference model is not a problem, if the model was already defined for example, the VRFT procedure can be a valuable tool for the data-driven MIMO control design.

Part II:

- The modeling of the LCC HVDC system as current sources is a suitable strategy for transient stability analysis. Yet, it is important to assure that the system has enough voltage support to maintain the HVDC system at its normal operation mode. It is possible to derive an equation to model the exact dynamics of the electric power

output of the generators. But, this equation has time-varying parameters and a series of approximations are necessary so it can be used to trace the power-angle curve of the system.

- The assumptions presented in Section 7.2 are valid for the test condition considered. The power-angle curves traced with the proposed equation are good approximations to the transient response of the system. The biggest limitation regarding the proposed assumptions is the voltage support of the system, that must be adequate to guarantee the normal operation of the HVDC system (constant current mode). Such voltage support is expected in a practical situation due to the shunt capacitor banks/filters of the HVDC system. The inclusion of those filters in the methodology is possible, as presented in Chapter 9, and have a positive effect over the voltage stability of the system. Those bank of capacitors/filters change the amount of reactive power generated at the equivalent generators and, therefore, change the impact of the generator-rejection over the reactive power flow. The results presented in Chapter 9 show that inclusion of the shunt capacitors/filters reduced the voltage drop at the converter buses and, therefore, the system could pass the first swing of oscillation without exceeding the operating limits of the converters.

- As long as the assumptions considered to derive the power-angle equation are respected, the proposed algorithm for generation-rejection control is a valuable tool for the transient stability assurance of two-areas systems with parallel AC and DC transmission. Regarding the SPS structure described in Section 6.3, it is still necessary to propose a procedure to build the reduced model. That is, to define what are the key quantities that should be measured at the power system and how to apply them to build the reduced model. The greatest challenge will be to assure that the reduced model captures the transient dynamics characteristics of the system, so the generator-rejection calculated for the reduced model is also valid for the real system.

10.3 Published work

Related work published as first author:

The preliminary results of this thesis were presented in:

- R. T. Bernardo, M. M. d. Nascimento and D. Dotta, "A Modified VRFT Approach for Retuning Power System Damping Controllers," *In proceedings of the 2020 IEEE Power & Energy Society General Meeting (PESGM)*, 2020, pp. 1-5.

Related work published as second author:

During the research period of this thesis the author collaborated with other works regarding the application of the VRFT in power systems.

- L. E. d. Santos, R. T. Bernardo, H. Alcahuaman, J. I. Y. Ota, J. A. Pomilio and D. Dotta, "An Online Data-Driven Tuning of Control Parameters for a Grid-Forming Inverter," *In proceedings of the 2022 IEEE Power & Energy Society General Meeting (PESGM)*, 2022, pp. 1-5.
- M. M. d. Nascimento, R. T. Bernardo and D. Dotta, "Data-Driven Secondary Voltage Control Design using PMU Measurements," *In proceedings of the 2020 IEEE Power & Energy Society Innovative Smart Grid Technologies Conference (ISGT)*, 2020, pp. 1-5.

10.4 Recommendations for Future Work

Based on the research carried out during the formulation of this thesis and in the results presented in this document, the following topics are recommended as research directions for futures works. As in the conclusions, the future research topics are also separated according to the two branches of this thesis.

Part I

- The VRFT formulations presented in this document were derived for noiseless processes. The presence of noise in the measured signals is expected in a practical implementation and may impact the results. Thus, the influence of noise in the proposed VRFT formulation should be investigated in further studies as well as techniques to overcome possible drawbacks, such as the use of instrument variables (BAZANELLA, 2011).
- In this work, a rational transfer function structure with a fixed denominator was used for the designed controllers. This structure was chosen for the practical reasons explained in the document and the results are very promising. However, it is possible to formulate the identification of rational system using an extended least-squares algorithm (BILLINGS; ZHU, 1991). This alternative formulation may lead to even better results, since it allows the parameterization of the denominator of the transfer-function. Also, it would be interesting to explore different formulations for the controller as well such as the traditional PID and lead-lag structures.
- The use of remotely measured bus frequencies as controller inputs has proven to be a well suited strategy for the design of SISO controllers for the inter-area oscillation damping problem, as shown in Chapter 4. This use of remote signals as control inputs was not explored in the MIMO case presented in Chapter 5. Instead, the

MIMO formulation was applied to simultaneously retune multiple traditional PSS, using only their local signals (rotor angular velocity). The use of remote signals, such as bus frequencies, can also be useful for a MIMO application, and should be explored in future studies. Those signals not necessarily need to be applied for the rPSS design, instead, they can be used as performance signals (Section 3.3) for the MIMO coordinated design (multiple PSS re-tuning).

- In the VRFT proposed in this work, a simple choice of filter is used. The reference model used as a filter so its inverse is eliminated from the cost function, following the strategy presented in Nakamoto (2004). In Campestrini, Eckhard, Chía and Boeira (2016), a less trivial formulations is proposed for the filter, for the MIMO reference tracking problem, so the error between the ideal controller and the estimated one is minimized. A similar approach for the MIMO oscillation damping problem would be interesting.

- In the present work, the VRFT was adapted for the design of PSS-like damping controllers. However, different control devices are available for the oscillation damping problem. Considering the promising results obtained with the proposed application, it would be also interesting to explore the method for the design of FACTS devices and POD controllers for HVDC systems.

Part II

- The proposed algorithm for the generator-rejection control in cases of forced outage of the HVDC transmission is based on the premise that a reduced two-area model is available. Thus, the construction of such model is a crucial part for implementation of the SPS proposed in Section 6.2. Therefore, one of the future tasks regarding the proposed transient stability analysis and generator-rejection control is the study of the available techniques for building reduced order two-area models using PMUs. In Moraes (2019) a series of PMU-based model estimation methods are presented, including methods that used measurements acquired at a terminal bus or a boundary bus of a two-area system. Those methods may be particularly suitable for the proposed application, since there are PMUs available at the boundary buses (rectifier and inverter buses) of the Brazilian HVDC system (Section 6.2) that inspired the SPS proposed in this thesis.

- The Brazilian HVDC system that inspired the research presented in the second part of this thesis is the *Belo Monte's* HVDC system, that is composed of two ±800 kV/9000 MW bipoles (*Xingu-Estreito* and *Xingu-Terminal Rio*). This HVDC system connects the north and south-eastern regions of Brazil and, even though, both bipoles are installed at the north city of Xingu (at *Xingu's* 500 kV bus), their

converter buses at the south-eastern region are in different locations (*Estreito* 500 kV bus ans *Terminal Rio* 500 kV bus). Therefore, a possible approach for future studies is to adapt the proposed algorithm for the generator-rejection control for a three-area system with two embedded HVDC transmission systems, as the one illustrated in Figure 10.1. Also, the further research with a three-area system includes the study of estimation methods for building the reduced system.

- The contingency considered in the present work was a fault followed by the permanent blocking of a pole/bipole without any power transfer to the remaining poles of the HVDC system. In a practical situation, a portion of the DC power lost is automatically transferred to the remaining pole/bipole by means of a run-up action. With the proposed algorithm for the generator-rejection control, it is possible to account for this power transfer by properly adjusting the value of $|S_{\text{rec},0}|$ in Equation (7.10). However, by doing so, the dynamic effect of the run-up is neglected, since it is considered that the power transfer happens simultaneously with the blocking of the pole/bipole. Further studies are needed to evaluate how this approximation affects the results of the proposed algorithm.

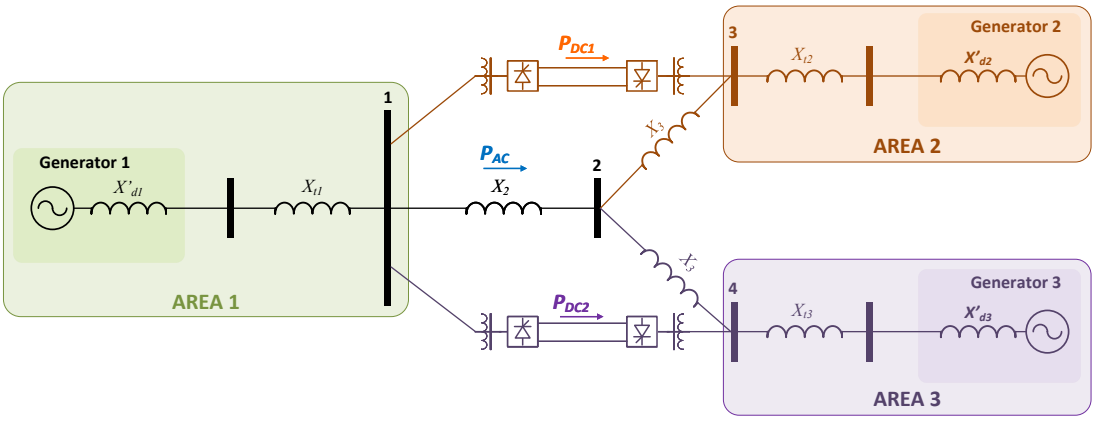

Figure 10.1 – Three area system with two embedded HVDC transmission systems.

Bibliography

ABDELAZIM, T.; MALIK, O. An adaptive power system stabilizer using on-line self-learning fuzzy systems. In: IEEE. *Proceedings of the 2003 IEEE Power & Energy Society General Meeting (PESGM)*. [S.l.], 2003. v. 3, p. 1715–1720. Cited on page 40.

ABIDO, M.; ABDEL-MAGID, Y. A hybrid neuro-fuzzy power system stabilizer for multimachine power systems. *IEEE Transactions on Power Systems*, IEEE, v. 13, n. 4, p. 1323–1330, 1998. Cited 2 times on pages 40 and 42.

ABOUL-ELA, M.; SALLAM, A.; MCCALLEY, J.; FOUAD, A. Damping controller design for power system oscillations using global signals. *IEEE Transactions on Power Systems*, v. 11, n. 2, p. 767–773, 1996. Cited on page 38.

ALAM, M. T.; AHSAN, Q. A mathematical model for the transient stability analysis of a simultaneous AC–DC power transmission system. *IEEE Transactions on Power Systems*, IEEE, v. 33, n. 4, p. 3510–3520, 2017. Cited 3 times on pages 108, 113, and 123.

ARRILLAGA, J. *High voltage direct current transmission*. 2nd. ed. [S.l.]: IET Power and Energy Series, 1998. v. 29. Cited 2 times on pages 129 and 212.

ATHAY, T.; PODMORE, R.; VIRMANI, S. A practical method for the direct analysis of transient stability. *IEEE Transactions on Power Apparatus and Systems*, IEEE, n. 2, p. 573–584, 1979. Cited on page 74.

AZAD, S. P.; IRAVANI, R.; TATE, J. E. Damping inter-area oscillations based on a model predictive control (MPC) HVDC supplementary controller. *IEEE Transactions on Power Systems*, v. 28, n. 3, p. 3174–3183, 2013. Cited on page 38.

BALLAL, M. S.; KULKARNI, A. R.; SURYAWANSHI, H. M. Methodology for the improvements in synchrophasor based system integrity protection schemes under stressed conditions. *Sustainable Energy, Grids and Networks*, v. 26, p. 100465, 2021. ISSN 2352-4677. Cited on page 107.

BAZANELLA, A. S.; CAMPESTRINI, L.; ECKHARD, D. *Data-driven controller design: the H_2 approach*. Amsterdam: Springer, 2011. ISBN 978-94-007-2299-6. Cited 4 times on pages 48, 49, 65, and 183.

BENTO, M. E. C.; DOTTA, D.; KUIAVA, R.; RAMOS, R. A. Design of coordinated decentralized damping controllers for power systems considering uncertainties. *Journal of Control, Automation and Electrical Systems*, v. 29, n. 1, p. 22–31, fev. 2018. Cited on page 39.

BERNADO, R. T.; DO NASCIMENTO, M. M.; DOTTA, D. A modified VRFT approach for retuning power system damping controllers. In: *Proceedings of the 2020 IEEE Power & Energy Society General Meeting (PESGM)*. [S.l.: s.n.], 2020. p. 1–5. Cited on page 57.

BERNARDO, R. T.; DOTTA, D. A simplified robust control design method for wide area damping controllers. *IEEE Latin America Transactions*, v. 16, n. 2, p. 453–459, 2018. Cited on page 40.

BERNARDO, R. T.; OLIVEIRA, R. C.; DOTTA, D. An improved LMI-based approach for the design of power system damping controllers. In: *Proceedings of the 9th IFAC Symposium on Robust Control Design ROCOND 2018*. Florianópolis, SC, Brazil: [s.n.], 2018. p. 287–292. Cited 2 times on pages 39 and 87.

BILLINGS, S. A.; ZHU, Q. M. Rational model identification using an extended least-squares algorithm. *International Journal of Control*, v. 54, n. 3, p. 529–546, 1991. Cited on page 183.

BOMFIM, A. L. B.; TARANTO, G. N.; FALCÃO, D. M. Simultaneous tuning of power system damping controllers using genetic algorithms. *IEEE Transactions on Power Systems*, v. 15, n. 1, p. 163–169, Feb. 2000. Cited on page 39.

BOYD, S.; GHAOUI, L. E.; FERON, E.; BALAKRISHNAN, V. *Linear matrix inequalities in system and control theory*. [S.l.]: SIAM, 1994. Cited on page 39.

BOYD, S.; VANDENBERGHE, L. *Introduction to applied linear algebra: vectors, matrices, and least squares*. [S.l.]: Cambridge university press, 2018. Cited on page 91.

CAMPESTRINI, L.; ECKHARD, D.; CHíA, L. A.; BOEIRA, E. Unbiased MIMO VRFT with application to process control. *Journal of Process Control*, v. 39, p. 35–49, 2016. ISSN 0959-1524. Cited 3 times on pages 48, 86, and 184.

CAMPI, M. C.; LECCHINI, A.; SAVARESI, S. M. Virtual reference feedback tuning: a direct method for the design of feedback controllers. *Automatica*, Elsevier, v. 38, n. 8, p. 1337–1346, 2002. Cited 2 times on pages 44 and 54.

CAMPI, M. C.; LECCHINI, A.; SAVARESI, S. M. Virtual reference feedback tuning: a direct method for the design of feedback controllers. *Automatica*, Elsevier, v. 38, n. 8, p. 1337–1346, 2002. Cited on page 51.

CANIZARES, C. et al. Benchmark models for the analysis and control of small-signal oscillatory dynamics in power systems. *IEEE Transactions on Power Systems*, IEEE, v. 32, n. 1, p. 715–722, 2017. Cited on page 68.

CASTOLDI, M.; SANCHES, D.; MANSOUR, M.; BRETAS, N.; RAMOS, R. A hybrid algorithm to tune power oscillation dampers for FACTS devices in power systems. *Control Engineering Practice*, v. 24, p. 25–32, 2014. ISSN 0967-0661. Cited on page 39.

CEPEL; ELETROBRAS. *Análise de Transitórios Eletromecânicos, ANATEM*: Manual do usuário. 11.9.0. [S.l.], 2020. Cited 7 times on pages 66, 68, 75, 138, 144, 166, and 235.

CEPEL; ELETROBRAS. *PacDyn*: User's manual. 9.9.11. [S.l.], 2020. Cited 2 times on pages 202 and 204.

CHAKRABORTTY, A. Wide-area control of power systems: Employing data-driven, hierarchical reinforcement learning. *IEEE Electrification Magazine*, IEEE, v. 9, n. 1, p. 45–52, 2021. Cited on page 41.

CHAUDHURI, B.; PAL, B. Robust damping of multiple swing modes employing global stabilizing signals with a TCSC. *IEEE Transactions on Power Systems*, v. 19, n. 1, p. 499–506, 2004. Cited on page 38.

CHAUDHURI, N. R.; DOMAHIDI, A.; CHAUDHURI, B.; MAJUMDER, R.; KORBA, P.; RAY, S.; UHLEN, K. Power oscillation damping control using wide-area signals: A case study on nordic equivalent system. In: IEEE. *Proceedings of the 2010 IEEE PES T&D*. [S.l.], 2010. p. 1–8. Cited 2 times on pages 41 and 42.

CHOW, J.; BOUKARIM, G.; MURDOCH, A. Power system stabilizers as undergraduate control design projects. *IEEE Transactions on Power Systems*, v. 19, n. 1, p. 144–151, 2004. Cited on page 39.

CHOW, J.; SANCHEZ-GASCA, J. Pole-placement designs of power system stabilizers. *IEEE Transactions on Power Systems*, v. 4, n. 1, p. 271–277, 1989. Cited on page 39.

CHOW, J.; SANCHEZ-GASCA, J.; REN, H.; WANG, S. Power system damping controller design-using multiple input signals. *IEEE Control Systems Magazine*, v. 20, n. 4, p. 82–90, Aug 2000. Cited 3 times on pages 38, 40, and 151.

CHOW, J. H.; SANCHEZ-GASCA, J. J. *Power system modeling, computation, and control*. [S.l.]: John Wiley & Sons, 2020. Cited 6 times on pages 15, 109, 114, 115, 116, and 128.

COSTA, A. S.; FREITAS, F.; PEÑA, H. Power system stabilizer design via structurally constrained optimal control. *Electric Power Systems Research*, v. 33, n. 1, p. 33–40, 1995. ISSN 0378-7796. Cited on page 39.

DEMARCO, C. L.; CAÑIZARES, C. A. A vector energy function approach for security analysis of ac/dc systems. *IEEE Transactions on Power Systems*, IEEE, v. 7, n. 3, p. 1001–1011, 1992. Cited on page 107.

DENG, J.; ZHANG, X.-P. Robust damping control of power systems with TCSC: A multi-model BMI approach with h_2 performance. *IEEE Transactions on Power Systems*, v. 29, n. 4, p. 1512–1521, 2014. Cited on page 39.

DILL, G. K. *Projeto de controladores robustos para sistemas de potência baseado em otimização paramétrica*. Thesis (PhD) — Departamento de Pós-Graduação em Engenharia Elétrica, UFSC, 2013. Cited on page 37.

DOSIEK, L.; AGRAWAL, U.; FOLLUM, J.; PIERRE, J. W.; TRUDNOWSKI, D. J. Analysis of power system mode meters under various oscillatory conditions. In: *Proceedings of the 2018 IEEE International Conference on Probabilistic Methods Applied to Power Systems (PMAPS)*. [S.l.: s.n.], 2018. p. 1–6. Cited on page 53.

DOTTA, D.; SILVA, A. S. e; DECKER, I. C. Wide-area measurements-based two-level control design considering signal transmission delay. *IEEE Transactions on Power Systems*, v. 24, n. 1, p. 208–216, fev. 2009. Cited 3 times on pages 38, 40, and 52.

DYSKO, A.; LEITHEAD, W. E.; O'REILLY, J. Enhanced power system stability by coordinated PSS design. *IEEE Transactions on Power Systems*, v. 25, n. 1, p. 413–422, 2010. Cited on page 39.

ELKINGTON, K.; GHANDHARI, M. Non-linear power oscillation damping controllers for doubly fed induction generators in wind farms. *IETRenewable Power Generation*, v. 7, n. 2, p. 172–179, 2013. Cited on page 39.

ERIKSSON, R. On the centralized nonlinear control of HVDC systems using lyapunov theory. *IEEE Transactions on Power Delivery*, IEEE, v. 28, n. 2, p. 1156–1163, 2013. Cited on page 108.

ERIKSSON, R.; SöDER, L. Coordinated control design of multiple hvdc links based on model identification. *Computers and Mathematics with Applications*, v. 60, n. 4, p. 944–953, 2010. ISSN 0898-1221. PCO' 2010. Cited on page 41.

FERNANDOPULLE, N.; ALDEN, R. Incorporation of detailed HVDC dynamics into transient energy functions. *IEEE Transactions on Power Systems*, v. 20, n. 2, p. 1043–1052, 2005. Cited on page 108.

FERNANDOPULLE, N.; ALDEN, R. T. Improved dynamic security assessment for AC/DC power systems using energy functions. *IEEE Transactions on Power Systems*, IEEE, v. 18, n. 4, p. 1470–1477, 2003. Cited on page 108.

FILHO, S. M.; DINIZ, S. S.; GASPAR, A. R.; TAKARATA, A. Y.; CASTRO, A.; XIMENES, M. J. C.; DECKER, I. C.; AQUINO, A. F.; ISSICABA, D.; DOTTA, D.; MORAES, G. R. Desenvolvimento de sistema especial de proteção baseado em sincrofasores para a UHE belo monte. In: *Proceedings of the XXVI SNPTEE - Seminário Nacional de Produção e Transmissão de Energia Elétrica*. Rio de Janeiro, Brazil: [s.n.], 2022. Cited on page 148.

FORMENTIN, S.; SAVARESI, S.; RE, L. D. Non-iterative direct data-driven controller tuning for multivariable systems: theory and application. *IET Control Theory & Applications*, v. 6, p. 1250–1257(7), June 2012. Cited on page 86.

GÓMEZ-EXPÓSITO, A.; CONEJO, A. J.; CAÑIZARES, C. *Electric energy systems: analysis and operation*. [S.l.]: CRC press, 2018. Cited on page 31.

GONZALEZ-TORRES, J. C.; COSTAN, V.; DAMM, G.; BENCHAIB, A.; BERTINATO, A.; POULLAIN, S.; LUSCAN, B.; LAMNABHI-LAGARRIGUE, F. HVDC protection criteria for transient stability of AC systems with embedded HVDC links. *Proceedings of the 14th International Conference on Developments in Power System Protection (DPSP 2018)*, IET, v. 2018, n. 15, p. 956–960, 2018. Cited 3 times on pages 108, 113, and 123.

GONZALEZ-TORRES, J. C.; DAMM, G.; COSTAN, V.; BENCHAIB, A.; LAMNABHI-LAGARRIGUE, F. Transient stability of power systems with embedded VSC-HVDC links: Stability margins analysis and control. *IET Generation, Transmission & Distribution*, IET, v. 14, n. 17, p. 3377–3388, 2020. Cited on page 108.

GUPTA, P.; PAL, A.; VITTAL, V. Coordinated wide-area control of multiple controllers in a power system embedded with HVDC lines. *IEEE Transactions on Power Systems*, v. 36, n. 1, p. 648–658, 2021. Cited 2 times on pages 38 and 40.

HATZIARGYRIOU, N.; MILANOVIC, J. V.; RAHMANN, C.; AJJARAPU, V.; CANIZARES, C.; ERLICH, I.; HILL, D.; HISKENS, I.; KAMWA, I.; PAL, B.; POURBEIK, P.; SANCHEZ-GASCA, J. J.; STANKOVIC, A. M.; CUTSEM, T. V.; VITTAL, V.; VOURNAS, C. Definition and classification of power system stability revisited & extended. *IEEE Transactions on Power Systems*, IEEE, v. 36, n. 4, p. 3271–3281, 2021. Cited 2 times on pages 13 and 31.

HUMPERT, C. Long distance transmission systems for the future electricity supply – analysis of possibilities and restrictions. *Energy*, v. 48, n. 1, p. 278–283, 2012. Cited on page 30.

IEEE, Power and Energy Society. IEEE guide for engineering, implementation, and management of system integrity protection schemes. *IEEE Std C37.250-2020*, p. 1–71, 2020. Cited on page 110.

JIANG, N.; CHIANG, H.-D. Energy function for power system with detailed DC model: construction and analysis. *IEEE Transactions on Power Systems*, IEEE, v. 28, n. 4, p. 3756–3764, 2013. Cited on page 108.

KAMWA, I.; GERIN-LAJOIE, L.; TRUDEL, G. Multi-loop power system stabilizers using wide-area synchronous phasor measurements. In: *Proceedings of the 1998 American Control Conference*. [S.l.: s.n.], 1998. v. 5, p. 2963–2967. Cited 2 times on pages 38 and 40.

KAMWA, I.; GRONDIN, R.; HEBERT, Y. Wide-area measurement based stabilizing control of large power systems-a decentralized/hierarchical approach. *IEEE Transactions on Power Systems*, v. 16, n. 1, p. 136–153, 2001. Cited 2 times on pages 38 and 40.

KIMBARK, E. W. *Power system stability*. [S.l.]: John Wiley & Sons, 1995. v. 1. Cited 2 times on pages 119 and 120.

KUIAVA, R.; DE OLIVEIRA, R. V.; RAMOS, R. A.; BRETAS, N. G. Simultaneous coordinated design of PSS and TCSC damping controller for power systems. In: *Proceedings of the 2006 IEEE Power & Energy Society General Meeting (PESGM)*. Montreal, Canada: [s.n.], 2006. p. 8–14. ISSN 1932-5517. Cited on page 39.

KUNDUR, P.; BALU, N. J.; LAUBY, M. G. *Power system stability and control*. [S.l.]: McGraw-hill New York, 1994. v. 7. Cited 8 times on pages 31, 38, 109, 114, 115, 125, 160, and 167.

KUNDUR, P.; PASERBA, J.; AJJARAPU, V.; ANDERSSON, G.; BOSE, A.; CANIZARES, C.; HATZIARGYRIOU, N.; HILL, D.; STANKOVIC, A.; TAYLOR, C.; VAN CUTSEM, T.; VITTAL, V. Definition and classification of power system stability. *IEEE Transactions on Power Systems*, v. 19, n. 2, p. 1387–1401, May 2004. Cited on page 32.

LARSEN, E. V.; SWANN, D. A. Applying power system stabilizers, parts I-III. *IEEE Transactions on Power Apparatus and Systems*, IEEE, PAS-100, n. 6, p. 3017–3046, 1981. Cited 2 times on pages 39 and 51.

LEANDRO, R. B.; SILVA, A. S. e; DECKER, I. C.; AGOSTINI, M. N. Identification of the oscillation modes of a large power system using ambient data. *Journal of Control, Automation and Electrical Systems*, v. 26, n. 1, p. 441–453, abr. 2015. ISSN 2195-3899. Cited on page 53.

LI, C.; DU, Z.; NI, Y.; ZHANG, G. Reduced model-based coordinated design of decentralized power system controllers. *IEEE Transactions on Power Systems*, v. 31, n. 3, p. 2172–2181, 2016. Cited on page 40.

LI, W.; VANFRETTI, L. A PMU-based state estimator considering classic HVDC links under different control modes. *Sustainable Energy, Grids and Networks*, v. 2, p. 69–82, 2015. ISSN 2352-4677. Cited on page 107.

LIU, D.; YAN, P.; WEI, Q. Data-based analysis of discrete-time linear systems in noisy environment: Controllability and observability. *Information Sciences*, v. 288, p. 314–329, 2014. Cited on page 53.

LIU, M.; DASSIOS, I.; MILANO, F. Delay margin comparisons for power systems with constant and time-varying delays. *Electric Power Systems Research*, v. 190, p. 106627, 2021. ISSN 0378-7796. Cited on page 53.

LIU, Y.; GRACIA, J. R.; KING, T. J.; LIU, Y. Frequency regulation and oscillation damping contributions of variable-speed wind generators in the U.S. eastern interconnection (EI). *IEEE Transaction on Sustainable Energy*, v. 6, n. 3, p. 951–958, 2015. Cited on page 38.

LJUNG, L. *System identification: Theory for the user*. 2nd. ed. New York, NY: Prentice Hall, 1999. Cited on page 45.

LJUNG, L. Black-box models from input-output measurements. In: *Proceedings of the 18th IEEE Instrumentation and Measurement Technology Conference (IMTC 2001)*. [S.l.: s.n.], 2001. v. 1, p. 138–146. Cited on page 60.

LU, C.; ZHAO, Y.; MEN, K.; TU, L.; HAN, Y. Wide-area power system stabiliser based on model-free adaptive control. *IET Control Theory & Applications*, IET, v. 9, n. 13, p. 1996–2007, 2015. Cited 2 times on pages 42 and 43.

LU, C.-F.; HSU, C.-H.; JUANG, C.-F. Coordinated control of flexible AC transmission system devices using an evolutionary fuzzy lead-lag controller with advanced continuous ant colony optimization. *IEEE Transactions on Power Systems*, v. 28, n. 1, p. 385–392, 2013. Cited on page 39.

MARTíNEZ-PARRALES, R.; FUERTE-ESQUIVEL, C. A new unified approach for the state estimation and bad data analysis of electric power transmission systems with multi-terminal VSC-based HVDC networks. *Electric Power Systems Research*, v. 160, p. 251–260, 2018. ISSN 0378-7796. Cited on page 107.

MILANO, F.; DöRFLER, F.; HUG, G.; HILL, D. J.; VERBIč, G. Foundations and challenges of low-inertia systems. In: *Proceedings of the 2018 Power Systems Computation Conference (PSCC)*. [S.l.: s.n.], 2018. p. 1–25. Cited on page 30.

MORAES, G. R. *Real-time PMU-based power system inertia monitoring considering dynamic equivalents*. Thesis (PhD) — Politecnico di Milano, Milan, Italy, December 2019. Cited on page 184.

MUKHERJEE, S.; BABAEI, S.; CHAKRABORTTY, A.; FARDANESH, B. Measurement-driven optimal control of utility-scale power systems: A New York state grid perspective. *International Journal of Electrical Power & Energy Systems*, Elsevier, v. 115, p. 105470, 2020. Cited on page 42.

NADUVATHUPARAMBIL, B.; VALENTI, M.; FELIACHI, A. Communication delays in wide area measurement systems. In: *Proceedings of the Thirty-Fourth Southeastern Symposium on System Theory (Cat. No.02EX540)*. [S.l.: s.n.], 2002. p. 118–122. Cited on page 53.

NAKAMOTO, M. An application of the virtual reference feedback tuning for an MIMO process. In: IEEE. *SICE 2004 Annual Conference*. [S.l.], 2004. v. 3, p. 2208–2213. Cited 3 times on pages 51, 86, and 184.

NANNI, M. *Modelagem e Análise dos Impactos da Inserção de Plantas PV na Operação e Controle de Sistemas Elétricos*. Thesis (PhD) — School of Electrical and Computer Engineering, UNICAMP, Campinas, Brazil, April 2021. Cited 2 times on pages 38 and 40.

NANNI, M.; BERNARDO, R. T.; DOTTA, D. Development of wide-area control scheme in power system toolbox. In: *Proceedings of the 2019 IEEE PES Innovative Smart Grid Technologies Conference - Latin America (ISGT Latin America)*. [S.l.: s.n.], 2019. p. 1–6. Cited 2 times on pages 38 and 40.

NOHARA, A. A.; AQUINO, A. F. C.; SARDINHA, S. L. A.; MASSAUD, A. G.; FERNANDES, R. D. O. Melhoria do desempenho dinâmico do SIN através das funções de estabilidade do primeiro bipolo de corrente contínua de belo monte. In: *Proceedings of the XXIV SNPTEE - Seminário Nacional de Produção e Transmissão de Energia Elétrica*. Curitiba, Brazil: [s.n.], 2017. Cited on page 148.

ONS, Operador Nacional do Sistema Elétrico. *Estudos Pré-Operacionais para interligação do Bipolo Xingu - Estreito ao Sistema Interligado Nacional*. Rio de Janeiro - RJ: [s.n.], 2017. Cited on page 110.

ONS, Operador Nacional do Sistema Elétrico. *Boletim de Interrupção do Suprimento de Energia - ONS 011/2018*. 2018. Available at: <https://sintegre.ons.org.br/sites/2/53/Produtos/63/BISE%20ONS%20011-18%20210318-15h48%20SIN.pdf>. Accessed: 2022-08-18. Cited on page 109.

ONS, Operador Nacional do Sistema Elétrico. *Estudos Pré-Operacionais para interligação do Bipolo Xingu - Terminal Rio ao Sistema Interligado Nacional*: Volume 4: Diretrizes para a operação elétrica. Rio de Janeiro - RJ: [s.n.], 2018. Available at: <https://sintegre.ons.org.br/sites/5/29/paginas/servicos/produtos-pasta.aspx?RootFolder=/sites/5/29/Produtos/125/PRE-OPERACIONAL%20BIPOLO%20XINGU%20-%20TERMINAL%20RIO>. Accessed: 2022-08-18. Cited on page 110.

ONS, Operador Nacional do Sistema Elétrico. *Nota à Imprensa - Ocorrência no SIN – 21/03/2018*. 2018. Available at: <http://www.ons.org.br/Paginas/Noticias/20180322-notaaimprensacomplementar2.aspx>. Accessed: 2022-08-18. Cited on page 109.

ONS, Operador Nacional do Sistema Elétrico. *Estudo Quadrimestral - 2° quadrimestre de 2020 - Carga Média*: Base de dados para estudos de transitórios eletromecânicos - março/2020. 2020. Available at: <https://sintegre.ons.org.br/sites/8/93/Produtos/211/BD0320R0.zip>. Accessed: 2022-08-18. Cited 3 times on pages 139, 155, and 167.

ONS, Operador Nacional do Sistema Elétrico. *Base de Dados de Operação para Estudos de Curto-Circuito*. 2022. Available at: <https://sintegre.ons.org.br/sites/8/32/85/Produtos/167/BR2206A.zip>. Accessed: 2022-10-18. Cited on page 139.

ONS, Operador Nacional do Sistema Elétrico. *Histórico da Operação*: Curva de carga horária. 2022. Available at: <http://www.ons.org.br/Paginas/resultados-da-operacao/historico-da-operacao/curva_carga_horaria.aspx>. Accessed: 2022-08-18. Cited on page 167.

ONS, Operador Nacional do Sistema Elétrico. *Sobre o SIN*: O sistema em números. 2022. Available at: <http://www.ons.org.br/paginas/sobre-o-sin/o-sistema-em-numeros>. Accessed: 2022-10-18. Cited on page 109.

OPPENHEIM, A. V.; WILLSKY, A. S.; NAWAB, S. H. *Signals and Systems*. 2nd. ed. [S.l.]: Prentice Hall, 1997. Cited on page 46.

PAI, M. A.; PADIYAR, K. R.; RADHAKRISHNA, C. Transient stability analysis of multi-machine AC/DC power systems via energy-function method. *IEEE Transactions on Power Apparatus and Systems*, PAS-100, n. 12, p. 5027–5035, 1981. Cited on page 107.

PAL, B.; CHAUDHURI, B. *Robust control in power systems*. [S.l.]: Springer, 2005. Cited on page 37.

PHADKE, A.; VOLSKIS, H.; MORAES, R. M. de; BI, T.; NAYAK, R.; SEHGAL, Y.; SEN, S.; SATTINGER, W.; MARTINEZ, E.; SAMUELSSON, O.; NOVOSEL, D.; MADANI, V.; KULIKOV, Y. A. The wide world of wide-area measurement. *IEEE Power and Energy Magazine*, v. 6, n. 5, p. 52–65, 2008. Cited on page 38.

RAMOS, R.; MARTINS, A.; BRETAS, N. An improved methodology for the design of power system damping controllers. *IEEE Transactions on Power Systems*, v. 20, n. 4, p. 1938–1945, 2005. Cited 2 times on pages 39 and 87.

RAMOS, R. A.; ALBERTO, L. F. C.; BRETAS, N. G. A new methodology for the coordinates design of robust decentralized power system damping controllers. *IEEE Transactions on Power Systems*, v. 19, n. 1, p. 69–79, 2004. Cited 2 times on pages 39 and 87.

RODRIGUES, G. *Inter-area oscillations in power systems with uncertainties: data-driven wide-area damping control design and monitoring enhancement using energy storage*. Thesis (PhD) — Universidade Federal do Rio Grande do Sul, Porto Alegre, Brazil, October 2019. Cited on page 48.

SAADAT, H. et al. *Power system analysis*. [S.l.]: McGraw-hill, 1999. v. 2. Cited on page 117.

SCHONLEBER, K.; OUDALOV, A.; KRONTIRIS, A.; LUNDBERG, P. Opportunities for embedded high-voltage direct current: Evaluating the benefits for the legacy ac grid. *IEEE Power and Energy Magazine*, v. 18, n. 5, p. 58–63, 2020. Cited on page 107.

SHAHGHOLIAN, G.; MOVAHEDI, A. Power system stabiliser and flexible alternating current transmission systems controller coordinated design using adaptive velocity update relaxation particle swarm optimisation algorithm in multi-machine power system. *IET Generation, Transmission & Distribution*, v. 10, n. 8, p. 1860–1868, 2016. Cited on page 39.

SHI, X.; CAO, Y.; LI, Y.; MA, J.; SHAHIDEHPOUR, M.; WU, X.; LI, Z. Data-driven model-free adaptive damping control with unknown control direction for wind farms. *International Journal of Electrical Power & Energy Systems*, Elsevier, v. 123, p. 106213, 2020. Cited 2 times on pages 42 and 43.

SILVA, G. R. Gonçalves da; BAZANELLA, A. S.; CAMPESTRINI, L. On the choice of an appropriate reference model for control of multivariable plants. *IEEE Transactions on Control Systems Technology*, v. 27, n. 5, p. 1937–1949, 2019. Cited on page 61.

SIMÕES, A. M.; SAVELLI, D. C.; PELLANDA, P. C.; MARTINS, N.; APKARIAN, P. Robust design of a TCSC oscillation damping controller in a weak 500-kV interconnection considering multiple power flow scenarios and external disturbances. *IEEE Transactions on Power Systems*, v. 24, n. 1, p. 226–236, 2009. Cited on page 38.

SIMÕES-COSTA, A. J. A.; FREITAS, F. D.; SILVA, A. S. e. Design of decentralized controllers for large power systems considering sparsity. *IEEE Transactions on Power Systems*, v. 12, p. 144–152, February 1997. Cited on page 39.

TANG, G.; XU, Z.; ZHOU, Y. Impacts of three MMC-HVDC configurations on AC system stability under DC line faults. *IEEE Transactions on Power Systems*, v. 29, n. 6, p. 3030–3040, 2014. Cited 3 times on pages 108, 113, and 123.

The MathWorks, Inc. *Estimate transfer function*. 2021. <https://www.mathworks.com/help/ident/ref/tfest.html>. Cited on page 64.

The MathWorks, Inc. *Option set for tfest*. 2021. <https://www.mathworks.com/help/ident/ref/tfestoptions.html>. Cited on page 64.

The MathWorks, Inc. *Simulated time response of dynamic system to arbitrary inputs*. 2021. <https://www.mathworks.com/help/control/ref/lti.lsim.html>. Cited 2 times on pages 56 and 66.

WU, H.; TSAKALIS, K.; HEYDT, G. Evaluation of time delay effects to wide-area power system stabilizer design. *IEEE Transactions on Power Systems*, v. 19, n. 4, p. 1935–1941, 2004. Cited on page 53.

XIE, X.; XIN, Y.; XIAO, J.; WU, J.; HAN, Y. WAMS applications in chinese power systems. *IEEE Power and Energy Magazine*, v. 4, n. 1, p. 54–63, 2006. Cited on page 38.

XU, Y.; QU, Z.; HARVEY, R.; NAMERIKAWA, T. Data-driven wide-area control design of power system using the passivity shortage framework. *IEEE Transactions on Power Systems*, IEEE, v. 36, n. 2, p. 830–841, 2020. Cited on page 42.

YOUNG, P.; JAKEMAN, A. Refined instrumental variable methods of recursive time-series analysis part III. extensions. *International Journal of Control*, Taylor & Francis, v. 31, n. 4, p. 741–764, 1980. Cited on page 64.

ZENG, L.; YAO, W.; ZENG, Q.; LI, D.; FANG, J.; AI, X.; WEN, J.; HE, H. Design and real-time implementation of data-driven adaptive wide-area damping controller for back-to-back VSC-HVDC. *International Journal of Electrical Power & Energy Systems*, Elsevier, v. 109, p. 558–574, 2019. Cited 2 times on pages 41 and 42.

ZHANG, G.; HU, W.; CAO, D.; YI, J.; HUANG, Q.; LIU, Z.; CHEN, Z.; BLAABJERG, F. A data-driven approach for designing STATCOM additional damping controller for wind farms. *International Journal of Electrical Power & Energy Systems*, Elsevier, v. 117, p. 105620, 2020. Cited 2 times on pages 41 and 42.

ZHANG, Q. F.; LUO, X.; LITVINOV, E.; DAHAL, N.; PARASHAR, M.; HAY, K.; WILSON, D. Advanced grid event analysis at ISO new england using phasorpoint. In: *Proceedings of the 2014 IEEE PES General Meeting | Conference & Exposition*. [S.l.: s.n.], 2014. p. 1–5. Cited on page 53.

ZHAO, Y.; YUAN, Z.; LU, C.; ZHANG, G.; LI, X.; CHEN, Y. Improved model-free adaptive wide-area coordination damping controller for multiple-input–multiple-output power systems. *IET Generation, Transmission & Distribution*, IET, v. 10, n. 13, p. 3264–3275, 2016. Cited 2 times on pages 42 and 43.

ZHOU, B.; WANG, Z.; ZHAI, Y.; YUAN, H. Data-driven analysis methods for controllability and observability of a class of discrete LTI systems with delays. In: *Proceedings of the 2018 IEEE 7th Data Driven Control and Learning Systems Conference (DDCLS)*. [S.l.: s.n.], 2018. p. 380–384. Cited on page 53.

Appendix

APPENDIX A – VRFT Preliminary Tests and Proof of Concept

The VRFT method described in Section2.4.3 and its adaptation for the proposed power systems application described in Section3 are formulated considering LTI systems. Even tough in the small-signal stability analysis it is considered that the perturbations are sufficiently small so that linearizations of the systems equations is permissible, the power systems have nonlinear dynamics. The purpose of this appendix section is to present a preliminary test that was performed with the VRFT method to validate it with the nonlinear model of one of the power systems considered. The goal of this study was to evaluate the impact of using a nonlinear model (simulated using the ANATEM software) in the proposed method.

The proposed VRFT method for the design of POD consists basically of three stages. First, a data acquisition experiment is performed to collect the data arrays $(\mathbf{u}, \mathbf{y})$. Second, a reference model is build by estimating a dynamic model from data and then imposing a minimum damping ratio to it. And third, solving the VRFT identification criterion, formulated as a least-squares problem, to find the parameter of the controller.

The preliminary test presented here, was elaborated to answer to questions regarding the application of the method.

1. Considering that an ideal closed-loop nonlinear dynamic model[1] of the power systems exists. If a data acquisition experiment is performed with this ideal model, the estimation method (described in Section 3.5) used to build $M_d(s)$ is able to estimate a model that contains the dynamic information needed to tune the controller? Or, is it possible to use data acquired from a nonlinear system to build the reference model $M_d(s)$ using the estimation procedure mentioned in Section 3.5.2?

2. Consider a nonlinear power system model with a bad oscillation damping performance. That is, its damping performance is different from the ideal closed-loop nonlinear dynamic model. Also, consider that the only difference between the two models is the parameters of a PSS. So, one of the systems has an ideal controller and the other one has a poorly tuned controller. If the reference model $M_d(s)$ built from the ideal system data is known, is it possible to find the parameters of the ideal controller using the VRFT method?

[1] By *ideal closed-loop nonlinear dynamic model* the author means a model were a POD controller exists and it is able to achieve the desired oscillation damping performance.

Note that the question 1 is about the estimation procedure not the modification to cope with the minimum damping performance. Once the model is considered to be ideal there is no need to impose any performance requirement to it.

The Brazilian 7-Bus Equivalent System, described in Section 4.1, in its original operating condition was considered to be the *ideal closed-loop nonlinear dynamic model* and the PSS installed at generator 4 was considered to be the ideal controller. A modified version the system was created to be the power system with the poorly tuned controller. This was done by changing the numerator of the PSS of the generator 4. The transfer function of the ideal PSS and the poorly tuned one are

$$PSS_{4-ideal}(s) = \frac{1024s^2 + 3938.46s + 3786.98}{s^2 + 30.77s + 236.7} \tag{A.1}$$

and

$$PSS_{4-bad}(s) = \frac{200s^2 + 2000s + 4000}{s^2 + 30.77s + 236.7}. \tag{A.2}$$

So, an identified model based on the *ideal system* is used as reference model $M_d(s)$ to re-tune the PSS4 of the second system, equipped with the PSS_{4-bad}. If the identification step succeeds and $M_d(s)$ is a good representation of the ideal dynamics, one can expect that the reference model is feasible, because the only difference between the ideal system and the one with the poorly tuned controller is the numerator of the transfer function of the PSS installed at Itaipu's generator. It is also known that the optimum controller $C(s, \rho^*)$ exists and the optimum solution of the problem (3.6) is the difference between the numerator parameters of (A.1) and (A.2), that is,

$$\rho^* = \begin{bmatrix} \rho_1 & \rho_2 & \rho_3 \end{bmatrix}' = \begin{bmatrix} 824 & 1938.46 & -213.02 \end{bmatrix}'. \tag{A.3}$$

A variation of the VRFT method presented in Section 3 was applied to retune the PSS_{4-bad}. The two differences from the method described in Section 3 are: no minimum damping requirement was used to build the reference model $M_d(s)$, as it was estimated from an *ideal closed-loop model*; and two data acquisition experiments were performed, one with the *ideal closed-loop model* and one with the system with the poorly tuned controller. In Figure A.1 is presented an illustration that summarizes the experiment.

The output signal of the data acquisition experiment, in both systems, is the filtered angular velocity of the generator 4, represented here by $y[n] = \hat{\omega}_4$. The input signal $u[n]$ is a 0.01 p.u. step applied to AVR reference input, at instant 1s and the data is collected for 5 seconds. In order to evaluate the influence of the sampling time over the proposed test, three values were considered 0.1s, 0.01s and 0.001s. Note that both $u[n]$ and $y[n]$ are sequences of samples of continuous-time systems, since the power system is a continuous-time system, as described in Section 3.2. The reference model $M_d(s)$ is a continuous-time identified model built with 9 poles and 8 zeros. The transfer function of

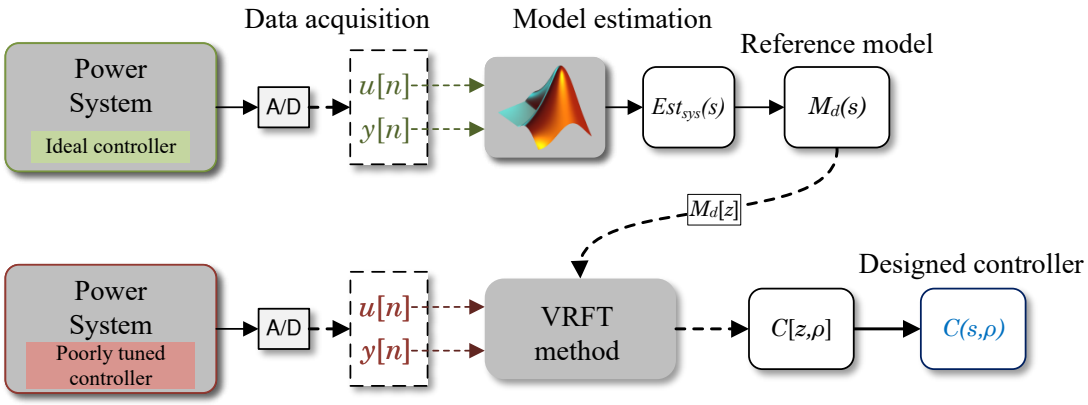

Figure A.1 – Summary of the preliminary test experiment.

$M_d(s)$ and fit to estimation data for each sampling time used are

$$M_{d-Ts1}(s) = \frac{0.00048312(s-138.6)(s+70.59)(s+3.745)(s+1.014)}{(s+0.8376)(s^2+2.276s+14.05)(s^2+0.8773s+27.23)} \times \frac{(s^2+1.334s+25.76)(s^2+10.12s+84.69)}{(s^2+9.123s+75.21)(s^2+10.49s+291.7)}, \tag{A.4}$$

with a fit of 100%,

$$M_{d-Ts2}(s) = \frac{0.00019461(s-222.8)(s+118.5)(s+3.326)(s+1.131)}{(s+0.9089)(s^2+2.314s+14.14)(s^2+0.8529s+27.19)} \times \frac{(s^2+1.283s+25.74)(s^2+11.89s+125.9)}{(s^2+12.03s+111.6)(s^2+10.54s+289)}, \tag{A.5}$$

with a fit of 99.99%, and

$$M_{d-Ts3}(s) = \frac{0.00019353(s-223.4)(s+118.9)(s+3.317)(s+1.135)}{(s+0.9111)(s^2+2.315s+14.14)(s^2+0.8522s+27.19)} \times \frac{(s^2+1.282s+25.74)(s^2+11.97s+126.5)}{(s^2+12.11s+112)(s^2+10.54s+288.9)}, \tag{A.6}$$

with a fit of 99.99%.

The solutions of the problem (3.6) for the three sampling times are shown in Table A.1. Those results revels that the solution approximates to the optimum values (A.3) as the sampling time decreases. However, the benefits of using the 0.001s sampling time is small when compared to the 0.01s sampling time result. The retuned PSSs, for the three sampling ratios are presented as follows.

$$\begin{aligned} PSS_{4-Ts1}(s) &= \frac{1038.85s^2+3959.02s+3817.76}{s^2+30.77s+236.7}, \\ PSS_{4-Ts2}(s) &= \frac{1014.51s^2+3909.45s+3791.49}{s^2+30.77s+236.7}, \\ PSS_{4-Ts3}(s) &= \frac{1014.28s^2+3908.98s+3791.23}{s^2+30.77s+236.7}. \end{aligned} \tag{A.7}$$

Table A.1 – VRFT solution for different sampling time values

T_s (s)	ρ_1	ρ_2	ρ_3
0.1	838.85	1959.02	-182.24
0.01	814.51	1909.45	-208.51
0.001	814.28	1908.98	-208.77

Considering a practical application, the solutions obtained with the three sampling times are sufficiently close to the ideal one. That is, all three PSSs of (A.7) are capable of making the closed-loop dynamics of the system very similar to the reference model. The simulations for all three cases are not presented to keep the document concise. Instead, the result obtained with Ts=0.01s was chosen to illustrate the method.

The measured output signal $y[n]$ (filtered angular velocity) for the input signal $u[n]$ (step on the AVR of gen. 4) is presented in Fig. A.2, together with estimated system output $y_{est}[n]$. Note that the desired response $y_d[n]$ is the same as $y_{est}[n]$, because no performance requirement was applied when building $M_d(s)$. Finally, the closed-loop response of the system $y_{CL}[n]$, obtained after updating the PSS_{4-bed} to PSS_{4-Ts2} in the power system model, is also presented, indicated by the red dashed line.

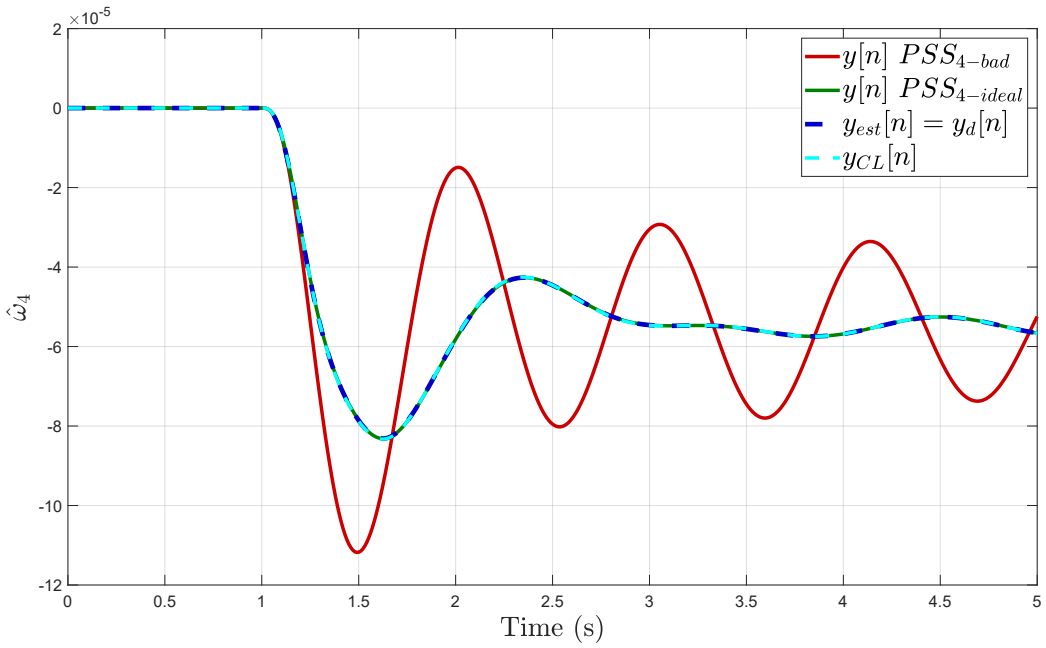

Figure A.2 – Brazilian 7-bus system response to a step in the voltage regulator with the ideal, poorly damped and retuned controller: filtered angular velocity of generator 4.

The oscillation damping efficiency of the retuned controller was tested over a more severe disturbance. A three-phase short-circuit was applied at bus 6 at instant 10s

and cleared after 30ms. As mentioned in Section 4.1, the inter-area mode corresponds to an oscillations between the four generators and the reference machine, but it is more evident at generator 4. Therefore the rotor angle of generator 4 is presented in Figure A.3, using the equivalent machine as angular reference. The response with the idela and poorly tuned controllers are also presented for comparison.

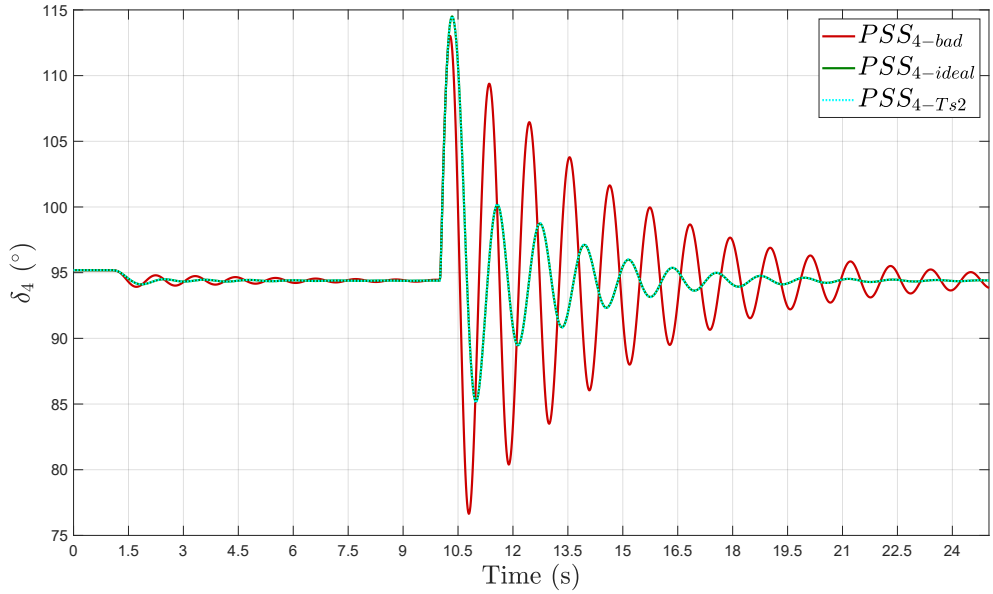

Figure A.3 – Brazilian 7-bus system response to a step in the voltage regulator followed by a short-circuit. Generator 4 rotor angle.

The dynamic response of the system with the retuned PSS is identical to the *ideal* system, even for larger disturbances. This preliminary test is a proof of concept to validate the method with a controlled and ideal scenario. The numerator parameters obtained with the method are sufficiently close to the optimum solution (ideal controller), even with a 5 seconds experiment. The results suggest that the identification method provided a good enough approximation for system dynamics. It also suggests that the small disturbance applied as a probe signal was small enough so the nonlinearities of the system did not affect the design procedure. This preliminary results encouraged the use of the proposed method on a more realistic scenario.

APPENDIX B – Controllability and Observability of the Inter-Area Modes

B.1 Brazilian 7-Bus Equivalent System Inter-Area Mode

As presented in Section 4.1, the Brazilian 7-Bus Equivalent System has an inter-area mode that corresponds to the oscillation between the SE Equivalent (G5) and the southern system (generators 1 to 4). The model of the system was linearized using the software PacDyn (CEPEL; ELETROBRAS, 2020b) and the characteristics of the oscillation mode are presented in Table B.1. The controllability factors of the generators field voltages over the inter-area oscillation mode are presented in Figure B.1. The generator 4 has the higher controllability (highlighted in purple) and was chosen to receive the rPSS. The values of magnitude and phase of the controllability factors, for each generator, are also presented. The observability factors of the mode are presented in Figure B.2, for the bus frequencies. Note that the mode is highly observable at the frequency of bus 7, as expected. The bus frequencies used in the rPSS design presented in Section 4.1 are highlighted in purple.

Table B.1 – Characteristics of the inter-area mode of the Brazilian 7-Bus Equivalent System.

Real	Imaginary	Module	Frequency (Hz)	Damping ratio (%)
-0.1584	±5.0978	5.1002	0.8113	3.1050

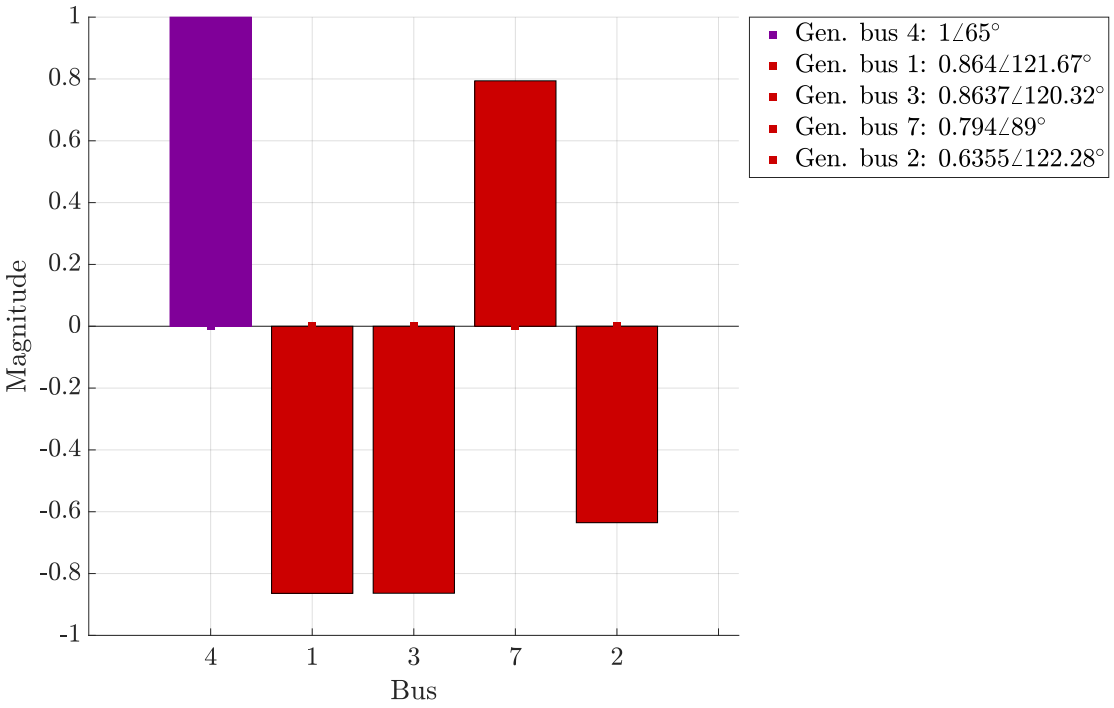

Figure B.1 – Controllability factors of the generators field voltages for the inter-area mode of the Brazilian 7-Bus Equivalent System.

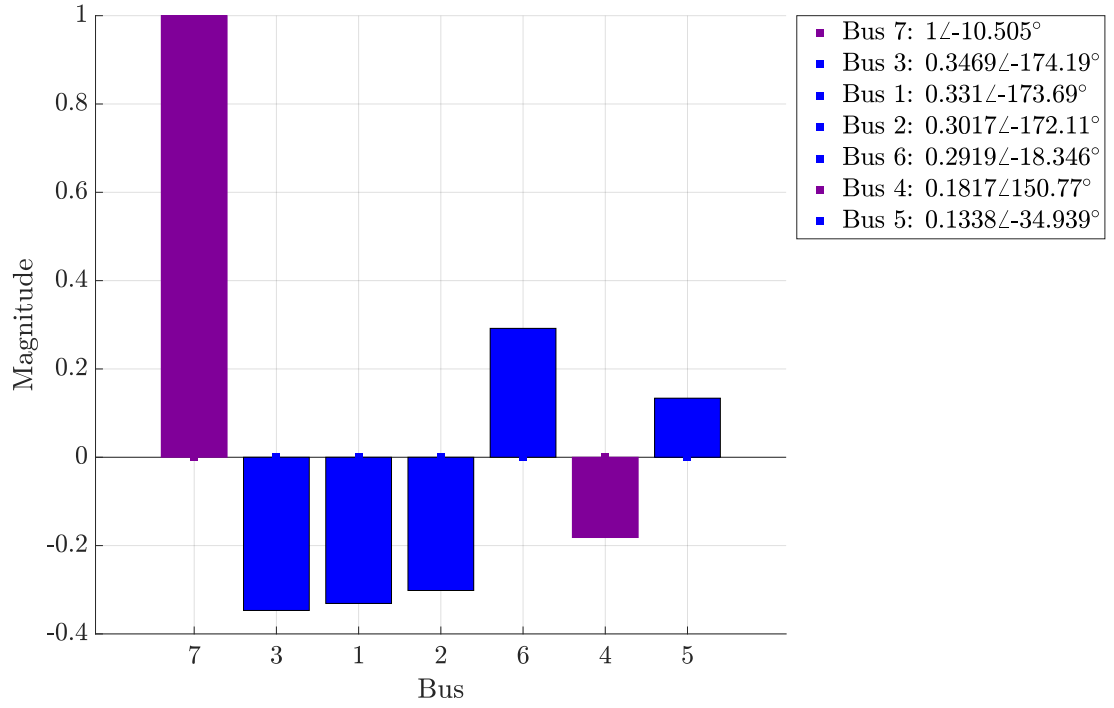

Figure B.2 – Observability factors of the bus frequencies for the inter-area mode of the Brazilian 7-Bus Equivalent System.

B.2 Modified 39-Bus New-England Test System Inter-Area Mode

As presented in Section 4.2, the modified version of the 39-Bus New-England Test System used in this work has an inter-area mode observed as the oscillation of generators 2 to 10 against generator 1. The model of the system was linearized using the software PacDyn (CEPEL; ELETROBRAS, 2020b) and the characteristics of the oscillation mode are presented in Table B.2. The controllability factors of the generators field voltages over the inter-area mode are presented in Figure B.3, and the generator selected to receive the rPSS is highlighted in purple. Note that the generator of bus 32 does not have the higher controllability factor. Even though, it was used for the rPSS design and, as presented in Section 4.2, the results were very promising. The observability factors of the oscillation mode for the bus frequencies are presented in Figure B.4 and confirms the inter-area characteristics of the mode. It is clear that bus 39 (gen. 1) is oscillating against the rest of the system.

Table B.2 – Characteristics of the inter-area mode of the modified 39-Bus New-England Test System.

Real	Imaginary	Module	Frequency (Hz)	Damping ratio (%)
-0.05363	±3.6951	3.6955	0.5881	1.4513

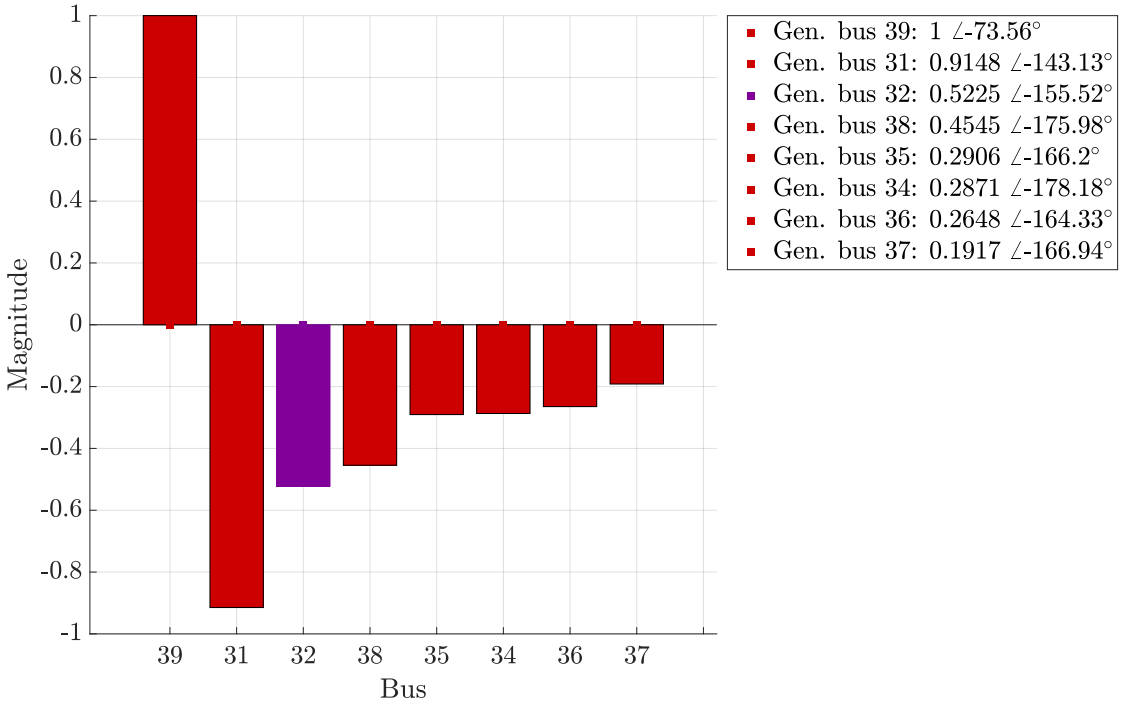

Figure B.3 – Controllability factors of the generators field voltages for the inter-area mode of the modified 39-Bus New-England Test System.

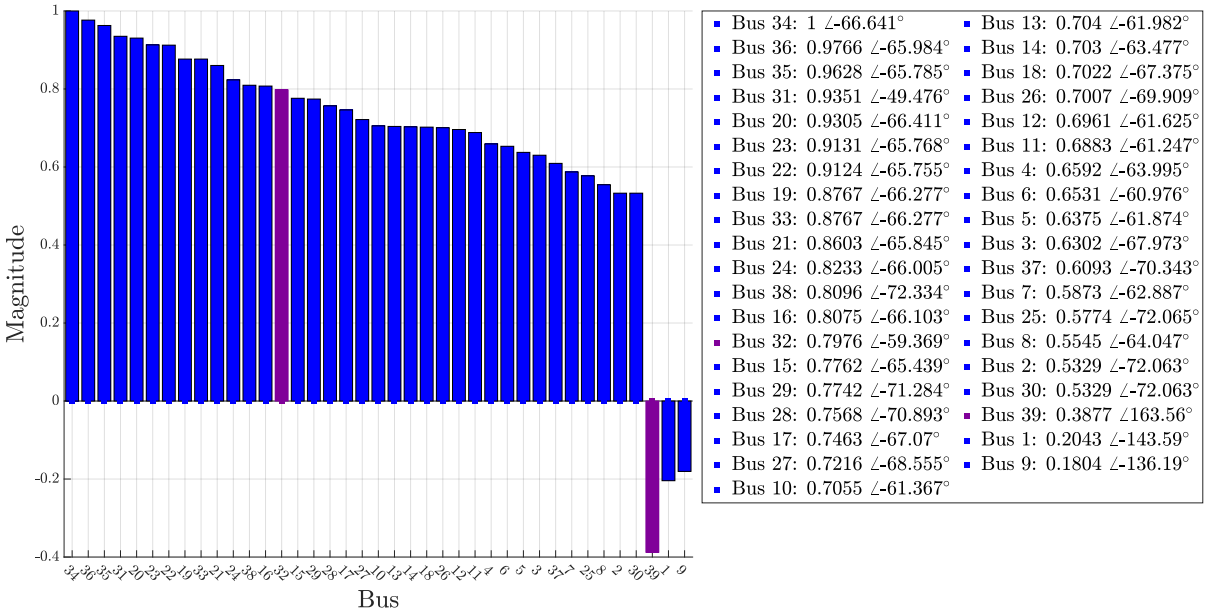

Figure B.4 – Observability factors of the bus frequencies for the inter-area mode of the modified 39-Bus New-England Test System.

APPENDIX C – Reference models used in the VRFT method

This appendix section presents the reference models used in Chapters 4 and 5.

C.1 Reference model for the Brazilian 7-Bus Equivalent System, SISO formulation

The reference model $M_d(s)$ used in Section 4.1.1.2 was built using the method described in Section 3.5.2. The estimated model has 9 poles and 8 zeros, with a 99.85% fit to estimation data and the resulting reference model, for a $\zeta_{min} = 10\%$ is

$$M_d(s) = e^{-0.15s}\frac{0.014124(s-217.3)(s-17.86)(s+1.005)(s-0.1585)}{(s+138.7)(s+3.061)(s+1.605)(s^2+2.857s+15.99)}\times \frac{(s^2+20.79s+129.5)(s^2+2.139s+24.28)}{(s^2+1.033s+26.66)(s^2+10.6s+297.1)} \tag{C.1}$$

C.2 Reference model for the 39-bus New-England test system, SISO formulation

The reference model $M_d(s)$ used in Section 4.2.1.2 was built using the method described in Section 3.5.2. The estimated model has 12 poles and 11 zeros, with a 99.99% fit to estimation data and the resulting reference model, for a $\zeta_{min} = 10\%$ is

$$M_d(s) = e^{-0.15s}\frac{0.0058386(s-999.9)(s-7.303)(s-0.1194)(s^2+1.932s+17.25)}{(s+74.38)(s+45.21)(s+5.835)(s+7.352)(s^2+0.7382s+13.62)}\times \frac{(s^2+25.96s+201.9)(s^2+2.162s+43)(s^2+3.272s+236.3)}{(s^2+3.703s+28.78)(s^2+3.012s+68.33)(s^2+3.267s+236.4)} \tag{C.2}$$

C.3 Reference model for the 39-bus New-England test system, SISO formulation re-tuning

The reference model $M_d(s)$ used in Section 4.2.2 was built using the method described in Section 3.5.2. The estimated model has 12 poles and 11 zeros, with a 86.23% fit to estimation data and the resulting reference model, for a $\zeta_{min} = 10\%$ is

$$M_d(s) = e^{-0.15s}\frac{-0.0029817(s+1169)(s-8.82)(s+3.241)(s^2-0.1697s+0.3098)}{(s^2+0.3787s+0.6802)(s^2+0.6842s+11.7)(s^2+1.495s+55.88)}\times \frac{(s^2+6.905s+42.54)(s^2+0.2868s+54.12)(s^2+3.903s+165.3)}{(s^2+1.994s+70.76)(s^2+3.761s+164.9)(s^2+75.44s+2027)} \tag{C.3}$$

C.4 Reference model for the Brazilian 7-Bus Equivalent System, MIMO formulation

The reference model $M_d(s)$ used in Section 5.2.2 was built using the method described in Section 3.5.2. The transfer functions related with the output 1 ($M_{d_{11}}(s), \ldots, M_{d_{14}}(s)$) were built with 9 poles and 7 zeros, the remaining models were built with 9 poles and 8 zeros. All estimated models have a fit to estimation data of at least 99.84% and a minimum damping of $\zeta_{min} = 15\%$ was used to convert the estimated models to the reference ones. The SISO transfer functions of the resulting reference model are

$$\begin{aligned}
M_{d_{11}}(s) &= \frac{-0.053848(s+305.2)(s^2+1.676s+2.088)(s^2+0.222s+23.82)(s^2+5.544s+85.99)}{(s+0.3185)(s^2+3.463s+15.95)(s^2+1.534s+26.15)(s^2+5.229s+86.24)(s^2+9.034s+243.1)},\\
M_{d_{12}}(s) &= \frac{-0.55289(s-58.15)(s-13.97)(s^2-0.03165s+9.719)(s^2-0.649s+20.91)(s^2+4.913s+2154)}{(s+2.372\times10^4)(s+7.947)(s+0.6457)(s^2+1.677s+12.65)(s^2+1.563s+27.16)(s^2+6.485s+204.8)},\\
M_{d_{13}}(s) &= \frac{-0.0020882(s-90.89)(s-9.742)(s^2-0.8692s+9.28)(s^2-0.1363s+19.98)(s^2+18.01s+2784)}{(s+100.5)(s+10.83)(s+0.5549)(s^2+2.014s+11.14)(s^2+1.574s+27.53)(s^2+7.003s+208.4)},\\
M_{d_{14}}(s) &= \frac{-0.00017322(s^2-1.698s+27.89)(s^2+3.249s+66.45)(s^2+4.688s+83.71)(s^2-53.11s+1609)}{(s+0.5356)(s^2+2.369s+15.13)(s^2+1.556s+26.88)(s^2+2.461s+67.29)(s^2+8.175s+124.6)},
\end{aligned} \tag{C.4}$$

$$\begin{aligned}
M_{d_{21}}(s) &= \frac{0.021935(s-11.59)(s^2-0.2879s+9.982)(s^2-0.5272s+19.87)(s^2+41.32s+3540)}{(s+25.87)(s+10.2)(s+0.8428)(s^2+1.514s+12.36)(s^2+1.566s+27.26)(s^2+6.567s+206.2)},\\
M_{d_{22}}(s) &= \frac{0.0013659(s-146.7)(s+77.7)(s+1.217)(s+0.3094)(s^2+0.2196s+24.48)(s^2+6.407s+85.19)}{(s+0.02473)(s^2+4.316s+17.24)(s^2+1.541s+26.39)(s^2+6.028s+85.33)(s^2+8.226s+233.2)},\\
M_{d_{23}}(s) &= \frac{-0.031336(s-63.36)(s-9.314)(s^2-0.7796s+9.679)(s^2-0.2446s+19.45)(s^2+4.632s+2381)}{(s+1322)(s+10.52)(s+0.737)(s^2+1.838s+12.31)(s^2+1.565s+27.22)(s^2+6.704s+200.1)},\\
M_{d_{24}}(s) &= \frac{7.2976\times10^{-5}(s-41.18)(s+9.052)(s^2-1.702s+26.48)(s^2+4.01s+101.4)(s^2+7.668s+1055)}{(s+0.6672)(s^2+2.338s+13.31)(s^2+1.539s+26.31)(s^2+4.657s+105.6)(s^2+8.388s+267.2)},
\end{aligned} \tag{C.5}$$

$$\begin{aligned}
M_{d_{31}}(s) &= \frac{0.027725(s-8.536)(s^2-1.267s+9.359)(s^2-0.1624s+19.59)(s^2+89.85s+8198)}{(s+54.24)(s+7.628)(s+0.8925)(s^2+2.131s+11.97)(s^2+1.568s+27.3)(s^2+7.183s+210.2)},\\
M_{d_{32}}(s) &= \frac{0.00081494(s-9.934)(s+0.03963)(s^2-0.6932s+9.62)(s^2-0.5574s+19.7)(s^2-32.01s+4424)}{(s+8.533)(s+0.5138)(s+0.1942)(s^2+1.38s+13.24)(s^2+1.557s+26.94)(s^2+6.933s+202.2)},\\
M_{d_{33}}(s) &= \frac{0.0015856(s-135.9)(s+60.02)(s^2+3.214s+3.317)(s^2+0.2614s+23.04)(s^2+11.32s+77.74)}{(s+0.6963)(s^2+2.66s+16.93)(s^2+1.518s+25.59)(s^2+8.893s+88)(s^2+10.16s+247.4)},\\
M_{d_{34}}(s) &= \frac{-0.00016311(s^2-1.709s+28.31)(s^2+6.098s+44.32)(s^2+3.576s+221)(s^2-52.68s+1634)}{(s+0.9783)(s^2+2.294s+14.8)(s^2+1.551s+26.73)(s^2+7.498s+52.29)(s^2+8.253s+281.1)},
\end{aligned} \tag{C.6}$$

$$\begin{aligned}
M_{d_{41}}(s) &= \frac{3.8757(s-5.585)(s^2+6.466s+29.54)(s^2-2.042s+29.54)(s^2-32.38s+1.281\times10^4)}{(s+4.08\times10^4)(s^2+4.215s+8.664)(s^2+2.072s+16.37)(s^2+1.57s+27.38)(s^2+9.454s+236.6)},\\
M_{d_{42}}(s) &= \frac{0.00029343(s+11.21)(s-5.358)(s^2+7.151s+28.95)(s^2-2.151s+29.84)(s^2-37.25s+5821)}{(s+16.87)(s^2+4.182s+7.532)(s^2+2.095s+15.72)(s^2+1.566s+27.23)(s^2+8.645s+251.4)},\\
M_{d_{43}}(s) &= \frac{0.00078432(s-5.773)(s+0.7528)(s^2-1.901s+28.85)(s^2+13.75s+113.7)(s^2-47s+2720)}{(s+33.01)(s+2.324)(s+0.9289)(s^2+2.33s+14.3)(s^2+1.554s+26.83)(s^2+7.108s+177.3)},\\
M_{d_{44}}(s) &= \frac{0.00019602(s-219.4)(s+121.3)(s+3.052)(s+1.485)(s^2+0.8742s+25.21)(s^2+8.586s+116)}{(s+0.9702)(s^2+2.208s+14.74)(s^2+1.547s+26.58)(s^2+8.78s+107.5)(s^2+10.67s+283.9)}.
\end{aligned} \tag{C.7}$$

C.5 Reference model for the 39-bus New-England test system, MIMO formulation

The reference model $M_d(s)$ used in Section 5.2.3 was built using the method described in Section 3.5.2. The transfer functions $M_{d_{11}}(s)$ and $M_{d_{12}}(s)$ were built with 9 poles and 7 zeros, the transfer function $M_{d_{21}}(s)$ with with 9 poles and 8 zeros, and $M_{d_{22}}(s)$ with 10 poles and 8 zeros. All estimated models have a fit to estimation data of at least 99.99% and the resulting reference model, for a $\zeta_{min} = 15\%$ is

$$
\begin{aligned}
M_{d_{11}}(s) =& \frac{-0.030252(s+421.1)(s^2+0.3511s+0.8424)}{(s+23.48)(s+0.9674)(s+0.4787)(s^2+1.109s+13.67)} \times \\
& \frac{(s^2+1.077s+13.79)(s^2+5.083s+92.21)}{(s^2+2.811s+38.07)(s^2+4.277s+82.76)} \\
M_{d_{12}}(s) =& \frac{0.0038216(s-519.3)(s^2-0.1824s+3.439)}{(s+13.43)(s+2.186)(s+0.3547)(s^2+1.113s+13.76)} \times \\
& \frac{(s^2+2.287s+16.73)(s^2+0.1006s+88.11)}{(s^2+2.913s+35.57)(s^2+3.074s+67.3)} \\
M_{d_{21}}(s) =& \frac{-0.00010692(s-171.5)(s+51.41)(s-11.03)(s+3.322)}{(s+13.89)(s^2+0.7965s+0.3832)(s^2+1.098s+13.39)} \times \\
& \frac{(s^2+0.5448s+4.683)(s^2+9.385s+29.34)}{(s^2+2.87s+41.17)(s^2+3.099s+71.12)} \\
M_{d_{22}}(s) =& \frac{-0.023089(s+780.8)(s+11.43)(s^2+0.2093s+0.699)}{(s+43.1)(s+5.475)(s^2+0.8182s+0.4225)(s^2+1.099s+13.42)} \times \\
& \frac{(s^2+0.7277s+14)(s^2+2.793s+40.11)}{(s^2+3.867s+38.77)(s^2+3.092s+68.56)}.
\end{aligned}
\tag{C.8}
$$

APPENDIX D – SMIB electric power equation deduction

This appendix chapter presents the deduction of an expression to approximate the power-angle curve of a Single-Machine Infinite-Bus system with parallel AC/DC transmission. The strategy adopted is to replace the HVDC bipoles by current sources, as shown in Figure D.1. So, each side of the bipole is replaced by a current source, were the magnitude of the current is equivalent to the one consumed by the original AC/DC converters.

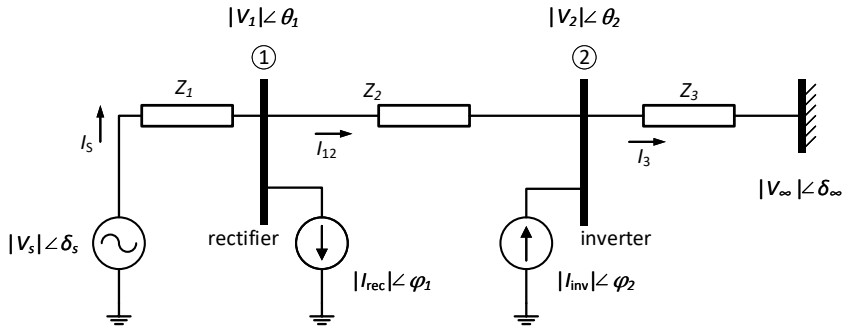

Figure D.1 – Diagram of an SMIB system with two current sources

Consider the system illustrated in Figure D.1, where the impedance of each line is constant and defined as

$$\begin{aligned} Z_1 &= R_1 + jX_1 = |Z_1|\angle\gamma_1, \\ Z_2 &= R_2 + jX_2 = |Z_2|\angle\gamma_2, \\ Z_3 &= R_3 + jX_3 = |Z_3|\angle\gamma_3, \end{aligned}$$

and that the power consumed by AC/DC converters of the bipoles at bus 1 (rectifier) and bus 2 (inverter) are, respectively,

$$S_{\text{rec},t} = P_{\text{rec},t} + jQ_{\text{rec},t} = |S_{\text{rec},t}|\angle\varphi_{\text{rec},t},$$

$$S_{\text{inv},t} = P_{\text{inv},t} + jQ_{\text{inv},t} = |S_{\text{inv},t}|\angle\varphi_{\text{inv},t}.$$

So, the complex current of each current source is defined as

$$\begin{aligned} I_{\text{rec},t} &= \left(\frac{S_{\text{rec},t}}{V_{1,t}}\right)^* = \frac{|S_{\text{rec},t}|}{|V_{1,t}|}\angle(\theta_{1,t} - \varphi_{\text{rec},t}) = |I_{\text{rec},t}|\angle\varphi_{1,t} \\ I_{\text{inv},t} &= \left(\frac{S_{\text{inv},t}}{V_{2,t}}\right)^* = \frac{|S_{\text{inv},t}|}{|V_{2,t}|}\angle(\theta_{2,t} - \varphi_{\text{inv},t}) = |I_{\text{inv},t}|\angle\varphi_{2,t}. \end{aligned} \tag{D.1}$$

Applying Kirchhoff's current law at nodes 1 and 2 we have

$$\begin{aligned} I_s &= I_{\text{rec}} + I_{12} \\ I_3 &= I_{12} - I_{\text{inv}}, \end{aligned} \tag{D.2}$$

and by Ohm's law we have

$$V_s = V_1 + Z_1 I_s, \tag{D.3}$$

where

$$\begin{aligned} V_1 &= V_2 + Z_2 I_{12}, \\ V_2 &= V_\infty + Z_3 I_3. \end{aligned} \tag{D.4}$$

Replacing (D.2) and (D.4) in (D.3), we have

$$V_s = V_\infty + Z_3(I_{12} - I_{\text{inv}}) + Z_2 I_{12} + Z_1(I_{\text{rec}} + I_{12})$$

and solving it for I_{12}, we have that

$$I_{12} = \frac{V_s - V_\infty - Z_1 I_{\text{rec}} + Z_3 I_{\text{inv}}}{Z_1 + Z_2 + Z_3}. \tag{D.5}$$

The output power if the generator is

$$S_s = V_s I_s^*. \tag{D.6}$$

Replacing (D.2) and (D.5) in (D.6) we have the following expression

$$\begin{aligned} S_{s,t} &= V_s \left(\frac{V_s - V_\infty - Z_1 I_{\text{rec},t} + Z_3 I_{\text{inv},t}}{Z_{eq}} + I_{\text{rec},t} \right)^* \\ S_{s,t} &= V_s \left(\frac{V_s - V_\infty + (Z_2 + Z_3) I_{\text{rec},t} + Z_3 I_{\text{inv},t}}{Z_{eq}} \right)^* \\ S_{s,t} &= \frac{|V_s|^2}{|Z_{eq}|} \angle \gamma_{eq} - \frac{|V_s||V_\infty|}{|Z_{eq}|} \angle \left(\gamma_{eq} + \delta_{s,t} - \delta_\infty\right) \\ &\quad + \frac{|V_s||Z_{23}||I_{\text{rec},t}|}{|Z_{eq}|} \angle (\delta_{s,t} - \varphi_{1,t} - \gamma_{23} + \gamma_{eq}) \\ &\quad + \frac{|V_s||Z_3||I_{\text{inv},t}|}{|Z_{eq}|} \angle (\delta_{s,t} - \varphi_{2,t} - \gamma_3 + \gamma_{eq}), \end{aligned} \tag{D.7}$$

where $|Z_{23}|\angle\gamma_{23} = |Z_2|\angle\gamma_2 + |Z_3|\angle\gamma_3$ and $|Z_{eq}|\angle\gamma_{eq} = |Z_1|\angle\gamma_1 + |Z_2|\angle\gamma_2 + |Z_3|\angle\gamma_3$, $\varphi_{1,t} = \theta_{1,t} - \varphi_{\text{rec},t}$ and $\varphi_{2,t} = \theta_{2,t} - \varphi_{\text{inv},t}$. The internal voltage magnitude $|V_s|$ and the infinite bus voltage phasor$|V_\infty|\angle\delta_\infty$ are considered to be constant.

D.1 Approximation of the power-angle equation

The Equation (D.7) computes the apparent power output of the generator in function of the rotor angle δ_s and the current phasors $|I_{\text{rec},t}|\angle\varphi_{1,t}$ and $|I_{\text{inv},t}|\angle\varphi_{2,t}$. That is, the equation depends on time varying parameters and, therefore, cannot be used to compute the power-angle curve beforehand. Some approximations are proposed in order to build an expression that computes the output active power in function of the rotor angle.

- First, it is considered that the resistance of the transmission lines are negligible, that is $Z_1 = jX_1$, $Z_2 = jX_2$ and $Z_3 = jX_3$.

Then, so the apparent power output of the generator becomes

$$\begin{aligned} S_{s,t} = & \frac{|V_s|^2}{X_1+X_2+X_3}\angle 90^\circ - \frac{|V_s||V_\infty|}{X_1+X_2+X_3}\angle\left(90^\circ + \delta_{s,t} - \delta_\infty\right) \\ & + \frac{(X_2+X_3)|V_s||I_{\text{rec}}|}{X_1+X_2+X_3}\angle(\delta_{s,t} - \theta_{1,t} + \varphi_{\text{rec},t}) \\ & + \frac{(X_3)|V_s||I_{\text{inv}}|}{X_1+X_2+X_3}\angle(\delta_{s,t} - \theta_{2,t} + \varphi_{\text{inv},t}). \end{aligned} \tag{D.8}$$

Separating the real component of (D.8), the following expression for the active power output P_s is obtained

$$\begin{aligned} P_{s,t} = & P_1 \sin\left(\delta_{s,t} - \delta_\infty\right) + P_2|I_{\text{rec},t}|\cos(\delta_{s,t} - \theta_{1,t} + \varphi_{\text{rec},t}) \\ & + P_3|I_{\text{inv},t}|\cos(\delta_{s,t} - \theta_{2,t} + \varphi_{\text{inv},t}), \end{aligned} \tag{D.9}$$

where

$$\begin{aligned} P_1 &= \frac{|V_s||V_\infty|}{X_1+X_2+X_3} \\ P_2 &= \frac{(X_2+X_3)|V_s|}{X_1+X_2+X_3} \\ P_3 &= \frac{X_3|V_s|}{X_1+X_2+X_3} \end{aligned} \tag{D.10}$$

Considering the time window used for transient stability analysis, the following assumptions are proposed over the AC/DC converters of the bipoles dynamics in order to simplify Equation (D.9)

- The magnitude of the current drained by the converters is constant

$$\begin{aligned} |I_{\text{rec}}| &= \frac{|S_{\text{rec,t}}|}{|V_{1,t}|} = \frac{|S_{\text{rec},0}|}{|V_{1,0}|} \\ |I_{\text{inv}}| &= \frac{|S_{\text{inv,t}}|}{|V_{2,t}|} = \frac{|S_{\text{inv},0}|}{|V_{2,0}|} \end{aligned} \tag{D.11}$$

- The power factor of each apparent power consumed is constant (no change in the power order of the converters).

$$\begin{aligned} \varphi_{\text{rec},t} &= \varphi_{\text{rec},0}, \\ \varphi_{\text{inv},t} &= \varphi_{\text{inv},0} \end{aligned} \tag{D.12}$$

- The values of active power consumed by the rectifier and inverter sides have approximately the same magnitude and opposite direction and the values of reactive

power consumed by both sides of the bipoles are approximately equal (ARRILLAGA, 1998). This is illustrated in a phasor diagram in Figure D.2.

$$\begin{aligned} P_{\text{inv},t} &\approx -P_{\text{rec},t} \\ Q_{\text{inv},t} &\approx Q_{\text{rec},t}. \end{aligned} \tag{D.13}$$

What leads to

$$\begin{aligned} |S_{\text{inv},0}| &\approx |S_{\text{rec},0}| \\ \varphi_{\text{inv}} &\approx 180^\circ - \varphi_{\text{rec}} \end{aligned} \tag{D.14}$$

- The initial condition values of the magnitudes of the bus 1 and bus 2 voltages are approximately equal.

$$|V_{1,0}| \approx |V_{2,0}| \tag{D.15}$$

This assumption combined with the previous ones leads to following equivalence

$$|I_{\text{red}}| \approx |I_{\text{inv}}| \tag{D.16}$$

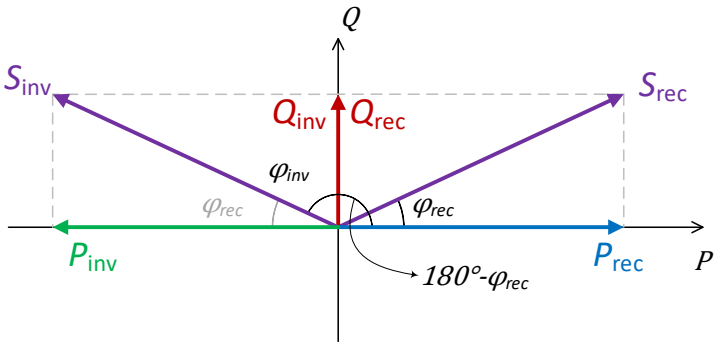

Figure D.2 – Phasor diagram of the approximated consumed power of the bipoles converters

The Equation (D.9) consists of three terms, the first one is SMIB power-angle expression and the second and third terms are related to the power consumed by the converters of the HVDC bipoles, at the rectifier and inverter sides. The assumptions proposed over the AC/DC converters dynamics leads to the following simplified Equation

$$\begin{aligned} P_{s2,t} =& \mathsf{P}_1 \sin(\delta_{s,t} - \delta_\infty) + \hat{P}_1 \cos(\delta_{s,t} - \theta_{1,t} + \varphi_{\text{rec}}) \\ & - \mathsf{P}_3 \cos(\delta_{s,t} - \theta_{2,t} - \varphi_{\text{rec}}), \end{aligned} \tag{D.17}$$

where

$$\begin{aligned} \mathsf{P}_1 &= \frac{|V_s||V_\infty|}{X_1 + X_2 + X_3} \\ \hat{P}_1 &= \frac{(X_2 + X_3)|V_s||I_{\text{rec}}|}{X_1 + X_2 + X_3} \\ \mathsf{P}_3 &= \frac{X_3|V_s||I_{\text{rec}}|}{X_1 + X_2 + X_3} \end{aligned} \tag{D.18}$$

However, Equation (D.17) still depends on the time varying parameters $\delta_{s,t}$, $\theta_{1,t}$ and $\theta_{s,t}$ and, therefore, two other assumptions are made

- The angle of bus 2 is approximately equal to the infinite-bus angle

$$\theta_{2,t} \approx \theta_{\infty} \tag{D.19}$$

- The difference between the rotor angle and the voltage angle of bus 1 is considered to be constant

$$\delta_{s,t} - \theta_{1,t} \approx \delta_{s,0} - \theta_{1,0} \tag{D.20}$$

As the infinite-bus angle is considered to be zero, the resulting equation for approximating the power-angle relation of the system of Figure D.1 is

$$\bar{P}_s(\delta_{s,t}) = \mathsf{P}_1 \sin \delta_{s,t} + \mathsf{P}_2 - \mathsf{P}_3 \cos(\delta_{s,t} - \varphi_{\text{rec}}), \tag{D.21}$$

where $\delta_{s,0}$ and $\theta_{1,0}$ are the initial condition values (pre-fault values) of the rotor angle and bus 1 voltage angle, and

$$\begin{aligned} \mathsf{P}_1 &= \frac{|V_s||V_\infty|}{X_1 + X_2 + X_3}, \\ \mathsf{P}_2 &= \frac{(X_2 + X_3)|V_s||I_{\text{rec}}|}{X_1 + X_2 + X_3} \cos(\delta_{s,0} - \theta_{1,0} + \varphi_{\text{rec}}), \\ \mathsf{P}_3 &= \frac{X_3|V_s||I_{\text{rec}}|}{X_1 + X_2 + X_3}. \end{aligned} \tag{D.22}$$

D.1.1 Equilibrium Points

The equilibrium points are essential for the transient stability analysis. At an equilibrium point, the mechanical power input matches the electric power output. On the power-angle diagram, those points corresponds to the intersection of the electric power curve and the mechanical input line, that is, $\bar{P}_s(\delta_{s,t}) = P_m$. Considering that the power-angle relation can be modeled by Equation (D.21), the rotor angle at the equilibrium points δ_{ep} can be found as follows

$$\bar{P}_s(\delta_{ep}) = \mathsf{P}_1 \sin \delta_{ep} + \mathsf{P}_2 - \mathsf{P}_3 \cos(\delta_{ep} - \varphi_{\text{rec}}) = P_m, \tag{D.23}$$

where P_1, P_2 and P_3 are defined in Equation (D.22). Rearranging Equation (D.23) we have,

$$\underbrace{(\mathsf{P}_1 - \mathsf{P}_3 \sin \varphi_{\text{rec}})}_{A} \sin \delta_{ep} \underbrace{-\mathsf{P}_3 \cos \varphi_{\text{rec}}}_{B} \cos \delta_{ep} + \underbrace{\mathsf{P}_2 - P_m}_{C} = 0. \tag{D.24}$$

Renaming some the variables we have

$$A \sin \delta_{ep} + B \cos \delta_{ep} + C = 0, \tag{D.25}$$

where

$$\begin{aligned} A &= \mathsf{P}_1 - \mathsf{P}_3 \sin \varphi_{\text{rec}}, \\ B &= -\mathsf{P}_3 \cos \varphi_{\text{rec}}, \\ C &= \mathsf{P}_2 - P_m. \end{aligned} \tag{D.26}$$

The term $\cos\delta_{ep}$ can be expressed in function of the $\sin\delta_{ep}$ as follows

$$\cos\delta_{ep} = \pm\sqrt{1-\sin^2\delta_{ep}},$$

so the Equation (D.25) can be rewritten as

$$\begin{aligned} &B(\pm\sqrt{1-\sin^2\delta_{ep}}) = -A\sin\delta_{ep} - C, \\ &B^2(1-\sin^2\delta_{ep}) = A^2\sin^2\delta_{ep} + 2AC\sin\delta_{ep} + C^2, \\ &\underbrace{(-A^2-B^2)}_{a}\sin^2\delta_{ep}\underbrace{-2AC}_{b}\sin\delta_{ep} + \underbrace{B^2-C^2}_{c} = 0. \end{aligned} \tag{D.27}$$

Replacing the variables, the following second degree equation is obtained

$$ax^2 + bx + c = 0, \tag{D.28}$$

where,

$$\begin{aligned} x &= \sin\delta_{ep}, \\ a &= -A^2 - B^2, \\ b &= -2AC, \\ c &= B^2 - C^2. \end{aligned} \tag{D.29}$$

So, the equilibrium points are

$$\delta_{ep} = \sin^{-1} x \tag{D.30}$$

where, x is calculated by solving Equation (D.28), considering the variables substitutions (D.22), (D.26) and (D.29). As (D.28) is a quadratic equation, two solutions are found

$$x = \frac{-AC \mp B\sqrt{A^2+B^2-C^2}}{A^2+B^2}. \tag{D.31}$$

what leads to two equilibrium points

$$\delta_{ep1} = \sin^{-1}\left(\frac{-AC - B\sqrt{A^2+B^2-C^2}}{A^2+B^2}\right) \tag{D.32}$$

and

$$\delta_{ep2} = \sin^{-1}\left(\frac{-AC + B\sqrt{A^2+B^2-C^2}}{A^2+B^2}\right). \tag{D.33}$$

With the substitution of variables (D.22), (D.26) and (D.29) we have

$$\begin{aligned} \delta_{ep1} = \sin^{-1}\Bigg(&\frac{(\mathsf{P}_3\sin\varphi_{\text{rec}} - \mathsf{P}_1)(\mathsf{P}_2 - P_m)}{\mathsf{P}_1^2 - 2\mathsf{P}_1\mathsf{P}_3\sin\varphi_{\text{rec}} + \mathsf{P}_3^2} + \\ &+ \frac{\mathsf{P}_3\cos\varphi_{\text{rec}}\sqrt{\mathsf{P}_1^2 - 2\mathsf{P}_1\mathsf{P}_3\sin\varphi_{\text{rec}} + \mathsf{P}_3^2 - (\mathsf{P}_2 - P_m)^2}}{\mathsf{P}_1^2 - 2\mathsf{P}_1\mathsf{P}_3\sin\varphi_{\text{rec}} + \mathsf{P}_3^2}\Bigg) \end{aligned} \tag{D.34}$$

and

$$\begin{aligned} \delta_{ep2} = \sin^{-1}\Bigg(&\frac{(\mathsf{P}_3\sin\varphi_{\text{rec}} - \mathsf{P}_1)(\mathsf{P}_2 - P_m)}{\mathsf{P}_1^2 - 2\mathsf{P}_1\mathsf{P}_3\sin\varphi_{\text{rec}} + \mathsf{P}_3^2} - \\ &- \frac{\mathsf{P}_3\cos\varphi_{\text{rec}}\sqrt{\mathsf{P}_1^2 - 2\mathsf{P}_1\mathsf{P}_3\sin\varphi_{\text{rec}} + \mathsf{P}_3^2 - (\mathsf{P}_2 - P_m)^2}}{\mathsf{P}_1^2 - 2\mathsf{P}_1\mathsf{P}_3\sin\varphi_{\text{rec}} + \mathsf{P}_3^2}\Bigg) \end{aligned} \tag{D.35}$$

APPENDIX E – Deduction of the electric power equation of the two machine system, considering shunt capacitor banks/filters and loads

This Appendix chapter presents the deduction of the proposed equation for the electric power output of the two machine system with parallel AC and DC transmission, considering shunt capacitor banks/filters and loads. The deduction is based on the premise that, for the purpose of the transient stability analysis, the AC/DC converters can be modeled by equivalent current sources.

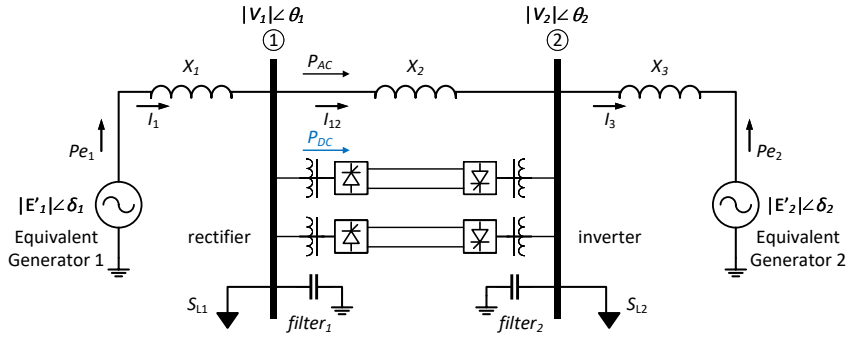

Figure E.1 – Two machine system with parallel AC and DC transmission and shunt capacitor banks/filters.

Consider the two machine system illustrated in Figure E.1, in order to build an expression for the electric power output for each of the generators, the following steps are done. First, the shunt capacitor banks/filters and loads are modeled as constant impedance loads, as follows

$$\dot{Z}_{sh1} = \dot{Z}_{L1} + \dot{X}_{sh1} \quad \text{and} \quad \dot{Z}_{sh2} = \dot{Z}_{L2} + \dot{X}_{sh2}, \tag{E.1}$$

where $\dot{X}_{sh1} = -jX_{sh1}$ and $\dot{X}_{sh2} = -jX_{sh2}$ are the reactances of the capacitor banks/filters and $\dot{Z}_{L1}$ and $\dot{Z}_{L2}$ are the impedances of the loads, defined as

$$\dot{Z}_{L1} = \frac{|V_{1,0}|^2}{S^*_{L1}} \quad \text{and} \quad \dot{Z}_{L2} = \frac{|V_{2,0}|^2}{S^*_{L2}}, \tag{E.2}$$

where $S_{L1} = P_{L1} + jQ_{L1}$ and $S_{L2} = P_{L2} + jQ_{L2}$ are the complex loads and $V_{1,0}$ and $V_{2,0}$ are the magnitude of the bus voltages at the rectifier and inverter buses, respectively. Once the load impedances are constant, i.e. they do not change with the voltage, they are defined using the initial condition of the bus voltages, indicated by the subscript notation

"$_{,0}$". Then, each side of the HVDC is replaced by an equivalent current source, according to Equation (7.1), as illustrated in Figure E.2a. Also, a $\Delta \rightarrow Y$ transformation is used to rearrange the impedances of the system. The resulting diagram is presented in Figure E.2b, where

$$\dot{Z}_a = \frac{\dot{Z}_{sh1}\dot{X}_2}{\dot{Z}_{sh1} + \dot{Z}_{sh2} + \dot{X}_2}, \quad \dot{Z}_b = \frac{\dot{Z}_{sh2}\dot{X}_2}{\dot{Z}_{sh1} + \dot{Z}_{sh2} + \dot{X}_2}, \quad \dot{Z}_c = \frac{\dot{Z}_{sh1}\dot{Z}_{sh2}}{\dot{Z}_{sh1} + \dot{Z}_{sh2} + \dot{X}_2}, \tag{E.3}$$

and $\dot{X}_2 = +jX_2$.

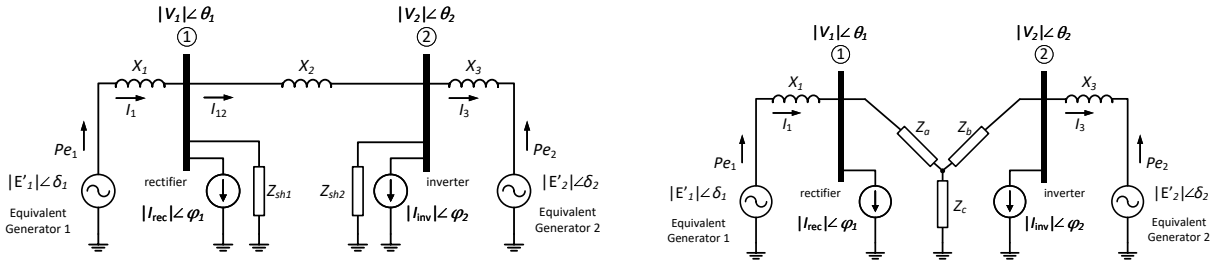

(a) Two machine system with shunt capacitor banks/filters and loads.

(b) Rearranged system.

Figure E.2 – Equivalent system using current sources to model the HVDC system, with shunt capacitor banks/filters and loads.

Supposing that the internal voltages and rotor angles of the generators are known, to compute the electric power output of the equivalent generator 1 it is necessary to compute the current I_1 that flows through X_1 in the diagrams of Figure E.2. Equivalently, to compute the electric power output of the equivalent generator 2 it is necessary to know I_3. Since the apparent electric power output of each is defined as

$$Se_{1,t} = |E'_1|\angle\delta_{1,t}\dot{I}_1^* \quad \text{and} \quad Se_{2,t} = |E'_2|\angle\delta_{2,t}\dot{I}_3^*, \tag{E.4}$$

where $\dot{I}_1$ and $\dot{I}_3$ are the complex currents flowing through the line inductances X_1 and X_3, respectively. The approach used to find the expressions for $\dot{I}_1$ and $\dot{I}_3$ is to compute the current for each source independently and combine them using the superposition theorem. So, the currents $\dot{I}_1$ and $\dot{I}_3$ are divided into four components, one for each source,

$$\dot{I}_1 = \dot{I}_1^I - \dot{I}_1^{II} + \dot{I}_1^{III} + \dot{I}_1^{IV} \quad \text{and} \quad \dot{I}_3 = \dot{I}_2^I - \dot{I}_2^{II} + \dot{I}_2^{III} + \dot{I}_2^{IV}. \tag{E.5}$$

To facilitate understanding of the following deduction, different colors are used to represent the currents $\dot{I}_1$ and $\dot{I}_3$, as displayed in the diagrams of Figure E.3.

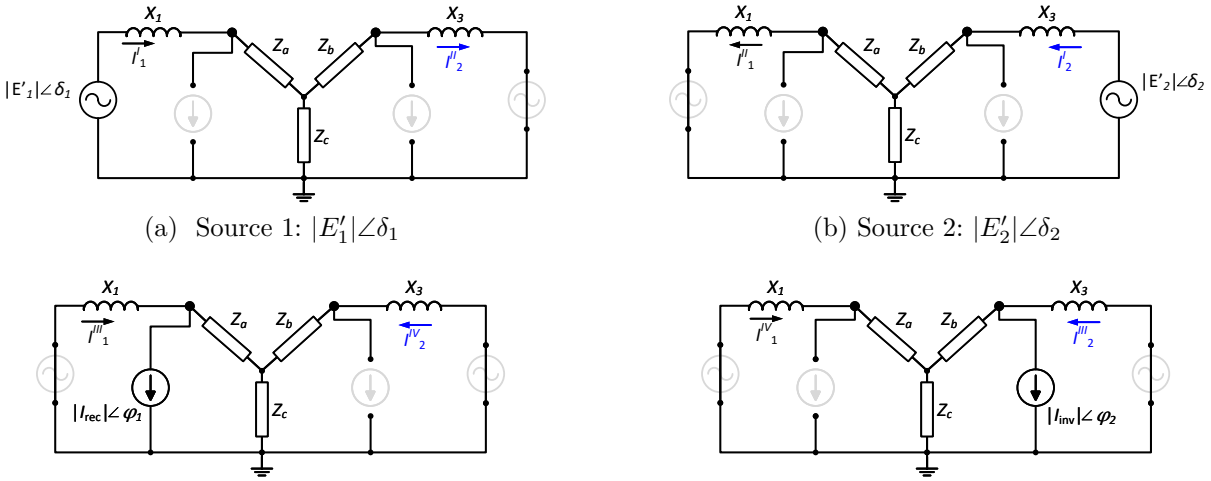

(a) Source 1: $|E_1'|\angle\delta_1$

(b) Source 2: $|E_2'|\angle\delta_2$

(c) Source 3: $|I_{rec}|\angle\phi_1$

(d) Source 4: $|I_{inv}|\angle\phi_2$

Figure E.3 – Superposition theorem applied to the two machine system with parallel AC and DC transmission and shunt capacitor banks/filters.

Source 1:

Solving the circuit of Figure E.3a one has that

$$\dot{I}_1^I = \frac{\dot{Z}_b + \dot{Z}_c + \dot{X}_3}{(\dot{Z}_a + \dot{X}_1)(\dot{Z}_b + \dot{Z}_c + \dot{X}_3) + \dot{Z}_c(\dot{Z}_b + \dot{X}_3)}\dot{V}_{G1} = \dot{Y}_{A1}\dot{V}_{G1} = |Y_{A1}|\angle\gamma_{A1}|E_1'|\angle\delta_1 \quad \text{(E.6)}$$

and

$$\dot{I}_2^{II} = \frac{\dot{Z}_c}{(\dot{Z}_a + \dot{X}_1)(\dot{Z}_b + \dot{Z}_c + \dot{X}_3) + \dot{Z}_c(\dot{Z}_b + \dot{X}_3)}\dot{V}_{G1} = \dot{Y}_{B2}\dot{V}_{G1} = |Y_{B2}|\angle\gamma_{B2}|E_1'|\angle\delta_1. \quad \text{(E.7)}$$

Source 2:

Solving the circuit of Figure E.3b one has that

$$\dot{I}_1^{II} = \frac{\dot{Z}_c}{(\dot{Z}_a + \dot{X}_1)(\dot{Z}_b + \dot{Z}_c + \dot{X}_3) + \dot{Z}_c(\dot{Z}_b + \dot{X}_3)}\dot{V}_{G2} = \dot{Y}_{B1}\dot{V}_{G2} = |Y_{B1}|\angle\gamma_{B1}|E_2'|\angle\delta_2 \quad \text{(E.8)}$$

and

$$\dot{I}_2^I = \frac{\dot{Z}_a + \dot{Z}_c + \dot{X}_1}{(\dot{Z}_a + \dot{X}_1)(\dot{Z}_b + \dot{Z}_c + \dot{X}_3) + \dot{Z}_c(\dot{Z}_b + \dot{X}_3)}\dot{V}_{G2} = \dot{Y}_{A2}\dot{V}_{G2} = |Y_{A2}|\angle\gamma_{A2}|E_2'|\angle\delta_2. \quad \text{(E.9)}$$

Source 3:

Solving the circuit of Figure E.3c one has that

$$\dot{I}_1^{III} = \frac{\dot{Z}_a(\dot{Z}_b + \dot{Z}_c + \dot{X}_3) + \dot{Z}_c(\dot{Z}_b + \dot{X}_3)}{(\dot{Z}_a + \dot{X}_1)(\dot{Z}_b + \dot{Z}_c + \dot{X}_3) + \dot{Z}_c(\dot{Z}_b + \dot{X}_3)}\dot{I}_{rec} = \dot{Y}_{C1}\dot{I}_{rec} = |Y_{C1}|\angle\gamma_{C1}|I_{rec}|\angle\phi_1 \quad \text{(E.10)}$$

and

$$\dot{I}_2^{IV} = \frac{\dot{Z}_c\dot{X}_1}{(\dot{Z}_a+\dot{X}_1)(\dot{Z}_b+\dot{Z}_c+\dot{X}_3)+\dot{Z}_c(\dot{Z}_b+\dot{X}_3)}\dot{I}_{rec} = \dot{Y}_{D2}\dot{I}_{rec} = |Y_{D2}|\angle\gamma_{D2}|I_{rec}|\angle\phi_1. \tag{E.11}$$

Source 4:

Solving the circuit of Figure E.3d one has that

$$\dot{I}_1^{IV} = \frac{\dot{Z}_c\dot{X}_3}{(\dot{Z}_a+\dot{X}_1)(\dot{Z}_b+\dot{Z}_c+\dot{X}_3)+\dot{Z}_c(\dot{Z}_b+\dot{X}_3)}\dot{I}_{inv} = \dot{Y}_{D1}\dot{I}_{rec} = |Y_{D1}|\angle\gamma_{D1}|I_{inv}|\angle\phi_2 \tag{E.12}$$

and

$$\dot{I}_2^{III} = \frac{\dot{Z}_b(\dot{Z}_a+\dot{Z}_c+\dot{X}_1)+\dot{Z}_c(\dot{Z}_a+\dot{X}_1)}{(\dot{Z}_a+\dot{X}_1)(\dot{Z}_b+\dot{Z}_c+\dot{X}_3)+\dot{Z}_c(\dot{Z}_b+\dot{X}_3)}\dot{I}_{inv} = \dot{Y}_{C2}\dot{I}_{inv} = |Y_{C2}|\angle\gamma_{C2}|I_{inv}|\angle\phi_2. \tag{E.13}$$

Thus, combining (E.4) with (E.5) to (E.13) one has that the apparent electric power output of the equivalent generators 1 and 2 are

$$\begin{aligned} Se_{1,t} =& |E_1'|\angle\delta_{1,t}(\dot{I}_1^I - \dot{I}_1^{II} + \dot{I}_1^{III} + \dot{I}_1^{IV})^* \\ Se_{1,t} =& |Y_{A1}||E_1'|^2\angle(-\gamma_{A1}) - |Y_{B1}||E_1'||E_2'|\angle\left(-\gamma_{B1}+\delta_{1,t}-\delta_{2,t}\right) \\ &+ |Y_{C1}||E_1'||I_{\mathrm{rec},t}|\angle\left(-\gamma_{C1}+\delta_{1,t}-\theta_{1,t}+\varphi_{\mathrm{rec},t}\right) \\ &+ |Y_{D1}||E_1'||I_{\mathrm{inv},t}|\angle\left(-\gamma_{D1}+\delta_{1,t}-\theta_{2,t}+\varphi_{\mathrm{inv},t}\right). \end{aligned} \tag{E.14}$$

and

$$\begin{aligned} Se_{2,t} =& |E_2'|\angle\delta_{2,t}(\dot{I}_2^I - \dot{I}_2^{II} + \dot{I}_2^{III} + \dot{I}_2^{IV})^* \\ Se_{2,t} =& |Y_{A2}||E_2'|^2\angle(-\gamma_{A2}) - |Y_{B2}||E_1'||E_2'|\angle\left(-\gamma_{B2}+\delta_{2,t}-\delta_{1,t}\right) \\ &+ |Y_{C2}||E_2'||I_{\mathrm{inv},t}|\angle\left(-\gamma_{C1}+\delta_{2,t}-\theta_{2,t}+\varphi_{\mathrm{inv},t}\right) \\ &+ |Y_{D2}||E_2'||I_{\mathrm{rec},t}|\angle\left(-\gamma_{D2}+\delta_{2,t}-\theta_{1,t}+\varphi_{\mathrm{rec},t}\right). \end{aligned} \tag{E.15}$$

where

$$\begin{aligned} \dot{Y}_{A1} &= |Y_{A1}|\angle\gamma_{A1} = \frac{\dot{Z}_b+\dot{Z}_c+\dot{X}_3}{(\dot{Z}_a+\dot{X}_1)(\dot{Z}_b+\dot{Z}_c+\dot{X}_3)+\dot{Z}_c(\dot{Z}_b+\dot{X}_3)}, \\ \dot{Y}_{B1} &= |Y_{B1}|\angle\gamma_{B1} = \frac{\dot{Z}_c}{(\dot{Z}_a+\dot{X}_1)(\dot{Z}_b+\dot{Z}_c+\dot{X}_3)+\dot{Z}_c(\dot{Z}_b+\dot{X}_3)}, \\ \dot{Y}_{C1} &= |Y_{C1}|\angle\gamma_{C1} = \frac{\dot{Z}_a(\dot{Z}_b+\dot{Z}_c+\dot{X}_3)+\dot{Z}_c(\dot{Z}_b+\dot{X}_3)}{(\dot{Z}_a+\dot{X}_1)(\dot{Z}_b+\dot{Z}_c+\dot{X}_3)+\dot{Z}_c(\dot{Z}_b+\dot{X}_3)}, \\ \dot{Y}_{D1} &= |Y_{D1}|\angle\gamma_{D1} = \frac{\dot{Z}_c\dot{X}_3}{(\dot{Z}_a+\dot{X}_1)(\dot{Z}_b+\dot{Z}_c+\dot{X}_3)+\dot{Z}_c(\dot{Z}_b+\dot{X}_3)}, \end{aligned} \tag{E.16}$$

and

$$\begin{aligned}
\dot{Y}_{A2} &= |Y_{A2}|\angle\gamma_{A2} = \frac{\dot{Z}_a + \dot{Z}_c + \dot{X}_1}{(\dot{Z}_a + \dot{X}_1)(\dot{Z}_b + \dot{Z}_c + \dot{X}_3) + \dot{Z}_c(\dot{Z}_b + \dot{X}_3)}, \\
\dot{Y}_{B2} &= |Y_{B2}|\angle\gamma_{B2} = \frac{\dot{Z}_c}{(\dot{Z}_a + \dot{X}_1)(\dot{Z}_b + \dot{Z}_c + \dot{X}_3) + \dot{Z}_c(\dot{Z}_b + \dot{X}_3)} = \dot{Y}_{B1}, \\
\dot{Y}_{C2} &= |Y_{C2}|\angle\gamma_{C2} = \frac{\dot{Z}_b(\dot{Z}_a + \dot{Z}_c + \dot{X}_1) + \dot{Z}_c(\dot{Z}_a + \dot{X}_1)}{(\dot{Z}_a + \dot{X}_1)(\dot{Z}_b + \dot{Z}_c + \dot{X}_3) + \dot{Z}_c(\dot{Z}_b + \dot{X}_3)}, \\
\dot{Y}_{D2} &= |Y_{D2}|\angle\gamma_{D2} = \frac{\dot{Z}_c\dot{X}_1}{(\dot{Z}_a + \dot{X}_1)(\dot{Z}_b + \dot{Z}_c + \dot{X}_3) + \dot{Z}_c(\dot{Z}_b + \dot{X}_3)}.
\end{aligned} \tag{E.17}$$

Assuming that the rotor angle of the equivalent generator 2 is the angular reference of the system, that is $\delta_{2,t} = 0°$ and $\delta_{r,t} = \delta_{1,t} - 0$, and separating the real component of the apparent power of each generator, one has that

$$\begin{aligned}
Pe_{1,t} =& P_{10} + P_{11}\cos(\delta_{r,t} - \gamma_{B1}) + P_{12}|I_{\text{rec},t}|\cos(\delta_{1,t} - \theta_{1,t} + \varphi_{\text{rec},t} - \gamma_{C1}) \\
&+ P_{13}|I_{\text{inv},t}|\cos(\delta_{1,t} - \theta_{2,t} + \varphi_{\text{inv},t} - \gamma_{D1}),
\end{aligned} \tag{E.18}$$

where

$$\begin{aligned}
P_{10} &= |Y_{A1}||E_1'|^2\cos(\gamma_{A1}), \quad & P_{11} &= -|Y_{B1}||E_1'||E_2'|, \\
P_{12} &= |Y_{C1}||E_1'|, & P_{13} &= |Y_{D1}||E_1'|.
\end{aligned} \tag{E.19}$$

and

$$\begin{aligned}
Pe_{2,t} =& P_{20} + P_{21}\cos(-\delta_{1,t} - \gamma_{B2}) + P_{22}|I_{\text{inv},t}|\cos(\delta_{2,t} - \theta_{2,t} + \varphi_{\text{inv},t} - \gamma_{C1}) \\
&+ P_{23}|I_{\text{rec},t}|\cos(\delta_{2,t} - \theta_{1,t} + \varphi_{\text{rec},t} - \gamma_{D2}),
\end{aligned} \tag{E.20}$$

where

$$\begin{aligned}
P_{20} &= |Y_{A2}||E_2'|^2\cos(\gamma_{A2}), \quad & P_{21} &= -|Y_{B2}||E_1'||E_2'|, \\
P_{22} &= |Y_{C2}||E_2'|, & P_{23} &= |Y_{D2}||E_2'|.
\end{aligned} \tag{E.21}$$

E.1 Equilibrium points of the **a.c.a.** curve

As presented in Chapter 9, the assumptions proposed in Section 7.2 are used to simplify the Equations (E.18) and (E.20), replacing the time-varying parameter by initial condition ones. The resulting equations for approximating the electric power output of equivalent generators 1 and 2 are (9.13) and (9.15). Then, the approximated equation for the equivalent electrical power output (or the approximated power-angle equation) is presented in Equation (9.17). Also, as described in Section 7.4, the change in the total reactance of the system caused by the disconnection of the GUs needs to be considered during the computation of generation-rejection. Therefore, Equation (9.17) is rearranged into two equations, one for **b.c.a.** and one for **a.c.a.**. As presented in Section 9.1.1.

To apply the Algorithm 3 and compute the generation-rejection, it is necessary to define the unstable equilibrium point δ_{ep}^{uns} of the **a.c.a.** curve $\bar{P}e''_{eqv}(\delta_{r,t})$. The proposed equation for this curve is defined in (9.20) and it is repeated here for convenience.

$$\begin{aligned}\bar{P}e''_{eqv}(\delta_{r,t}) = C'' &+ N''_1\cos\left(\delta_{r,t} - \gamma''_{B1}\right) + N''_2\cos\left(\delta_{r,t} + \beta''_1\right) + N''_3\cos\left(\delta_{r,t} + \gamma''_{B2}\right) \\ &+ N''_4\cos\left(\delta_{r,t} - \beta''_2\right),\end{aligned} \tag{E.22}$$

where

$$\begin{aligned}C'' &= \frac{H_2(\mathsf{P}''_{10} + \mathsf{P}''_{12}) - H''_1(\mathsf{P}''_{20} + \mathsf{P}''_{22})}{H''_1 + H_2}, \\ N''_1 &= \frac{H_2\mathsf{P}''_{11}}{H''_1 + H_2},\ N''_2 = \frac{H_2\mathsf{P}''_{13}}{H''_1 + H_2},\ N''_3 = -\frac{H''_1\mathsf{P}''_{21}}{H''_1 + H_2},\ N''_4 = -\frac{H''_1\mathsf{P}''_{23}}{H''_1 + H_2}.\end{aligned} \tag{E.23}$$

and P''_{10}, P''_{11}, P''_{12}, P''_{13}, P''_{20}, P''_{21}, P''_{22}, P''_{23}, β''_1, and β''_2 are the weights defined with equations (9.14) and (9.16), but using the change of variables (7.17). And H''_1 is inertia constant of the equivalent generator 1 after the disconnection of the GUs, defined using the change of variables (7.18). That is, the parameters of the Equation (E.22) are defined as functions of a variable $x \in \mathrm{R}$.

The equilibrium points of Equation (E.22) are defined as the angles at which the electrical output power equals the mechanical input power. That is, $\bar{P}e''_{eqv}(\delta_{r,t}) = \bar{P}m_{eqv,1}$, where $\bar{P}m_{eqv,1}$ is the mechanical input after the control action (generation rejection). Thus, the rotor angle at the equilibrium points δ_{ep} can be found as follows

$$\begin{aligned}\bar{P}e''_{eqv}(\delta_{r,t}) = C'' &+ N''_1\cos\left(\delta_{r,t} - \gamma''_{B1}\right) + N''_2\cos\left(\delta_{r,t} + \beta''_1\right) + N''_3\cos\left(\delta_{r,t} + \gamma''_{B2}\right) \\ &+ N''_4\cos\left(\delta_{r,t} - \beta''_2\right) = \bar{P}m_{eqv,1}.\end{aligned} \tag{E.24}$$

Rearranging Equation (E.24) one has,

$$\begin{aligned}&\underbrace{\left(N''_1\sin(\gamma''_{B1}) - N''_2\sin(\beta''_1) - N''_3\sin(\gamma''_{B2}) + N''_4\sin(\beta''_2)\right)}_{\mathsf{A}}\sin\delta_{ep} \\ &+\underbrace{\left(N''_1\cos(\gamma''_{B1}) + N''_2\cos(\beta''_1) + N''_3\cos(\gamma''_{B2}) + N''_4\cos(\beta''_2)\right)}_{\mathsf{B}}\cos\delta_{ep} \\ &+\underbrace{C'' - Pm_{eqv,1}}_{\mathsf{C}} = 0,\end{aligned} \tag{E.25}$$

that can be presented as

$$\mathsf{A}\sin\delta_{ep} + \mathsf{B}\cos\delta_{ep} + \mathsf{C} = 0, \tag{E.26}$$

where

$$\begin{aligned}\mathsf{A} &= N''_1\sin(\gamma''_{B1}) - N''_2\sin(\beta''_1) - N''_3\sin(\gamma''_{B2}) + N''_4\sin(\beta''_2) \\ \mathsf{B} &= N''_1\cos(\gamma''_{B1}) + N''_2\cos(\beta''_1) + N''_3\cos(\gamma''_{B2}) + N''_4\cos(\beta''_2) \\ \mathsf{C} &= C'' - Pm_{eqv,1}.\end{aligned} \tag{E.27}$$

The term $\cos\delta_{ep}$ can be expressed in function of the $\sin\delta_{ep}$ as follows

$$\cos\delta_{ep} = \pm\sqrt{1 - \sin^2\delta_{ep}},$$

so the Equation (E.26) can be rewritten as

$$\begin{aligned} &\mathsf{B}(\pm\sqrt{1-\sin^2\delta_{ep}}) = -\mathsf{A}\sin\delta_{ep} - \mathsf{C}, \\ &\mathsf{B}^2(1-\sin^2\delta_{ep}) = \mathsf{A}^2\sin^2\delta_{ep} + 2\mathsf{AC}\sin\delta_{ep} + \mathsf{C}^2, \\ &\underbrace{(-\mathsf{A}^2-\mathsf{B}^2)}_{a}\sin^2\delta_{ep}\underbrace{-2\mathsf{AC}}_{b}\sin\delta_{ep} + \underbrace{\mathsf{B}^2-\mathsf{C}^2}_{c} = 0. \end{aligned} \tag{E.28}$$

Replacing the variables, the following second degree equation is obtained

$$a\mathsf{x}^2 + b\mathsf{x} + c = 0, \tag{E.29}$$

where,

$$\begin{aligned} \mathsf{x} &= \sin\delta_{ep}, \\ a &= -\mathsf{A}^2 - \mathsf{B}^2, \\ b &= -2\mathsf{AC}, \\ c &= \mathsf{B}^2 - \mathsf{C}^2. \end{aligned} \tag{E.30}$$

So, the equilibrium points are

$$\delta_{ep} = \sin^{-1}\mathsf{x} \tag{E.31}$$

where, x is calculated by solving Equation (E.29), considering the variables substitutions (E.27) and (E.30). As (E.29) is a quadratic equation, two solutions are found

$$\mathsf{x} = \frac{-\mathsf{AC} \mp \mathsf{B}\sqrt{\mathsf{A}^2+\mathsf{B}^2-\mathsf{C}^2}}{\mathsf{A}^2+\mathsf{B}^2}. \tag{E.32}$$

what leads to two equilibrium points

$$\delta_{ep1} = \sin^{-1}\left(\frac{-\mathsf{AC} - \mathsf{B}\sqrt{\mathsf{A}^2+\mathsf{B}^2-\mathsf{C}^2}}{\mathsf{A}^2+\mathsf{B}^2}\right) \tag{E.33}$$

and

$$\delta_{ep2} = \sin^{-1}\left(\frac{-\mathsf{AC} + \mathsf{B}\sqrt{\mathsf{A}^2+\mathsf{B}^2-\mathsf{C}^2}}{\mathsf{A}^2+\mathsf{B}^2}\right), \tag{E.34}$$

where A, B and C are defined in (E.27).

APPENDIX F – Parameters of the two-area test systems

F.1 SMIB test system parameters

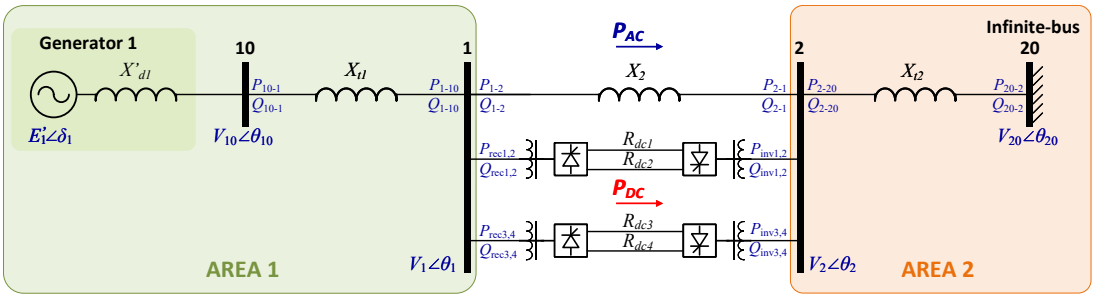

Figure F.1 – SMIB test system with parallel AC and DC transmission.

This appendix section presets the parameters regarding the initial condition (power flow) of the SMIB test system presented in Section 8.1.1. The line resistances of the HVDC poles are $R_{dc1} = R_{dc2} = R_{dc3} = R_{dc4} = 5\ \Omega$ and the line reactances are presented in Table F.1. The power flow of each operating point is presented in Figures F.2 to F.5 and the active and reactive power drained by each converter at the initial condition is presented in Tables F.2 and F.3, for a 100 MVA power base.

Table F.1 – Reactances of the system

$X'_{d1}(\%)$	$X_{t1}(\%)$	$X_2(\%)$	$X_{t2}(\%)$
0.18851	0.125	4.0	0.1

Table F.2 – Active and reactive power drained by the HVDC converters at the rectifier side, at each operating point.

Operating	Pole 1		Pole 2		Pole 3		Pole 4	
Point	P_{rec1}	Q_{rec1}	P_{rec2}	Q_{rec2}	P_{rec3}	Q_{rec3}	P_{rec4}	Q_{rec4}
1	5	1.7268	5	1.7268	5	1.7268	5	1.7268
2	10	4.0762	10	4.0762	10	4.0762	10	4.0762
3	15	6.9273	15	6.9273	15	6.9273	15	6.9273
4	20	10.216	20	10.216	20	10.216	20	10.216

Table F.3 – Active and reactive power drained by the HVDC converters at the inverter side, at each operating point.

Operating	Pole 1		Pole 2		Pole 3		Pole 4	
Point	P_{inv1}	Q_{invc1}	P_{inv2}	Q_{inv2}	P_{inv3}	Q_{inv3}	P_{inv4}	Q_{inv4}
1	-4.9805	1.8735	-4.9805	1.8735	-4.9805	1.8735	-4.9805	1.8735
2	-9.9219	4.3186	-9.9219	4.3186	-9.9219	4.3186	-9.9219	4.3186
3	-14.824	7.2321	-14.824	7.2321	-14.824	7.2321	-14.824	7.2321
4	-19.688	10.555	-19.688	10.555	-19.688	10.555	-19.688	10.555

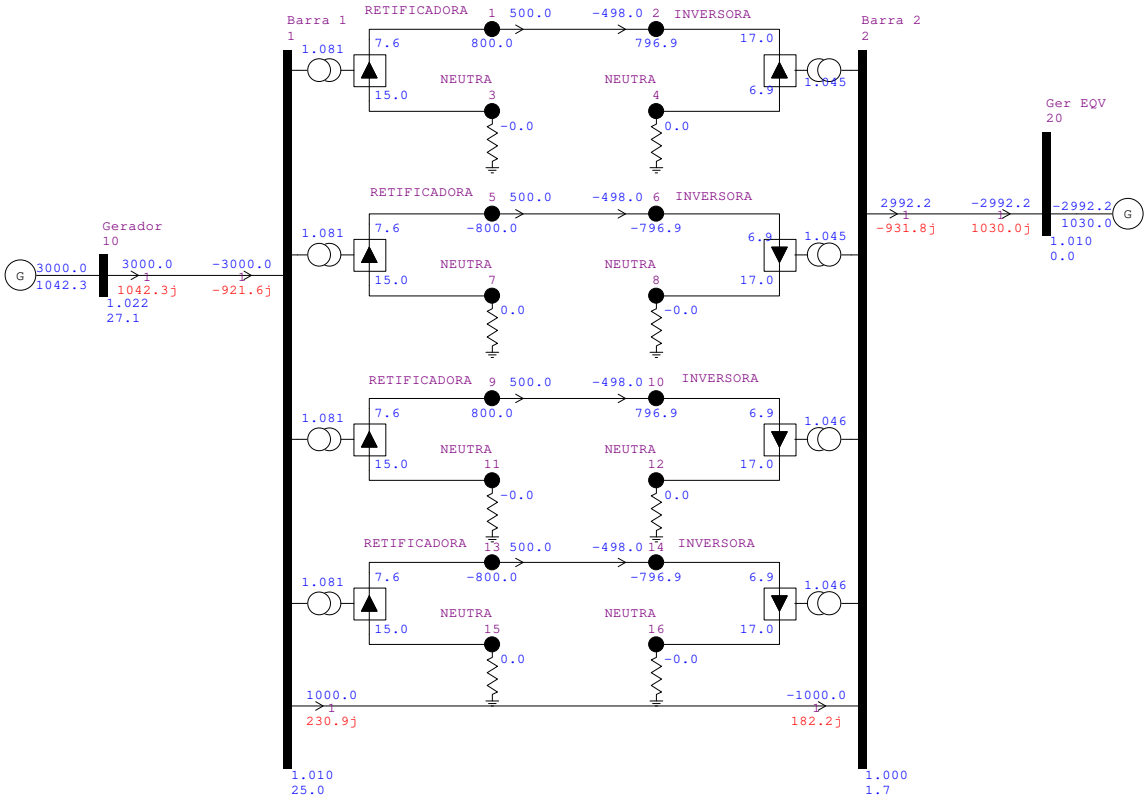

Figure F.2 – SMIB test system power flow, operating point 1.

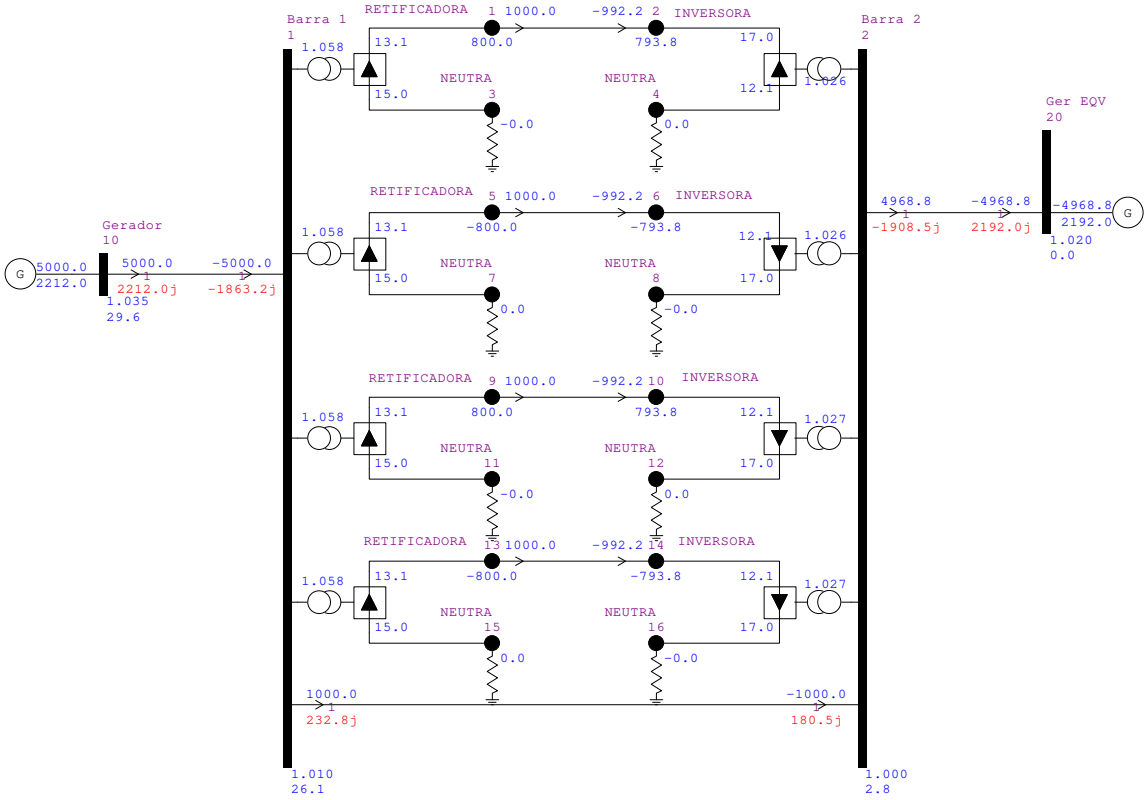

Figure F.3 – SMIB test system power flow, operating point 2.

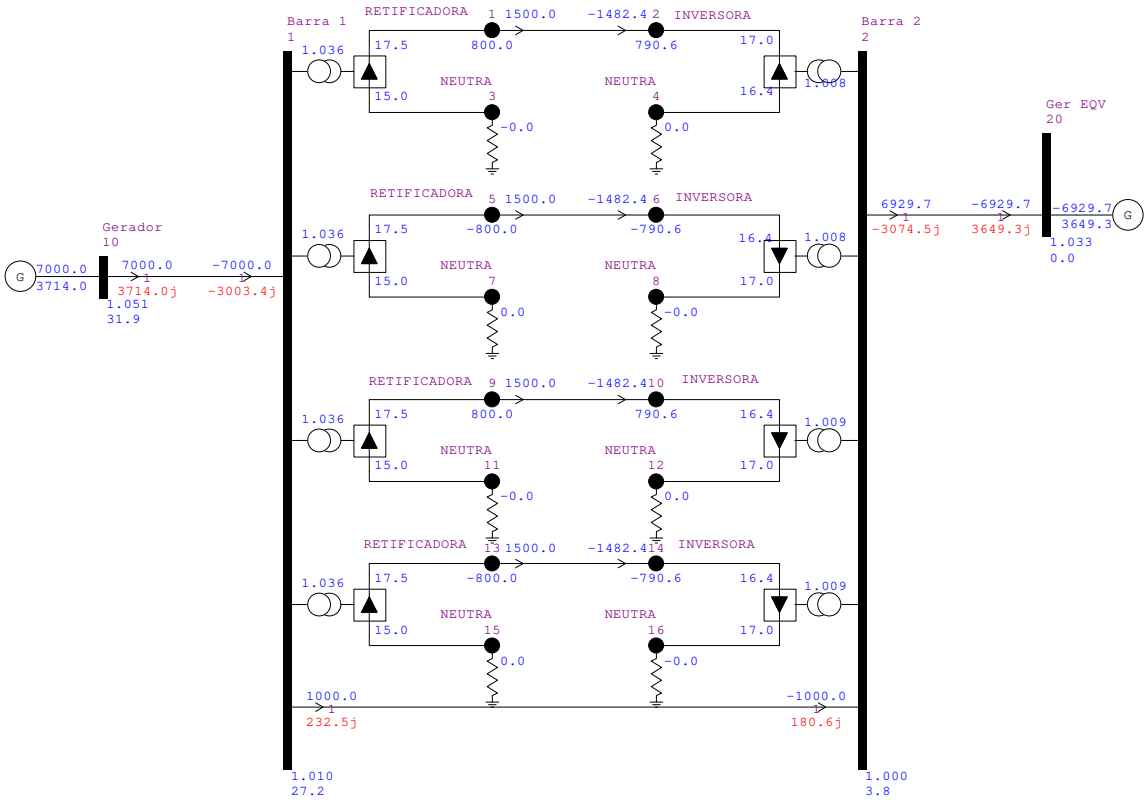

Figure F.4 – SMIB test system power flow, operating point 3.

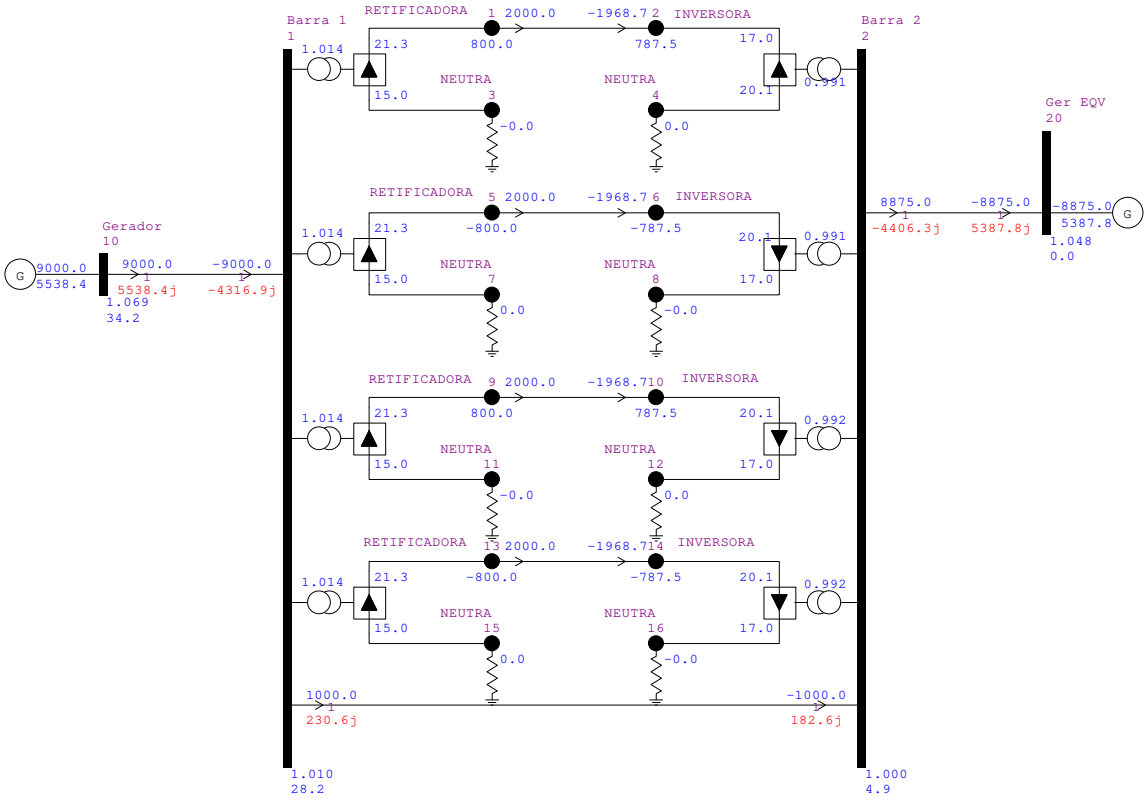

Figure F.5 – SMIB test system power flow, operating point 4.

F.2 Two-machines test system parameters

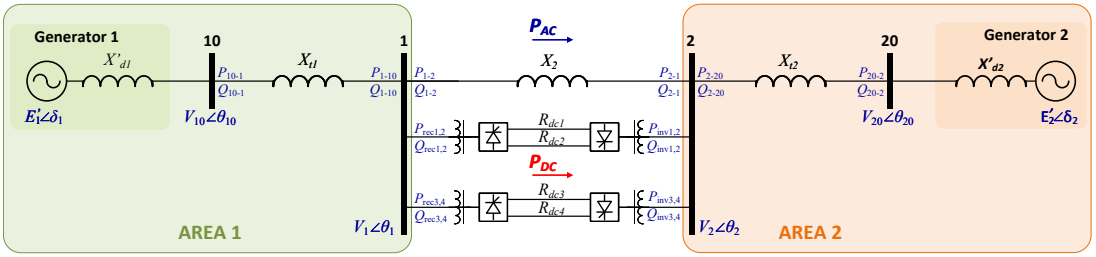

Figure F.6 – Two-machine system with parallel AC and DC transmission.

This appendix section presets the parameters regarding the initial condition (power flow) of the two-machines test system presented in Section 8.2.1. The line resistances of the HVDC poles are $R_{dc1} = R_{dc2} = R_{dc3} = R_{dc4} = 5\ \Omega$ and the line reactances are presented in Table F.4. The power flow of each operating point is presented in Figures F.7 to F.10 and the active and reactive power drained by each converter at the initial condition is presented in Tables F.5 and F.6, for a 100 MVA power base.

Table F.4 – Reactances of the system

$X'_{d1}(\%)$	$X_{t1}(\%)$	$X_2(\%)$	$X_{t2}(\%)$	$X'_{d2}(\%)$
0.18851	0.125	4.0	0.03	0.07

Table F.5 – Active and reactive power drained by the HVDC converters at the rectifier side, at each operating point.

Operating	Pole 1		Pole 2		Pole 3		Pole 4	
Point	P_{rec1}	Q_{rec1}	P_{rec2}	Q_{rec2}	P_{rec3}	Q_{rec3}	P_{rec4}	Q_{rec4}
1	5	1.7268	5	1.7268	5	1.7268	5	1.7268
2	10	4.0762	10	4.0762	10	4.0762	10	4.0762
3	15	6.9273	15	6.9273	15	6.9273	15	6.9273
4	20	10.216	20	10.216	20	10.216	20	10.216

Table F.6 – Active and reactive power drained by the HVDC converters at the inverter side, at each operating point.

Operating	Pole 1		Pole 2		Pole 3		Pole 4	
Point	P_{inv1}	Q_{invc1}	P_{inv2}	Q_{inv2}	P_{inv3}	Q_{inv3}	P_{inv4}	Q_{inv4}
1	-4.9805	1.8735	-4.9805	1.8735	-4.9805	1.8735	-4.9805	1.8735
2	-9.9219	4.3186	-9.9219	4.3186	-9.9219	4.3186	-9.9219	4.3186
3	-14.824	7.2321	-14.824	7.2321	-14.824	7.2321	-14.824	7.2321
4	-19.688	10.555	-19.688	10.555	-19.688	10.555	-19.688	10.555

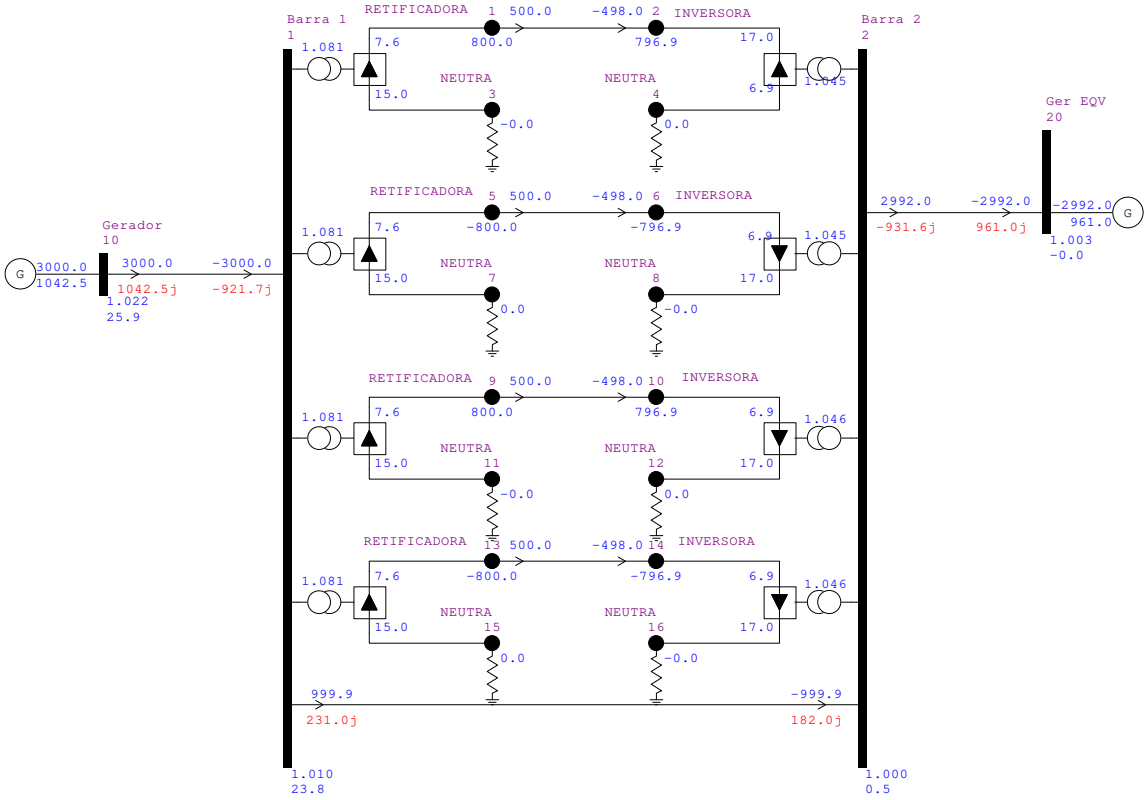

Figure F.7 – Two-machines test system power flow, operating point 1.

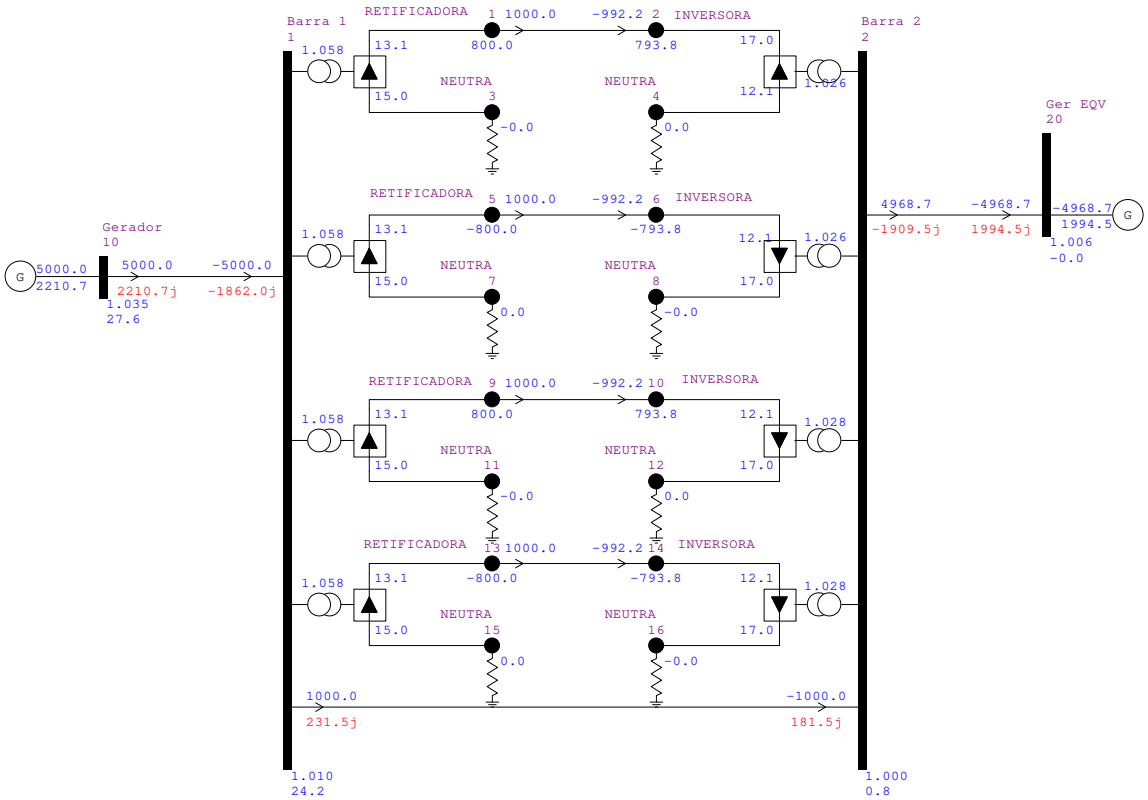

Figure F.8 – Two-machines test system power flow, operating point 2.

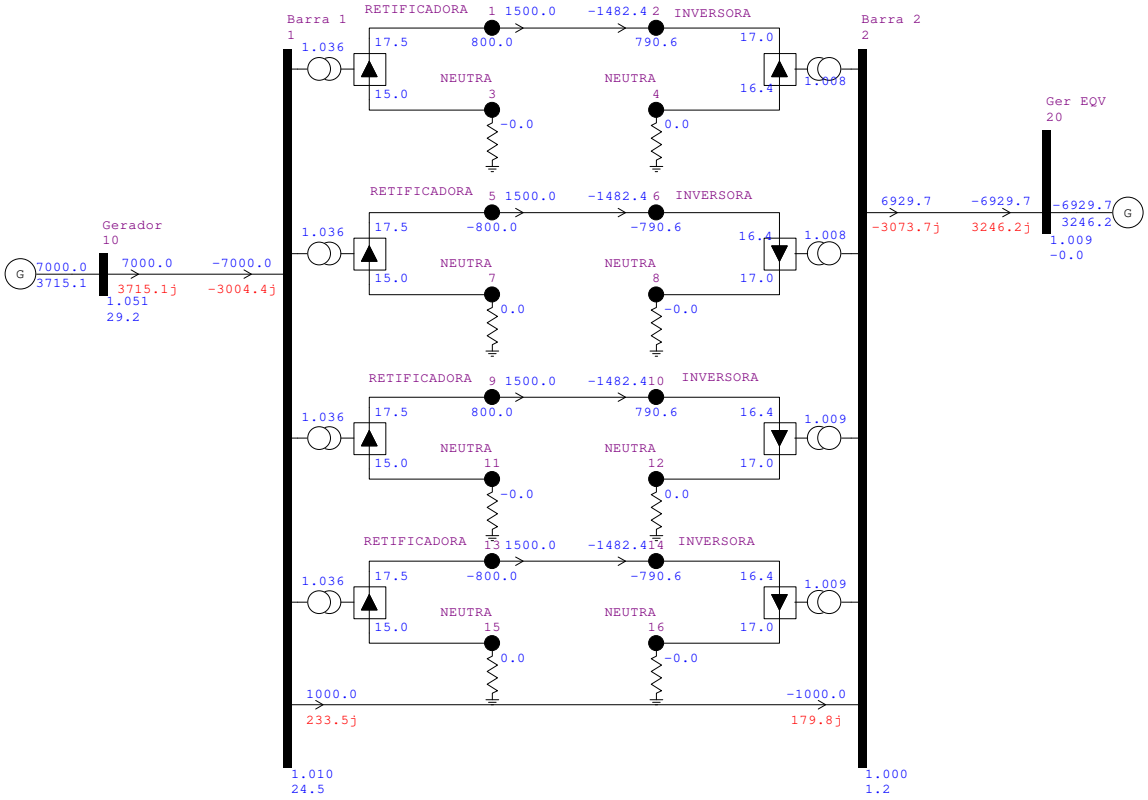

Figure F.9 – Two-machines test system power flow, operating point 3.

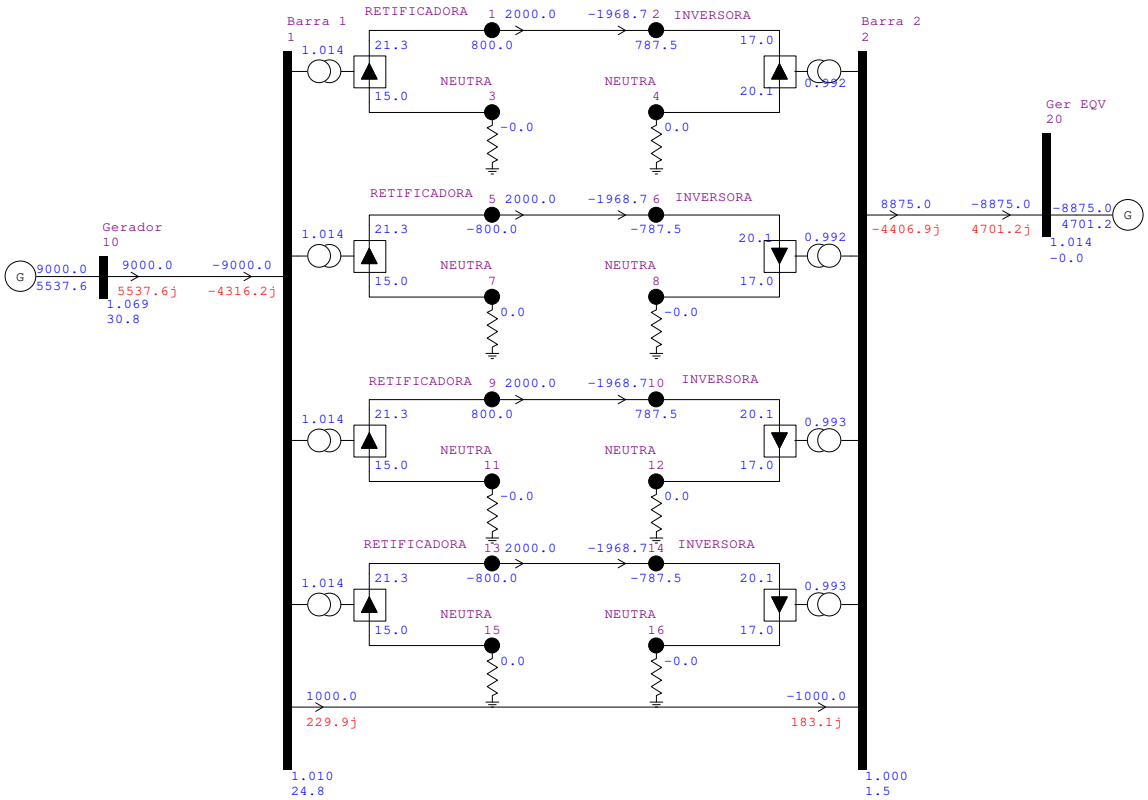

Figure F.10 – Two-machines test system power flow, operating point 4.

F.3 Two-machines test system with shunt and load parameters

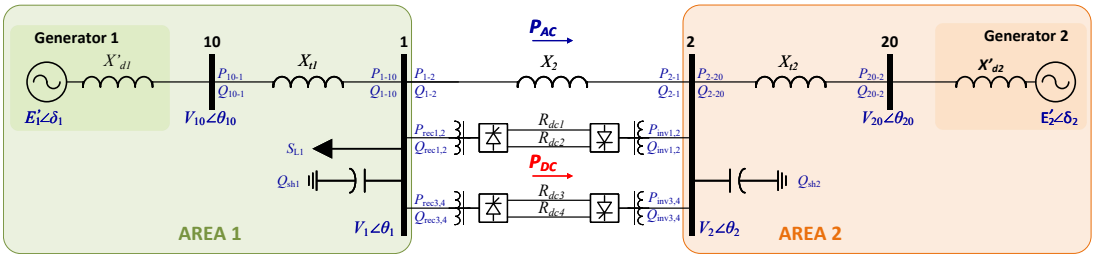

Figure F.11 – Two-machine system with parallel AC and DC transmission, with shunt capacitor banks/filters and load.

This appendix section presets the parameters regarding the initial condition (power flow) of the two-machines test system presented in Section 9.2.1. The line resistances of the HVDC poles are $R_{dc1} = R_{dc2} = R_{dc3} = R_{dc4} = 5\ \Omega$ and the line reactance of the AC line is $X_2 = 4\%$ in a 100 MVA power base. The parameters of the equivalent generators including their transient reactances and the transformers reactances are presented in Table F.7. The power flow of each operating point is presented in Figures F.7 to F.10 and the active and reactive power drained by each converter at the initial condition is presented in Tables F.8 and F.9, for a 100 MVA power base.

Table F.7 – Equivalent generator parameters - Two-machine system, with shunt capacitor banks/filters and load.

	Operating Point	Number of GUs	X'_d/GU (%)*	H/GU (s)	Base (MVA)	X'_d (%)$^\diamond$	X_t (%)$^\diamond$
Eq. gen. 1	1	39	32.0	4.8	679	0.12084	0.08013
	2	42	32.0	4.8	679	0.11221	0.0744
	3	50	32.0	4.8	679	0.09426	0.0625
	4	42	32.0	4.8	679	0.11221	0.0744
	5	39	32.0	4.8	679	0.12084	0.08013
Eq. gen. 2	1-5	1	35.0	3.5	50000	0.07	0.03

*at the generator power base.
$^\diamond$for a 100 MVA power base.

Table F.8 – Active and reactive power drained by the HVDC converters at the rectifier side, at each operating point.

Operating	Pole 1		Pole 2		Pole 3		Pole 4	
Point	P_{rec1}	Q_{rec1}	P_{rec2}	Q_{rec2}	P_{rec3}	Q_{rec3}	P_{rec4}	Q_{rec4}
1	5	1.7268	5	1.7268	5	1.7268	5	1.7268
2	10	4.0762	10	4.0762	10	4.0762	10	4.0762
3	20	10.2156	20	10.2156	20	10.2156	20	10.2156
4	20	10.2156	20	10.2156	20	10.2156	20	10.2156
5	20	10.2156	20	10.2156	20	10.2156	20	10.2156

Table F.9 – Active and reactive power drained by the HVDC converters at the inverter side, at each operating point.

Operating	Pole 1		Pole 2		Pole 3		Pole 4	
Point	P_{inv1}	Q_{invc1}	P_{inv2}	Q_{inv2}	P_{inv3}	Q_{inv3}	P_{inv4}	Q_{inv4}
1	-4.9805	1.8735	-4.9805	1.8735	-4.9805	1.8743	-4.9805	1.8743
2	-9.9219	4.3186	-9.9219	4.3186	-9.9219	4.3212	-9.9219	4.3212
3	-19.6875	10.5551	-19.6875	10.5551	-19.6875	10.5638	-19.6875	10.5638
4	-19.6875	10.5551	-19.6875	10.5551	-19.6875	10.5638	-19.6875	10.5638
5	-19.6875	10.5551	-19.6875	10.5551	-19.6875	10.5638	-19.6875	10.5638

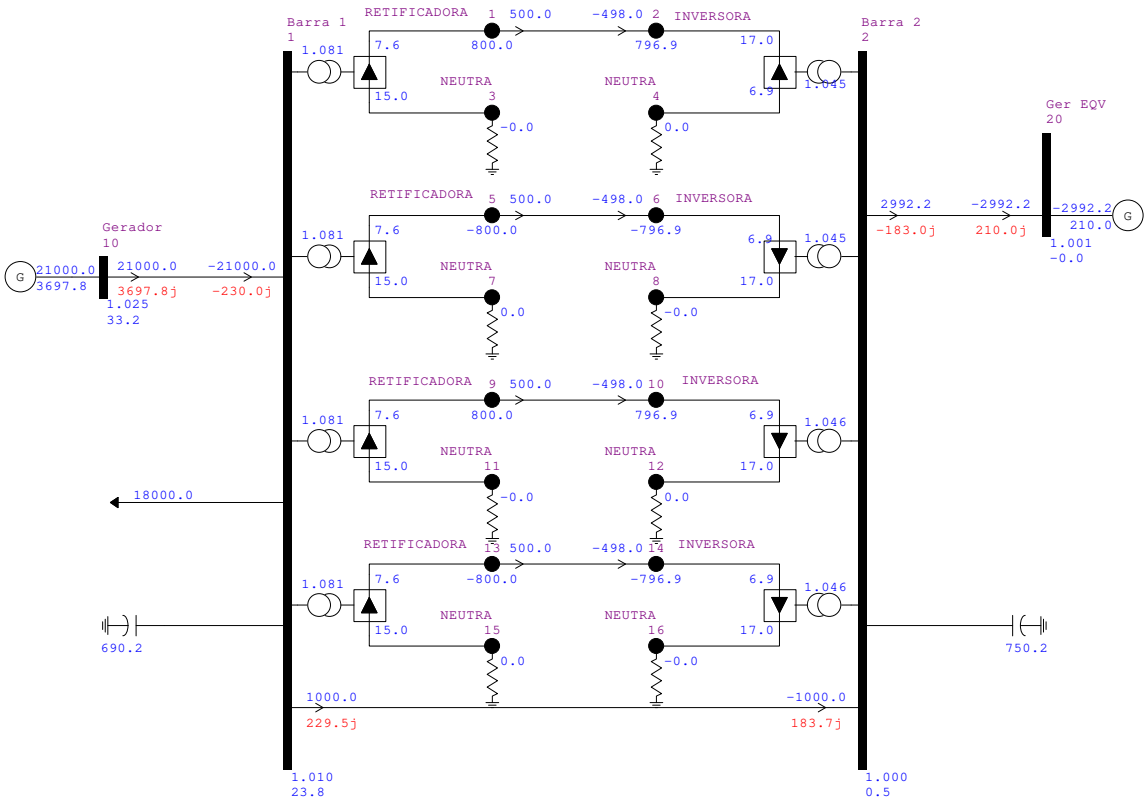

Figure F.12 – Two-machines test system power flow, operating point 1.

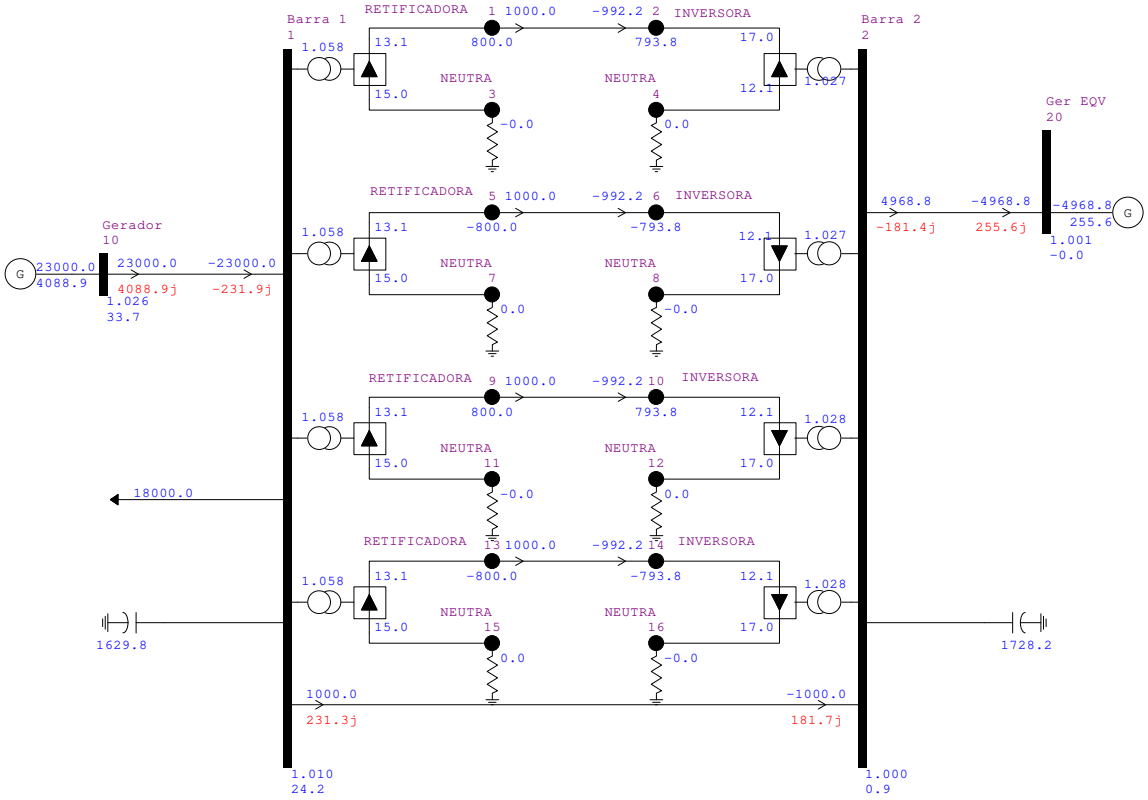

Figure F.13 – Two-machines test system with shunt capacitor banks/filters and load power flow, operating point 2.

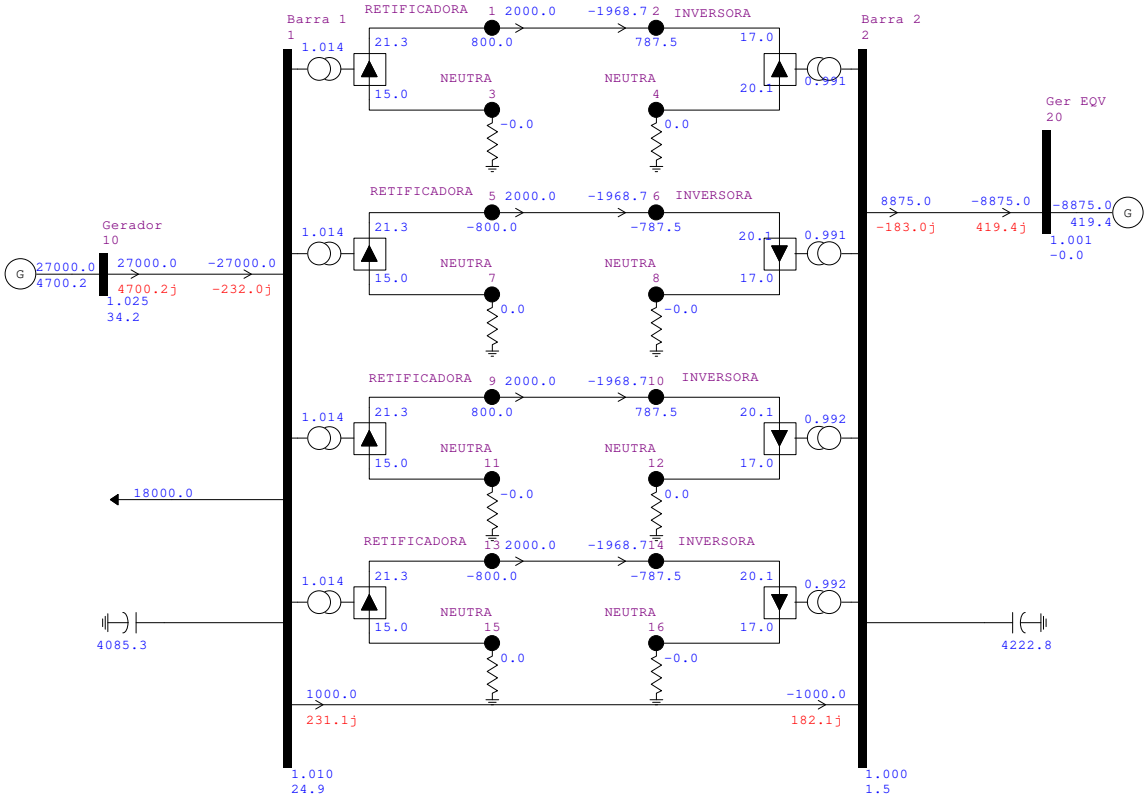

Figure F.14 – Two-machines test system with shunt capacitor banks/filters and load power flow, operating point 3.

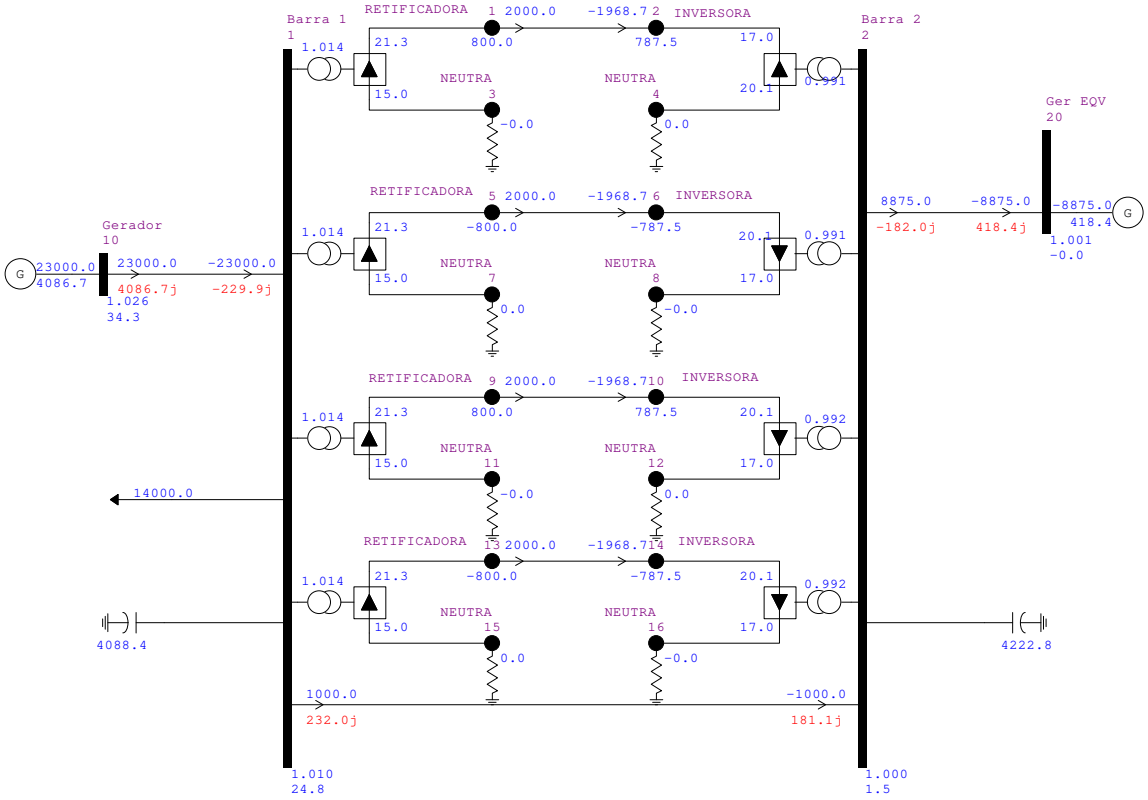

Figure F.15 – Two-machines test system with shunt capacitor banks/filters and load power flow, operating point 4.

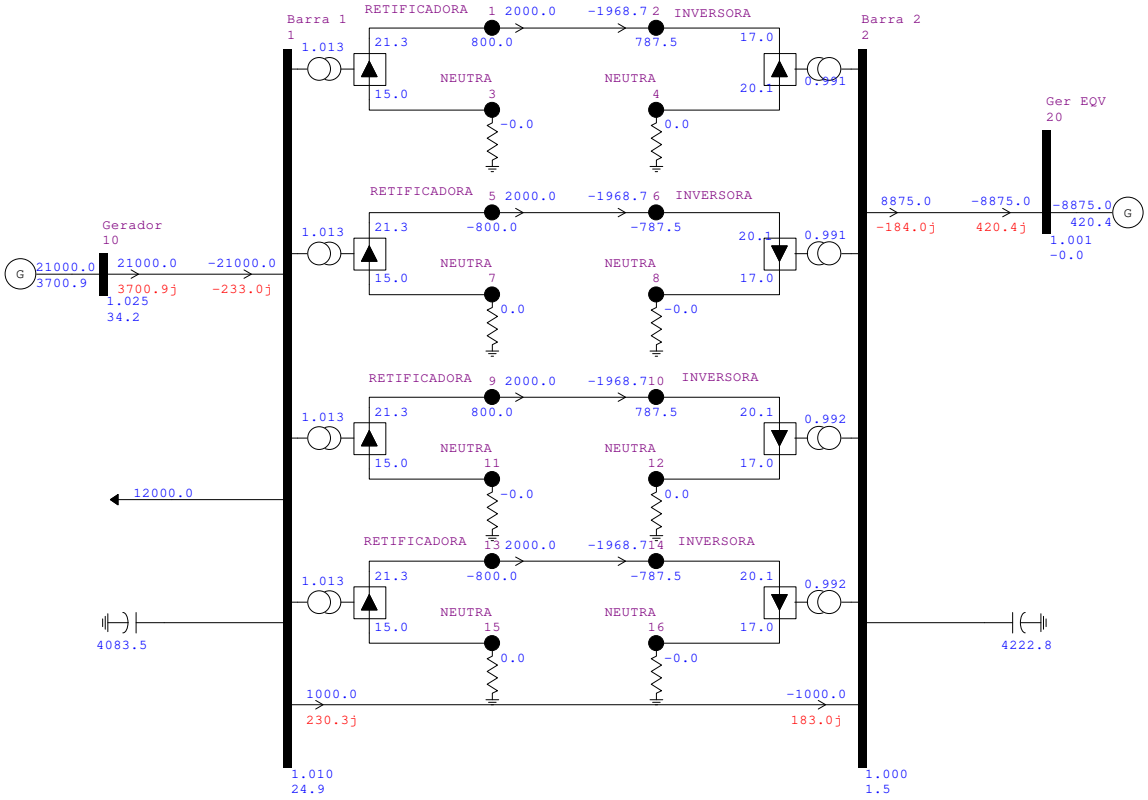

Figure F.16 – Two-machines test system with shunt capacitor banks/filters and load power flow, operating point 5.

APPENDIX G – Parameters of the HVDC converters

This appendix chapter presents the parameters used to model the HVDC converters of the test system used in Sections 8.1.1, 8.2.1, and 9.2.1. The converter were modeled using the predefined MD01 model of the ANATEM software (CEPEL; ELETROBRAS, 2020a) with the following parameters.

Parameters of the control model of the AC-DC converters:

```
DMCV MD01
(
(..... retificador
(No)   (Vmn)(Tvp)(Tx1)(Td1)(Yal)(Tmx)(Amx)(Gmx)(Stx) F
11    0.45  0.5 18.6 2.00 0.00  1.0 4.51.051440.99
(No)   (Tvd)(Tvs)(Vdn)(Vdx)(Frn)(Imn)(Imx)(Img)(Ki )(Kp )(To )(Kcg)
11   .0054  .08 32.6  93. 35.0  10. 140.     2500. 102..0017
(
(..... inversor
(No)   (Vmn)(Tvp)(Tx1)(Td1)(Yal)(Tmx)(Amx)(Gmx)(Stx) F
12    0.45  0.5 18.6 2.00 0.00  1.0 4.51.051440.99
(No)   (Tvd)(Tvs)(Vdn)(Vdx)(Frn)(Imn)(Imx)(Img)(Ki )(Kp )(To )(Kcg)
12    .004  .05 27.9  93. 30.0  10. 140.  10.5000.  47..0014
(
999999
```

Parameters of the AC-DC converter and association with the respective control model:

```
DCNV
(Nc)   (Gkb)(Amn)(Amx)(Gmn)( Mc )u( S1 )u( S2 )u( S3 )u( S4 )u
1           5. 163.          11
2          90.       17.     12
(Nc)   (Gkb)(Amn)(Amx)(Gmn)( Mc )u( S1 )u( S2 )u( S3 )u( S4 )u
3           5. 163.          11
4          90.       17.     12
(
```

```
(Nc)   (Gkb)(Amn)(Amx)(Gmn)( Mc )u( S1 )u( S2 )u( S3 )u( S4 )u
5           5. 163.         11
6          90.       17.    12
(Nc)   (Gkb)(Amn)(Amx)(Gmn)( Mc )u( S1 )u( S2 )u( S3 )u( S4 )u
7           5. 163.         11
8          90.       17.    12
999999
```

Parameters for commutation failure of the AC-DC converters:

```
DFCM
(Nm) (Vfc) (Gfc) (Thd)
2        14.1 0.016   ( POLO 1 )
4        14.1 0.016   ( POLO 2 )
6        14.1 0.016   ( POLO 3 )
8        14.1 0.016   ( POLO 4 )
999999

DFCM
(Nm) (Vfc) (Gfc) (Thd)
   2        14.1 0.016   ( POLO 1 )
   4        14.1 0.016   ( POLO 2 )
   6        14.1 0.016   ( POLO 3 )
   8        14.1 0.016   ( POLO 4 )
999999
```